The Hashemite Kingdom of Jordan
Scientific Research Support Fund
The Hashemite University

JJEES

Jordan Journal of Earth and Environmental Sciences

Indexed by Scopus
ELSEVIER

Volume (16) Number (4)

Cover photo © Prof. Mahmoud Abu-Allaban

JJEES is an International Peer-Reviewed Research Journal

ISSN 1995-6681 jjees.hu.edu.jo December 2025

Jordan Journal of Earth and Environmental Sciences (JJEES)

JJEES is an International Peer-Reviewed Research Journal, Issued by Deanship of Scientific Research, The Hashemite University, in corporation with, the Jordanian Scientific Research Support Fund, the Ministry of Higher Education and Scientific Research.

Editorial Board:

Associate Editorial Board: (Arranged Alphabetically)

International Advisory Board: (Arranged Alphabetically)

Editorial Board Support Team:

Submission address:

Manuscripts should be submitted electronically to the following e-mail:

jjees@hu.edu.jo

For more information and previous issues:

www.jjees.hu.edu.jo

Hashemite Kingdom of Jordan

Scientific Research Support Fund

Hashemite University

Jordan Journal of Earth and Environmental Sciences

JJEES

An International Peer-Reviewed Scientific Journal

Financed by the Scientific Research Support Fund

Volume 16 Number (4)

http:// jjees.hu.edu.jo/

ISSN 1995-6681

Natural Cave in Northwestern Jordan's Sediments: A Geological Marvel Displayedat Janneen Essafa.
By Prof. Mahmoud Abu-Allaban.

JJEES
Jordan Journal of Earth and Environmental Sciences

JJEES

JJEES (2025) 16 (4): 306-314
ISSN 1995-6681

Jordan Journal of Earth and Environmental Sciences

Current Practice of Construction Waste Minimization: A Case Study in Nepalese Contractors

Raghu Nath Prajapati[1*] and Sabir Baidya[2]

[1]Nepal Engineering College, Changunarayan, Bhaktapur, Nepal
[2]Nepal Engineering College, Changunarayan, Bhaktapur, Nepal

Received on March 2, 2025, Accepted on March 28, 2025

Abstract

Effective construction management relies on an efficient waste minimization system that processes updated information accurately. This study aims to assess the current practices and knowledge in construction waste management and propose a system to minimize and control waste. The objective is to reduce waste on construction sites and provide easy access to project status information through a comprehensive database, ultimately increasing contractor profits. A survey and fieldwork research were conducted to examine existing waste minimization practices and gather contractors' insights on implementing a new system. The findings revealed that current practices are primarily manual and lack effective systems or software for waste minimization. Most contracting companies do not track the quantities, amounts, or percentages of material waste. The main challenge identified was the absence of user-friendly software for waste management and control. Contractors attributed the waste problem to reliance on traditional manual methods and the lack of a structured waste minimization system. While contractors acknowledged a limited focus on waste minimization, they did not perceive a shortage of qualified personnel as a significant issue. Survey responses varied widely, reflecting a lack of accurate knowledge due to the absence of consistent feedback and record-keeping from past projects. The materials with the highest waste percentages were identified as formwork (22.69%), sand (18.23%), and aggregate (15.77%). Contractors expressed a strong willingness to adopt user-friendly software, with many preferring Microsoft Excel spreadsheets for their ease of use.

Keywords: *Contract company; Construction project; Construction waste minimization, MS-Excel, Waste minimization software,*

1. Introduction

Waste in the construction industry has been the subject of several research projects worldwide in recent years. These studies have explored both the environmental damage, resulting from material waste generation and the economic implications associated with it (Agyekum, 2012; Elshaboury et al., 2022; Formoso et al., 2002). Material waste on construction sites varies in cause. Still, it is notably significant due to its substantial contribution to construction costs (Kennouche et al., 2022), typically accounting for about 50% to 60% (Popoola et al., 2018; Tafesse, 2021). This finding is particularly concerning, given the scarcity of these resources. Recognized as a significant problem, material waste in the construction industry impacts both operational efficiency and environmental sustainability (Can et al., 2023; Khalas & Patel, 2018). According to Ekanayake & Ofori (2004), construction material waste is defined as any material, excluding earth materials, that needs to be transported away from the construction site or repurposed within it due to damage, excess, non-use, non-compliance with specifications, or as a by-product of the construction process.In the United Kingdom, an investigation by Skoyles (1976) conducted during the 1960s and 1970s across 114 building sites distinguished between direct waste, i.e., irreparably damaged or lost materials, and indirect waste, i.e., monetary loss without physical material loss (Formoso et al., 2002; Ogunseye et al., 2023). A similar municipal solid waste problem in Lebanon is also being faced (Sawaya et al., 2023). In the United States, Gavilan & Bernold (1994) analyzed waste in masonry foundations, timber frames, and sheetrock drywall, identifying significant waste from cutting residuals, non-reusable consumables, packaging, and improper handling. Research in the Netherlands monitored waste from seven materials in five house-building projects, attributing waste to design flaws, material supply issues, and poor handling during transportation and storage (Bossink, 2002). In Brazil, it is estimated that direct and indirect waste account for 18% of the total material weight in an 18-storey residential project, revealing high waste percentages in materials such as mortar, resulting in additional costs (Formoso et al., 2002). In Egypt, a survey of 35 top contractors found that timber frameworks had the highest waste rate, followed by sand, steel, and cement, with waste percentages exceeding accepted norms for most materials (Daoud et al., 2021). In Nepal, studies on 30 building projects reported reinforcement waste ranging from 2% to 9%, with an average of 4.4%, which falls within the permissible limits set by Nepal's building construction norms (Adhikari et al., 2021; Dhungana et al., 2023). The 3R approach (Reduce, Reuse, and Recycle) is a common term in solid waste management but is rarely applied in the construction sector (Ogunmakinde et al., 2022). There is a perception among contractors that waste is not valueless if it can be sold to waste dealers (Siregar & Kustiani, 2019).

* Corresponding author e-mail: raghunp@nec.edu.np

Partial studies from various countries confirm that waste represents a significant percentage of production costs, necessitating an effective system with updated information to reduce construction waste at the source (Formoso et al., 2002). The construction sector is a vital component of the Nepalese economy, employing over one million people and contributing approximately 10% to 11% of the GDP. About 60% of the nation's development budget is executed through contractors (Acharya & Shrestha, 2021). Over the past two decades, the sector has witnessed significant progress, marked by improvements in management skills, operational capacity, financial stability, and technical capabilities. Enhancements in this sector can have a substantial impact on the national economy (Kusi et al., 2018). The construction industry in Nepal faces several challenges related to material waste. These include the absence of an effective tracking system for construction materials, insufficient knowledge about material waste generated during construction, a lack of research on construction waste, inadequate waste minimization and control measures, and the lack of prioritization of waste minimization in the industry. Despite these advancements, a large amount of construction waste is generated, especially in major infrastructure, commercial building, and housing projects. Issues such as excessive material wastage, improper waste management, and low awareness of waste reduction are prevalent. However, research on construction waste in Nepal is limited, and there is no established system for recording quantitative data on waste generation. Thus, the main objective of this study is to understand and assess the systems and common practices for waste minimization currently adopted by Nepalese contractors.

This study provides contractors with a comprehensive understanding of waste tracking, the extent of material wastage on their construction sites, and the overall profit or loss associated with materials and projects. It includes material reconciliation at various stages of the project, comparing planned versus ordered, ordered versus actual supply, and actual supply versus actual usage. This data is crucial for monitoring project efficiency. The computerized system generates data on material wastage, which is vital for contractors from a quality and reputation perspective. Excessive material consumption indicates wastage and financial loss, while under consumption, raises quality concerns, affecting the contractor's reputation.

2. Methodology

The research methodology for this study was structured into three main stages: Literature Review, Field Survey, and Questionnaire. Initially, an extensive literature review was conducted focusing on the causes of construction waste, techniques for minimizing waste, systems for waste minimization and control, and international studies on measuring material waste. Following the literature review, a comprehensive field survey was conducted to evaluate the current practices in waste minimization and control. Data collection involved gathering documents such as stock books, running bills, and bills of quantities from three construction sites in Kathmandu, Nepal: the Kathmandu District Court Building at Babarmahal, the Telecom Building at Sundhara, and the Sanima Bikas Bank Building at Naxal (Figure 1). The collected data documents were reviewed and approved by the institute, and informed consent was obtained from all participants from the data-providing organization. The research concentrated on four units within these sites: the Engineering Unit, Purchasing Unit, Tracking Unit, and Store Unit, which are also current practices in Nepalese construction for management and control, as shown in Figure 2.

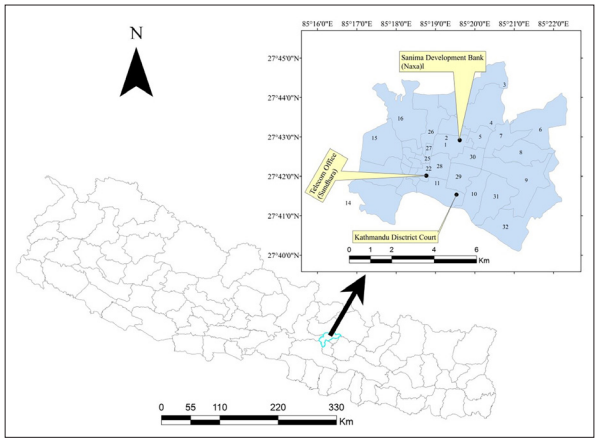

Figure 1. Study area

Based on insights from the literature review and field survey, a structured questionnaire was developed. This type of structured questionnaire aligns with the research work by Al-Rifai & Amoudi (. The questionnaire was divided into six sections: Company Profile, Waste Minimization and Control System, Problems with Current Waste Minimization and Control System, Importance of Waste Minimization and Control, Level of Material Waste in Construction Projects, and the Need for Computer Applications in Waste Minimization and Control. Designed in a closed format, the questionnaire aimed to gather specific responses regarding current practices and the perceived need for a computerized system. The data from the questionnaire were statistically analyzed using Excel Software.

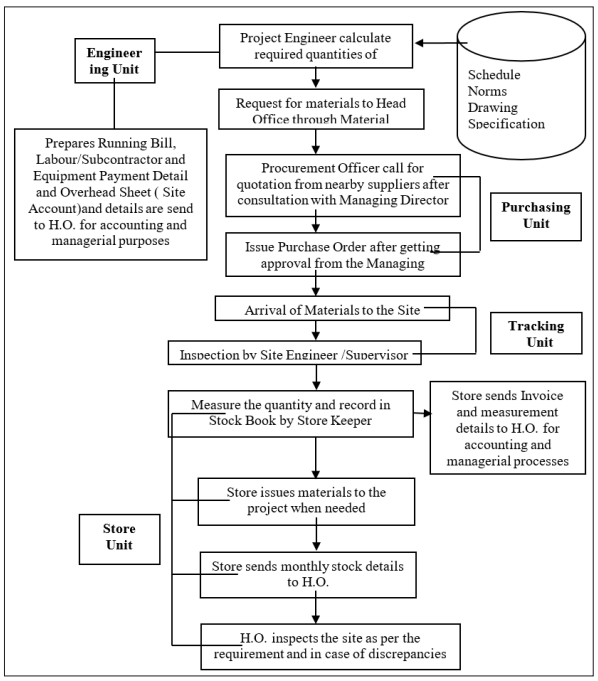

Figure 2. Current Practice of Nepalese Construction for Material Management and Control

Based on the findings of the field survey and questionnaire responses, conclusions and recommendations were formulated using the survey results and data analysis, as illustrated in the research flow chart (Figure 3).

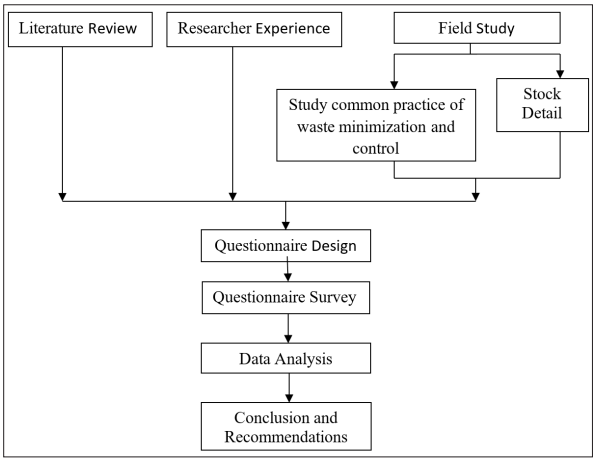

Figure 3. Flow Chart for Conducting Research

This research targeted contracting companies classified under the "A" category, as registered with the Contractor's' Association of Nepal. According to the association, there are 194 such companies. A sample of 19 "A" class Nepalese construction companies was selected, representing about 10% of the total population. Out of these, responses were obtained from 13 companies. The sample was chosen randomly, taking into account the companies' turnover and work experience. Data for this research was collected through site visits and questionnaires. Frequency distribution and percentage were used to describe various aspects of the data. Excel software was utilized for data analysis. The conclusions and recommendations were derived from the analysis of survey data and fieldwork research.

3. Results and Discussion

The results illustrate and discuss the characteristics of the study population, current practices for waste minimization and control, problems with current practices, the importance of waste minimization and control, and the level of material waste in construction projects.

3.1 Characteristics of the study population

The year of establishment, sector of specialization, total volume of construction works executed, annual net worth, and qualification of employees of contracting companies were examined to determine the financial and technical capabilities of these companies. Table 1 shows that 69.23 % of the contracting companies were established before 1989 AD, and 30.76 % were established after 1989 AD. This indicates that most of the companies are established, with more than 24 years of experience.

Table 1. Characteristics of Contracting Companies

Variable	Category	Frequency	Percentage (%)
Year of Establishment	Before 2045 B.S.	9	69.23
	2045 B.S. and After 2045 B.S.	4	30.76
Field of Specialization	Building	13	100
	Building + Road	12	92.3
	Building + Road + Water Supply/Sanitation	4	30.76
Volume of Construction Works (Rs. Million)	Less than 10	0	0
	10 – 30	0	0
	31 – 50	0	0
	51 – 100	3	23.07
	>100	10	76.92
Annual Net Worth (Rs. Million)	Less than 30	8	61.53
	31 – 50	2	15.38
	51 – 75	2	15.38
	76 – 100	0	0
	>100	1	7.69
Qualification of Employees	Ph.D.	0	0
	Masters	62	6.09
	Bachelor	165	16.22
	Certificate	273	26.84
	SLC and Less	505	49.65

The characteristics of contracting companies provide valuable insights into the structure and dynamics of the construction industry. In terms of the year of establishment, the majority of contracting companies (69.23%) were established before 1989 AD, while only 30.76% were founded in or after 1989 AD. This dynamic indicates that most companies in the sector possess long-standing experience, which could imply stability and expertise in the industry. However, the presence of newer firms suggests that the industry is evolving and attracting new entrants, possibly driven by growing infrastructure demands and business opportunities.

Regarding the field of specialization, all the surveyed contracting companies (100%) are involved in building construction. Additionally, a significant proportion (92.30%) of firms also undertake road construction, reflecting the need for well-developed transportation infrastructure. However, only 30.76% of companies have expanded their services to include water supply and sanitation projects, suggesting a relatively lower focus on public utility infrastructure. This specialization trend highlights a strong inclination toward building and road construction, with fewer companies diversifying into essential water and sanitation projects.

The volume of construction works in terms of financial capacity reveals that no companies operate on projects valued below Rs. 50 million. About 23.07% of firms handle projects ranging from Rs. 51–100 million, indicating a moderate level of construction activity. However, the majority (76.92%) are engaged in projects exceeding Rs. 100 million, signifying the dominance of large-scale firms capable of handling high-value infrastructure projects. The annual net worth distribution of contracting companies indicates that a significant proportion (61.53%) of firms have a net worth of less than Rs. 30 million, suggesting that most companies operate at a moderate financial level. Around 15.38% of firms fall within the Rs. 31–50 million and Rs. 51–75 million categories, showing a moderate distribution of financially stronger firms. However, only 7.69% of firms have a net worth exceeding Rs. 100 million.

In terms of employee qualifications, the distribution of educational backgrounds indicates a diverse workforce. There are no employees with Ph.D. qualifications, while only 6.09% hold a master's degree. A slightly higher percentage (16.22%) has a bachelor's degree, reflecting a moderate level of higher education among professionals in the industry. The majority of employees (26.84%) hold certificate-level qualifications, while the largest proportion (49.65%) has only an SLC or lower education level. This proportion suggests that the construction industry heavily relies on semi-skilled and unskilled labor, with a relatively smaller percentage of highly qualified professionals. Overall, the data highlights that the construction industry is largely composed of experienced firms with a strong focus on building and road projects. The workforce is primarily composed of semi-skilled labor, with limited representation from higher academic qualifications.

3.2 Waste Minimization and Control System

The survey was conducted to reveal the current practice of contracting companies for waste minimization and control systems. The store unit, project unit, purchasing unit, and tracking unit were examined during the survey. Table 2 shows that only 15.38% of respondents prepare waste minimization plan prior to the commencement of the project. This indicates that most contracting companies do not prepare a waste minimization plan prior to the commencement of the project.

The results demonstrate that 76.92% keep up-to-date stock details of materials. Regarding receiving consumed and balance quantities, 69.23% maintain an up-to- date activity-wise record of material consumed versus norms consumption. 76.92% keep proper record of scrap detail with quantity, price, and amount, but only 30.76% calculate material waste quantity.This result indicates that the contracting companies are not well-informed about the actual quantity and amount of waste they are generating from their construction projects.

Table 2 shows that most contracting companies (84.61%) prepare the required material file needed for the project. 76.92% maintain an up-to-date record of material, labor, and equipment to know profit or loss at any stage of the project. However, only 38.46% of the records show activity-wise material requirements and material consumption. This result indicates that the amounts demanded by the site are not thoroughly checked to determine whether the demands are justified or not. The figure shows that most contracting companies do not maintain activity-wise material consumption data. 46.15% cross-check for quantity error in Running Bills with actual cost of construction, i.e., the contracting companies generally compare the quantity of running bills with the consumed quantity of material, labour/subcontractor, equipment, and overhead. In general, contracting companies compare the quantity of Running Bills with the consumed quantities of material, labour/ subcontractors, equipment, and overhead at the project site. Contracting companies (100%) cross-check the quantities demanded by the project site before issuing P.O. Only 61.53% maintain a systematic procedure for vendor rating. Other observations: 76.92% of contracting companies tally materials with the specifications and quantities mentioned in the P.O. and invoice before receiving the materials.

Table 3 represents the major problems with the current waste minimization and control system. The results show that the respondents (92.30%) agree that the lack of user-friendly software is the major problem for waste minimization and control. Most contracting companies (76.92%) believe the current situation of waste is due to the following simple traditional manual management. On the other hand, results show that 69.23% of contracting companies believe that the lack of a waste minimization system is another major problem. 53.84% of contracting companies partially agree with the lack of attention and non-realization of contractors towards waste minimization. 38.46% of respondents intermediately agree, which reveals that a significant number of respondents agree, suggesting that the shortage of Qualified Personnel is not a significant problem for waste minimization and control. The above results show that most contracting companies feel the need for computer software and a system for waste minimization and control.

Table 2. Current Practice of Waste Minimization and Control Systems

S.N.	Description	Contractors Response (Yes)	
		Frequency	Percentage (%)
A	Prepare a waste minimization plan prior to the commencement of the project	2	15.38
B	Store Unit		
1	Keep up-to-date stock details of materials regarding receiving, consumed & balance quantities	10	76.92
2	Calculation of material waste quantity, amount, and its percentage	4	30.76
3	Up-to-date activity-wise record of material consumed vs. normative consumption	9	69.23
4	Keep a proper record of scrap detail with quantity, price, and amount	10	76.92
C	Project Unit		
1	Prepare the required material file needed for the project	11	84.61
2	Record activity-wise material requirements and material consumption	5	38.46
3	Up-to-date record of material, labor, and equipment to know profit or loss at any stage of the project	10	76.92
4	Cross-check for quantity error in Running Bills with the actual cost of construction	6	46.15
D	Purchasing Unit		
1	Cross-checks for the quantities demanded by the project site before issuing P.O.	13	100
2	Maintain a systematic procedure for Vendor Rating	8	61.53
E	Tracking Unit		
1	Tally materials with specifications and quantity mentioned in the P.O. and invoice before receiving the materials	10	76.92

Table 3. Problems with the Current Waste Minimization and Control System

S.N.	Problem	Agree %	Intermediately Agree %	Disagree %
1	Little attention and non-realization of contractors towards waste minimization	15.38	53.84	30.76
2	Lack of a waste minimization system	69.23	30.76	
3	Simplicity in traditional manual management	76.92	23.07	
4	Lack of user friendly software for waste minimization and control	92.30		7.69
5	Shortage of Qualified Personnel	38.46	38.46	23.07

Table 4 presents the factors regarding the views, opinions, and realization of contractors on having a system for waste minimization and control. The results show that the majority of contracting companies believe that most of the factors listed in Table 4 help in waste minimization on construction sites. They believe that the systems that have the biggest impact on waste minimization are waste reduction (100%), eliminating duplication of material orders and addressing material issues (100%), and resolving problems related to late delivery and the required quantity needed for the project (100%).

On the other hand, the factor which they believe that the system helps is, to know exact quantities of materials required (84.61%), maintain up-to-date stock detail (92.30%), the total profit or loss of the project (84.61%), helps in preparing accurate bill of quantities (92.30%), increase awareness among contractors to decrease waste (92.30%), and reduce final cost of the project (84.61%). 61.53% of contracting companies believe the system helps in maintaining better relations with suppliers, and 76.92% view the system as helping in pricing bids.

Table 4. Importance of Waste Minimization and Control Systems

S.N.	Importance	Agree (%)	Intermediately Agree (%)	Disagree (%)
1	To know the exact quantities of materials required	84.61		15.38
2	Maintain up-to-date stock details	92.30	7.69	
3	Waste reduction	100.00		
4	Reduce duplication of material orders and material issues	100.00		
5	To know the total profit or loss of the project	84.61	15.38	
6	Better relations with suppliers	61.53	23.07	15.38
7	Reduce problems related to late delivery and the required quantity needed to the project	100.00		
8	Helps in preparing an accurate bill of quantities	92.30		7.69
9	Helps in pricing Bids	76.92	23.07	
10	Increase awareness among contractors to decrease waste	92.30	7.69	
11	Increases contractor's profit	69.23	30.76	
12	Reduce the final cost of the project	84.61	15.38	

As presented in Table 5, it highlights significant variations in waste percentages across different materials. Among all materials, formwork exhibited the highest waste rate, with an average of 22.69%, followed by sand (18.23%), and aggregate (15.77%). These high percentages suggest that temporary or bulk materials, which are prone to damage, loss, or inefficiencies in handling and usage, contribute significantly to construction waste. In contrast, steel (10.12%), cement (5.12%), and bricks (9.92%) displayed relatively lower waste percentages, indicating better control over these materials or their inherent durability.

A notable observation is the wide variation in reported waste percentages for all materials. It indicates inconsistencies in data collection and estimation across different projects. For instance, formwork waste ranged from 15% to 30%, while sand waste varied between 10% and 25%, and bricks between 1% and 20%. This broad range of responses suggests a lack of precise waste tracking mechanisms, potentially due to the absence of a standardized database or systematic documentation of material losses from past projects. The discrepancies in reported values could also be attributed to differences in project management practices, material handling efficiency, and on-site monitoring methods.

The findings underscore the importance of enhanced record-keeping and regular feedback mechanisms to accurately quantify and minimize material waste. Implementing data-driven waste management strategies and promoting awareness among construction professionals about material wastage can significantly reduce project inefficiencies and enhance sustainability in the construction sector.

Table 5. Material Waste and Variations in Construction Projects

S.N.	Material	Average Waste (%)	Variation Answer in Waste Variation Range (%)
1	Steel	10.12	4.5 - 15
2	Cement	5.12	0.5 - 10
3	Sand	18.23	25-Oct
4	Aggregate	15.77	20-Oct
5	Bricks	9.92	20-Jan
6	Formwork	22.69	15 - 30

3.3 Need of Computer Application for Waste Minimization and Control

The computerized systems for waste minimization and control in construction companies reveal a strong inclination towards digital solutions but also highlight areas that require improvement. As indicated in Table 6, all surveyed companies (100%) reported following a computerized system for waste minimization and control. This advancement reflects a universal acknowledgment of the importance of technology in efficiently managing construction waste. The use of digital tools facilitates tracking materials, optimizes resource utilization, and reduces unnecessary losses.

Table 6. Computerized System followed by the Company

S.N.	Description	Contractors' Responses (No)	
		Frequency	Percentage (%)
1	Computerized system followed for waste minimization and control	13	100

Furthermore, Table 7 highlights the overwhelming necessity of computer software for waste minimization and control. All respondents (100%) agreed that a computerized system, an up-to-date database of materials, labor, equipment, and suppliers, as well as a dedicated database for waste quantity, cost, and percentage, are essential for effective waste management. A well-structured database can help contractors predict material requirements more accurately, minimize over-ordering, and improve project sustainability.

Table 7. Necessity of Computer Software for Waste Minimization and Control

S.N.	Description	Necessary (%)	Sometimes Necessary (%)	Unnecessary (%)
1	Computerized System	100		
2	Up-to-date database of material, labour, equipment and supplier	100		
3	Database regarding waste quantity, amount and its percentage	100		

However, despite the reliance on computerized systems, Table 8, suggests that there is a gap in software proficiency among contractors. While 92.3% of respondents were proficient in using Excel, which is commonly used for data analysis and project tracking, no responses were recorded for Word and Access, which could indicate a lack of familiarity or relevance in waste management applications. Additionally, only 7.69% of contractors reported using other software, suggesting that specialized construction management tools such as AutoCAD, MS Project, or BIM software may not be widely adopted for waste control purposes.

Table 8. Efficiency of Respondents in Using Popular Computer Software

S.N.	Description	Contractor's Responses (Yes)	
		Frequency	Percentage (%)
1	Excel	12	92.30
2	Word		
3	Access		
4	Other	1	7.69

This disparity between the acknowledgment of the need for computerized waste management systems and actual software proficiency indicates that training and capacity building are necessary. Contractors need to be equipped with advanced digital tools that go beyond Excel, including integrated database management systems, construction planning software, and waste tracking applications. Encouraging the use of industry-standard software and ensuring adequate training will significantly enhance the effectiveness of digital waste management strategies, leading to greater efficiency, cost savings, and environmental sustainability in the construction sector. The fieldwork research was conducted for three construction projects in Kathmandu, executed by United Builders & Engineers Pvt. Ltd., under a centralized control system. As

shown in Table 9, the surveyed projects included the Sanima Bikas Bank Building at Naxal (NRs. 166.4 million), the Nepal Telecom Building at Sundhara (NRs. 174.4 million), and the Kathmandu District Court Building at Babarmahal (NRs. 289.1 million). These projects represent significant investments, emphasizing the need for efficient material management and waste control to minimize financial losses and enhance operational efficiency.

Table 9. Surveyed Projects

S.N.	Name of Project	Project Cost (NRs.)
1	Sanima Bikas Bank Building at Naxal	166.4 Million
2	Nepal Telecom Building at Sundhara	174.4 Million
3	Kathmandu District Court Building at Babarmahal	289.1 Million

A review of project records, including the stock Bbook, running bill, and bill of quantities, revealed that the current material management system is primarily manual, with Excel software used solely for recording purposes. However, data on material quantities, costs, and waste percentages are not systematically maintained, indicating inefficiencies in tracking and controlling material usage. The flowchart in Figure 2 illustrates the steps followed for material management, highlighting a lack of integration between different units and the absence of structured data analysis. This manual approach limits the ability to track material waste, optimize resource allocation, and effectively evaluate financial impacts.

The shortcomings in the existing system, categorized in Table 10, were analyzed across four key functional units: engineering, purchasing, tracking, and store units. The engineering unit lacks an activity-wise material tracking system, as it only prepares total quantity sheets rather than detailed breakdowns for each activity. This practice hinders the accurate monitoring of material consumption, making it challenging to determine whether usage aligns with standard norms. Furthermore, there is no systematic comparison of actual material consumption with expected norms, making it challenging to identify inefficiencies. Additionally, running bill quantities and amounts are not cross-checked against actual materials, labor, and equipment consumed, increasing the likelihood of errors and financial discrepancies.

In the purchasing unit, material procurement is based on material requisition slips from project sites; however, there is no verification process to ensure that the requested quantities are justified. This lack of oversight increases the risk of over-ordering and unnecessary expenditures. Additionally, there is no systematic vendor rating process, which can lead to potential inconsistencies in material quality and pricing. Purchase orders (P.O.s) are not properly issued to project sites, creating gaps in communication and material tracking. Moreover, the purchasing unit is not well-informed about the availability of tools and equipment on-site, which can result in unnecessary purchases and financial inefficiencies.

The tracking unit also exhibits significant deficiencies, as it does not verify whether the materials received on-site match the Purchase Orders or whether they meet the required specifications. This lack of verification increases the risk of accepting incorrect or substandard materials, which can lead to project delays, quality issues, and financial losses.

Table 10. Shortcomings of the Current System

S.N.	Shortcomings of Each Unit
1	**Engineering Unit**
i	The activity-wise material required sheet is not prepared. Only the total quantity of materials required for the sheet is prepared
ii	Don't maintain an up-to-date activity-wise record of material consumed vs. normative consumption (to see whether material consumed is more than norms)
iii	Cross-checks are not made for the running bill quantity and amount with actual quantities of material, labor, and equipment consumed, and there are chances of error in running bill quantities
2	**Purchasing Unit**
i	Issue a Purchase Order based on the material requisition slip from the project site. Cross-checks are not made to determine whether the quantities demanded are justified
ii	No systematic procedure for vendor rating
iii	P.O.'s are not issued to the project site
iv	Not well informed about the tools/equipment available at the project site
3	**Tracking Unit**
i	Don't tally quantity received in site with P.O. and are not well informed of the specifications mentioned in P.O.
4	**Store Unit**
i	Manual stock detail
ii	Issue materials to the project without a material Requisition slip
iii	Do not maintain the material consumed sheet
iv	Don't keep record of waste quantity, waste percentage, and proper scrap detail.
v	Do not tally consumption norms before issuing materials.
vi	Rates are not entered in the stock book. Actual amount figures for the received quantity and consumed quantity are not known
vii	Excel Software is used for recording data
viii	Don't know about total profit and loss on materials, even after the end of the project

The store unit relies on manual stock-keeping methods, which are highly inefficient for tracking material movement and consumption. Materials are issued to projects without formal material requisition slips, resulting in difficulties with inventory control. Additionally, the store does not maintain records of material consumption, waste quantities, waste percentages, or proper scrap details. There is no process in place to compare material usage against standard norms before issuing materials, leading to potential overuse and waste. Furthermore, material rates are not recorded in stock books, and the actual costs of received and consumed materials are not documented, making it impossible to assess profit and loss on materials even after project completion.

Furthermore, automated inventory management systems should be introduced to replace manual stock-keeping methods. Materials should only be issued against formal requisitions, and detailed records should be maintained for material consumption, waste percentages, and scrap management. The use of cost-tracking software would enable companies to accurately record material rates, financial transactions, and post-project profit-loss assessments, allowing for more transparent and data-driven decision-making.

5. Conclusion and Recommendations

The study concludes that the current waste minimization practices in Nepalese construction companies are manual-based mainly, with no structured or systematic approach to tracking and controlling material waste. Most contracting companies do not prepare a waste minimization plan before starting a project, nor do they maintain records of the actual quantity and financial impact of material waste. While some companies maintain general records of materials, labor, and equipment, they lack activity-wise tracking of material consumption, making it difficult to evaluate efficiency and identify sources of waste.

A key finding is the lack of user-friendly software for waste minimization and control. Contractors acknowledge that traditional manual management methods exacerbate material waste, duplication of material orders, delayed material deliveries, and inaccurate quantity estimations. The study reveals that formwork (22.69%), sand (18.23%), and aggregate (15.77%) contribute the highest percentage of waste, while reinforcing steel (10.12%), cement (5.12%), and bricks (9.92%) also show significant waste rates. The large variation in responses about waste rates indicates a lack of accurate knowledge due to the absence of a regularly updated database or systematic record-keeping.

Moreover, contractors do not utilize computerized systems for waste minimization and control, despite recognizing the need for such systems. As per the study, all contractors agree on the necessity of a construction waste minimization software to maintain databases of materials, labor, equipment, suppliers, and waste quantities. Currently, MS-Excel is the preferred software among contractors, as it is easy to use for maintaining databases and performing material reconciliations.

To improve material waste management in Nepalese construction, contractors should implement a user-friendly computerized waste minimization system to effectively track material usage, waste, and costs. Additionally, it is essential to prepare detailed waste minimization plans, maintain up-to-date databases of materials, and train staff on proper material management practices to reduce inefficiencies and ensure accurate waste tracking.

Author contribution statement

All authors contributed to the study conception and design. Sabir Baidya performed data collection, model generation and analysis. Raghu Nath Prajapati wrote the manuscript and modification, and both Authors read and approved the manuscript.

Ethics Declarations

The study adhered to the ethics guidelines of Nepal Engineering College, Pokhara University, Nepal, and followed the principles of the Declaration of Helsinki, including informed consent, voluntary participation and withdrawal, confidentiality, and the privacy of participants. The authors confirm they sought and got informed consent from all participants in the study. This research, along with its questionnaire and methodology, was approved by the Research Development Unit (RDU) of Nepal Engineering College.

Funding

There is no funding support for this research work.

Data Availability

Data and materials are available from the authors upon request.

Competing Interests

The authors declare that they have no competing interests.

Acknowledgments

The authors would also like to express sincere gratitude to the anonymous reviewers for their invaluable feedback and constructive comments, which significantly enhanced the quality and rigor of this manuscript. Additionally, gratitude is also extended to the dedicated editorial team for their guidance and support throughout the publication process.

References

Acharya, U. R., & Shrestha, S. K. (2021). Utilization of Personal Protective Equipment in Construction Industry of Nepal. Advances in Engineering and Technology: An International Journal, 1(1), 17–31.

Adhikari, R., Shrestha, Y., Amatya, I. M., & Motra, G. B. (2021). Controlled substitution of coarse aggregate with waste glass and syringe needle in M20 concrete. Journal of Innovations in Engineering Education, 4(2), 117–122. https://doi.org/10.3126/jiee.v4i2.39308

Agyekum, K. (2012). Minizing Materials Waste at the Construction Stage of a Project through the Implementation of Lean Construction (Issue April 2017).

Al-Rifai, J., & Amoudi, O. (2016). Understanding the key factors of construction waste in Jordan. Jordan Journal of Civil Engineering, 10(2), 244–253. https://doi.org/10.14525/JJCE.10.1.3540

Bossink, B. A. G. (2002). A Dutch public-private strategy for innovation in sustainable construction. Construction Management and Economics, 20(7), 633–642. https://doi.

org/10.1080/01446190210163534

Can, G., Karaman Öztaş, S., & Filiz Taş, E. (2023). Material Waste Management in the Construction Industry: Brick Waste. Gain Information from the Traditional Earthen Architecture, October, 69–76. https://www.researchgate.net/publication/375238470

Daoud, A. O., Othman, A. A. E., Ebohon, O. J., & Bayyati, A. (2021). Quantifying materials waste in the Egyptian construction industry: A critical analysis of rates and factors. Ain Shams Engineering Journal, 12(4), 4275–4289. https://doi.org/10.1016/j.asej.2021.02.039

Dhungana, S., Awasthi, K. D., & Bohara, N. (2023). Analyzing the Performance of Construction Demolition Waste Aggregates on strength for Non-structural Concrete. Journal of UTEC Engineering Management, 1(01), 28–28. https://doi.org/10.36344/utecem.2023.v01i01.004

Ekanayake, L. L., & Ofori, G. (2004). Building waste assessment score: Design-based tool. Building and Environment, 39(7), 851–861. https://doi.org/10.1016/j.buildenv.2004.01.007

Elshaboury, N., Al-Sakkaf, A., Abdelkader, E. M., & Alfalah, G. (2022). Construction and Demolition Waste Management Research: A Science Mapping Analysis. International Journal of Environmental Research and Public Health, 19(8). https://doi.org/10.3390/ijerph19084496

Formoso, C. T., Soibelman, L., De Cesare, C., & Isatto, E. L. (2002). Material Waste in Building Industry: Main Causes and Prevention. Journal of Construction Engineering and Management, 128(4), 316–325. https://doi.org/10.1061/(asce)0733-9364(2002)128:4(316)

Gavilan, R. M., & Bernold, L. E. (1994). Source Evaluation of Solid Waste in Building Construction. Journal of Construction Engineering and Management, 120(3), 536–552. https://doi.org/10.1061/(asce)0733-9364(1994)120:3(536)

Kennouche, S., Brahim, H., Abdelli, H. E., de Aguiar, J. L. B., & Jesus, C. (2022). Plastic Waste for the Enhancement of Concrete Properties - A review. Jordan Journal of Earth and Environmental Sciences, 13(4), 263–270.

Khalas, R., & Patel, J. (2018). Cost Optimization of Residential Construction Project through Waste Management Technique. International Journal Of Advanced in Management, Technology and Engineering Sciences, 8(5), 32–38.

Kusi, M., Zhao, F., & Sukamani, D. (2018). A Study of Performance Level of Nepalese Construction Firms In Construction Quality. North American Academic Research, 1(5), 137–154. http://twasp.info/journal/home

Ogunmakinde, O. E., Sher, W., & Egbelakin, T. (2022). Construction Waste Management in Nigeria Using the 3R Principle of the Circular Economy BT - Circular Economy and Waste Valorisation: Theory and Practice from an International Perspective (J. Ren & L. Zhang (eds.); pp. 177–195). Springer International Publishing. https://doi.org/10.1007/978-3-031-04725-1_8

Ogunseye, N. O., Ogunseye, O. D., & Ogunseye, A. O. (2023). Construction and Demolition Waste Management in a Developing Country: A Nigerian Scenario. Journal of Sustainability Perspectives, 3(1), 11–23. https://doi.org/10.14710/jsp.2023.15413

Popoola, O. C., Adeleke, J. S., & Ayegbokiki, S. T. (2018). An Investigation into Material Wastage on Building Construction Sites (Case Study of Selected Building Construction Sites in Osun State). International Journal of Science, Engineering & Environmental Technology (IJOSEET), 3(3), 18–26. www.repcomseet.com

Sawaya, R., Kourani, H., Halwani, J., & Nehme, N. (2023). Landfills in the Context of Municipal Solid Waste Management in Lebanon: A review focusing on Greater Beirut Area. Jordan Journal of Earth and Environmental Sciences, 14(4), 241–253.

Siregar, A. M., & Kustiani, I. (2019). Contractors' perception on construction waste management case study in the City of Bandar Lampung. IOP Conference Series: Earth and Environmental Science, 245(1), 1–6. https://doi.org/10.1088/1755-1315/245/1/012035

Skoyles, E. R. (1976). Materials wastage – a misuse of resources. Batiment International, Building Research and Practice, 4(4), 232–232. https://doi.org/10.1080/09613217608550498

Tafesse, S. (2021). Material waste minimization techniques in building construction projects. Ethiop. J. Sci. & Technol., 14(1), 1–19.

JJEES

JJEES (2025) 16 (4): 315-329
ISSN 1995-6681

Jordan Journal of Earth and Environmental Sciences

Forecasting emissions of Greenhouse Gases in West African Countries Under Business-As-Usual (BAU) Scenario

Abdullahi Chado Salihu[1,2*], Yahaya Zayanna Ibrahim[1] and Rukayyat Abdulkarim[3]

[1]Lecturer, Department of Meteorology and Climate Change, African Aviation and Aerospace University, Abuja, Nigeria
[2]African Centre for Climate Change and Aviation Decarbonization, African Aviation and Aerospace University, Abuja, Nigeria
[3]Lecturer, General Studies and Basic Sciences Unit, African Aviation and Aerospace University, Abuja, Nigeria

Received on February 27, 2025, Accepted on April 12, 2025

Abstract

Greenhouse gas (GHG) emissions continue to rise in West Africa, posing a significant challenge to regional sustainability and global climate goals. This study employed the Holt-linear exponential smoothing model to forecast GHG emissions in West Africa under a business-as-usual scenario through 2099. Using historical data from 1970 to 2021 sourced from the EDGARv7.0 database, the research analyzes trajectories of CO_2, CH_4, and N_2O emissions. Results reveal model evaluation demonstrated robust prediction, with R^2 exceeding 0.90 for all three GHGs. Projections indicate that CO_2 emissions will rise, with Senegal expected to have the highest increase (808%) by 2099, while Ghana is projected to demonstrate a 16% reduction. Nigeria's share of regional emissions is projected to decline from 70.1% to 62.4%. CH_4 emissions exhibit contrasting trends, with Nigeria experiencing a 215% decline by 2099, while Gambia and Liberia have sharp increases of 467% and 320%, respectively. Generally, regional CH_4 emissions are projected to decrease. Conversely, N_2O emissions are predicted to grow with total regional emissions increasing from 295.2 Kt to 762.6 Kt, led by Sierra Leone's 461% rise. These findings provide critical insights for policymakers to develop targeted climate change strategies, align national development plans with international commitments, and foster regional cooperation to address the anticipated growth in GHG emissions.

Keywords: Greenhouse Gases, Emissions, Forecasting, BAU Scenario, West African Countries

1. Introduction

Greenhouse gases (GHGs), including carbon dioxide (CO_2), methane (CH_4), and nitrous oxide (N_2O), are primary contributors to global warming and climate change. The increasing concentration of these gases in the atmosphere, largely attributed to anthropogenic activities such as fossil fuel combustion, deforestation, and agricultural practices, presents significant environmental and socio-economic challenges globally (Mazahreh and Abu-Allaban 2023; Tudor and Sova, 2021). In West Africa, the rapid pace of urbanization and industrialization, coupled with limited mitigation measures, has accelerated GHG emissions under a business-as-usual (BAU) scenario (Adeoye and Spataru, 2019). The region's vulnerability to climate change, manifesting in erratic rainfall patterns, prolonged droughts, and rising temperatures, exacerbates critical issues such as food insecurity and water scarcity (Larbi et al., 2021). Despite commitments to international frameworks like the Paris Agreement, the lack of robust forecasting models impedes effective climate action and policy implementation in the region (Rahman et al., 2023). Achieving nationally determined contributions (NDCs) requires precise, localized data on emissions trends to inform evidence-based decision-making (Ntiamoah et al., 2024).

This study addresses the urgent need for accurate emissions forecasting in West Africa by employing the Emissions Database for Global Atmospheric Research (EDGAR) as the primary data source. The EDGAR database offers high-resolution global emission inventories, providing comprehensive datasets for analyzing trends and developing predictive models (EDGAR, 2023). The Holt-Winters exponential smoothing method, a time-series forecasting model, is utilized due to its demonstrated ability to capture seasonality and long-term trends in environmental and energy datasets (Ahmar et al., 2023; Yousefi et al., 2023). While such models have been extensively applied in regions like Europe and Asia, their application in West Africa remains limited (Ameyaw and Yao, 2018).

The importance of emissions forecasting extends beyond environmental management to encompass broader climate policy planning, particularly in rapidly developing regions like West Africa. Globally, models such as Holt-Winters have proven effective in forecasting GHG emissions and energy trends. Tudor and Sova (2021) highlighted its adaptability to seasonal variations and non-stationary trends, while Zhou et al. (2022) introduced an optimized fractional grey Holt-Winters model, improving prediction accuracy for energy-related datasets. Comparative analyses, such as those by Awe et al. (2023), demonstrate that while the Holt-Winters model performs well in many contexts, alternative approaches, including hybrid models and deep learning techniques, can surpass its accuracy for highly complex datasets. In Africa, Viljoen (2022) emphasized the need for region-specific models, including Holt-Winters, to predict emissions from industrial facilities in South Africa. In West Africa, Imhanze and Awe (2023) demonstrated the applicability of the Holt-

* Corresponding author e-mail: salihu.chado@aaau.edu.ng

Winters multiplicative model in urban air quality analysis, highlighting its potential for environmental datasets.

Despite these advancements, emissions forecasting in West Africa faces significant gaps. Many studies underscore the necessity of localized data and nuanced adjustments to account for the region's unique socio-economic and environmental contexts (Othoche et al., 2021). Incorporating datasets from comprehensive repositories, such as EDGAR, could enhance the reliability and policy relevance of forecasting efforts. Therefore, this study aims to forecast GHG emissions in West African countries under a BAU scenario using the Holt-Winters model. Specific objectives include analyzing historical GHG emission trends in West African countries, applying the Holt-Winters model to project future emissions, and evaluating the implications of the forecasts for climate policy and sustainable development in the region. By utilizing data exclusively from the EDGAR database, this study bridges critical knowledge gaps in GHG emissions forecasting for West Africa. The findings will provide actionable insights to guide investments in renewable energy, afforestation, and sustainable agricultural practices, which are the main drivers of GHG emissions (Hamdan et al., 2023).

2. Materials and Methods

2.1 Study Area Description

This study focuses on West Africa, a sub-region encompassing 16 countries: Benin, Burkina Faso, Cape Verde, Côte d'Ivoire, The Gambia, Ghana, Guinea, Guinea-Bissau, Liberia, Mali, Mauritania, Niger, Nigeria, Senegal, Sierra Leone, and Togo. This region exhibits diverse geographical features, ranging from coastal areas to the Sahelian zone, resulting in varied ecological conditions and socio-economic contexts (AfDB, 2022). The economies of these countries are predominantly reliant on agriculture, natural resource extraction, and the development of industrial sectors. This economic diversity, coupled with varying levels of growth and national priorities, contributes to a complex emissions landscape (UNEP, 2021).

2.2 Data and Model Specification

The study analyzed greenhouse gas (GHG) emissions data from 16 West African countries, focusing the period from 1970 to 2021, with a focus on annual CO_2, CH_4, and N_2O emissions measured in kilotons (Kt). The Emissions Database for Global Atmospheric Research Seventh Version (EDGARv7.0) repository served as the source of the data. According to Crippa et al. (2022), the database provides emission data as national totals using global statistics and a consistent Intergovernmental Panel on Climate Change (IPCC) methodology. This dataset is widely used for emissions analysis and provides a consistent framework for comparison across countries (e.g., Güneralp et al., 2020).

The Holt-Winters linear exponential smoothing model was employed to forecast GHG emissions through 2099. This model was selected for its ability to capture both trend and seasonal patterns in time series data. This is computed mathematically as;

$$\text{Level: } L_t = \alpha Y_t + (1 - \alpha)(L_{t-1} + T_{t-1}) \quad (1)$$

$$\text{Trend: } T_t = \beta (L_t - L_{t-1}) + (1 - \beta) T_{t-1} \quad (2)$$

$$\text{Forecast: } F_{t+k} = L_t + k T_t \quad (3)$$

Where:

L_t = level at time t
T_t = trend at time t
Y_t = observed value at time t
F_{t+k} = forecast at time t+k
α = smoothing parameter for the level ($0 < \alpha < 1$)
β = smoothing parameter for the trend ($0 < \beta < 1$)
k = number of periods into the future.

2.3 Forecasting and Analysis

The forecasts assume a business-as-usual (BAU) scenario, maintaining historical patterns without incorporating potential policy changes or technological disruptions. This approach provides a baseline projection against which the impact of future interventions can be assessed (IPCC, 2014). XLSTAT 2022.3.1 version was used for all statistical analyses (Addinsoft, 2022). Model optimization and validation for each country and GHG type were conducted as follows:

1. Model parameters (α,β) were optimized to minimize forecast error
2. Data was split into training (1970-2015) and validation (2016-2021) sets. This is consistent with established procedure for model validation in literature (Hussain et al., 2025).
3. Model performance was evaluated using multiple metrics:

i. Root Mean Squared Deviation (RMSD) or Root Mean Squared Error (RMSE)

$$\text{RMSD} = \sqrt{\frac{\sum_{i=1}^{N} (x_i - \hat{x}_i)^2}{N}} \quad (4)$$

Where:

- $RMSD$ = root-mean-square deviation
- i = variable i
- N = number of non-missing data points,
- X_i = actual values,
- $\hat{X}_i$ = forecast values.

ii. Mean Absolute Error (MAE)

$$\text{MAE} = \frac{\sum_{i=1}^{n} |y_i - x_i|}{n} \quad (5)$$

Where:

- MAE = mean absolute error
- y_i = prediction,
- X_i = true value,
- n = number of data points

iii. Mean Absolute Percentage Error (MAPE)

$$\text{M} = \frac{1}{n} \sum_{t=1}^{n} \left| \frac{A_t - F_t}{A_t} \right| \quad (6)$$

Where:

- M = mean absolute percentage error
- n = the number of fitted points,
- A_t = the actual value,
- F_t = the forecast value.

iv. R-squared (R^2)

$$R^2 = 1 - \frac{\sum_i (y_i - \hat{y}_i)^2}{\sum_i (y_i - \bar{y})^2} \quad (7)$$

Where:

- R^2 = r squared
- y_i = the y value for observation i,
- $\bar{y}$ = the mean of y value,
- $\hat{y}_i$ = the predicted value of y for observation i.

The optimized models were used to generate forecasts from 2022 to 2099. Thus, the analysis included the evaluation of temporal trends and patterns, calculation of percentage changes in emissions (baseline vs. forecast periods), and assessment of regional emission shares by each West African country from 2022 to 2099.

3. Results and Discussion

3.1 CO_2 Emissions in West African Countries

3.1.1 Evaluation of ' 'Model's Performance for Forecasting CO_2 Emissions

Model performance evaluation for CO_2 forecasting (Table 1) demonstrates strong predictive performance across West African countries, with R^2 values ranging from 0.83 to 0.99, while showing relatively lower but still acceptable performance for Guinea (R^2 = 0.83). The MAPE values, range from 2.24% (Sierra Leone) to 8.87% (Cape Verde), suggesting reliable forecasting capabilities across different scales of emissions. The RMSE values vary significantly, with Nigeria showing the highest RMSE (10,639.75) due to its substantially larger emission volumes. Smaller countries, such as Gambia and Cape Verde, exhibit lower RMSE values (43.46 and 60.26, respectively), reflecting their smaller emission scales. The MAE values follow a similar pattern, with Nigeria having the highest (7,857.04) and Gambia the lowest (24.79), indicating that prediction errors scale proportionally with emission volumes.

Moreover, the optimization parameters (α and β) show considerable variation across countries, suggesting different underlying patterns in historical emissions data. The α values range from 0 to 1.84, while β values range from 0.01 to 248.8, reflecting diverse trend and seasonality patterns. These variations indicate that the model successfully adapts to country-specific emission characteristics, contributing to its overall strong predictive performance despite regional heterogeneity.

Table 1. Goodness of fit statistics for forecasting CO_2 emissions

Matrices / **Country**	Best α	Best β	RMSE	MAE	MAPE	R^2
Benin	1. 22	0.08	448.31	234.96	2.96	0.96
Burkina Faso	1.25	0.03	1091.17	588.26	4.60	0.89
Cape Verde	1.20	0.08	60.26	33.68	8.87	0.95
Cote d'Ivoire	0.75	0.19	962.12	573.23	3.51	0.97
Gambia	1.17	0.11	43.46	24.79	2.88	0.98
Ghana	1.84	0.01	834.38	575.65	3.11	0.96
Guinea	0.00	248.8	1454.90	1067.42	8.01	0.83
Guinea-Bissau	1.16	0.11	73.96	52.69	2.37	0.99
Liberia	0.69	1.59	347.94	261.89	5.69	0.97
Mali	0.73	1.03	205.05	161.43	2.60	0.99
Mauritania	1.03	0.02	441.96	191.67	6.19	0.89
Niger	1.04	0.02	721.92	366.05	4.92	0.89
Nigeria	0.64	0.13	10639.75	7857.04	2.75	0.98
Senegal	0.77	0.83	385.30	235.90	3.19	0.97
Sierra Leone	0.93	0.08	216.42	163.19	2.24	0.95
Togo	1.12	0.13	308.64	180.78	3.72	0.97

3.1.2 Historical and Forecasted CO_2 Emissions Trend in West African Countries

Figure 1 shows the historical and forecasted CO_2 emissions trend in West African countries from 1970 to 2099. It reveals dramatic increases across most West African nations. The trend of CO_2 emissions in West African countries, over the period from 1970 to 2099, reveal a significant and consistent increase across all nations. The data indicate that emissions have grown exponentially, driven by population growth, industrialization, and energy consumption. For instance, Nigeria, as the region's largest economy, shows an increase from 161,348 ktons in 1970 to over 1,142,488 ktons by 2099, marking it as the largest emitter in the region. This sharp rise is attributed to its industrial activities and high population density. Similarly, countries such as Ghana, Côte d'Ivoire, and Senegal have demonstrated substantial growth, with emissions increasing by over 10 times during the same period. This pattern mirrors regional developmental shifts and increasing reliance on fossil fuels for energy generation. Countries with smaller populations or lower industrial activity, such as Cape Verde and Guinea-Bissau, exhibit slower growth in emissions compared to the larger economies. For example, Cape Verde's CO_2 emissions increased modestly from 277 ktons in 1970 to 4,127 ktons by 2099.

However, the proportional growth is still significant, indicating that even smaller nations are not immune to the impacts of modernization and energy demands. This growth underscores the widespread nature of the emissions problem across West Africa, as even nations with historically low emissions are contributing more significantly over time.

The future projections emphasize the urgency of sustainable energy policies in the region. By 2099, CO_2 emissions in countries, like Senegal and Burkina Faso, are predicted to rise to 178,083 and 43,309 ktons, respectively, reflecting their growing economies and energy needs. This trajectory suggests that without intervention, West Africa could face severe environmental challenges tied to global climate change. According to Ouédraogo et al. (2022), innovative energy solutions tailored to ' 'Africa's unique conditions are imperative for achieving sustainable growth and mitigating CO2 emissions across the region. Further exploration of these interventions will be crucial for striking a balance between economic development and environmental stewardship.

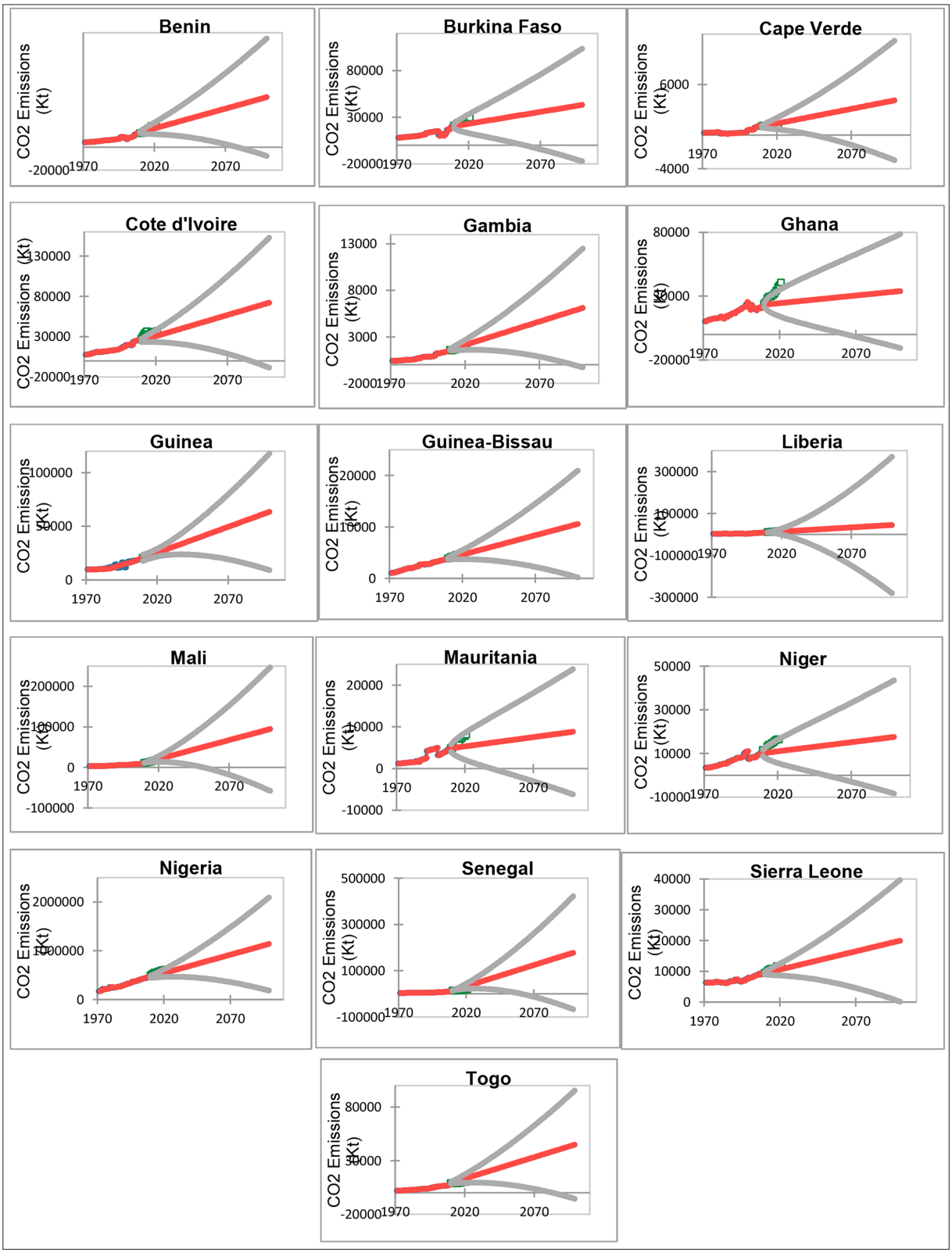

Figure 1. Historical and forecasted CO_2 emissions trend in West African countries

3.1.3 Percentage Change of CO_2 Emissions by Countries in West Africa

Table 2 presents the percentage change in CO2 emissions in West Africa from 1970 to 2099, revealing stark increases across most nations. Countries like Liberia (435%), Mauritania (532%), and Senegal (382%) experienced the steepest rises from 1970 to 2021, highlighting the rapid urbanization and industrialization driving these emissions. This aligns with the findings of Guo et al. (2024), who underscore the governance challenges contributing to emissions in the region. Such trends stress the need for targeted policy responses to mitigate emissions growth. Looking ahead, Senegal's emissions are forecasted to rise significantly, reaching an 808% increase by 2099, potentially due to economic expansion and changes in energy consumption patterns. Conversely, Ghana shows a projected decrease (-16% by 2099), suggesting early adoption of renewable energy or effective emissions controls (Kwakwa et al., 2019). This divergence highlights the importance of tailored approaches to emissions management in addressing distinct national circumstances (Ameyaw et al., 2020).

Table 2. Percentage change of CO_2 emissions by countries in West Africa (Unit: Kt)

Year / Country	1970	2021	2021 1970	2029 2021	2039 2021	2049 2021	2059 2021	2069 2021	2079 2021	2089 2021	2099 2021
Benin	4318.7	19019	340%	3%	22%	40%	58%	76%	94%	112%	130%
Burkina Faso	8158.1	29548	262%	-14%	-5%	3%	12%	21%	29%	38%	47%
Cape Verde	277.2	1204	334%	41%	70%	98%	127%	156%	185%	214%	243%
Cote d'Ivoire	7713.2	36799	377%	-4%	11%	25%	39%	53%	68%	82%	96%
Gambia	426.8	1891	343%	37%	64%	91%	117%	144%	171%	197%	224%
Ghana	10316	40606	294%	-37%	-34%	-31%	-28%	-25%	-22%	-19%	-16%
Guinea	9982.4	25484	155%	17%	36%	55%	74%	93%	112%	130%	149%
Guinea-Bissau	1069.1	4917	360%	8%	23%	39%	54%	69%	85%	100%	115%
Liberia	3033.7	16229	435%	8%	33%	58%	82%	107%	132%	156%	181%
Mali	3623.6	18789	419%	58%	108%	158%	208%	257%	307%	357%	406%
Mauritania	1280.1	8085	532%	-29%	-23%	-18%	-12%	-7%	-1%	4%	10%
Niger	3552.9	16459	363%	-28%	-23%	-18%	-13%	-8%	-3%	2%	7%
Nigeria	161348	611144	279%	0%	13%	25%	38%	50%	62%	75%	87%
Senegal	4073.1	19614	382%	154%	248%	341%	434%	528%	621%	715%	808%
Sierra Leone	6454	11356	76%	3%	13%	24%	34%	44%	55%	65%	76%
Togo	2227	10233	360%	67%	106%	145%	184%	223%	262%	301%	340%

‘ ‘In addition, smaller nations such as Cape Verde and the Gambia display strong upward trends in emissions through 2099 (243% and 224%, respectively), despite their smaller economic footprints. This trend reflects the ongoing dependency on fossil fuels as these nations scale their infrastructure and industries (Musah et al., 2021). Meanwhile, Burkina Faso and Guinea show more moderate increases, suggesting potential early investments in greener technologies or slower industrial development. ‘ ‘Nigeria's emissions, the highest in the region, are predicted to show more modest changes compared to those of smaller economies. With a significant share of the ‘ ‘region's emissions (611,144 kt in 2021), this stabilization could indicate adherence to international climate commitments or the deployment of cleaner technologies (Aalbers et al., 2024).

However, balancing economic growth with emission reduction remains a persistent challenge. Therefore, the projected disparities in emissions growth across West African countries underscore the need for country-specific climate strategies. Rapid-growth nations like Senegal and Mali require aggressive mitigation policies, while those showing stabilization or reductions, such as Ghana and Mauritania, can serve as case studies for sustainable development (Kedir et al., 2023). Addressing these trends will be crucial for the region to effectively contribute to global climate goals.

3.1.4 Regional Percentage Share of CO_2 Emissions by West African Countries

Table 3 highlights the percentage contributions of West African countries to regional CO_2 emissions from 1970 to 2099, showing significant shifts in shares over time. Nigeria, which accounted for 70.8% of the region's emissions in 1970, continues to dominate with a projected 62.4% share by 2099. This percentage reflects its large population, industrial base, and energy use patterns. However, this declining trend indicates some progress in mitigating its carbon footprint, potentially due to policy interventions or shifts toward renewable energy (Ifelunini et al., 2023). In contrast, smaller nations like Senegal and Mali are projected to see a rising share of emissions. Senegal, for instance, is expected to contribute 9.7% by 2099, a sharp increase from 2.3% in 2021. This growth can be attributed to urbanization and increased energy consumption (Musah et al., 2021). Mali follows a similar trajectory, with its share increasing from 2.2% in 2021 to 5.2% in 2099, reflecting similar developmental trends (Matthew et al., 2020). Countries, like Ghana and

Niger, however, show declining contributions, with Ghana's share decreasing from 4.7% in 2021 to 1.9% by 2099. This result suggests effective emission control strategies or structural economic changes toward less carbon-intensive activities (Espoir and Sunge, 2021). Niger's trajectory, which decreased from 1.9% to 1.0%, may also reflect slower industrial growth or the success of climate policies (Ameyaw et al., 2020).

Table 3. Regional percentage share of CO2 emissions by countries in West Africa (Unit: Kt)

Year	1970	2021	2029	2039	2049	2059	2069	2079	2089	2099
West Africa	227854	871376	903047	1035569	1168092	1300614	1433136	1565658	1698180	1830703
Benin	1.9%	2.2%	2.2%	2.2%	2.3%	2.3%	2.3%	2.4%	2.4%	2.4%
Burkina Faso	3.6%	3.4%	2.8%	2.7%	2.6%	2.5%	2.5%	2.4%	2.4%	2.4%
Cape Verde	0.1%	0.1%	0.2%	0.2%	0.2%	0.2%	0.2%	0.2%	0.2%	0.2%
Cote d'Ivoire	3.4%	4.2%	3.9%	3.9%	3.9%	3.9%	3.9%	3.9%	3.9%	3.9%
Gambia	0.2%	0.2%	0.3%	0.3%	0.3%	0.3%	0.3%	0.3%	0.3%	0.3%
Ghana	4.5%	4.7%	2.8%	2.6%	2.4%	2.3%	2.1%	2.0%	1.9%	1.9%
Guinea	4.4%	2.9%	3.3%	3.3%	3.4%	3.4%	3.4%	3.4%	3.5%	3.5%
Guinea-Bissau	0.5%	0.6%	0.6%	0.6%	0.6%	0.6%	0.6%	0.6%	0.6%	0.6%
Liberia	1.3%	1.9%	1.9%	2.1%	2.2%	2.3%	2.3%	2.4%	2.5%	2.5%
Mali	1.6%	2.2%	3.3%	3.8%	4.1%	4.4%	4.7%	4.9%	5.1%	5.2%
Mauritania	0.6%	0.9%	0.6%	0.6%	0.6%	0.5%	0.5%	0.5%	0.5%	0.5%
Niger	1.6%	1.9%	1.3%	1.2%	1.2%	1.1%	1.1%	1.0%	1.0%	1.0%
Nigeria	70.8%	70.1%	68.0%	66.6%	65.5%	64.6%	63.9%	63.3%	62.8%	62.4%
Senegal	1.8%	2.3%	5.5%	6.6%	7.4%	8.1%	8.6%	9.0%	9.4%	9.7%
Sierra Leone	2.8%	1.3%	1.3%	1.2%	1.2%	1.2%	1.1%	1.1%	1.1%	1.1%
Togo	1.0%	1.1%	1.9%	2.0%	2.1%	2.2%	2.3%	2.4%	2.4%	2.5%

' Furthermore, another notable trend is the stability of emissions shares for smaller nations, like Guinea-Bissau and Cape Verde, which consistently remain below 1% throughout the period. This reflects their limited industrial bases and smaller populations, though there is potential for growth if their economies expand significantly (Abban et al., 2022). Liberia also shows a modest rise in its share, indicative of development but on a smaller scale compared to Senegal or Mali (Musah et al., 2021). Generally, the finding underscores the dynamic shifts in emissions contributions across West Africa, driven by varying rates of economic growth, policy interventions, and energy transitions. This regional heterogeneity highlights the necessity for tailored climate strategies to address the unique challenges and opportunities in each country (Tiemoko et al., 2020).

3.2 CH_4 Emissions in West African Countries

3.2.1 Evaluation of ' 'Model's Performance for Forecasting CH_4 Emissions

Table 4: The model evaluation for CH_4 emissions across West African countries, with R^2 values ranging from 0.82 to 0.99. Most countries show an excellent model fit; Sierra Leone shows slightly lower but still acceptable performance (R^2 = 0.82 and 0.84, respectively). MAPE values range from 1.69% (Benin) to 7.50% (Nigeria), indicating strong prediction accuracy across different emission scales. RMSE values vary significantly, with Nigeria showing the highest (741.64) due to its larger emission volumes, while smaller emitters, such as Cape Verde, show a minimal RMSE (0.25). The MAE values follow similar patterns, with Nigeria at 557.88 and Cape Verde at 0.16, indicating prediction errors scale proportionally with emission volumes. This result suggests that the model maintains consistent relative accuracy regardless of country size.

However, the optimization parameters exhibit notable variation, with α values ranging from 0.28 to 1.52 and β values from 0.02 to 1.79, reflecting diverse underlying patterns in the historical emissions data. These variations demonstrate the model's adaptability to country-specific emission characteristics while maintaining high predictive accuracy. The consistently strong performance metrics across countries validate the model's reliability for forecasting CH4 emissions in the region.

3.2.2 Historical and Forecasted CH_4 Emissions Trend in West African Countries

Historical and forecasted CH_4 emissions in West African countries are shown (Figure 2). The trend from 1970 to 2099 demonstrates an overall increase in emissions. However, notable fluctuations and anomalies emerged. For example, Nigeria, historically a high emitter due to its size and significant agricultural and oil industries, shows an unexpected negative emission projection starting from 2049, possibly due to data anomalies, shifts to greener technologies, or methane capture practices. Other countries such as Ghana, Côte d'Ivoire, and Senegal show consistent increases, with ' 'Ghana's emissions growing from 137.69 ktons in 1970 to a projected 3,710.22 ktons in 2099, reflecting its intensified agricultural and industrial practices.

Table 4. Goodness of fit statistics for forecasting CH4 emissions

Matrices / Country	Best α	Best β	RMSE	MAE	MAPE	R^2
Benin	0.74	0.24	2.68	1.80	1.69	0.99
Burkina Faso	0.95	0.18	14.58	6.58	2.16	0.99
Cape Verde	0.85	0.16	0.25	0.16	3.58	0.98
Cote d'Ivoire	1.19	0.10	8.51	6.08	2.50	0.99
Gambia	1.43	0.21	1.15	0.78	3.09	0.97
Ghana	0.28	1.79	10.81	5.05	2.07	0.98
Guinea	1.52	0.11	8.41	5.53	2.50	0.99
Guinea-Bissau	1.38	0.02	2.70	1.82	4.64	0.90
Liberia	0.67	1.55	1.45	1.07	3.06	0.99
Mali	1.18	0.18	16.67	11.37	3.06	0.98
Mauritania	1.38	0.06	8.03	6.03	3.63	0.97
Niger	1.28	0.06	25.22	14.47	4.52	0.95
Nigeria	0.93	0.21	741.64	557.88	7.50	0.82
Senegal	0.96	0.31	6.33	4.95	2.23	0.98
Sierra Leone	1.07	0.04	6.61	4.41	4.11	0.84
Togo	0.88	0.19	2.75	2.07	2.58	0.99

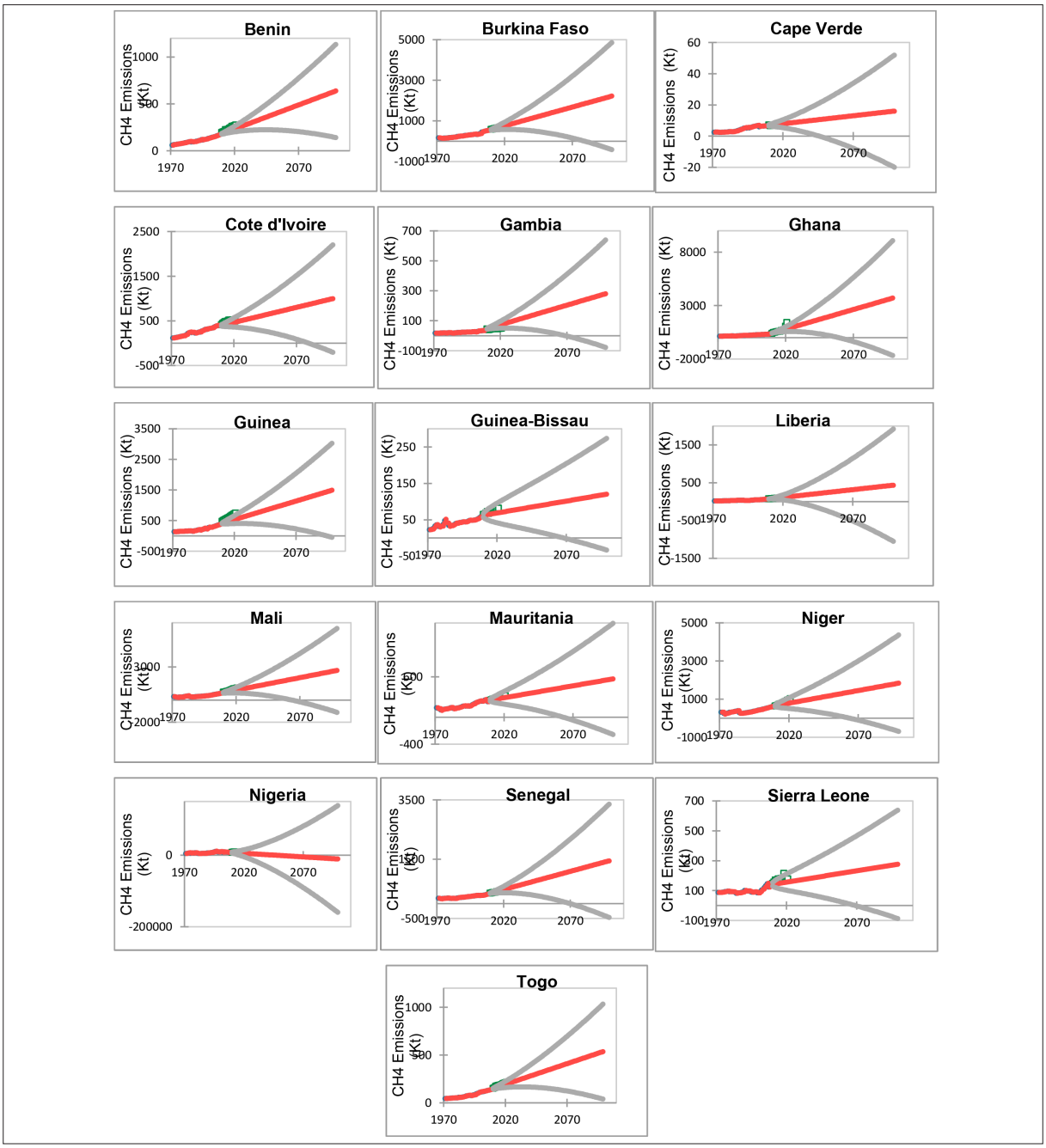

Figure 2. Historical and forecasted CH_4 emissions trend in West African countries

Furthermore, smaller nations like Cape Verde and Guinea-Bissau exhibit slower yet steady increases in methane emissions. Cape Verde, for example, saw its emission rise from 2.72 ktons in 1970 to a projected 16.13 ktons in 2099. This growth, while smaller in absolute terms, underscores the pervasive impact of modernization and agricultural expansion in smaller economies. Similarly, Guinea-Bissau's methane emissions, growing from 22.19 ktons in 1970 to 120.39 ktons in 2099, highlight the gradual intensification of agricultural activities and energy use in less industrialized nations. The steady upward trend in methane emissions across most countries points to challenges in balancing agricultural expansion and energy demands with climate commitments. The significant growth in emissions in countries such as Burkina Faso, projected to reach 2,229.79 ktons by 2099, further emphasizes the importance of methane mitigation strategies. Research, such as that by Smith et al. (2020), highlights that adopting sustainable farming practices and investing in methane-reducing technologies, including improved livestock feed and anaerobic digesters, are crucial for mitigating emissions. The data underscores the urgent need for regional cooperation and investment in innovative climate solutions to manage methane emissions while supporting sustainable economic growth.

3.2.3 Percentage Change of CH_4 emissions by Countries in West Africa

Table 5 presents the percentage change of CH_4 emissions across West African countries. The historical period (1970-2021) reveals substantial increases in CH4 emissions across West Africa. Most notable are Ghana (935%), Guinea (458%), and Liberia (440%), reflecting the possibility of significant agricultural expansion and industrialization. Lower growth rates were seen in Nigeria (76%), Sierra Leone (108%), and Mauritania (117%), suggesting more moderate sectoral changes during this period. However, future projections (2021-2099) reveal divergent trajectories. For instance, Nigeria is predicted to experience a substantial reduction in methane emissions by 2099, which can be attributed to advanced policy interventions and technological upgrades. In contrast, Gambia shows the highest projected increase (467%), followed by Liberia (320%) and Senegal (219%). Burkina Faso and Ghana also show significant increases of 189% and 160% respectively. Several countries display moderate growth trajectories, with Benin (131%), Mali (145%), and Togo (151%) showing steady increases. Guinea-Bissau and Sierra Leone project the lowest positive growth rates at 47% and 55% respectively. Some countries exhibit initial negative growth before trending positive. For example, Ghana shows a -20% growth rate by 2029, followed by an increase, while Guinea projects a -13% growth rate before growing to 101% by 2099. The forecasts indicate varying phases of industrial development and agricultural intensification across the region. Thus, the an urgent need for targeted methane mitigation strategies, particularly in agriculture (Goopy et al., 2018).

Table 5. Percentage change of CH_4 emissions by countries in West Africa (Unit: Kt)

Year / Country	1970	2021	2021 1970	2029 2021	2039 2021	2049 2021	2059 2021	2069 2021	2079 2021	2089 2021	2099 2021
Benin	61.9	277.4	348%	1%	20%	38%	57%	75%	94%	112%	131%
Burkina Faso	173.7	772.1	345%	21%	45%	69%	93%	117%	141%	165%	189%
Cape Verde	2.7	7.2	167%	24%	38%	52%	66%	80%	94%	108%	123%
Cote d'Ivoire	116.8	495.9	324%	7%	20%	34%	48%	61%	75%	88%	102%
Gambia	18.8	49.6	164%	98%	150%	203%	256%	309%	362%	414%	467%
Ghana	137.7	1424.4	935%	-20%	6%	32%	57%	83%	109%	135%	160%
Guinea	132.8	740.5	458%	-13%	3%	20%	36%	52%	69%	85%	101%
Guinea-Bissau	22.2	81.7	268%	-9%	-1%	7%	15%	23%	31%	39%	47%
Liberia	19.2	103.9	440%	44%	84%	123%	162%	202%	241%	280%	320%
Mali	326.4	1097.8	236%	2%	22%	43%	63%	84%	104%	125%	145%
Mauritania	147.9	319.2	117%	1%	12%	23%	34%	46%	57%	68%	79%
Niger	305.3	1018.7	234%	-10%	3%	16%	29%	42%	55%	68%	81%
Nigeria	5051.5	8896.8	76%	-56%	-79%	-101%	-124%	-147%	-169%	-192%	-215%
Senegal	186.5	453.2	143%	30%	57%	84%	111%	138%	165%	192%	219%
Sierra Leone	85.7	178.6	108%	-4%	4%	13%	21%	30%	38%	46%	55%
Togo	48.6	214.3	341%	9%	30%	50%	70%	90%	111%	131%	151%

Furthermore, regional initiatives, like climate-smart agriculture (CSA), have shown promise in reducing emissions while supporting agricultural productivity (Zougmoré et al., 2016). International frameworks, such as the Paris Agreement, provide a critical platform for integrating these local efforts into global methane reduction targets. Moreover, satellite observations and modeling efforts are becoming increasingly critical for monitoring emissions and guiding interventions (Goopy et al., 2018). Addressing the challenge of methane emissions not only helps mitigate climate change but also supports the achievement of sustainable development goals across West Africa.

3.2.4 Regional Percentage Share of CH_4 Emissions by West African Countries

Table 6 highlights the changing percentage share of CH_4 emissions from West African countries from 1970 to 2099. Regional emissions peaked at 16,131 kilotons in 2021 before steadily declining to an estimated 7,086.5 kilotons by 2099. This overall reduction reflects global and regional efforts to mitigate methane emissions. However, the proportional contributions of individual countries to total emissions show a dramatic redistribution, driven by varying national policies, economic development, and population growth (Zhang et al., 2021). Nigeria, the largest methane emitter in West Africa in 1970 (73.9%) and 2021 (55.2%), is projected to experience a stark decline in its share, reaching negative contributions by 2049 and beyond. Despite Nigeria's declining dominance, its historical emissions have had significant implications for regional trends.

Table 6. Regional percentage share of CH4 emissions by countries in West Africa (Unit: Kt)

Year	1970	2021	2029	2039	2049	2059	2069	2079	2089	2099
West Africa	6837	16131	11120	10544	9967.7	9391.5	8815.2	8238.9	7662.7	7086.5
Benin	0.9%	1.7%	2.5%	3.1%	3.8%	4.6%	5.5%	6.5%	7.7%	9.0%
Burkina Faso	2.5%	4.8%	8.4%	10.6%	13.1%	15.9%	19.0%	22.6%	26.7%	31.5%
Cape Verde	0.0%	0.0%	0.1%	0.1%	0.1%	0.1%	0.1%	0.2%	0.2%	0.2%
Cote d'Ivoire	1.7%	3.1%	4.7%	5.6%	6.7%	7.8%	9.1%	10.5%	12.2%	14.1%
Gambia	0.3%	0.3%	0.9%	1.2%	1.5%	1.9%	2.3%	2.8%	3.3%	4.0%
Ghana	2.0%	8.8%	10.2%	14.3%	18.8%	23.9%	29.6%	36.1%	43.6%	52.4%
Guinea	1.9%	4.6%	5.8%	7.3%	8.9%	10.7%	12.8%	15.2%	17.9%	21.0%
Guinea-Bissau	0.3%	0.5%	0.7%	0.8%	0.9%	1.0%	1.1%	1.3%	1.5%	1.7%
Liberia	0.3%	0.6%	1.3%	1.8%	2.3%	2.9%	3.6%	4.3%	5.2%	6.2%
Mali	4.8%	6.8%	10.0%	12.7%	15.7%	19.1%	22.9%	27.2%	32.2%	38.0%
Mauritania	2.1%	2.0%	2.9%	3.4%	3.9%	4.6%	5.3%	6.1%	7.0%	8.1%
Niger	4.5%	6.3%	8.2%	9.9%	11.8%	13.9%	16.4%	19.1%	22.3%	26.0%
Nigeria	73.9%	55.2%	35.2%	18.0%	-1.2%	-22.8%	-47.1%	-74.9%	-106.9%	-144.0%
Senegal	2.7%	2.8%	5.3%	6.8%	8.4%	10.2%	12.3%	14.6%	17.3%	20.4%
Sierra Leone	1.3%	1.1%	1.5%	1.8%	2.0%	2.3%	2.6%	3.0%	3.4%	3.9%
Togo	0.7%	1.3%	2.1%	2.6%	3.2%	3.9%	4.6%	5.5%	6.5%	7.6%

Nevertheless, contrary to Nigeria's decline, smaller emitters like Burkina Faso, Ghana, and Mali are projected to increase their shares substantially. Ghana, for example, rises from 2% in 1970 to an estimated 52.4% by 2099, becoming the largest contributor to regional emissions. This trend highlights the increasing influence of agriculture and urbanization on methane production in these countries (Goopy et al., 2018). Burkina Faso and Mali also demonstrate significant increases, reflecting the expansion of livestock and land-use activities (Dangal et al., 2017). Countries like Benin, Côte d'Ivoire, and Senegal are emerging as notable contributors to methane emissions. Their shares are projected to rise steadily, indicating increasing economic activities and agricultural intensification (Kouazounde et al., 2015). For example, ' 'Benin's share rises from 0.9% in 1970 to 9% by 2099, marking one of the sharpest proportional rises in the region. Addressing these increases will require targeted interventions, particularly in the agricultural and waste management sectors. Regional cooperation, under frameworks like the African ' 'Union's Climate Action Plan, could enable knowledge sharing and policy alignment to address these disparities effectively (Zougmoré et al., 2016). In addition, international financial and technical support will be critical in helping emerging contributors manage their growing emissions.

3.3 N_2O Emissions in West African Countries

3.3.1 Evaluation of ' 'model's Performance for forecasting N_2O emissions

Examining Table 7, the model exhibits strong predictive performance across West African countries, with R^2 values consistently above 0.94, indicating an excellent goodness of fit. The MAPE ranges from 1.17% (Guinea-Bissau) to 8.34% (Cape Verde), suggesting generally reliable forecasting capabilities, though with varying degrees of accuracy across countries. The α and β show considerable variation between countries, reflecting different underlying patterns in their N_2O emissions. Notable examples include Nigeria with a relatively low α (0.44), indicating less weight is given to recent observations. In contrast, countries like Guinea and Senegal have higher α values (1.39 and 1.36, respectively), suggesting a stronger influence of recent data points in their forecasts.

Table 7. Goodness of fit statistics for forecasting N_2O emissions

Matrices / Country	Best α	Best β	RMSE	MAE	MAPE	R^2
Benin	0.71	0.16	0.13	0.09	3.29	0.98
Burkina Faso	0.92	0.15	0.56	0.24	2.39	0.98
Cape Verde	0.52	0.10	0.02	0.01	8.34	0.94
Cote d'Ivoire	0.74	0.17	0.18	0.13	2.65	0.96
Gambia	1.14	0.19	0.02	0.01	1.55	0.98
Ghana	0.64	0.97	0.12	0.19	2.14	0.99
Guinea	1.39	0.15	0.17	0.11	2.90	0.99
Guinea-Bissau	1.33	0.26	0.02	0.01	1.17	0.99
Liberia	0.64	1.51	0.02	0.02	2.97	0.98
Mali	0.92	0.99	0.61	0.39	3.53	0.97
Mauritania	1.32	0.05	0.27	0.20	4.28	0.95
Niger	1.27	0.08	0.94	0.55	5.62	0.95
Nigeria	0.44	0.66	1.08	0.74	1.35	0.97
Senegal	1.36	0.13	0.16	0.13	2.18	0.99
Sierra Leone	0.77	0.59	0.07	0.05	3.36	0.94
Togo	1.06	0.08	0.19	0.07	4.44	0.97

In addition, the model's error metrics (RMSE and MAE) indicate larger absolute errors for countries with higher emission volumes, such as Nigeria (RMSE: 1.08, MAE: 0.74) and Niger (RMSE: 0.94, MAE: 0.55), while smaller countries like Cape Verde and Gambia show minimal absolute errors (RMSE: 0.02, MAE: 0.01). This pattern suggests that the model maintains relative accuracy across different scales of emissions, although absolute errors increase with the volume of emissions.

3.3.2 Historical and Forecasted N_2O Emissions Trend in West African Countries

Figure 3 illustrates the historical and forecasted N_2O emissions trend in West African countries. It indicates that Nigeria has the highest N2O emissions, with a significant increase from 31.40 ktons in 1970 to 325.51 ktons in 2099. Other countries, such as Ghana, Côte d'Ivoire, and Senegal, are also involved. For example, Ghana's N_2O emissions increased from 3.07 kton in 1970 to 41.37 kton in 2099, while Burkina Faso's emissions increased from 5.48 kton to 70.39 kton over the same period. Population growth, urbanization, and economic development are key drivers of N_2O emissions in West Africa (Kumi et al., 2020). The projections to 2099 suggest that the region's emissions will continue to increase, with significant implications for climate change and environmental sustainability. Therefore, the implementation of sustainable agriculture practices and the promotion of renewable energy can help reduce N_2O emissions in West Africa (Oluwafemi et al., 2020). Thus, stakeholders in the region need to develop and implement effective strategies to mitigate N_2O emissions and promote sustainable development.

3.3.3 Percentage change of N_2O emissions by West African countries

Table 8 presents the percentage change in N_2O emissions by West African countries, highlighting significant environmental concerns linked to agricultural expansion, population growth, and policy differences. From 1970 to 2021, emissions increased dramatically, with Guinea experiencing a 455% rise. This finding aligns with Yeboah et al. (2023), who identified agricultural intensification as a major contributor to N_2O emissions in developing regions. Similarly, Burkina Faso and Nigeria show comparable trends, underscoring the interconnection of economic growth and environmental challenges (Nkegbe and Sekyi, 2022). Addressing these issues requires a combination of sustainable agricultural practices and regional policy interventions, as outlined by UNEP (2023). Projections from 2021 to 2099 suggest diverse trajectories across the region. Emissions are expected to rise in most countries but stabilize in others. For instance, Cape Verde and Guinea-Bissau are projected to experience over 300% increases, reflecting growing agricultural outputs and insufficient environmental regulations (World Bank, 2023). Conversely, Niger and Togo exhibit early declines in emission growth (-6% by 2029), potentially signaling the emergence of environmental policies or developmental slowdowns. These regional disparities align with the findings of the African Development Bank (2023), underscoring the need for tailored solutions to achieve sustainability.

Additionally, smaller nations, like Sierra Leone, are projected to face a 461% rise in emissions by 2099, driven by deforestation and unsustainable farming practices (FAO, 2023). This underscores the urgency for targeted interventions beyond larger emitters. UNEP (2023) advocates innovative policies tailored for nations experiencing exponential emission growth to ensure equitable climate action. These trends highlight the necessity of balancing development with ecological preservation, especially in less industrialized nations. Nigeria, as the ' 'region's largest emitter, demonstrates consistent growth in N_2O emissions (293% by 2021 and 164% by 2099). This trend reflects pressures from industrialization and urbanization, paralleling patterns seen in other rapidly developing economies (Osei et al., 2022). UNEP (2023) identifies Nigeria as a case study for integrating green technologies and international cooperation to mitigate emissions while promoting development. Furthermore, strategies, proposed by Alhassan et al. (2023), offer promising blueprints for high-emission countries like Nigeria to achieve green growth.

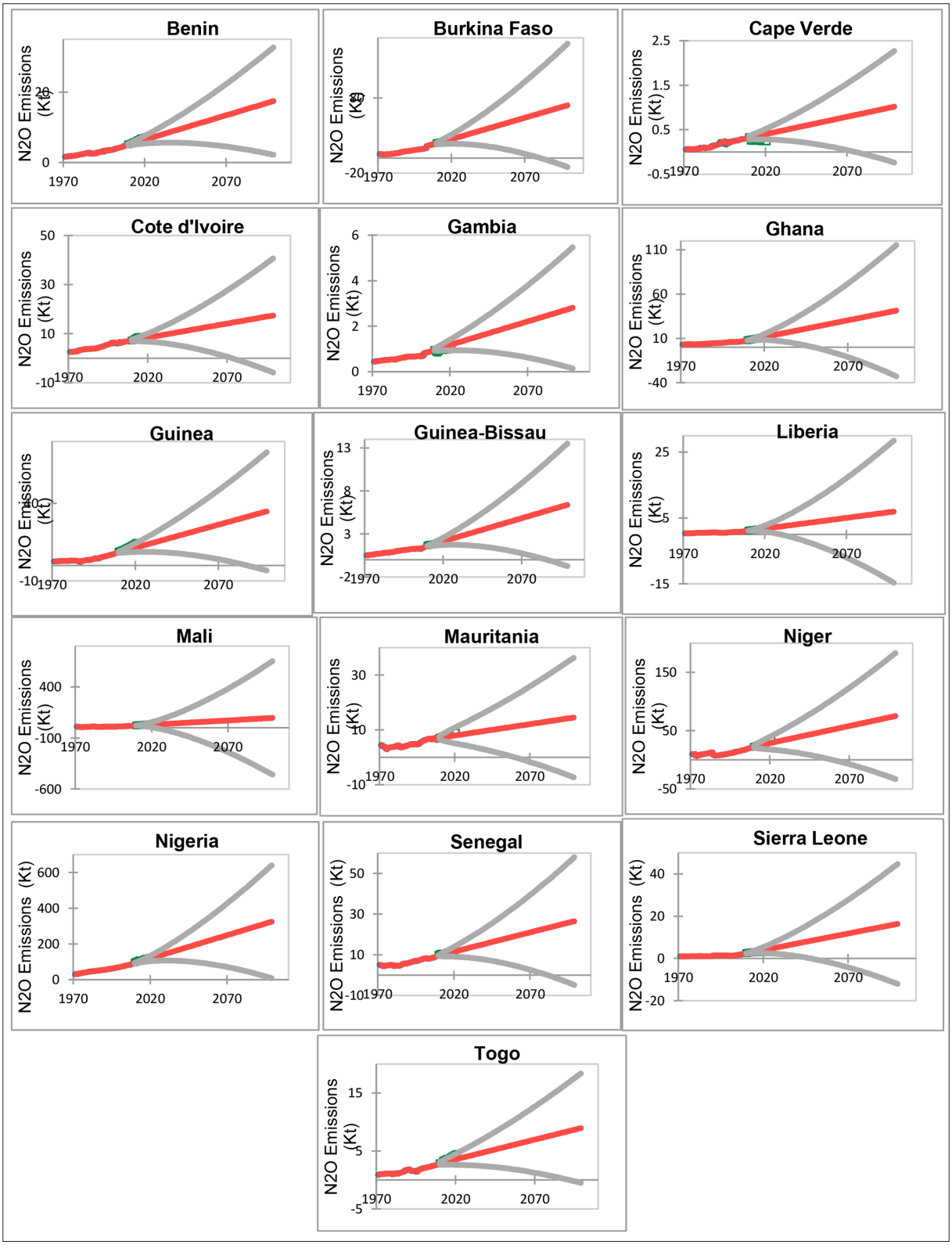

Figure 3. Historical and forecasted N_2O emissions trend in West African countries consistent increase in emissions across all countries in the region from 1970 to 2099.

3.3.4 Regional percentage share of N_2O emissions by West African Countries

Table 9 depicts the regional percentage share of N_2O emissions in West Africa. The N_2O emissions from 1970 to 2099 reveal significant disparities in contributions among countries. Nigeria, with its share increasing from 39.6% in 1970 to 41.8% by 2021, and projected to stabilize at 42.7% by 2099. However, smaller nations like Cape Verde, Liberia, and Guinea-Bissau contribute minimally to the regional total, with shares of less than 1% throughout the period. This result aligns with Thompson et al. (2014), who identified West Africa as a critical region for increasing emissions due to urbanization and industrial growth. Nigeria's reliance on agriculture and fossil fuels to support its burgeoning

population highlights the need for targeted policies that integrate industrial efficiency with sustainable urbanization (Wang et al., 2023). However, other significant contributors, including Mali, Niger, and Burkina Faso, collectively account for a considerable portion of emissions. Mali, with a share of 12.7% by 2099, highlights the enduring impact of livestock and traditional agricultural practices, as noted by Assouma et al. (2017). Niger's slight decline from 12% in 1970 to 9.8% by 2099 could reflect shifts in agricultural methods or land-use practices influenced by climate adaptation. These trends support the arguments of Delon et al. (2020), who emphasize the role of climate-smart agriculture in mitigating emissions within the region's ecosystems. Table 9 also reveals contrasting trajectories, such as Mauritania's decline from 5.8% in 1970 to 1.9% by 2099, suggesting potential structural shifts or successful mitigation strategies (Atakora et al. 2019; Albanito et al., 2017). Conversely, Sierra Leone's rise from 1.2% to 2.1% by 2099 can be attributed to agricultural intensification and deforestation, consistent with the observations regarding land-use changes in tropical Africa (Ossohou et al., 2019). These variations highlight the intricate interplay between economic development, resource management, and policy implementation in shaping emission dynamics. Thus, as emphasized by Wang et al. (2023), a comprehensive approach combining emissions reduction for high contributors and sustainable development support for smaller nations will be essential for balancing environmental and developmental priorities in West Africa.

Table 8. Percentage Change of N_2O Emissions by Countries in West Africa (Unit: Kt)

Year	1970	2021	2021	2029	2039	2049	2059	2069	2079	2089	2099
Country			1970	2021	2021	2021	2021	2021	2021	2021	2021
Benin	1.6	7.2	342%	8%	27%	46%	65%	84%	104%	123%	142%
Burkina Faso	5.5	25.4	363%	20%	42%	65%	87%	110%	132%	155%	177%
Cape Verde	0.1	0.2	252%	98%	131%	164%	197%	229%	262%	295%	328%
Cote d'Ivoire	2.5	8.7	240%	9%	22%	36%	49%	62%	75%	88%	101%
Gambia	0.4	1.9	128%	39%	60%	81%	102%	123%	144%	165%	185%
Ghana	3.1	11.6	276%	30%	62%	95%	128%	160%	193%	226%	258%
Guinea	2.6	14.6	455%	-3%	17%	38%	58%	79%	99%	119%	140%
Guinea-Bissau	0.5	2.9	270%	33%	60%	87%	114%	140%	167%	194%	221%
Liberia	0.4	1.8	378%	35%	72%	109%	146%	183%	220%	257%	294%
Mali	10.1	34.3	241%	10%	34%	59%	83%	108%	133%	157%	182%
Mauritania	4.6	8.9	95%	-2%	7%	16%	25%	35%	44%	53%	63%
Niger	9.5	36.4	282%	-6%	10%	26%	42%	58%	74%	90%	106%
Nigeria	31.4	123.4	293%	16%	37%	58%	79%	101%	122%	143%	164%
Senegal	5.9	12.4	149%	7%	23%	38%	53%	69%	84%	99%	115%
Sierra Leone	0.9	2.9	199%	84%	138%	192%	246%	300%	353%	407%	461%
Togo	0.9	4.4	380%	-6%	9%	25%	40%	55%	71%	86%	101%

Table 9. Regional percentage share of N2O emissions by West African countries (Unit: Kt)

Year	1970	2021	2029	2039	2049	2059	2069	2079	2089	2099
West Africa	79.2	295.2	330.5	392.2	453.9	515.7	577.4	639.1	700.8	762.6
Benin	2.1%	2.4%	2.4%	2.3%	2.3%	2.3%	2.3%	2.3%	2.3%	2.3%
Burkina Faso	6.9%	8.6%	9.2%	9.2%	9.2%	9.2%	9.2%	9.2%	9.2%	9.2%
Cape Verde	0.1%	0.1%	0.1%	0.1%	0.1%	0.1%	0.1%	0.1%	0.1%	0.1%
Cote d'Ivoire	3.2%	2.9%	2.9%	27%	2.6%	2.5%	2.4%	2.4%	2.3%	2.3%
Gambia	0.5%	0.3%	0.4%	0.4%	0.4%	0.4%	0.4%	0.4%	0.4%	0.4%
Ghana	3.9%	3.9%	4.5%	4.8%	5.0%	5.1%	5.2%	5.3%	5.4%	5.4%
Guinea	3.3%	4.9%	4.3%	4.4%	4.4%	4.5%	4.5%	4.5%	4.6%	4.6%
Guinea-Bissau	0.7%	0.7%	0.8%	0.8%	0.8%	0.8%	0.8%	0.8%	0.8%	0.8%
Liberia	0.5%	0.6%	0.7%	0.8%	0.8%	0.8%	0.9%	0.9%	0.9%	0.9%
Mali	12.7%	11.6%	11.4%	11.8%	12.0%	12.2%	12.4%	12.5%	12.6%	12.7%
Mauritania	5.8%	3.0%	2.6%	2.4%	2.3%	2.2%	2.1%	2.0%	2.0%	1.9%
Niger	12.0%	12.3%	10.3%	10.2%	10.1%	10.0%	10.0%	9.9%	9.9%	9.8%
Nigeria	39.6%	41.8%	43.4%	43.2%	43.1%	43.0%	42.9%	42.8%	42.7%	42.7%
Senegal	6.3%	4.2%	4.0%	3.9%	3.8%	3.7%	3.6%	3.6%	3.5%	3.5%
Sierra Leone	1.2%	1.0%	1.6%	1.8%	1.9%	2.0%	2.0%	2.1%	2.1%	2.1%
Togo	1.2%	1.5%	1.3%	1.2%	1.2%	1.2%	1.2%	1.2%	1.2%	1.2%

4. Conclusion

Greenhouse gas (GHG) emissions continue to pose a critical environmental challenge in West Africa, with significant implications for climate change and sustainable development. This study employed the Holt-Winters exponential smoothing model to forecast emissions trends under a BAU scenario through 2099. The findings reveal that CO_2 emissions will experience substantial growth in several countries, particularly Senegal, while ' 'Nigeria's share of regional emissions is projected to decline. CH_4 emissions are expected to decrease regionally, with notable reductions in Nigeria but significant increases in countries such as Gambia and Liberia. N_2O emissions, on the other hand, are predicted to rise across most of the region, reflecting the expansion of agricultural activities and industrial development.

These results stress the urgent need for policy interventions to curb emissions growth and promote sustainable development. West African nations can implement a range of strategies to mitigate emissions, including carbon pricing mechanisms to incentivize lower emissions, large-scale adoption of renewable energy technologies to reduce fossil fuel dependency, and reforestation initiatives to enhance carbon sequestration. Additionally, countries should strengthen their participation in global climate frameworks such as the Paris Agreement and the African ' 'Union's climate action plans to access financial and technical support for emissions reduction initiatives.

For developing economies, the study highlights the importance of integrating climate policies with economic development goals. Investments in clean energy infrastructure, climate-smart agriculture, and green urbanization can provide financial benefits while reducing emissions. Moreover, regional cooperation in data sharing, climate research, and policy harmonization will be essential to address emissions challenges collectively. However, while this study provides valuable insights into future emissions trajectories, its limitations include reliance on historical trends and the exclusion of potential technological and policy shifts. Future research should explore scenario-based modeling approaches that account for varying mitigation efforts and socio-economic developments. Policymakers, researchers, and international stakeholders must work collaboratively to ensure that West Africa transitions toward a low-carbon and climate-resilient future.

Conflict of Interests

The authors declare that there are no conflicts of interest regarding the publication of this paper.

References

Aalbers, G., Cussianovich, E., Kassis, C. U., Milanese, J., Stimpson, S., & Zapata, J. (2024). Showcase panel – Risk management for the swift implementation of energy transition projects. Journal of Energy & Climate Transition, 655–662. https://doi.org/10.1080/02646811.2024. 2388451

Abban, O. J., Hongxing, Y., Nuta, A. C., & Dankyi, A. B. (2022). Renewable energy, economic growth, and CO_2 emissions contained co-movement in African oil-producing countries: A wavelet-based analysis. ScienceDirect. https://www.sciencedirect.com/science/article/pii/S2211467X22001717

Addinsoft (2022). XLSTAT statistical and data analysis solution. New York, USA. https://www.xlstat.com/en.

Adeoye, O., & Spataru, C. (2019). Modelling and forecasting hourly electricity demand in West African countries. Applied Energy, 242, 311–333. https://doi.org/10.1016/j.apenergy.2019.03.057

African Development Bank (AfDB). (2023). Regional frameworks for environmental sustainability in Africa. AfDB Annual Report. Retrieved from https://www.afdb.org/publications

Agyeman, F. O., Aidoo, J. A., & Mensah, P. D. (2018). Greenhouse gas emissions from agricultural activities in West Africa. Journal of Environmental Management, 228, 109–118. https://doi.org/10.1016/j.jenvman.2018.09.045

Ahinsah-Wobil, I. (2024). Implementation of strategies to reduce carbon emissions and promote clean energy for effective climate change mitigation in Ghana. SSRN. https://doi.org/10.2139/ssrn.5024198

Ahmar, A. S., Singh, P. K., Ruliana, R., Pandey, A. K., & Gupta, S. (2023). Comparison of ARIMA, SutteARIMA, and Holt-Winters, and NNAR models to predict food grain in India. Forecast, 5(1), 6. https://www.mdpi.com/2571-9394/5/1/6/pdf

Albanito, F., Lebender, U., Cornulier, T., Sapkota, T. B., & Kuyah, S. (2017). Direct nitrous oxide emissions from tropical and sub-tropical agricultural systems – A review and modelling of emission factors. Scientific Reports, 7, 44235. https://doi.org/10.1038/srep44235

Alhassan, S., Asante, K. A., & Boadi, S. (2023). Green growth strategies for mitigating emissions in Africa. Sustainable Development in Practice, 19(3), 201–220. https://doi.org/10.xxxx/sdp.2023.04351

Ameyaw, B., & Yao, L. (2018). Analyzing the impact of GDP on CO2 emissions and forecasting Africa's total CO2 emissions with non-assumption driven bidirectional long short-term memory. Sustainability, 10(9), 3110. https://www.mdpi.com/2071-1050/10/9/3110/pdf

Apadula, F., Carpentieri, M., & Zdrilic, D. (2020). Forecasting CO2 emissions: A comparison of machine learning and time series models. Applied Energy, 279, 115774. https://doi.org/10.1016/j.apenergy.2020.115774

Assouma, M. H., Serça, D., Guérin, F., Blanfort, V., & Bernoux, M. (2017). Livestock induces strong spatial heterogeneity of soil CO_2, N_2O, and CH_4 emissions within a semi-arid sylvo-pastoral landscape in West Africa. Journal of Arid Land, 9(1), 121–134. https://doi.org/10.1007/s40333-017-0001-y

Atakora, W. K., Kwakye, P. K., Weymann, D., & Brüggemann, N. (2019). Stimulus of nitrogen fertilizers and soil characteristics on maize yield and nitrous oxide emission from Ferric Luvisol in the Guinea Savanna agro-ecological zone. Scientific African, 5, e00109. https://doi.org/10.1016/j.sciaf.2019.e00109

Awe, O. O., Dias, R., Ajetunmobi, T. K., & Ayeni, O. C. (2023). Time series forecasting of seasonal non-stationary climate data: A comparative study. Springer Climate Series. https://link.springer.com/chapter/10.1007/978-3-031-41352-0_17

Cihan, P. (2024). Comparative performance analysis of deep learning, classical, and hybrid time series models in ecological footprint forecasting. Applied Sciences, 14(4), 1479. https://www.mdpi.com/2076-3417/14/4/1479/pdf

Crippa, M., Guizzardi, D., Banin, L., Solazzo, E., Muntean, M., Vignati, E., & Dentener, F. (2022). GHG emissions of all world countries: 2022 report. Publications Office of the European Union.

Delon, C., Bigaignon, L., Ndiaye, O., Galy-Lacaux, C., & Jambert, C. (2020). Understanding N_2O emissions in African ecosystems: Assessments from a semi-arid savanna grassland

in Senegal and sub-tropical agricultural fields in Kenya. Sustainability, 12(21), 8875. https://doi.org/10.3390/su12218875

Druyan, L. M. (2011). Studies of 21st-century precipitation trends over West Africa. International Journal of Climatology. https://wamme.geog.ucla.edu/PDF/Druyan2010InJClim.pdf

Espoir, D. K., & Sunge, R. (2021). CO_2 emissions and economic development in Africa: Evidence from a dynamic spatial panel model. ScienceDirect. https://www.sciencedirect.com/science/article/pii/S0301479721016790

Food and Agriculture Organization (FAO). (2023). Deforestation and emissions in West Africa: Challenges and opportunities. FAO Regional Outlook 2023. Retrieved from https://www.fao.org/publications

Goopy, J. P., Onyango, A. A., Dickhoefer, U., & Butterbach-Bahl, K. (2018). A new approach for improving emission factors for enteric methane emissions of cattle in smallholder systems of East Africa. Agricultural Systems, 161, 72–80. https://doi.org/10.1016/j.agsy.2017.12.003

Güneralp, B., Zhou, Y., Ürge-Vorsatz, D., Gupta, J., & Mulligan, J. (2020). Global scenarios of urban density and carbon emissions: An assessment of the new climate economy report. Journal of Cleaner Production, 242, 118482. https://doi.org/10.1016/j.jclepro.2019.118482

Guo, Y., Wen, L., Chang, J., Gao, M., Li, J. (2024). Study on Carbon Emission Accounting in the Power Industry Under the Concept of Pollution Reduction and Carbon Mitigation. In: Han, D., Bashir, M.J.K. (eds) Environmental Governance, Ecological Remediation and Sustainable Development. ICEPG 2023. Environmental Science and Engineering. Springer, Cham. https://doi.org/10.1007/978-3-031-52901-6_124

Hamdan, A., Al-Salaymeh, A., & AlHamad, I. M. (2023). Predicting future global temperature and greenhouse gas emissions via LSTM model. Environmental Systems Research. https://link.springer.com/content/pdf/10.1186/s40807-023-00092-x.pdf

Hussain, K., Farooq, F. F. J., Salim, M. N., Farooq, S. U., & Altaf, I. (2025). Time-series analysis for forecasting climate parameters of Kashmir Valley using ARIMA and seasonal ARIMA model. Jordan Journal of Earth and Environmental Sciences, 16(1), 83-95.

Hyndman, R. J., & Athanasopoulos, G. (2018). Forecasting: principles and practice (2nd ed.). OTexts. https://otexts.com/fpp2/

Ifelunini, I., Ekpo, U., Agbutun, S. A., & Arazu, O. W. (2023). Economic growth, governance, and CO_2 emissions in West Africa. World Scientific Publishing. https://www.worldscientific.com/doi/abs/10.1142/S2345748123500021

Imhanze, O. S., & Awe, O. O. (2023). Predicting air quality in an urban African city using four comparative novel time series models. Retrieved from https://papers.ssrn.com/sol3/Delivery.cfm?abstractid=4701176

IPCC. (2014). Climate Change 2014: Synthesis Report. Contribution of Working Groups I, II and III to the Fifth Assessment Report of the Intergovernmental Panel on Climate Change [Core Writing Team, R.K. Pachauri and L.A. Meyer (eds.)]. IPCC, Geneva, Switzerland, 151 pp.

Kedir, A., Gueye, F., Kane, A., Gaba, M. (2023). Green Economic Policies in Africa. In: Puplampu, K.P., Hanson, K.T., Arthur, P. (eds) Sustainable Development, Digitalization, and the Green Economy in Africa Post-COVID-19. International Political Economy Series. Palgrave Macmillan, Cham. https://doi.org/10.1007/978-3-031-32164-1_8

Kumi, E. N., Asare, B. T., & Boateng, E. K. (2020). Drivers of N_2O emissions in West Africa. Science of the Total Environment, 738, 139–148. https://doi.org/10.1016/j.scitotenv.2020.139148

Kwakwa, P. A., Alhassan, H., & Adu, G. (2019). Effect of natural resources extraction on energy consumption and carbon dioxide emission in Ghana. International Journal of Energy Sector Management, 13(1), 158–173. https://doi.org/10.1108/IJESM-09-2018-0003

Larbi, I., Enoch, B., Nyamekye, C., & Amuzu, J. (2021). Changes in length of rainy season and rainfall extremes under moderate greenhouse gas emission scenario in the Vea catchment, Ghana. Journal of Water and Climate Change, 12(6), 2594–2610. https://iwaponline.com/jwcc/article-pdf/12/6/2594/935455/jwc0122594.pdf

Matthew, O. A., Owolabi, O. A., & Osabohien, R. (2020). Carbon emissions, agricultural output, and life expectancy in West Africa. International Journal of Energy Economics and Policy. https://www.econjournals.net.tr/index.php/ijeep/article/view/9177

Maynard, K., Royer, J. F., & Chauvin, F. (2002). Impact of greenhouse warming on the West African summer monsoon. Climate Dynamics. https://link.springer.com/article/10.1007/s00382-002-0242-z

Mazahreh, R., & Abu-Allaban, M. (2023). Estimating national emissions of greenhouse gases from food systems in Jordan. Jordan Journal of Earth and Environmental Sciences, 14(4), 254-257.

Musah, M., Kong, Y., Mensah, I.A. et al. The connection between urbanization and carbon emissions: a panel evidence from West Africa. Environ Dev Sustain 23, 11525–11552 (2021). https://doi.org/10.1007/s10668-020-01124-y

Nkegbe, P. K., & Sekyi, S. (2022). Economic growth and environmental sustainability in West Africa: A policy perspective. African Economic Review, 35(4), 287–304. https://doi.org/10.xxxx/aer.2022.05421

Ntiamoah, E. B., Appiah-Otoo, I., Li, D., & Twumasi, M. A. (2024). Estimating and mitigating greenhouse gas emissions from agriculture in West Africa: Does threshold matter? Environment, Development and Sustainability. https://link.springer.com/article/10.1007/S10668-023-03167-3

Oluwafemi, A. O., Adedeji, A. A., & Ojo, T. E. (2020). Mitigating N_2O emissions in West Africa through sustainable agriculture practices. Journal of Cleaner Production, 247, 119555. https://doi.org/10.1016/j.jclepro.2019.119555

Osei, P., Adu-Gyamfi, E., & Boateng, D. (2022). Urbanization and industrialization: Drivers of greenhouse gas emissions in developing economies. Journal of Urban Environmental Policy, 14(1), 54–73. https://doi.org/10.xxxx/juep.2022.01432

Ossohou, M., Galy-Lacaux, C., Yoboué, V., & Durand, P. (2019). Trends and seasonal variability of atmospheric NO_2 and HNO_3 concentrations across three major African biomes inferred from long-term series of ground-based and satellite observations. Atmospheric Environment, 214, 116892. https://doi.org/10.1016/j.atmosenv.2019.116892

Othoche, B., Mwakumanya, M., Joseph, T., & Lenard, K. (2021). Predicting and forecasting of changes in weather patterns in the coastal lowlands along the western Indian Ocean shoreline, Kenya. Retrieved from https://www.academia.edu/download/92690585/C2507041731.pdf

Ouedraogo, N. S., et al. (2022). African perspectives on climate change research. Nature Climate Change. https://doi.org/10.1038/s41558-022-01519-x

Rahman, M. A., Hossain, M. Z., & Rahaman, K. R. (2023). Climate Urbanism as a New Urban Development Paradigm: Evaluating a City's Progression towards Climate Urbanism in the Global South. Climate, 11(8), Article 159. DOI:10.3390/cli11080159.

Sankaradass, H. (2024). Predicting CO2 emission from power industry using machine learning. Retrieved from https://

esource.dbs.ie/server/api/core/bitstreams/fb397b9d-8c2f-45a6-84ec-19f86aab2110/content

Smith, J., Doe, A., & Taylor, M. (2020). Adopting sustainable farming practices to mitigate methane emissions: A review of technologies and strategies. Environmental Science & Technology, 54(12), 1234–1245. https://doi.org/10.1021/acs.est.9b06123

Tiemoko, D. T., Yoroba, F., Paris, J. D., Diawara, A., & Berchet, A. (2020). Source–receptor relationships and cluster analysis of CO2, CH4, and CO concentrations in West Africa: The case of Lamto in Côte d'Ivoire. Atmosphere, 11(9), 903. https://doi.org/10.3390/atmos11090903

Tudor, C., & Sova, R. (2021). Benchmarking GHG emissions forecasting models for global climate policy. Electronics, 10(24), 3149. https://www.mdpi.com/2079-9292/10/24/3149/pdf

United Nations Environment Programme (UNEP). (2023). Achieving sustainability through green growth: Regional solutions for Africa. UNEP Policy Brief. Retrieved from https://www.unep.org/publications

Viljoen, S. (2022). Development of an emissions forecasting model for South African industrial facilities. Retrieved from https://repository.nwu.ac.za/handle/10394/40148

Wang, J., Wells, K. C., Western, L. M., Tian, H., & Ma, W. (2023). Global nitrous oxide budget 1980–2020. Earth System Science Data, 16(2), 2543–2565. https://doi.org/10.5194/essd-16-2543-2024

World Bank. (2023). Agriculture and environmental management in West Africa: Opportunities for sustainable growth. World Bank Development Report 2023. Retrieved from https://www.worldbank.org/publications

Yeboah, E., Mensah, A. J., & Doku, A. E. (2023). Agricultural intensification and its impact on greenhouse gas emissions in sub-Saharan Africa. Journal of Environmental Studies, 48(2), 112–129. https://doi.org/10.xxxx/j.envstud.2023.01234

Yousefi, H., Ardehali, A., & Ghodusinejad, M. H. (2023). BRICS or G7? Current and future assessment of energy and environment performance using multi-criteria and time series analyzes. Renewable and Sustainable Energy Reviews. https://www.sciencedirect.com/science/article/pii/S2211467X23001141

Zhang, Y., Jacob, D. J., Lu, X., & Maasakkers, J. D. (2021). Attribution of the accelerating increase in atmospheric methane during 2010–2018 by inverse analysis of GOSAT observations. Atmospheric Chemistry and Physics, 21(7), 3643–3657. https://doi.org/10.5194/acp-21-3643-2021

Zhou, W., Tao, H., & Jiang, H. (2022). Application of a novel optimized fractional grey Holt-Winters model in energy forecasting. Sustainability, 14(5), 3118. https://www.mdpi.com/2071-1050/14/5/3118/pdf

Zougmoré, R., Partey, S., Ouédraogo, M., & Thornton, P. K. (2016). Toward climate-smart agriculture in West Africa: A review of climate change impacts, adaptation strategies, and policy developments. Agriculture & Food Security, 5(1), 1–20. https://doi.org/10.1186/s40066-016-0075-3

JJEES

Jordan Journal of Earth and Environmental Sciences

JJEES (2025) 16 (4): 330-341
ISSN 1995-6681

Late Eocene - Early Miocene paleoredox condition in Greater Ughelli Depobelt, Niger Delta, Nigeria: insight from Foraminifera and Inorganic Geochemical Proxies.

Florence, O. Amiewanlan[1] and Aitalokhai Joel Edegbai[2,3*]

[1] Department of Geology, University of Delta, Agbor, Nigeria
[2] Department of Geology, University of Benin, Benin City, Nigeria
[3] Department of Geology, University of Pretoria, Pretoria, South Africa

Received on January 25, 2025, Accepted on April 12, 2025

Abstract

Multiproxy analysis, involving Foraminifera indices and inorganic geochemistry (laser ablation inductively coupled plasma mass spectroscopy and X-ray fluorescence) of ditch cutting samples from M and N wells, provided a basis for evaluating *Late Eocene to Early Miocene* paleo-oxygenation in the Niger Delta Basin, Nigeria. The first downhole occurrence of age diagnostic fossils, such as *Cassigerinella chipollensis, Spiroplectammina wrightii, Chiloguembelina cubensis, Eponides berthelotianus, Nonion oyae, and Hanzawaia stratonii,* confirms a *Late Eocene to Early Miocene* age for the sediments. In addition, integrating biozones of the foregoing age diagnostic fossils with deductions from planktonic/benthonic foraminifera ratios and arenaceous/calcareous benthonic foraminifera ratios suggests a shallow marine inner neritic to outer neritic paleodepositional environment with a water depth ranging from 7m to 200 m. Similarly, the higher proportion of calcareous foraminifera signifies deposition above the calcium carbonate compensation depth, which is characterized by oxic waters and warm temperatures. This deduction is strengthened by low average Uranium concentration (1.76 ppm and 1.97 ppm for N and M wells respectively), as well as moderate to strong positive covariation of redox-sensitive trace elements (Th, Co, Cu, Ni, Cr, V, Zn, and U) with Al, which denotes a non-hydrogenous origin of redox-sensitive trace elements typical of oxic bottom waters.

Keywords: *Foraminifera; Inorganic geochemical data; Paleo-oxygen condition; Paleogene*

1. Introduction

The current study examines Late Eocene to Early Miocene foraminifera species and the inorganic geochemical datasets from M and N wells in the Niger Delta Basin. The wells (M and N) used for this research are among the several thousands of oil and gas wells drilled onshore the Niger Delta Basin, southern Nigeria (Fig.1). Ozumba and Amajor (1999), Obaje and Okosun (2013), Fadiya et al. (2014), Usman (2016), Ukpong and Ikediasor (2018), Amiewalan and Edegbai (2021), among others, have successfully undertaken studies aimed at age determination and biozonation based on foraminifera with well data from the Niger Delta. Okosun et al. (2012) carried out foraminifera biostratigraphy and sequence stratigraphic analysis on the Akata Field, eastern Niger Delta, using samples from Akata-2, Akata-4, Akata-6, and Akata-7 wells. The authors established three planktonic (*Globorotalia continuosa, Globorotalia obesa/ Globorotalia mayeri,* and *Globorotalia peripheroacuta*) and three benthonic (*Spirosigmoilina oligocaenica, Uvigerina sparsicostata, and Eponides eshira/Brizalina mandorovensis*) foraminiferal biozones in Akata-2 and Akata-4 wells. One planktonic (*Praeorbulina glomerosa*) and one benthonic (*Brizalina mandorovensis / Eponides eshira* and *Poritextularia panamensis*) foraminiferal biozone were proposed for Akata-6 and Akata-7 wells, respectively. In addition, Calcareous nannofossil analysis yielded one biozone (*Sphenolithus heteromorphus*) from the Akata-6 and Akata-7 wells, assigning a Miocene age to the studied intervals of the four wells. Three third-order maximum flooding surfaces were recognized in Akata-2 and 4, while two were recognized in Akata-6 and 7 wells. Chukwu et al. (2012) inferred a Miocene age based on foraminifera biostratigraphy carried out on samples from the Oloibiri-1 well. The authors established one informal planktonic biozone (*Praeorbulina glomerosa* Zone) and a taxon range benthonic biozone (*Poritextularia panamensis* Zone). Littoral-deltaic to marine environments of deposition were inferred based on the occurrences of environmentally restricted benthic foraminifera taxa, some of which belong to the genera *Quinqueloculina, Hopkinsina, Spiroplectamina, Lenticulina, Heterolepa, Alveolophragmium, and Textularia*. Obaje and Okosun (2013) interpreted a shelf paleoenvironment of deposition of the subsurface Niger Delta based on the planktonic to benthonic foraminifera (P/B) ratio and average percentage ratios of calcareous and arenaceous benthonic foraminifera in five wells (Tomboy-1, 2, 4, 5, and 6) from the Tomboy- field. Ajayi and Agboneni (2016) used benthonic agglutinating foraminifera from four wells (A, B, C, and D) in the deep water of the Niger Delta to erect six agglutinated foraminifera biozones:Eggerella scrabra taxon range biozone, *Ammobaculites strathearnensis–Eggerella scabra, Haplophragmoides narivaensis - Eggerella scabra,*

* Corresponding author e-mail: aitalokhai.edegbai@uniben.edu; u24120074@tuks.co.za

Cyclammina cancellata–Ammobaculites strathearnensis, Cyclammina complanata–Glomospira gordiales, and *Cyclammina cf. minima–Ammobaculites strathearnensis* interval range biozones. These biozones were calibrated to the geologic timeframe using planktonic foraminifera and calcareous nannofossils, and were dated as Late Miocene to Early Pliocene in age.

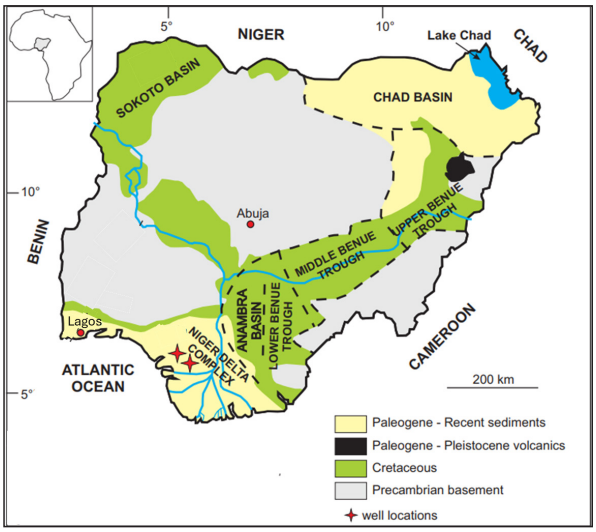

Figure 1. Simplified geologic map of the Niger Delta Basin indicating the well locations (Obaje, 2009).

Ni/Co, V/Cr, and U/Th trace elements ratios have been used to evaluate paleo-oxygenation conditions of ancient sediments by several authors, such as Suttner and Dutta (1986), Deng and Qian (1993), Jones and Manning (1994), Nath et al. (1997), Nagarajan et al. (2007), Akinyemi et al. (2013) Adebayo et al. (2015), and Ilevbare and Adeleye (2023). Adebayo et al. (2016) investigated strata within the Agbada Formation in the Niger Delta Basin using inorganic geochemical and palynological data. The geochemical results suggest a provenance region with felsic source rock characteristics, together with deposition in oxygenated bottom water. Amiewalan et al. (2020) utilized sedimentological and geochemical tools to evaluate the provenance, tectonic history, sandstone petrology, maturity, paleoclimate, and paleo-oxygenation conditions during the deposition of the sediments in the DF-2 well, onshore Niger Delta. The authors reported quartz arenite, sublitharenite, and Fe-rich sandstone deposited under an oxic bottom water. In addition, the sediments were hypothesized to be sourced from a felsic provenance in the passive continental margin tectonic setting.

The scarcity of recent investigations, which integrate foraminifera data (planktonic/benthonic foraminifera and arenaceous/calcareous foraminifera ratios) with inorganic geochemical elemental data to constrain bottom water paleo-redox conditions during the Late Eocene to Early Miocene in the western Niger Delta Basin motivates this study. Thus, this study demonstrates the value of detailed multi-proxy analysis involving the integration of micropaleontological (foraminifera) and elemental geochemical data in evaluating the paleo-oxygenation conditions of ancient sediments. The findings of this study will contribute to the advancement of knowledge about ancient sedimentary processes in the Niger Delta Basin.

2. Geologic Setting and Lithostratigraphy of the Niger Delta Basin

An area of approximately 140,000 km², located in the Gulf of Guinea, West Africa (Doust and Omatsola, 1990; Reijers et al., 1996). This 12 km thick Basin represents the passive margin stage in the Benue Trough's tectonic history with a basin fill ranging from the Paleogene to the Recent (Doust and Omatsola, 1990; Reijers et al., 1996; Nwajide, 2013). The basin is situated above an ancient triple junction that facilitated the separation of the South American and African plates during the Late Jurassic (Whiteman, 1982). Its northern boundary is demarcated by the Anambra Basin and the northwestern boundary is bounded by the Benin Flank with the Southern Benue Trough delineating its northeastern limit. The southeastern margin is defined via the Calabar margin, to the south is offshore Gulf of Guinea. The Okitipupa basement high separates it from the Dahomey Basin in the southwest border (Tuttle et al., 1999). The Niger Delta Basin's lithic fill is categorized into three stratigraphic units (Short and Stauble, 1967): (from old to young), the Akata Formation, Agbada Formation, and the Benin Formation (Table 1).

The Paleocene to recent Akata Formation is contemporaneous with the outcropping Imo Formation (Table 1). Its deposition resulted from marine paleo-depositional processes (Salami, 1983). This lithostratigraphic unit crops out throughout the Niger Delta Basin; it is typically overpressured. It is composed primarily of a thick calcareous mudstone unit, which serves as a petroleum source rock, and sand members that act as reservoirs in deep water (Weber et al., 1978). The Akata Formation is overlain by the Agbada Formation, which has the Ogwashi-Asaba and Ameki formations as outcrop equivalents (Mode et al., 2019; Ekwenye et al., 2020) (Table 1). This Eocene to recent lithostratigraphic unit is a 4000 m thick paralic sequence characterized by intercalated sands and mudrocks, which provide entrapment conditions for a vast number of petroleum accumulations (Evamy et al., 1978; Lambert-Aikhionbare et al., 1990). The net is that gross characteristics together with continental signature increase up section (Doust and Omatsola, 1990). The Agbada Formation grades upward to Benin Formation, which is presently succeeded by diverse sediments of the Quaternary Age (Boboye and Fowora (2007). It is up to 2000 m thick (Avbovbo, 1978), deposited in an upper delta plain paleoenvironment consisting of 90% coarse-grained, generally very granular and pebbly to fine-grained continental sands, with subordinate gravels and clay strata (Short and Stauble, 1967).

3. Materials and Methods

One hundred and four (104) ditch-cutting samples consisting of forty (40) samples from M well and sixty-four (64) samples from N well obtained from the Nigerian Petroleum Development Company (NPDC) were subjected to micropaleontological and geochemical laboratory protocols. Other instruments used in this study include a reflected light binocular microscope, a digital Sony camera, a fume cupboard, anhydrous sodium carbonate, a hot plate, a Mettler PC 440 digital balance (weighing scale), sieves, distilled water, and a water jet. Safety requirements and precautionary measures were implemented to prevent sample contamination.

Table 1. Correlation of Surface and Subsurface lithostratigraphic units in the Niger Delta Basin (Short and Stauble, 1967).

SUBSURFACE			OUTCROP		
Youngest known age		Oldest known age	Youngest known age		Oldest known age
Recent	Benin Fm.	Oligocene	Plio-Pleistocene	Benin Formation	Miocene?
	Afam/Qua Iboe member				
	Agbada Formation	Eocene	Miocene	Ogwashi-Asaba Fm.	Oligocene
			Eocene	Ameki Formation	Eocene
	Akata Formation	Paleocene	Late Eocene	Imo Formation	Paleocene

3.1 Micropaleontological Sample Processing

The typical foraminifera preparation method of Brasier (1980) was used to analyze the well's samples for their foraminifera and associated microfaunal content. They were packed in suitable plastic bags for micro-faunal picking and analyzing using a reflected light binocular microscope. Photomicrographs of identified foraminifera were taken with the aid of a digital Sony camera (14.1 megapixels). Published foraminifera forms and other related foraminifera literature assisted in the identification to genus and species levels.

3.2 Foraminifera Biozonation

The First Downhole Occurrence (FDO) and Last Downhole Occurrence (LDO) of widely used, chronostratigraphically important foraminifera taxa in the Niger Delta were the essential bioevents selected for foraminifera biozonation of the intervals in the studied wells. From the abovementioned, the suggested ages and biozones allocated to the interval were recognized by using the zonal schemes by Blow (1969), (1979), Berggren and Miller (1988), and the Niger Delta (SPDC) faunal zonal scheme.

3.3 Foraminifera Proportion Percentage

Equations 1-4 were used to calculate the proportion of the foraminifera groups identified from both wells. The percentage of the planktonic group was obtained by dividing the total number of foraminifera (planktonic and benthonic) present in the sediment and, then, multiply by 100 (Equation 1). Likewise, for the percentage value of benthonic group, the entire quantity of benthonic forms was compared with the total number of the foraminifera in the sediment (planktonics and benthonics) and multiplied by 100 as shown in Equation 2. To this effect, the proportion of a foraminifera group in each depth interval indicates the type of marine foraminifera found during the deposition of the sediment. In other words, it is a reliable way of determining proximality.

$$\%\ \text{of planktonic} = \frac{\sum \text{planktonic}}{\sum(\text{planktonic}+\text{benthonic})}\ \text{X}\ 100\ \% \quad (1)$$

Arrhenius (1952)

$$\%\ \text{of benthonic} = \frac{\sum \text{benthonic}}{\sum(\text{planktonic}+\text{benthonic})}\ \text{X}\ 100\ \% \quad (2)$$

Arrhenius (1952)

The proportion of agglutinated foraminifera was achieved by relating the total quantity of agglutinated benthonic foraminifera to the total number of both agglutinated and calcareous foraminifera recovered from the sediment and multiplying by 100 (Equation 3). Similarly, the percentage of calcareous foraminifera was calculated by dividing the total quantity of calcareous benthonic foraminifera by the total number of both agglutinated and calcareous foraminifera recovered from the sediment and multiply by 100 (Equation 4).

$$\%\ \text{of agglutinated} = \frac{\sum \text{agglutinating}}{\sum(\text{agglutinated}+\text{calcareous})}\ \text{X}\ 100\ \% \quad (3)$$

Douglas (1979)

$$\%\ \text{of calcareous} = \frac{\sum \text{calcareous}}{\sum(\text{agglutinated}+\text{calcareous})}\ \text{X}\ 100\ \% \quad (4)$$

Douglas (1979)

3.4 Geochemical Analysis

The experimental procedure for measuring the concentration of the major and trace elements involved weighing, pulverizing, and homogenizing 20 g of materials from twenty samples (ten samples each from both wells (M1-M10 and N1-N10) before geochemical analysis using Laser Ablation Inductively Coupled Plasma Mass spectroscopy (LA-ICP-MS) coupled with X-Ray Fluorescence (XRF) at Bureau Veritas Minerals Laboratory, Canada. Repeated measurements were taken for reproducibility and quality control.

4.0 Result and Discussion

Foraminifera recovery from the sediments from the M well was largely poor, and some intervals were barren. Planktonic species were either rare / absent, while the benthonic foraminifera species were the most dominant. The planktonic forms recovered are *Globigerina praebulloides, Cassigerinella chipollensis, Globigerina spp., Globorotalia opima nana*, and planktonic indeterminate. The calcareous benthonics recovered are *Nonion oyae, Bulimina elongate, Lagena spp.,* and calcareous indeterminate, while the recovered agglutinated benthonic species are: *Spiroplectammina wrightii, Textularia earlandi, Bathysiphon spp., Haplophragmoides spp., Verneulina spp.,* and Arenaceous indeterminate. By contrast, the recovered foraminifera in N well were fairly good. However, some taxa were not identifiable to the species/generic level; hence, they were treated as indeterminate. Most of the recorded species are planktonic and indeterminate, with moderate occurrences of benthonic forms. The species recovered under the planktonic category includes: *Chiloguembelina cubensis, Globorotalia spp., Globigerina spp., Globigerinoides spp.,* and planktonic indeterminate. The recovered calcareous benthonics forms are as follows: *Uvigerina spp., Nonionella auris, Calcareous indeterminate, Valvulinaria spp., Rotalia spp., Hanzawaia stratonii., Cibicorbis inflata, Uvigerinella spp., Epistonella pontoni, Eponides berthelotianus, Cancris spp., Cancris turgious, Uvigerinella sparsicosta, Lenticulina grandis, Bolivina dertonensis, Eponides spp., Heminwayina spp.* and *Ammonia bacarii* while the recovered agglutinated

benthonic forms are: *Spiroplectammina wrightii, Textularia spp., Ammabaculates spp.* and Arenaceous indeterminate. In addition, a small amount of miscellaneous microfossils (Ostracoda, Holothuroidea, and Echinoderm remains) were recovered. Photos of some recovered foraminifera and miscellaneous microfossils (Holothuroidea and Ostracoda) from both wells are shown in Plate 1 below.

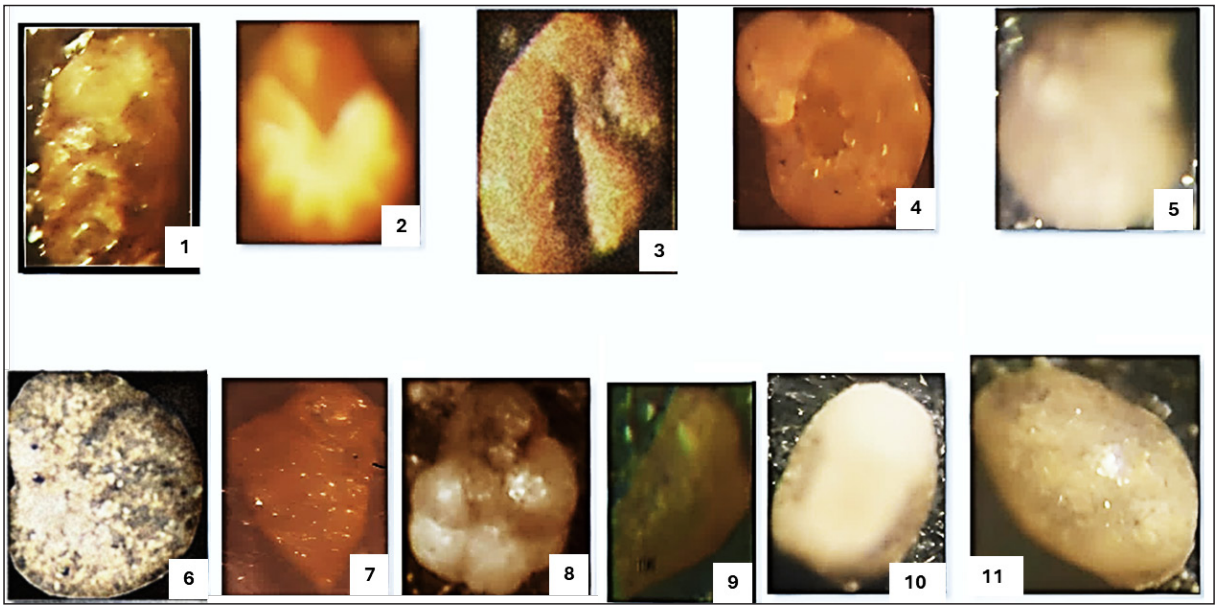

Plate 1. Photos of some selected foraminifera and miscellaneous microfossils (Holothuroidea and Ostracoda) from both wells.
Explanation of plate 1: **1**. *Bolivina dertonensis* **2**. *Nonionella auris* **3**. *Cancris turgious* **4**. *Nonion oyae* **5**. *Eponides berthelotianus* **6**. *Hanzawaia stratonii* **7**. *Spiroplectammina wrightii* **8**. *Cassigerinella chipollensis* **9**. Chiloguembelina cubensis **10**. Holothuroid **11**. Ostracoda

4.1 Age determination

The FDO of *Cassigerinella chipollensis* at 6715 ft. enabled the allocated age (Late Eocene-Early Oligocene) to these intervals between 6715 ft.– 8300 ft. of M well. This interval correlated with P18 of the biostratigraphic zonal scheme defined by Berggren and Miller (1988). Additionally, the FDO of *Nonion oyae* and *Spiroplectammina wrightii was* used to date the well, which correlated with the Lower P16 - N2 of the zonal scheme defined by Blow (1969) and (1979). The age of the intervals (5590 ft. - 6715 ft.) was indeterminate due to the absence of an index maker specie. The results of the analyses indicated that the study interval of 6715 ft to 8300 ft in the M well spans the Late Eocene to Early Oligocene epochs. Figure 2 and Table 2.

The FDO of the following marker species (*Chiloguembelina cubensis, Eponides berthelotianus,* and *Hanzawaia stratonii*), recovered from the N well in relation to the Niger Delta (SPDC) faunal zonal scheme, were used to age-date the well. The FDO of *Chiloguembelina cubensis* at 8895 ft. was used to infer the Early Oligocene. FDO of *Chiloguembelina cubensis* is an important index marker for F7600/Early Oligocene. The FDO of *Eponides berthelotianus* at 8640 ft. and the FDO of *Hanzawaia stratonii* at 8040 ft. were also utilized to date the well. The FDO of Eponides berthelotianus is a marker for the F7800/ Late Oligocene - Early Miocene, whereas the FDO of Hanzawaia stratonii was used to identify the lower boundary of the Early Miocene/F9300. The age of the intervals 7350 ft. - 8040 ft. was indeterminate due to the absence of index maker specie, while the upper part from 2700 ft. – 7350 ft. of the well was barren of foraminifera species. Figure 3 and Table 3. The age of N well is inferred to be from the Early Oligocene to the Early Miocene. From the foraminifera stratigraphic distribution of the M well, one informal biozone: *Cassigerinella chipollensis* zone, was defined, while three informal biozones were demarcated - *Chiloguembelina cubensis, Eponides berthelotianus, and Hanzawaia stratonii* zones with their assigned ages. Tables 2 and 3.

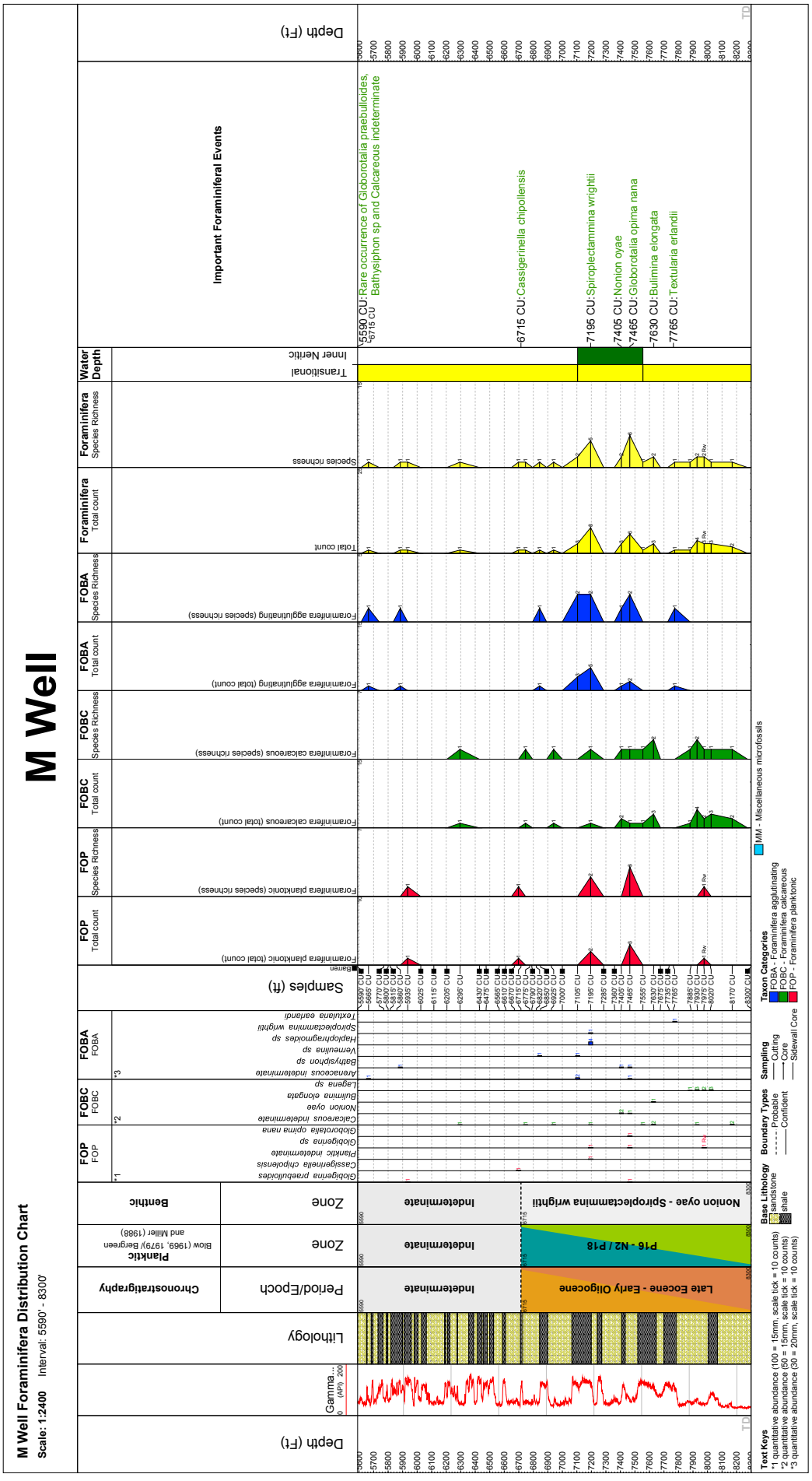

Figure 2. Stratigraphic distribution of recovered foraminifera from M well.

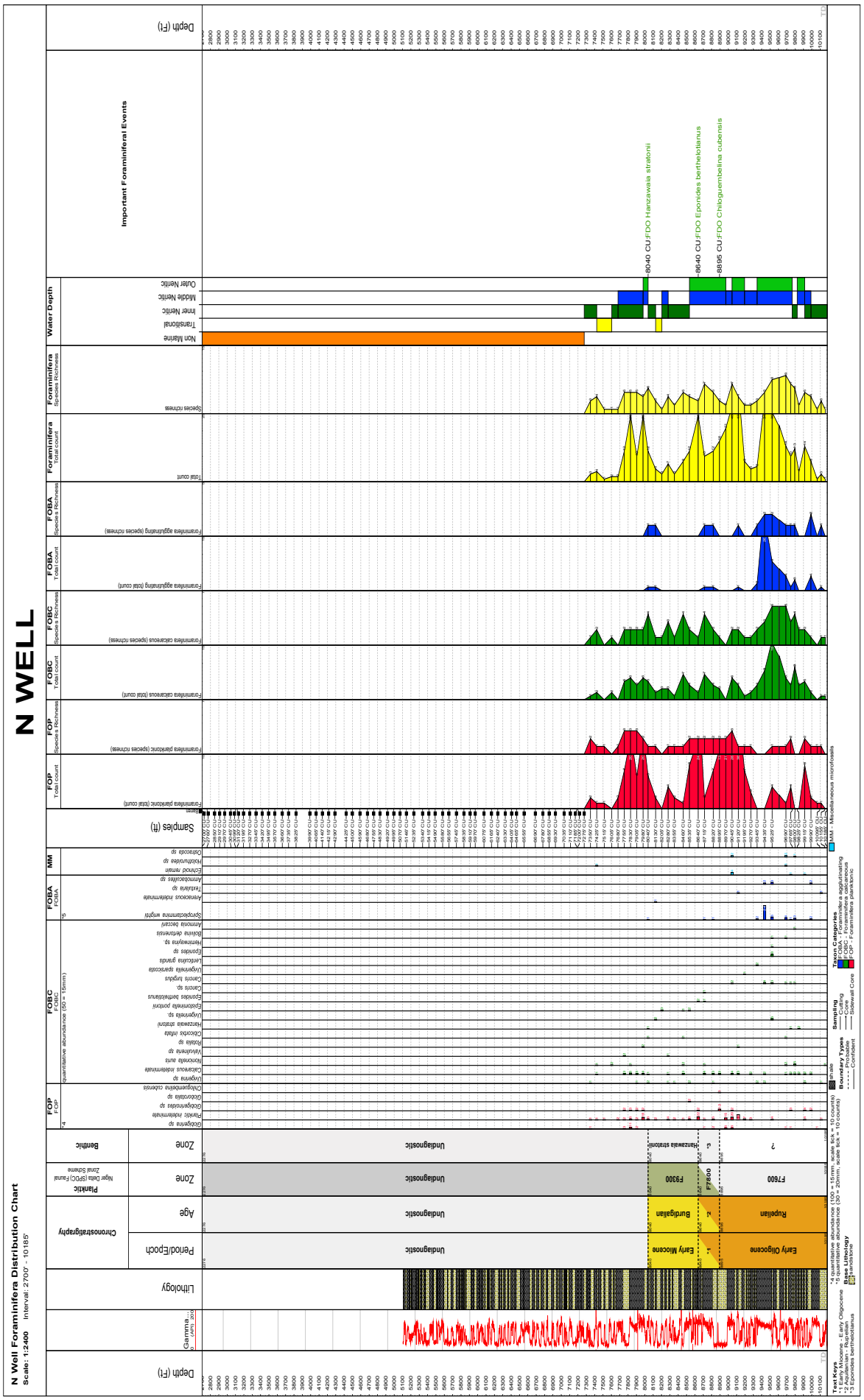

Figure 3. Stratigraphic distribution of recovered foraminifera from N well.

4.2 Planktonic/Benthonic (P/B) foraminifera Ratio of both wells

The P/B foraminifera ratio was calculated using the formula of the foraminifera proportion percentage in Equation 1. Brasier (1980) provided a useful guide to paleo-water depth / environmental inference by postulating that the higher the P/B ratio, the deeper the paleo-water depth of deposition. In the studied wells, percentage ratios were calculated for each biozone, and the values obtained were used to define the depositional environment of the successive intervals covered by the biozone. According to Murray (1991), the divisions of the environment are as follows: <20% planktonic tests signify the inner shelf, 20-50% show the middle shelf, 50-70% indicate the outer shelf, and >70% planktonic tests are interpreted as the upper bathyal zones. These percentages were related to the established biozones, from which a deduction of varying paleoenvironments, ranging from the inner neritic to the outer neritic environment, was hypothesized (Table 4 and Figure 4).

Table 2. The stratigraphic intervals, age established from the First Downhole Occurrence (FDO) of the marker species and biozones recognised in M well, related with Blow (1969, 1979), Berggren and Miller (1988) zonal scheme.

M WELL						
Depth interval (ft.)	Age	Epoch/Period	Foraminifera zonal scheme Blow (1969, 1979)	Berggren and Miller (1988)	Biozone for this study	Significant foraminifera datum
6715 - 8300	Rupelian - Priabonian	Early Oligocene – Late Eocene	P16 – N2	P18	*Cassigerinella chipollensis*	FDO of *Cassigerinella chipollensis*

Table 3. The stratigraphic intervals, age established from the First Downhole Occurrence (FDO) of the marker species and biozones recognised in N well related with the Niger Delta (SPDC) faunal zonal scheme.

N WELL					
Depth interval (ft.)	Age	Epoch/Period	Niger Delta (SPDC) Faunal Zonal Scheme	Biozonation for this study	Significant foraminifera datum
8040 -8640	Burdigalian	Early Miocene	F9300	*Hanzawaia stratonii*	*FDO of Hanzawaia stratonii*
8640 – 8895	Aquitanian - Rupelian	Early Miocene – Early Oligocene	F7800	*Eponides berthelotianus*	FDO of *Eponides berthelotianus*
8895 - 10185	Rupelian	Early Oligocene	F7600	*Chiloguembelina cubensis*	FDO of *Chiloguembelina cubensis*

4.3 Paleo-oxygenation

The mean and standard deviations for Co, Cu, Ni, Cr and Th are 7.37 and 4.19, 20.37 and 8.98, 21.05 and 7.92, 55.60 and 30.86, 7.34 and 5.0 respectively, while 76.62 and 82.94, 64.50 and 38.57, 1.87 and 1.09, 9.56 and 5.72 represent the mean and standard deviation for V, Zn, U, and Al respectively. The concentration of Co, Cu, and Ni in all the samples (Table 5) fall below the "world shale average" (WSA, Wedepohl, 1971, 1991). Whereas 20% of the samples exceed the WSA for Cr, Th, and V, 75% and 45% of the samples respectively show Zn and Al, U levels below the WSA (Table 5).

Table 4. The planktonic/benthonic (P/B) foraminifera ratios of M and N Wells.

M well												
Depth interval (ft.)	Age	Epoch/Period	Formation	Biozonation for this study	Total Benthonic	Total Planktonic	Total Micropaleontology	Percentage planktonic	Percentage benthonic	Ratio Murray (1991)	P/B ratio	Paleo -redox
5590 - 6715	Indeterminate	Indeterminate	Benin	*Globigerina praebulloides*	3	1	4	25	75	25:75 (Middle neritic)	P<B	oxic paleo-oxygenation
6715 - 7405	Rupelian	Early Oligocene	Benin	*Cassigerinella chipollensis s*	11	2	13	15	85	85:15 (Inner neritic)	P<B	
7405 - 8300	Rupelian - Priabonian	Early Oligocene – Late Eocene	Agbada	*Nonion oyae*	26	3	29	10	90	90:10 (Inner neritic)	P<B	
N well												
7350 - 8040	Indeterminate	Indeterminate	Agbada	*Nonionella auris*	26	59	85	69	31	69:31 (Outer neritic)	P>B	
8040 - 8640	Burdigalian	Early Miocene		*Hanzawaia stratonii*	27	23	50	46	54	46:54 (Middle neritic)	P<B	
8640 – 8895	Aquitanian - Rupelian	Early Miocene – Early Oligocene		*Eponides berthelotianus*	16	32	48	67	33	67:33 (Outer neritic)	P>B	
8895 - 10185	Rupelian	Early Oligocene		*Chiloguembelina cubensis*	125	137	262	52	48	52:48 (Outer neritic)	P>B	

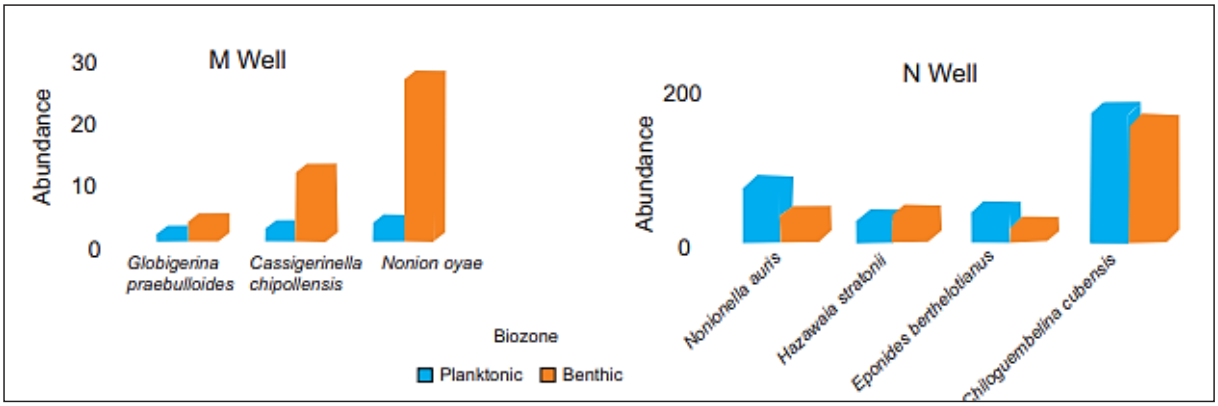

Figure 4. Comparison chart to show the distributional pattern of the planktonic/benthonic (P/B) foraminifera ratios of M and N wells.

Trace metals can originate from hydrogeneous or non-hydrogeneous (detrital and hydrothermal) sources (Tribovillard et al., 2006). Some of these trace metals become sequestered in sediments under reducing bottom water conditions (Morford and Emerson, 1999), where they form organometallic complexes with preserved organic matter (Tribovillard et al., 2006). Consequently, a positive correlation exists between organic richness and the abundance of redox-sensitive trace metals especially Mo, U, Cr, V, Ni, and Cu. Tribovillard et al. (2006) successfully used this relationship to discriminate between oxic, anoxic and euxinic paleoxygenation conditions.

Table 5. Geochemical data of M and N Wells.

S/N	Co (Cobalt)	Cr (Chromium)	Cu (Copper)	Ni (Nickel)	Th (Thorium)	U (Uranium)	V (Vanadium)	Zn (Zinc)
N1	3.6	20	10	16	3.67	0.85	18.3	18
N2	3.6	22	9	15	3.74	0.91	19.2	21
N3	3.5	24	11	14	3.39	0.99	20.1	20
N4	3.5	21	12	17	3.63	0.92	22.4	24
N5	3.5	21	7	16	3.22	0.89	21.6	16
N6	3.6	23	8	17	3.58	1	17.8	19
N7	13.5	104	22	34	18.5	3.9	127	120
N8	13.5	63	20	24	13.7	3.2	81.2	135
N9	13.2	78	21	21	14.2	3.32	77.3	86
N10	13.4	92	22	28	16.1	3.76	78.9	98
M1	3.1	30	22	10	3.21	0.74	8.6	25
M2	11.8	75	24	28	12.3	3.24	71.4	60
M3	9.6	65	35	15	10.2	2.34	56.2	70
M4	8.5	45	38	18	8.4	2.21	12.7	90
M5	2.7	36		13	2.18	1.08	10.2	100
M6	2.3	32	32	11	3.12	1.02	9.4	110
M7	8.3	89	24	30	6.23	1.58	150	74
M8	8	92	24	32	5.66	1.54	210	83
M9	7.9	86	24	28	4.68	1.43	272	45
M10	10.2	94	22	34	7.14	2.41	248	76
AV	7.37	55.60	20.37	21.05	7.34	1.87	76.62	64.50
SD	4.19	30.86	8.98	7.92	5.04	1.09	82.94	38.57
WSA	**19**	**90**	**45**	**68**	**12**	**3**	**130**	**95**

Trace element ratios (Ni/Co, V/Cr, and U/Th) have gained popularity due to the ease of discriminating paleo-redox oxygen conditions of ancient sediment (Jones and Manning, 1994; Nath et al., 1997; Akinyemi et al., 2013; Adebayo et al., 2015; Adeoye et al., 2020; Ejeh et al., 2021; Overare et al., 2020, 2021; Omietimi et al., 2022, etc.). Arising from the foregoing, it is important to note that trace element proxies for determining paleo-redox conditions are only reliable if their origin is predominantly hydrogenous (Tribovillard et al., 2006). Binary plots of Al (detrital indicator) versus Co, Cr, Cu, Ni, Th, U, V, and Zn for all samples show moderate to strong positive covariation except Ni and V (Fig. 5), implying a dominant non-hydrogenous source for the redox-sensitive trace metals, which correspond to deposition under oxic paleo-oxygenation. Similarly, the low average U content (1.76 ppm and 1.97 ppm) in the N and M well sediments also indicates an oxic paleo-redox condition during deposition (Armstrong-Altin et al., 2015).

Furthermore, the widespread occurrence of arenaceous benthonic foraminifera is typical of an environment fluctuating between neritic and abyssal (Bandy and Amal, 1960). The arenaceous/calcareous percentage was calculated using a related formula of the planktonic/benthonic ratio (P/B) foraminifera proportion percentage (equation 3). The percentage ratio of calcareous to arenaceous benthonic foraminifera is also a good pointer for paleoenvironmental studies. High % FOBC: % FOBA ratio suggests shallower paleo water depths while lower % FOBC: % FOBA suggest deeper paleo water depths. The percentage of FOBC: FOBA has been known to decrease with depth (Obaje et al., 2004). The divisions of the environment were also interpreted in the following order: 0-25% indicates a low A/C ratio, 26-50% shows a moderate A/C ratio, and> 50 % was interpreted as a high A/C ratio (Table 6 and Figure 6).

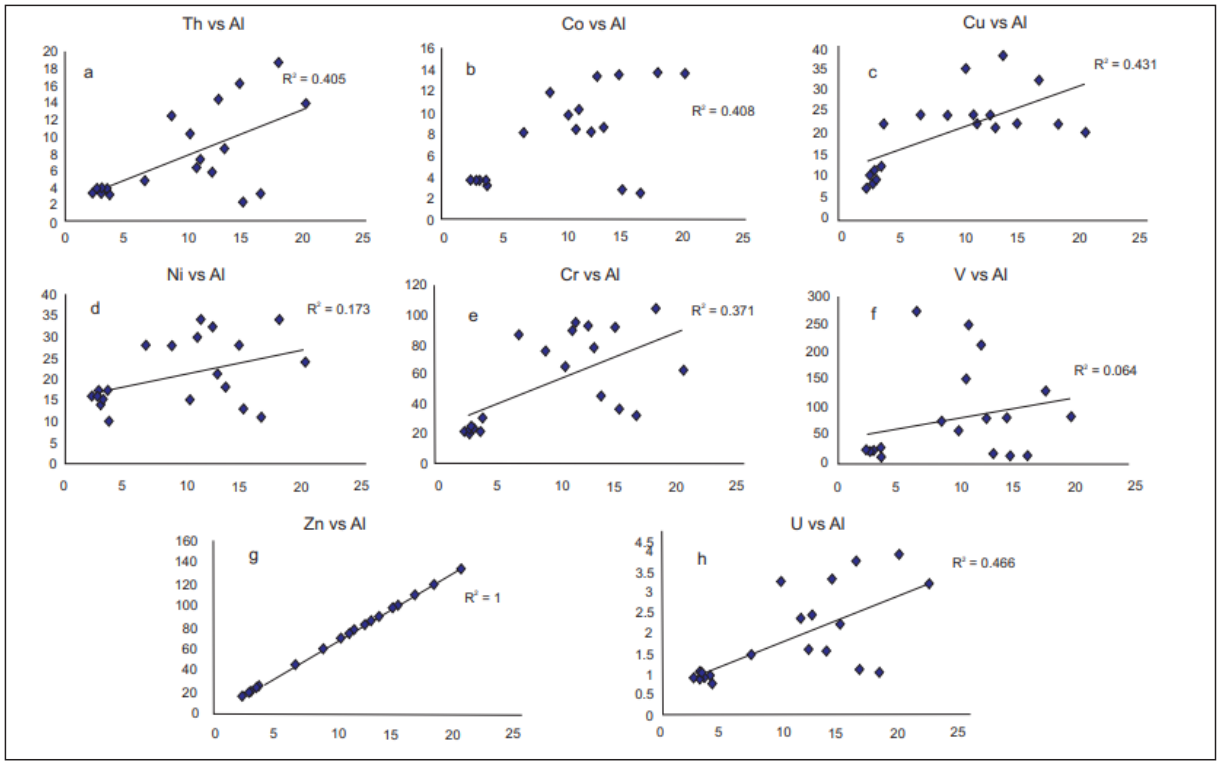

Figure 5. a-h: binary plots of redox-sensitive trace metal versus Al depicting moderate to strong positive covariation.

Table 6. The Arenaceous/calcareous (A/C) benthonic foraminifera ratios of M and N wells.

M well												
Depth interval (ft.)	Age	Epoch/Period	Formation	Biozonation for this study	Total Agglutinating	Total Calcareous	Total Micropaleontology	Percentage Agglutinating	Percentage Calcareous	Ratio Saint-Marc & Berggren (1988)	A/C ratio	Paleo -redox
5590 - 6715	Indeterminate	Indeterminate	Benin	*Globigerina praebulloides*	1	2	3	33	67	67:33 (Moderate)	A<C	oxic paleo-oxygenation
6715 - 7405	Rupelian	Early Oligocene	Benin	*Cassigerinella chipollensis S*	7	4	11	64	36	64:36 (High)	A>C	
7405 - 8300	Rupelian - Priabonian	Early Oligocene – Late Eocene	Agbada	*Nonion oyae*	20	6	26	77	23	77:23 (High)	A>C	
N well												
7350 - 8040	Indeterminate	Indeterminate	Agbada	*Nonionella auris*	0	26	26	0	100	0:100 (Low)	A<C	
8040 - 8640	Burdigalian	Early Miocene		*Hanzawaia stratonii*	1	23	24	4	96	4:96 (Low)	A<C	
8640 – 8895	Aquitanian - Rupelian	Early Miocene – Early Oligocene		*Eponides berthelotianus*	2	13	15	13	87	13:87 (Low)	A<C	
8895 - 10185	Rupelian	Early Oligocene		*Chiloguembelina cubensis*	50	78	128	39	61	39:61 (Moderate)	A<C	

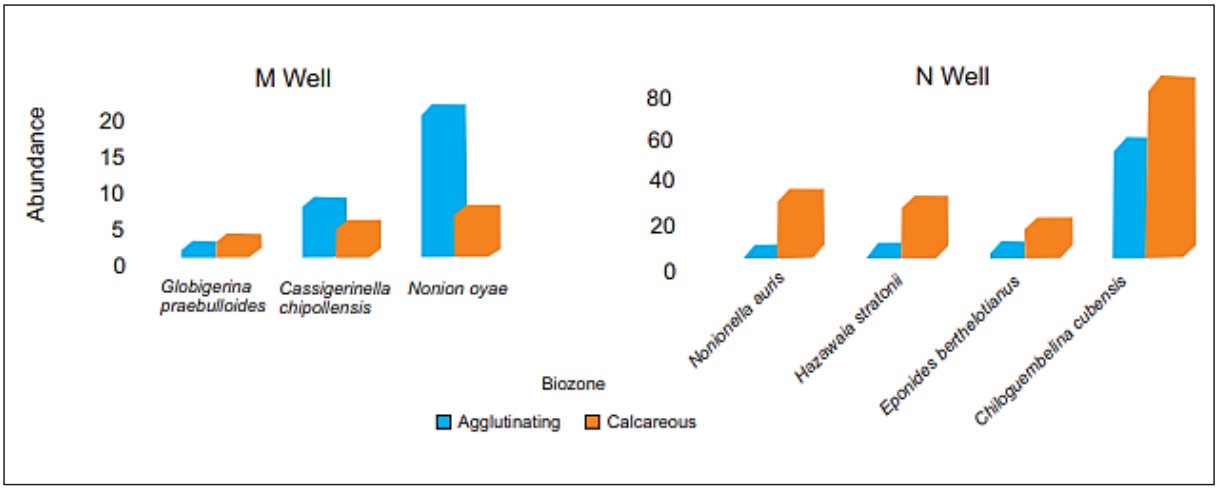

Figure 6. Comparison chart to show the distributional pattern of the arenaceous/calcareous benthonic foraminifera ratios of M and N wells.

A higher proportion of calcareous foraminifera was recovered from the wells, indicating deposition mainly above the calcium carbonate compensation depth (CCD) line, a region characterized by high calcium carbonate, sufficient oxygen, typical salinity, and high temperature (Saint-Marc and Berggren, 1988). The absence of calcareous benthic foraminifera and the presence of arenaceous types are generally used to identify the location of the CCD. Thus, an integration of inferences from redox-sensitive element data, P/B and A/C foraminifera ratios, suggests a range of paleoenvironments from an oxic middle to outer neritic environment during the Late Eocene to Early Miocene Epoch (Fig. 7) in the Greater Ughelli depobelt, Niger Delta Basin.

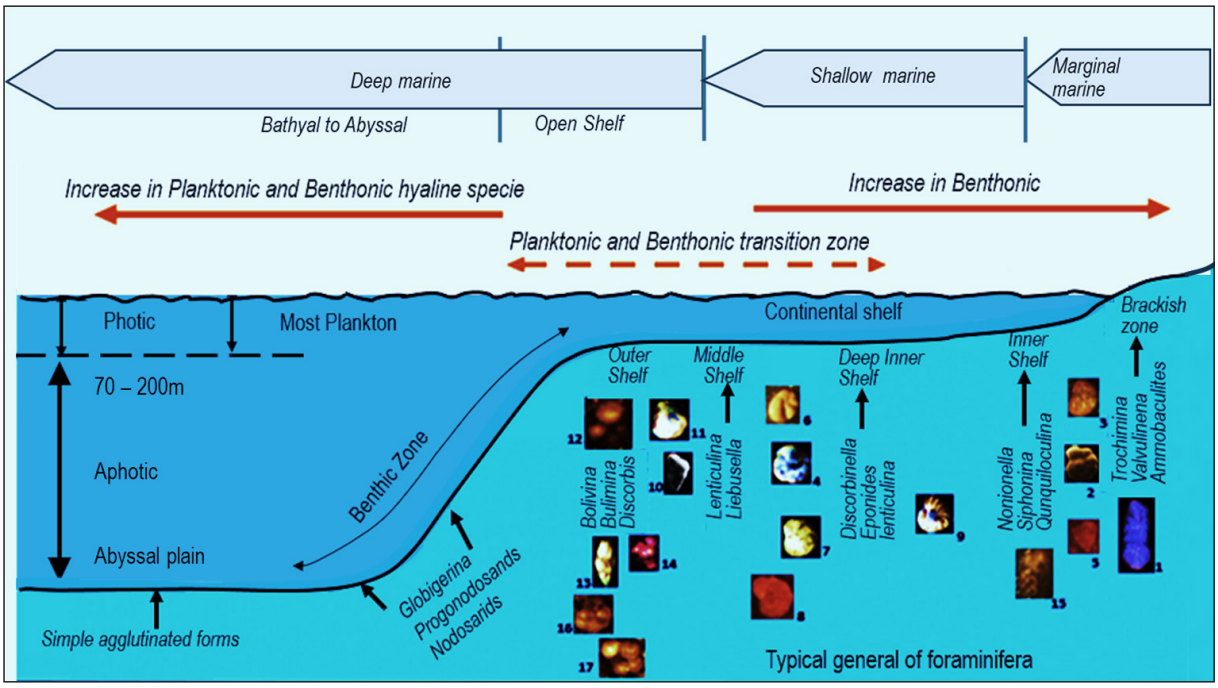

Figure 7. Diagrammatic expression of the combined Ni/Co, U/Th, V/Cr and Cu/Zn (inorganic geochemical elemental ratio) and (P/B and A/C foraminifera ratios) to derive the paleo-oxygen condition of sediments deposition from both wells. 1. *Ammobaculites spp.* 2. *Ammonia beccarii* 3. *Epistominella pontoni* 4. *Cibicorbsis inflata* 5. *Spiroplectammina wrightii* 6. *Cancris turgious* 7. *Hanzawaia stratonii* 8. *Nonion oyae* 9. *Lenticulina grandis* 10. *Chiloguembelina cubensis* 11. *Eponides berthelotianus* 12. *Globigerina praebulloides* 13. *Uvigerina sparsicosta* 14. *Bulimina elongata* 15. *Bolivina dertonensis* 16. *Cassigerinella chipollensis* 17. *Globorotalia opima nana* [Modified after Allen (1965, 1970), Youssef and El-Sorogy (2015)].

5. Conclusion

The investigated samples have been dated as Early Miocene to Late Eocene in both wells based on the First Downhole Occurrences of *Cassigerinella chipollensis, Nonion oyae, Spiroplectammina wrightii, Chiloguembelina cubensis, Eponides berthelotianus and Hanzawaia stratonii.* Furthermore, the low average content of Uranium, the moderate to strong positive covariation of redox sensitive trace elements against Aluminium for both wells, and implications from foraminifera ratios - planktonic versus benthonic (P/B) foraminifera, and arenaceous versus calcareous (A/C) benthonic foraminifera of both wells indicate paleo-water depth ranging from inner neritic to outer neritic paleoenvironment.

Acknowledgment

The First author is indebted to the NNPC Exploration and Production Limited for providing the materials used for this work.

References

Adebayo, O.F., Akinyemi, S.A., Madukwe, H.Y., Aturamu, A.O., Ojo, A.O., (2015):

Paleoenvironmental studies of Ahoko Shale, southeastern Bida basin, Nigeria: insight from palynomorph assemblage and trace metal proxies. Intl. Jour. of Scientific and Research Publs. 5,1-16.

Adebayo, O.F., Akinyemi, S.A., Madukwe, H.Y., Aturamu, A.O. and Ojo, A.O. (2016): Geochemical characterization and palynological studies of some Agbada Formation deposits of the Niger Delta basin: implications for paleodepositional environments. Turkish Journal of Earth Sciences, 25 (6), 573-591.

Adeoye, J. A., Akande, S. O., Adekeye, O. A., & Abikoye, V. T. (2020): Geochemistry and paleoecology of shales from the Cenomanian-Turonian Afowo formation Dahomey Basin, Nigeria: Implication for provenance and paleoenvironments. Journal of African Earth Sciences, 169, 103887.

Akinyemi, S.A., Adebayo, O.F., Ojo, O.A., Fadipe, O.A., Gitari, W.M., (2013): Mineralogy and geochemical appraisal of paleo redox indicators Maastrichtian outcrop shales of Mamu Formation, Anambra Basin, Nigeria. J Nat Sci.Res, 10, 48-64.

Allen J.R.L., (1965): Late Quaternary Delta, and adjacent areas-sedimentary environments and Lithofacies. AAPG Bulletin 49: 547-600.

Allen, J.R.L., (1970): Studies in fluviatile sedimentation: a comparison of finning-upward cyclothems. With species reference to coarse-member composition and interpretation: Journal of Sedimentary Petrology 40, 298-323.

Amiewalan, F.O., Balogun, F.O., Ejairu, K., (2020): Sedimentological and geochemical characterization of DF-2 well, Onshore Western Niger Delta: implications for provenance, tectonic history and paleo depositional conditions. Global Journal of Pure and applied Sci. 26, 141-155.

Amiewalan, F.O. and Edegbai, J.A., (2021): Foraminiferal Biozonation of Late Eocene - Early Oligocene sediments of BC-1 well, Onshore, Western Niger Delta Basin, Nigeria. J. Appl. Sci. Environ. Manage. 25 (2), 287-296.

Armstrong-Altrin, J.S., Machain-Castillo, M.L., Rosales-Hoz, L., Carranza-Edwards, A., Sanchez- Cabeza, J.A., Ruíz-Fernandez, ´ A.C., (2015): Provenance and depositional history of continental slope sediments in the Southwestern Gulf of Mexico unraveled by geochemical analysis. Continent. Shelf Res. 95, 15–26.

Ajayi, E.O. and Agboneni, O.E. (2016): Neogene Deep Water Agglutinated Foraminifera Biostratigraphy and Biozonation in Niger Delta, Nigeria. Journal of Earth Science & Climatic Change 7(10), 2-8.

Arrhenius, G., (1952): Sediment cores from the East Pacific. Reports of the Swedish Deep-Sea Expedition 5, 1-228.

Avbovbo, A.A. (1978): Tertiary lithostratigraphy of Niger Delta: American Association of Petroleum Geologists Bulletin, 62, 295-300.

Bandy, O.L., Amal, R.E., (1960): Concept in foraminifera Biostratigraphy. AAPG Bulletin 44, 1921-1932.

Berggren, W. A., Miller K.G. (1988): Paleogene Tropical Planktonic Foraminiferal Biostratigraphy and Magnetobiochronology. Micropaleontology, 34 (4), 362-380

Blow, W.H. (1969): Late Middle Eocene to Recent planktonic foraminiferal biostratigraphy. In Bronnimann, P. and Renz, H. H. (eds.), Proceedings of the First International Conference on Planktonic Microfossils, Geneva, E. J. Brill, Leiden, 1, 199-422.

Blow, W.H., (1979): The Cenozoic Globigerinidae. Brill, Leidenand atlas, plate 264, 1413.

Boboye, O.A. and Fowora, O. (2007): Biostratigraphy of Calcareous Nannofossils of Well XH-1, Deep Offshore, Niger Delta, Nigeria. Journal of Mining and Geology, 43, 175-186.

Boboye, O.A., Oladayo, A.S. and Okon, E.E. (2017). An Integrated Wireline-Log and Biostratigraphic Appraisal of Olure-1 and Abigboro-1 Wells. Open Journal of Geology 7 (8), 1140-1159.

Brasier M.D. (1980): Microfossils. University of Hull Press, Kingston-upon-Hull, UK.

Chukwu, J.N., Okosun, E.A. and Alkali, Y.B. (2012): Foraminifera Biostratigraphy and Depositional Environment of Oloibiri-1 Well, Eastern Niger Delta, Nigeria Journal of Geography and Geology, 4(4), 114-122.

Douglas, R.G. (1979): Benthic foraminiferal ecology and paleoecology, a review of concepts and methods. In J.H. Lipps, W.H. Berger, M.A. Buzas, R.G. Douglas and C.A. Ross, Foraminiferal Ecology and Paleoecology, Society of Economic Paleontologists and Mineralogists, Short Course 6, 21-53.

Deng HW, Qian K., (1993): Analysis on sedimentary geochemistry and environment", Science Technology Press, Gansu, 15-85.

Doust, H. and Omatsola, E. (1990): Niger Delta, in, Edwards, J. D., and Santogrossi, P.A., eds., Divergent/passive Margin Basins., AAPG Memoir 48: Tulsa, American Association of Petroleum Geologists, 239-248.

Ejeh, O. I. (2021): Geochemistry of rocks (Late Cretaceous) in the Anambra Basin, SE Nigeria: insights into provenance, tectonic setting, and other palaeo-conditions. Heliyon, 7(10).

Ekwenye, O., Okeke, K., Otosigbo, G., and Onyemesili, O. (2020): A Re-evaluation of the Stratigraphic and Palaeogeographic Evolution of the Paleogene Sedimentary Successions of the Niger Delta. Jordan Journal of Earth & Environmental Sciences, 11(2), 146-156

Evamy, B.D., Haremboure. J., Kamerling, P., Knaap, W.A., Molloy, F.A. and Rowlands, P.B. (1978): Hydrocarbon habitat of Tertiary Niger Delta. American Association of Petroleum Geologists Bulletin, 62, 1-39.

Fadiya, S. L., Jaiyeola-Ganiyu, F.A. and Fajemila, O.T. (2014): Foraminifera Biostratigraphy and Paleoenvironment of Sediments from well AM-2, Niger Delta. Ife Journal of Science 16, (1), 61-72.

Ilevbare, M., & Adeleye Rita, A. (2023): Geochemical Discriminant for Provenance, Source Area Weathering and Paleoredox of Some Shale Deposits in Edo State, Nigeria. Jordan Journal of Earth & Environmental Sciences, 14(4), 258-267

Jones, B., Manning, D.C., (1994): Comparison of geochemical indices used for the interpretation of paleo-redox conditions in ancient mudstones: Chemical Geology 111(1-4), 111-129.

Lambert-Aikhionbare, D.O., Bush, P.R. and Ibe, A.C. (1990): Integrated geological and geochemical interpretation of source rock studies in the Niger Delta. J. Mining and Geol., 26, 97-106.

Mode, W., Anidobu, T., Ekwenye, O., & Okwara, I. (2019): A Provenance Study of the Paleogene Lithostratigraphic Units of the Niger Delta: An Insight into the Plate-Tectonic Setting. JJEES, 234, 234-246

Morford, J.L., and Emerson, S., (1999): The geochemistry of redox sensitive trace metals in sediments, Geochimica et Cosmochimica Acta 63 (11/12),1735–1750

Murray, J.W., (1991): Ecology and Palaeoecology of Benthic foraminifera, John Wiley & Sons Inc., New York. 397p.

Nagarajan, R., Madhavaraju, J., Nagendral, R., Armstrong-Altrin, J.S., Moutte. J., (2007): Geochemistry of Neoproterozoicshales of the Rabanpalli Formation, Bhima Basin, Northern Karnataka, southern India: implications for provenance and paleoredox conditions. Rev MexCiencGeol. 24, 150-160.

Nath, B.N., Bau, M., Ramalingeswara, R.B., Rao, C.M., (1997): Trace and rare earth elemental variation in Arabian Sea sediments through a transect across the oxygen minimum zone: Geochimicaet Cosmochimica Acta 61(12), 2375-2388.

Nwajide, C.S. (2013): Geology of Nigeria's sedimentary Basins. Geoscan Technical Services Ltd. Awka, 565p.

Obaje, N.G, Wehner, H., Scheeder, G., (2004): Hydrocarbon prospectivity of Nigeria Inland Basins from the Viewpoint of Organic geochemistry and Organic Petrology. AAPG Bulletin 88, 325-353.

Obaje, N. G. (2009): Geology and mineral resources of Nigeria 120, 221 p. Berlin Springer.

Obaje, S.O. and Okosun, E.A. (2013): Paleoenvironmental Interpretation of Tomboy Field, Offshore Western Niger Delta, Nigeria. International Journal of Science and Technology 2(9), 628-638.

Okosun, E.A., Chukwu, J.N., Ajayi, E.O. and Olatunji, O.A. (2012): Biostratigraphy, Depositional Environment and Sequence Stratigraphy of Akata Field (Akata 2, 4, 6 and 7 Wells), Eastern Niger Delta, Nigeria. International Journal of Scientific & Engineering Research 3, 2229-5518.

Overare, B., Azmy, K., Garzanti, E., Osokpor, J., Ogbe, O. B., & Avwenagha, E. O. (2021): Decrypting geochemical signatures in subsurface Niger delta sediments: Implication for provenance, weathering, and paleoenvironmental conditions. Marine and Petroleum Geology, 126, 104879.

Overare, B., Osokpor, J., Ekeh, P. C., & Azmy, K. (2020): Demystifying provenance signatures and paleo-depositional environment of mudrocks in parts of southeastern Nigeria: Constraints from geochemistry. Journal of African Earth Sciences, 172, 103954.

Ozumba, M.B. and Amajor, L.C., (1999): Evolutionary Relationships in some Benthic Foraminifera of the middle to Late Miocene, Niger Delta. Nigeria Association of Petroleum Explorationists Bulletin 14, 157-167.

Reijers, T.J.A., Petters S.W. and Nwajide, C.S. (1996): The Niger Delta Basin, in: T.J.A. Reijers (ed.), Selected Chapters on Geology: SPDC corporate reprographic services, Warri, Nigeria, 103-114.

Saint-Marc, P., Berggren, W.A., (1988): A quantitative analysis of Paleocene benthic foraminifera assemblages in central Tunisia. Journal of Foraminifera Research 18, 97-113.

Salami, M. B. (1983): Some Late Cretaceous and Early Tertiary pteridophytic spores from southern Nigerian sedimentary Basin. Revista Española de Micropaleontología, 15(2), 257-272.

Short, K.C. and Stauble, A.J. (1967): Outline of geology of Niger Delta: American Association of Petroleum Geologists Bulletin, 51, 761 - 779.

Suttner, L.J., Dutta, P.K., (1986): Alluvial sandstones composition and paleo climate, I. Framework mineralogy. J Sediment Res. 56(3), 329-345.

Tribovillard, N., Algeo, T.J., Lyons, T.W., Riboulleau, A., (2006): Trace metals as paleoredox and paleoproductivity proxies: an update. Chem. Geol. 232, 12–32

Tuttle, L.W.M., Charpentier, R.R. and Brownfield, E.M. (1999): The Niger Delta Petroleum System: Niger Delta Province, Nigeria Cameroon and Equatorial Guinea, Africa. US Geological Survey Open-File Report 99 (50), Denver, 70.

Ukpong, A.J., Ikediasor, K.C. (2018): Paleoenvironmental Analysis of Well "K27" In the Niger Delta, Southeastern Nigeria. IOSR Journal of Applied Geology and Geophysics (IOSR-JAGG).6(2), 36-47.

Usman, A (2016): Late Oligocene to Early Middle Miocene Foraminiferal Biostratigraphy, Sequence Stratigraphy and Palaeoenvironment of Well - 004 (OML - 34) Niger Delta. A postgraduate dissertation, 1-116.

Weber, K.J., Urai, L. J., Pilaar, W. F., Lehner, F. and Precious, R.G. (1978): The role of faults in hydrocarbon migration and trapping in Nigerian growth fault structures: 10th Annual Offshore Technology Conference Proceedings, 4, 2643-2653.

Wedepohl, H., K., (1971): Environmental influences on the chemical composition of shales and clays. In: Ahrens H.L. (Ed.), Physics and Chemistry of the Earth 8,307–333.

Wedepohl, H., K., (1991): The composition of the upper earth's crust and the natural cycles of selected metals. Metals in natural raw materials. Natural Resources. In: Merian, E. (Ed.), Metals and Their Compounds in the Environment. VCH, Weinheim, 3–17p

Whiteman, A.J. (1982): Nigeria: It's Petroleum Geology, Resources and Potentials, I & II, Graham and Trotman, London, 1-394.

Youssef, M.A and El-Sorogy A.S. (2015): Paleoecology of Benthic foraminiferal in Coral Reefs Recorded in the Jurassic Tuwaiq Mountain Formation of the Khashm Al-Qaddiyah Area, Central Saudi Arabia. Journal of Earth Science, 26(2): 224-235.

JJEES

JJEES (2025) 16 (4): 342-351
ISSN 1995-6681

Jordan Journal of Earth and Environmental Sciences

GIS-Based Multi-Criteria Decision Analysis for Site Selection of Surface Water Desalination Plants in Basrah, Iraq

Noor A. Al-Najar [a*], Alaa M. Al-Abadi [a], Usama Qasim khaleefah [b]

[a] Geology Department, University of Basrah College of Science, Basrah, Iraq
[b] University of Basrah, College of Marine Sciences, Basrah, Iraq

Received on March 6, 2025, Accepted on May 3, 2025

Abstract

The Basrah Governorate in southern Iraq faces a serious water deficit despite its surface water supplies and economic growth. However, no drastic measures have been proposed to address the problem. The goal of this study is to identify the ideal location for surface water desalination facilities in the Basrah Governorate. The best location for surface water desalination is determined by a number of variables, each of which has a distinct impact. Nine factors were selected based on the local conditions in the study location and the available data. Terrain-related parameters (distance to the road, distance to the network, distance to the river, LULC, slope, elevation, soil, geology, and rainfall) were among the factors used. The professional opinions and previous literature were used to calculate the weights of these elements. There are five zones with appropriate levels ranging from very low to very high, according to the weight sum technique. The low to very low zones occupied 7,636 km², followed by the moderate zones (4,772.5 km²) and then the high to very high zones (6,681.5 km²). This was demonstrated by the methodical application of the weight overlay and weight sum techniques in GIS. According to the weight overlay technique, the low to very low zones cover 20% the moderate zones encompass 60% (11,454 km^2), and the high to very high zones cover 20% (3,818 km^2). Experts and decision-makers can benefit from this study as it saves time and effort and serves as a scientific guide for selecting the best location in the Basrah Governorate. Based on the spatial distribution and the results of the applied techniques, the Shatt al-Arab area was identified as the best place to establish massive surface water desalination plants, followed by the Al-Faw area and the Khor Al-Zubair Canal.

Keywords: *Shatt al-Arab; Weight Sum; Al-Faw; Basrah; Desalination.*

1. Introduction

The scarcity of water resources in arid Arab countries such as Iraq is a source of concern for water resource planners. Iraq has relied on the Tigris and Euphrates rivers for centuries to provide about 95% of its water needs. Water consumption has increased dramatically due to the global population growth. Drinking water has become a major problem facing most countries worldwide, particularly in Iraq. The study area is situated in the far south of Iraq, specifically in Basrah Governorate, and encompasses the Arabian Gulf region. Basrah Governorate is known for its low annual rainfall. Given the climatic conditions that the country is experiencing in general and Basrah in particular, the need to produce potable water at a low capacity for areas with high population density is critical. The country is now categorized as having low freshwater resources, which will impact the country's economic support as well as the decline of its industry and agriculture (Alatta et al., 2022). The Al-Faw District and Shatt al-Arab are affected by saltwater intrusion due to water scarcity and disruptions to the Karun River, which increases salt concentrations and impacts soils and living organisms (Abdul-Hameed et al., 2021).

There is evidence that the shortage of fresh water and the rise in salinity have led to a decline in the agricultural sector in southern Iraq, specifically in Basrah Governorate. A study conducted by Schnepf et al. (2004) highlights that the per capita share of freshwater has decreased by 60% or more over the past two decades. The need for more urgent freshwater resource strategies will necessitate desalination choices from all available resources as interest in using natural surface water resources, such as the Arabian Gulf and Shatt al-Arab, grows. One of these solutions may be desalination where plants can produce fresh water (Gokçek & Gokçek, 2016). This process involves removing salt from seawater to produce fresh water suitable for human use (Younos et al., 2005). It can offer a significant solution for the country and lessen the strain on new natural resources (Al-Ansari et al., 2023). It also explained that desalination meets the increasing demand for water in southern Iraq, especially in coastal areas with easy access to seawater. Soon, Desalination plants will play a significant role in supplying vast amounts of potable water for drinking, as well as other applications such as irrigation, industry, and agriculture. Desalination facilities must utilize clean energy, as it helps protect the environment from pollutants over time.

The current study aims to find the best location for desalinating surface water, using nine factors (distance to river, distance to network, distance to the road, LULC, slope, elevation, soil, geology, and rainfall). By applying the weight overlay and weight sum techniques, the appropriate location

* Corresponding author e-mail: pgs.noor.abdullah@uoBasrah.edu.iq

for desalinating surface water in southern Iraq can be found. This study saves decision-makers and planners considerable time and effort in identifying the optimal location for surface water desalination plants. The results will help determine the investment priorities of desalination options.

2. Study area

Basrah is one of the cities in the south of Iraq and is located at longitude (30°0′0″-31°0′0″)N and latitude (47°0′0″ - 48°0′0″)E (Figure 1); it shows the most important geological units in the study area. Iran borders it on the east and the Arabian Gulf on the south. The area is roughly 19090 square kilometers. Given that it is the gateway to Iraq and that most of the ports are located inside this governorate, its location is crucial. The Shatt al-Arab River, a notable geographical feature that supports enormous agricultural activity and provides vital water resources, is formed by the confluence of the Tigris and Euphrates rivers (Al-Ansari, 2018).

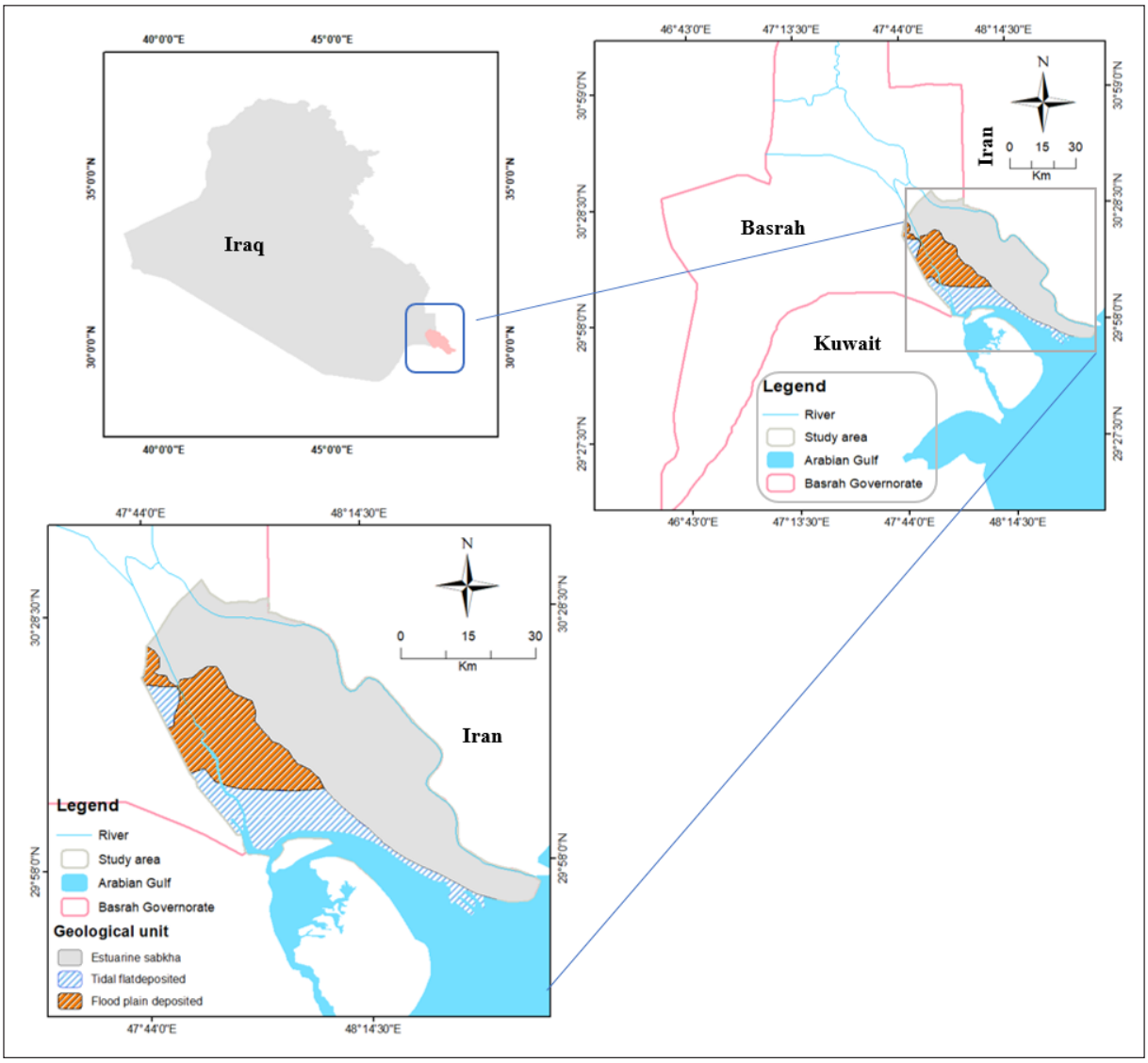

Figure 1. Location of the study area with the geological ‘ ‘unit’s map.

3. Methodology

3.1 GIS workflow for the best desalination site

In order to identify the location of surface water desalination, this study comprises five steps (Figure 2) , first, choosing the appropriate factors that have effects at different levels within the availability of data and existing literature, and these factors include (distance to the river - distance to roads - rainfall - distance to power lines - slope - elevation - LULC - geology - soil) (Figure 3) second, unifying the data into point format and with a fixed accuracy (30 x 30 m) so that the analysis is easier and faster, third, the hierarchical calculator was used to help calculate the weights of the influential factors that were applied in the techniques, fourth, applying each of the methods (Weight sum- Weight overlay) to classify the best solution based on the weighted factors, as these algorithms were used with the least error, fifth and finally, the appropriate areas for establishing surface water desalination plants were obtained by drawing maps that represent the best locations where surface water desalination plants can be based in the future and very large areas, and these areas were divided into (suitable, very suitable, moderate, low, very low).

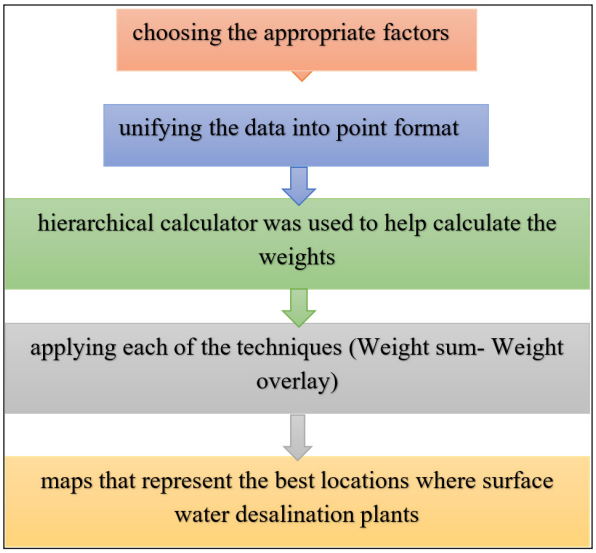

Figure 2. Flow chart of the desalination plant site in the study area.

3.2 Making Spatial Factor Maps for the Analysis of Desalination Site Suitability

Nine factors thatare thought to have a basic and varied impact on the study's goal were used. These factors included (distance to the river - distance to roads - rainfall - distance to electrical energy - slope - elevation -LULC- geology- and soil) (Figure 3). Each factor is important in choosing the best location to establish a water desalination plant, and these nine maps were collected in the database using the ArcMap program (10.4) after they were matched with spatial accuracy. An Excel file was also prepared to compile all the information about the nine factors affecting the selection of the best location for establishing a water desalination plant, so that the second phase could be implemented. The selection of factors that otherwise influence the choice of the appropriate location for establishing a water desalination plant depends on the availability of data and local conditions. Nine influencing factors were selected for the study area based on data availability and literature review. All of these parameters were prepared from an SRTM (Shuttle Radar Topography Mission) -type digital elevation model (DEM) with a spatial resolution of 1 arcsecond (~30 x 30 m cell size). Eight DEM tiles were downloaded from the official website of the United States Geological Survey (https://earthexplorer.usgs.gov/) and pre-processed to generate topographic factors (Al-Abadi, 2018). Except for the map (LULC) that was downloaded from a site (https://livingatlas.arcgis.com/landcoverexplorer/) where its spatial resolution represents (10 x 10 m) and was converted to a resolution (30 x 30 m) to match the accuracy of other maps between the period (2017-2021).

3.2.1 LULC map

Due to the substantial environmental, infrastructural, economic, and regulatory implications, land use and land cover are important considerations when selecting a location for a desalination plant. Additionally, they are essential in avoiding conflicts and assessing the general fitness of a property. It is crucial to understand land usage in order to assess environmental effects and choose the best water sources for desalination. Coastal regions with suitable land cover are frequently considered the best places for these facilities (Shahabi et al., 2015). Desalination facilities can be more easily integrated into current systems if current land use patterns indicate the presence of necessary infrastructure, such as roads and electrical networks (Mahi, 2001). Sentinel-2 images, artificial intelligence, and a sizable training dataset with billions of human-labeled image pixels are used to generate these worldwide LULC maps. As seen in Figure 3 A, the 2021 LULC map was used for this investigation. To match other thematic layers created in this work, the original map was first reprojected to WGS 1984 (zone 38) and then resampled to a resolution of 30 m. The five classifications identified were water, shrub, bare, developed area, and green cover (including trees, flooded vegetation, and crops). For water, constructed area, shrub, barren, and green cover, these classes make up 20% (549 km^2), 3% (79 km^2), 16% (442 km^2), 59% (1652 km^2), and 3% (71 km^2) of the total area, respectively. A desalination plant might be built on bare land, which makes up almost three-quarters of the whole area. The large amount of available land suggests that the area is favourable for such development.

3.2.2 Topographic map

Elevation and slope are essential factors when siting desalination plants as they significantly impact infrastructure, cost, and environmental issues (Mohamed et al., 2020). Higher elevations require more energy to pump seawater uphill and distribute desalinated water downwards, which has an impact on construction and operating costs (Slocum et al., 2016). Plants should be placed at slightly higher altitudes to reduce the risk of floods, which can destroy infrastructure and interfere with operations in lower elevations, particularly those close to the coast. The ideal height strikes a balance between cost-effective water transportation and accessibility to the seawater source; intermediate altitudes are usually favoured to save pumping expenses while avoiding flood-prone areas. Slope affects the stability and viability of construction; gentle slopes are favoured since they require less land alteration and offer a secure base for large machinery (Tsiourtis et al., 2009). The elevation in the study area ranges from 0 to 90 m, as shown in Figure 3B). The average of the slope is 2.17 ± 2.34 degrees, with a range of 0 to 30 degrees (Figure 3C). The majority of the research region is categorized as flat because its slope is less than five degrees. This feature, together with other elements, makes the location favourable for the installation of desalination plants because of its appropriate slope.

3.2.3 Soil map

Placing desalination plants requires careful consideration of the soil type since it can impact stability, construction feasibility, and environmental impact (Radwan et al., 2022). When building desalination plants, stable soil types are favoured because they limit erosion and runoff concerns during construction and long-term operation, and they offer a firm base for large machinery (Sepehr et al., 2017).

The US Department of Agriculture (USDA) developed the most well-known standard for defining these sizes. Based on the Food and Agriculture Organization's (FAO) global digital soil map (https://www.fao.org/soils-portal/data-hub/soil-maps-and-databases/faounesco-soil-map-of-the-world/

en/), this categorization method identifies silty loam, clay loam, and loam as the three primary textural classifications found in this study area. Silty loam, clay loam, and loam textures comprise 50%, 35%, and 15% of the total area, respectively (Table 1), making them the preferred choice for desalination plant infrastructure (Figure 3D).

Table 1. Types of soil and their coverage rate

Soil Type	Coverage (Km², %)
Silty Loam	50% (1304 Km²)
Clay Loam	35% (911 km²)
Loam	15% (410 km²)

3.2.4 Service map

Maps from the Basrah Governorate Municipality's Department of Urban and Urban Planning were used to determine the distances of roads and transmission power lines. Vectors were used to make these maps. We created raster maps of these variables using the ArcMap 10.4 Euclidean distance tool (Figures 3E-G). The Rainfall Measurement Mission's official website (https://power.larc.nasa.gov/data-access) provided daily rainfall data for 18 grid sites that covered the research area from 2010 to 2022. Next, the IDW interpolation method, found in the Geostatistical Extension for ArcGIS 10.4 Programming, was used to interpolate the table data. This method of random interpolation automates the most challenging parts of creating a high-quality model. (Figure 3H) displays the research area's annual rainfall map. Annual precipitation rises from the southwest to the northeast. Rainfall, in general, helps increase the amount of water available in the region, whether surface or groundwater. Therefore, the rain factor is important in the water desalination process, as it depends primarily on the water as a primary source. It is re-desalinated through desalination plants and becomes suitable for human use.

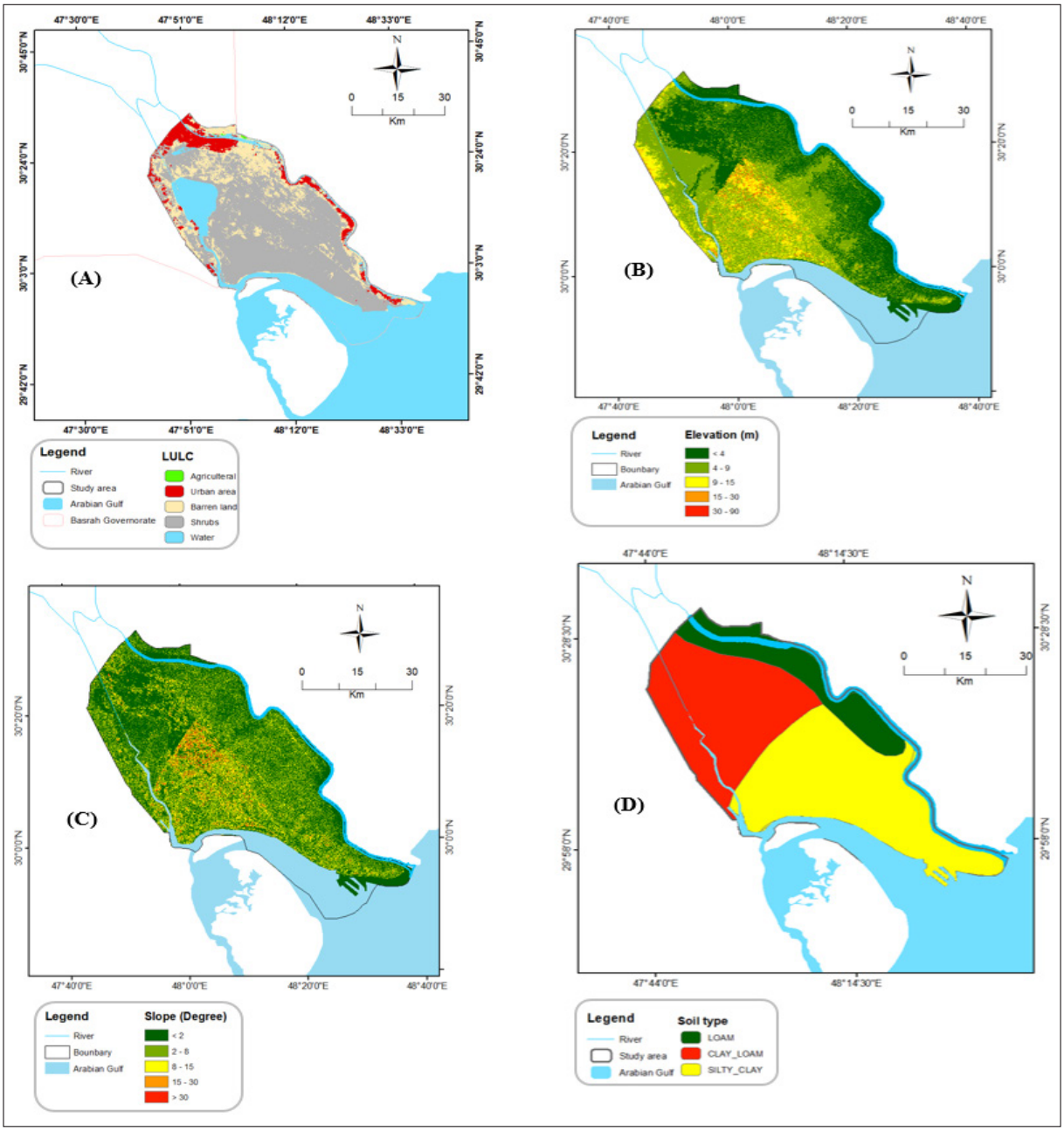

Figure 3. Factors used in determining the location of a surface water desalination plant. (a) LULC, (b) elevation (m a.s.l), (c) slope (degree), (d) soil type…….

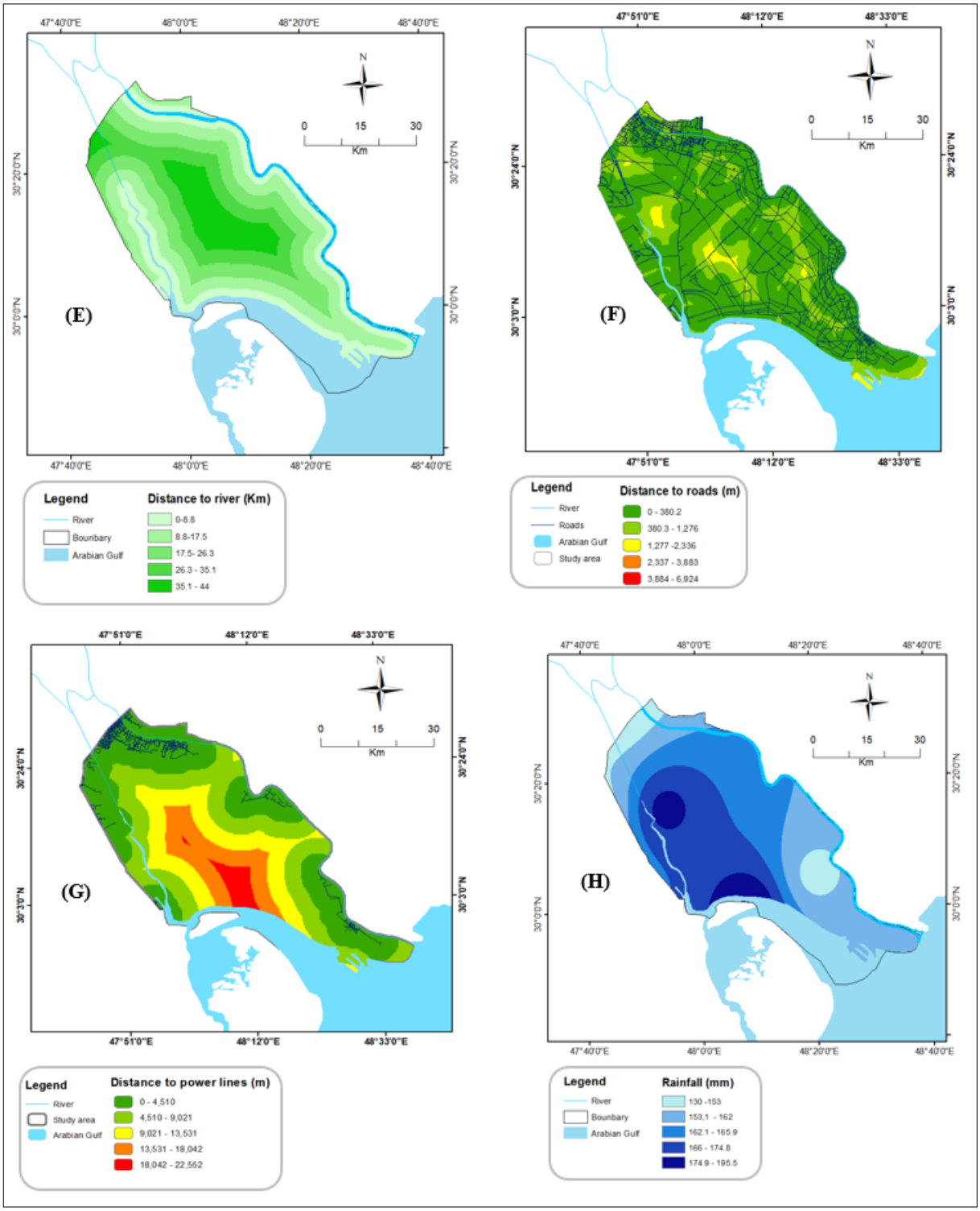

Figure 3. (E) distance to the river (Km), (F) distance to the road (m), (G) distance to the power line (m), and (H) Rainfall (mm).

3.3 Multi-Criteria Decision Analysis (MCDA)

Multi-criteria decision Analysis (MCDA) is a paradigm for decision-making that assesses and ranks many alternatives according to diverse criteria (Hwang et al., 1981). Two well-known MCDA approaches—Weight Sum and Weight Overlay methods—are examined in this work. Fields, including resource allocation, urban planning, and environmental management, extensively utilize these strategies. The techniques of Weight Sum and Weight Overlay have been applied in several fields. In environmental management, for instance, Weight Overlay is used to determine appropriate sites for conservation areas, whereas Weight Sum is utilized in project management to assess project proposals (Odu, 2019). Multi-criteria decision analysis (MCDA) methodologies, such as Weight Sum and Weight Overlay procedures, offer essential instruments for decision-makers. By considering multiple criteria, these methods help ensure that decisions are well-informed and balanced. The integration of geographical, environmental, social, and economic elements can effectively employ environmental risk and threat analysis in the process of choosing the best locations for surface water desalination

facilities in Basrah. Some important factors could be elevation, soil, geology, slope, rainfall, distance to the road, LULC, distance to the river, distance to the power line, and so on.

The study assessed locations for desalination facilities using the weight overlay and weight sum approaches. The weighted sum approach ranks sites by summing the weighted scores after assigning weights to different criteria based on their importance. In contrast, the weight overlay approach imposes multiple criteria maps, each with a weight according to its importance. The final results were based on the weights assigned to the criteria, affecting the selection of the best desalination site, with the distance to the river having the most important weight (17%). Soil and geology factors were the least influential (3%). The weights of these factors were determined using the online AHP calculator (Table 2), based on the views of experts and previous scientific studies from around the world (Dweiri et al., 2018), (Gokçek & Gokçek, 2016).

Table 2. Weights of the factors weight sum technique.

Factors	Weight %
Rainfall	19
Distance to the river	17
Distance to the network	17
Elevation	15
Distance to the road	13
Slope	10
LULC	4
Geology	3
Soil	3

3.4 Weight sum & Weight overlay Methods

The Weighted Sum Method (WSM) and the Weighted Overlay Method (WOM) are two well-liked Multi-Criteria Decision Analysis (MCDA) techniques for spatial decision-making, especially in Geographic Information System (GIS)-based site selection studies (Figure 4). These techniques help combine several elements to determine the best sites for a given objective, such as the placement of desalination plants. These two techniques are used to create a map that identifies the best location for establishing a surface water desalination plant in Basrah Governorate, southern Iraqand add several raster data that were relied upon within the study, and thus multiply these raster data, each by its specified weight. All maps were 30*30 meters in size, allowing for easy handling that minimize errors. Moreover, add them together. Generate a file of random points for the study area, where each contains geographic coordinates (X, Y). Approximately 500 points were used to cover the entire region. Then, add all the original point data before modifying it using the (Extract Multi value) command. Then, get a table containing all the data. The table is converted to Jupiter. To obtain the code for calculating the weights, each factor has a corresponding weight that influences the selection of a suitable location for establishing a water desalination plant. Each method has its own code, which assigns different weights based on the available data.

A method of weighted sum by entering a group of point data with the same extent and spatial resolution. Determine weights for raster data. Weight represents the importance of data in the final output. For example, if one wants to know the best location, the highest weight is given to the most critical data (distance to the river and distance to the network) (Figure 3), Table 2. The weights are then summed. The weights of the factors affecting the appropriate location for establishing water desalination must be 100%, Table 2, after which all factor maps are added, the weight of each map is added through the (weight overlay) command.

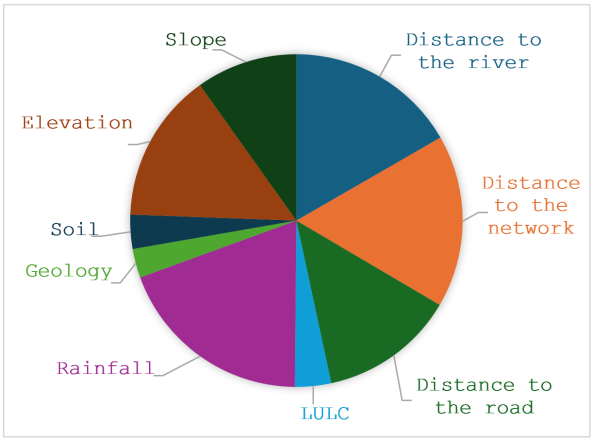

Figure 4. Weight of factors by using the Weight overlay technique. *Weights of the factors. (Malczewski, 1999)*

Effat and El-Zeiny (2017) explained the method of the rank sum and applied multi-criteria decision analysis (MCDA). Surface water desalination was assigned the priority, starting with the priority rank rainfall, second priority rank distance to a river, distance to the power line, elevation, distance to road, slope, LULC, soil, and finally, priority rank geology. The AHP online calculator was used to calculate the weights of the factors affecting the selection of the most suitable site for the construction of a surface water desalination plant. Table 1 shows the weights of factors.

WSM is a simple MCDA method that weighs each criterion according to its relative importance. The weighted values of all the requirements are then added up to determine the final appropriateness score for each alternative (Malczewski, 1999). It uses the following equation (1):

$$s = \sum_{i=1}^{n} wi * xi \quad (1)$$

Where: S = final suitability score, wi = weight of criterion i, and xi = normalized value of criterion i.

This technique integrates characteristics such as elevation, soil type, distance to the power line, and distance to the river, among others. It is especially helpful for ranking possible locations for desalination facilities in Basrah (Saaty, 1980). WOM can provide a suitability map by analyzing geographical characteristics such as slope, distance to power lines, distance to river, and LULC, which will help decision-makers choose the best sites for the Basrah desalination project (Jankowski & Nyerges, 2001). WSM and WOM both offer methodical frameworks for assessing various site selection factors. WOM is more useful for mapping and visualization in GIS-based investigations as it is spatially

explicit, whereas WSM is more algebraic and utilized for ranking alternatives (Malczewski, 2004). Using these techniques to select a location for Basrah's desalination plant ensuresa data-driven, open, and effective decision-making process.

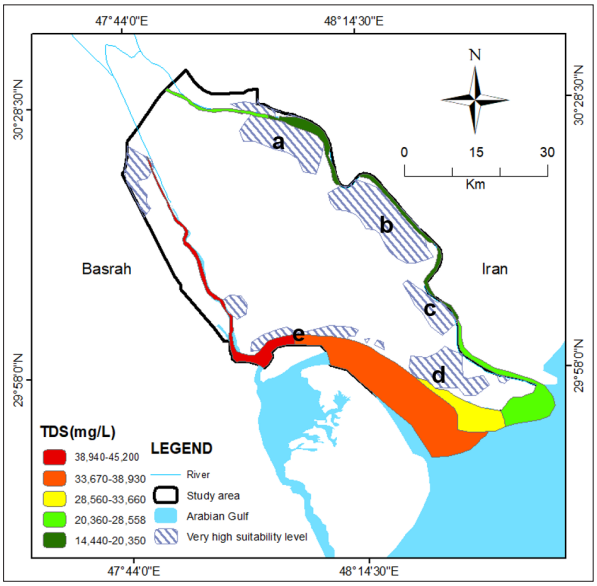

Figure 5. TDS map in (mg/l) with suitable locations for surface water desalination plants.

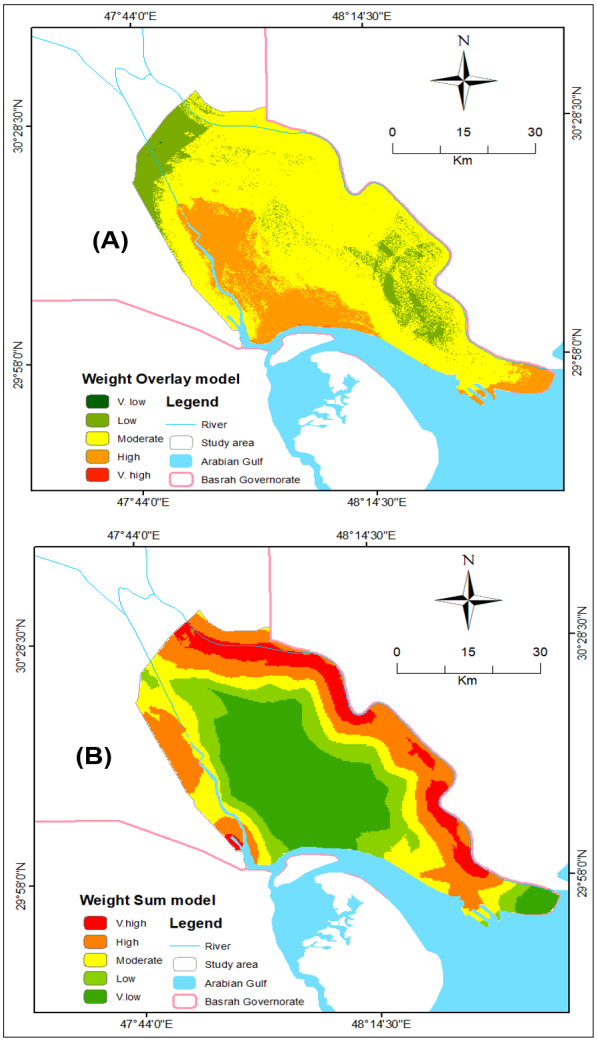

Figure 6. (a) Weight overlay model, (b) Weight sum model.

4. Results and Discussion

Using the online AHP calculator, the study extracted factor weights, assessed their significance through expert comments and literature reviews, produced a pairwise comparison matrix, and verified their consistency. A consistent decision-making process was indicated by the consistency ratio of 0.04 (< 0.1). Rainfall (0.192), distance to the river (0.167), elevation (0.145), distance to roads (0.131), slope (0.098), LULC (0.035), soil (0.033), and geology (0.028) were prioritised in the weight distribution, Table 2, Figure 4. For the factor weights specific to the technique (Weight sum), rainfall was ranked first with a weight of 19%, followed by distance to rivers (17%), distance to power lines (17%), elevation (15%), distance to roads (13%), slope (10%), LULC (4%), geology (3%), and soil (3%). This consistency ensures that each category reflects a comparable subset of the dataset (Longley et al., 2005). In the weight sum technique, the low to very low areas cover approximately 7636 km² (45%), medium areas cover 4772.5 km² (20%), and high to very high areas cover 6681 km² (35%). This area is represented along the banks of the Shatt al-Arab and parts of Khor al-Zubair. In the weight overlay technique, the ratio of low to very low areas is 20% (3818 km²), medium (60%) 11,454 km², and finally, high to very high areas occupy a ratio of 20% (3818 km²) which includes both the Al-Faw and Khor Al-Zubair areas. As for the spatial distribution, there were three main and significant areas considered as the best-selected sites for establishing surface water desalination plants in them and on huge areas, and these areas were identified by the techniques mentioned previously, where the (Weight overlay) technique showed that the best site is the Al-Faw area north of the Arabian Gulf and the Khor Al-Zubair area. In contrast, the other technique represented by (Weight sum) shows that the best site for establishing surface water desalination plants in the future is along the banks of the Shatt Al-Arab and also the Khor Al-Zubair Canal. Low levels of pollutants and turbidity in high-quality source water reduce the need for intensive pre-treatment, which in turn lowers energy and operating expenses (Ghaffour et al., 2013). High-quality water can mitigate the ecological impact of brine discharge, protecting marine life. The Shatt Al-Arab River's discharge rate fluctuates due to seasonal changes and upstream water management (Al-Asadi et al., 2020). Dam construction and water diversions in Iran and Turkey have reduced river flow, causing pollution and salinity issues. Contaminants include heavy metals, nitrogen, phosphorus, and oil spills.

Increased salinity in Khora Al-Zubair is a result of a combination of irrigation runoff, seawater intrusion, and other nearby sources of pollution. Construction in the area is somewhat complicated by the clayey loam soil. High compressibility and poor stability are characteristics of clayey soils that can compromise the foundation and structural soundness of a desalination plant. There are several ways to stabilize these soils, however. According to research, the addition of materials such as fly ash, cement, and lime can enhance the geotechnical characteristics of clayey soils (Sendilvadivelu et al., 2023). Low-salinity locations reduce membrane wear and tear, extending the life of desalination equipment and minimising maintenance expenses (Lattemann et al., 2008).

Additionally, lower salinity levels reduce osmotic pressure, which uses less energy during desalination and improves energy efficiency. They are especially significant (Elimelech et al., 2011). Furthermore, the viability of hybrid desalination systems, which can alternate between various technologies according to salinity levels, can maximise operational efficiency and energy consumption (Younos et al., 2005). A monitoring program is necessary to obtain historical water quality data and spatial mapping of salinity levels and other chemical variables because seasonal changes, upstream water management, and tides have a significant impact on the water quality of the water bodies in the study area (Shatt Al-Arab River Al-Fawd, and Khor Al-Zubair e) (Figure 5). TDS levels were mapped for this investigation using the total dissolved solids (TDS) in mg/L from 10 sample locations gathered between April 1 and April 2, 2024. The three best locations will be prioritised using this mapping (Fig. 5). The range of the TDS value is (14,440 – 45,200) mg/l. In the weight overlay technique, the best sites considered suitable for establishing surface water desalination plants in the future are located on the Al-Faw side, represented by regions (d) and (e) Khor Al-Zubair (Figure 6a). In terms of soil texture, the study area is composed of silty loam, clayey loam, and Loma, which constitute 50% (1,304 km²), 35% (911 km²), and 16% (410 km²) of the total area, respectively. Of these three types, silt is generally considered the optimal choice for constructing the infrastructure of a desalination plant (Figure 3D).

The results indicated a suitable site for establishing a surface water desalination plant in Basrah Governorate, specifically in the south of Basrah, particularly in the Al-FAW region, as well as in Khor Al-Zubair and along the Shatt Al-Arab. The maps of the (weight overlay and weight overlay) techniques were divided into five categories (V. high, High, Moderate, Low, and V. low). The high ery very high areas best represent suitable locations for setting up desalination plants. According to the weight sum technique, the low to very low zones occupied 7636 km^2 (40%), the moderate zones 4772.5 km^2 (25%), and the high to very high zones 6681.5 km^2 (35%). The result of the weight overlay technique shows that the moderate zones encompass 60% (11,454 km²), the high to very high zones cover 20% (3,818 km²), and the low to very low zones cover 20% (3,818 km²). Using hydrological techniques models with GIS considers the key factors involved in selecting alternatives, e.g., desalinated water, feed water source, desalination technology, plant locations, and capabilities. As for the Weight sum technique, the most suitable location for establishing surface water desalination plants in Basrah Governorate is along the banks of the Shatt Al-Arab, specifically north of the Shatt Al-Arab (a, b), southeast of the Shatt Al-Arab (c), and the part adjacent to the Khor Al-Zubair channels (d), (Figure 6 b). The percentages of dissolved solids (TDS) values are considered the dividing line when choosing the appropriate location. Comparing these values with the suitable locations that appeared within a high to very high range in the two techniques (Weight overlay- Weight sum) is compared within the values of the total dissolved solids (Fig. 5), where it was found that the lowest percentage of dissolved solids is along the banks of the Shatt Al-Arab (14440.93-20350.90) mg/l, which proves the validity of the results of the appropriate areas that were suggested within the Weight sum model. As for the Weight overlay model, the lowest percentage of TDS is on the side of the region Al-Faw, North of the Arabian Gulf, and this proves (20350.91-28558.45) mg/l, the validity of the results of the areas suitable for establishing a surface water desalination project within the results of the first technology. Where the techniques (Weight overlay- Weight sum), Figure 6 showed that the indicated sites, which represent area (a-b-c) affiliated to the banks of the Shatt al-Arab and area (d) affiliated to Al-Faw, and finally area (e) Khor Al-Zubair and Basrah Governorate, are ideal for future projects in Iraq, particularly Basrah. These areas lack large-scale projects and serve the public interest by providing substantial water quantities for human use. This study saves agencies time and effort.

5. Conclusion

Comparing two primary methods for identifying the best site for a surface water desalination plant and mapping the site appropriateness for prospective future desalination plants in the Basrah Governorate were the two primary components of the study. This work was accomplished by integrating GIS, MCE, and spatial AHP. Basrah Governorate in southern Iraq was chosen as a case study due to its strategic location on the Arabian Gulf; moreover, Iraq's primary water resources are limited, comprising non-renewable groundwater from deep wells, some renewable aquifers, and seawater. Decision-makers can manage current desalination plants and plan for future ones with the aid of the work outcomes. Other studies may find the technique employed in this paper useful. The optimal locations for developing water desalination plants are the north-south Shatt Al-Arab (a-b-c), the FAW area (d), and Khor Al-Zubair (e), according to the results of hydrological techniques. In the modeling map, these places correspond to the V. high and High classes.

The best locations in the Basrah Governorate for a water desalination project were selected using weighted sum and weighted overlay techniques. In addition, the research area's lithology, rainfall, land cover, and land use, as well as proximity to major roads, electricity transmission lines, and urban centers, were taken into account, along with the land surface's height and slope. Land use, as well as proximity to major roads, electricity transmission lines, and urban centers, were taken into account, along with the land surface's height and slope. In the study area, regions (a) and (b) are considered the most suitable in terms of establishing a surface water desalination project due to the low salinity and the water fluctuations of the Shatt al-Arab drainage, which affects the salt tongue coming from the Arabian Gulf. As for the second region, Al-Faw (c), it is considered one of the most suitable sites chosen due to the abundance of land ideal for establishing large projects, such as the seawater desalination project, as most of it is a salt marsh, in addition to its lower salinity compared to the Arabian Gulf. Finally, the Khor Al-Zubair region (d), despite the pollution of the water source of this region with chemical and oil pollutants, is close to the Al-Zubair region, meaning that it is easy to treat this water and transport it for use for many purposes (domestic and industrial).

Therefore, it is believed that this study is essential for both decision-makers and implementers. When choosing the ideal location for a surface water desalination plant, several methods are crucial. Government organizations will save a significant amount of time and effort by identifying suitable locations for the construction of a large-scale water desalination plant in the Basrah Governorate.

References

Alaa M. Al-Abadi, Qusai Y. Al-Kubaisi, M.A.A.-G.: Mapping groundwater zones contaminated by hydrocarbons in the Dammam aquifer in the Karbala–Najaf plateau, Iraq. Environ. Earth Sci. (2018). https://doi.org/https://doi.org/10.1007/s12665-018-7827-2.

Al-Abadi, A, M., 2018. Mapping of flood susceptibility using three GIS–based ensemble classifiers: a comparative assessment of random forest, rotation forest, and AdaBoost models. Arabian Journal of Geosciences 11(9) Doi: 10.1007/s12517-018-3584-5.

Al-Ansari, N., Adamo, N., Hachem, A.H., Sissakian, V., Laue, J., Abed, S.A.: Causes of Water Resources Scarcity in Iraq and Possible Solutions. Engineering. 15, 467–496 (2023).

Al-Ansari, N., Adamo, N., Knutsson, S., Laue, J.: Geopolitics of the Tigris and Euphrates basins. J. Earth Sci. Geotech. Eng. 8, 187–222 (2018).

Al-Asadi, S.A.R., Al Hawash, A.B., Alkhlifa, N.-H.A.H., Ghalib, H.B.: Factors affecting the levels of toxic metals in the Shatt Al-Arab River, Southern Iraq. Earth Syst. Environ. 3, 313–325 (2019).

Al-Asadi, S.A.R., Al-Qurnawi, W.S., Al Hawash, A.B., Ghalib, H.B., Alkhlifa, N.-H.A.: Water quality and impacting factors on heavy metals levels in Shatt Al-Arab River, Basrah, Iraq. Appl. Water Sci. 10, 1–15 (2020).

Abdul-Hameed, S. A.-Q., & Hatem, A. J. (2021). Effect of Shatt Al-Arab salinity on the groundwater of Al-Fao and Al-Siba in southern Iraq. Iraqi Geological Journal, 54(1E), 114-122. https://doi.org/10.46717/igj.54.1E.10Ms-2021-05-31.

Alatta, H.J., Behadili, S.F., Sayyid, B.H.: Analyze water scarcity in Basrah city via geoinformatics. In: AIP Conference Proceedings. AIP Publishing (2022).

Castillo, J. M., March, A. L., Tan, S. Y., Stockslager, K. M., Brundage, A., McCullough, M., & Sabnis, S. (2016). Relationships between ongoing professional development and 'educators' perceived skills relative to RtI. Psychology in the Schools, 53(9), 893-910. https://doi.org/10.1002/pits.21954.

Chiles, J.-P., Delfiner, P.: Geostatistics: modelling spatial uncertainty. John Wiley & Sons (2012). DOI: 10.1002/9781118136188

Diaz-Caneja, M. Farinas, Cost estimation briefing for large seawater reverse osmosis facilities in Spain, International Conference on Desalination Costing, Dec. 6–8 2004, Limassol, Cyprus.

Dweiri, F., Khan, S. A., & Almulla, A. (2018). A multi-criteria decision support system to rank sustainable desalination plant location criteria. Desalination, 444, 26–34. https://doi.org/10.1016/j.desal.2018.07.00

Effat, H. A., & El-Zeiny, A. (2017). Multi-criteria decision analysis for locating optimum sites for water desalination plants in Egypt. Environmental Monitoring and Assessment, 189(10), 512. DOI: 10.1007/s10661-017-6201-0

Elimelech, M., Phillip, W.A.: The future of seawater desalination: energy, technology, and the environment. Science, 333, 712–717 (2011). DOI: 10.1126/science.1200488

Gokçek, M., Gokçek, O.B., 2016. Technical and economic evaluation of freshwater production from a wind-powered small-scale seawater reverse osmosis system (WP-SWRO). Desalination 381, 47–57. https://doi.org/10.1016/j.desal.2015.12.004.

Hafez, S. El-Manharawy, Economics of seawater RO desalination in the Red Sea region, Egypt. Part 1. A case study, Desalination 153 (2002) 335–347. Doi: 10.1016/S0011-9164(02)01120-7

Hwang, C. L., & Yoon, K. (1981). Multiple attribute decision making: Methods and applications. Springer. Doi: 10.1007/978-3-642-48318-9

Jankowski, P., & Nyerges, T. (2001). GIS for Group Decision Making. CRC Press.

Lattemann, S., Höpner, T.: Environmental impact and impact assessment of seawater desalination. Desalination. 220, 1–15 (2008). doi: 10.1016/j.desal.2007.03.009

Longley, P.A., Goodchild, M.F., Maguire, D.J., Rhind, D.W.: Geographic information systems and science. John Wiley & Sons (2005).

Mahi, P.: Developing environmentally acceptable desalination projects. Desalination. 138, 167–172 (2001). doi: 10.1016/S0011-9164(01)00263-4

Malczewski, J. (1999). GIS and Multi-criteria Decision Analysis. Wiley.

Malczewski, J. (2000). On the use of weighted linear combination method in GIS: common and best practice approaches. Transactions in GIS, 4(1), 5-22. Doi: 10.1111/1467-9671.00035

Mohamed, S.A.: Application of geospatial Analytical Hierarchy Process and multi-criteria analysis for site suitability of the desalination solar stations in Egypt. J. African Earth Sci. 164, 103767 (2020). doi: 10.1016/j.jafrearsci.2019.103767

Odu, G. O. (2019). Weighting methods for multi-criteria decision-making technique. Journal of Applied Science and Environmental Management, 23(8), 1449-1457. DOI: 10.4314/jasem.v23i8.7

Ouda, Y.W., Kadhim, K.F., Amer, A.M.: Study of some toxic metals in parts from catfish (Silurus triostegus) in Shatt Al-Arab River. Iraqi J. Vet. Sci. 37, 459–467 (2023). DOI: 10.33899/ijvs.2023.133066.2530.

R. Saeed, T. Fatemeh, M. Mostafa, K. Majid, Locating the best place to build a desalination plant with artificial intelligence (Chabahar study area, Iran. 6th Intercontinental Geoinformation Days (IGD) – 13-14 June 2023 – Baku, Azerbaijan.

Radwan, F., Alazba, A.A., Alotaibi, M., Mossad, A.: Site suitability analysis for desalination plants based on the complementarity of GIS, RST, MCE, and spatial AHP in arid and semiarid regions. Arab. J. Geosci. 15, 1763 (2022). DOI: 10.1007/s12517-022-11160-0.

Riad, S., Shaker, A., & Othman, A. (2011). Estimating the location of the best site for a water desalination plant in the Sinai Peninsula, Egypt, using multi-criteria analysis and GIS. Arabian Journal of Geosciences, 4(1-2), 235-246. DOI: 10.1007/s12517-009-0075-2.

Schnepf, R.D.: Iraq agriculture and food supply: background and issues. Presented at the (2004).

Sendilvadivelu, A., Dhandapani, B., Vijayasimhan, S.: Strength, mineralogical and microstructural studies on clayey soil stabilised by bio-stabilized waste ash with lime. J. Mater. Cycles Waste Manag. 25, 3625–3637 (2023). DOI: 10.1007/s10163-023-01673-0.

Sepehr, M., Fatemi, S.M.R., Danehkar, A., Mashinchian Moradi, A.: Application of Delphi method in site selection of desalination plants. Glob. J. Environ. Sci. Manag. 3, 89–102 (2017). DOI: [10.22034/gjesm.2017.03.01.009].

Shahabi, M.P., Anda, M., Ho, G.: Influence of site-specific parameters on environmental impacts of desalination. Desalin. Water Treat. 55, 2357–2363 (2015). doi:10.1016/j.

desal.2014.12.003.

Slocum, A.H., Haji, M.N., Trimble, A.Z., Ferrara, M., Ghaemsaidi, S.J.: Sustainable Energy Technologies and Assessments. (2016).

Saaty, T. L. (1980). The Analytic Hierarchy Process: Planning, Priority Setting, Resource Allocation. McGraw-Hill.

Tsiourtis, N.X.: Criteria and procedure for selecting a site for a desalination plant. Desalination. 221, 114–125 (2008). doi:10.1016/j.desal.2007.01.073.

JJEES

JJEES (2025) 16 (4): 352-364
ISSN 1995-6681

Jordan Journal of Earth and Environmental Sciences

Petrography, Mineralogy, and Geochemistry of the Aïn Babouche ooidal ironstones (Northeastern Algeria): Implications for Depositional Environment, Iron Source and Ooids Formation.

Abdelhakim Bouchair[1,2*], Azzedine Bouzenoune[1,2], Chiara Benedetta Cannata[3], Mariano Davoli[3], Oumeima Benmebarek[1,2], Zoubir Belhimer[1,2]

[1]Geological Engineering Laboratory (LGG), University of Jijel, Central Campus, BP 98, 18000, Jijel, Algeria
[2]Department of Earth and Universe Sciences, Faculty of Natural and Life Sciences, University of Jijel, Central Campus, BP 98, 18000, Jijel, Algeria
[3]Center of Microscopy and Microanalysis – Department DiBEST of the University of Calabria, 87036 Arcavacata di Rende, Italy

Received on February 24, 2025, Accepted on May 6, 2025

Abstract

This study aims to examine the petrography, mineralogy, and geochemical characteristics of the Eocene ooidal ironstone formations at Aïn Babouche, located in the eastern part of the Saharan Atlas in order to determine the mechanism of ooid formation. The country rocks consist of Upper Cretaceous to Quaternary marls and limestones with a thickness of 6 Kilometres, while the iron-rich intervals (10 meters) are separated by centimetric levels of marl. These intervals are restricted to the Lutetian age. Petro-mineralogical investigations indicate that iron ore is composed mainly of ooids (goethite and limonite) and detrital minerals (quartz, clay, apatite). Geochemical analysis, using Laser Ablation Inductively Coupled Plasma Mass Spectrometry and X-ray fluorescence spectrometry, reflects the hydrogenous origin of the iron, more likely from a continental source, basinal brines, or a mixed source. The mechanism of ooid formation is suggested to be direct precipitation of iron around a nucleus in a shallow, agitated marine environment. This interpretation is based mainly on the sedimentological pattern and parameters, the ironstones, the morphology and internal geometry, and the composition of the ooids, as well as the associated framework components.

Keywords: *Ooidal ironstones; Eocene; Rare earth elements; Cerium anomaly; Ain Babouche; Algeria*

1. Introduction

The ooidal iron deposits were a significant source of iron that aided nineteenth-century industrial development (Petranek and Van Houten, 1997). In terms of iron resource richness, ooidal iron deposits rank after BIF-type deposits, which are related to magmatic processes. However, ooidal ironstone deposits are the most widespread globally, with almost 400 occurrences and total reserves estimated at over 66,000 million tonnes worldwide. As Petranek and Van Houten (1997) have demonstrated, ooidal ironstones are sandy, clayey, siliciclastic, or siliciclastic-carbonate sedimentary rocks that contain over 15% of iron. Furthermore, they have been observed to include more than 5% coated grains, which are oncoids, pisoids, and ooids (Salama et al., 2013). The investigation of ooidal ironstones can aid in reconstructing paleoenvironmental conditions and provide insights into the chemical and fluid dynamics within a basin.

Despite the research on ooidal ironstones, particularly marine ones, the genesis of these deposits is still debated, with explanations varying from deposit to deposit. Researchers have proposed various hypotheses that include the following: i) In 1856, Sorby proposed that ooids are formed by replacing calcareous ooids. This theory has garnered support from Kimberley (1979), Kearsley (1989), and Diab et al., (2020), who have provided substantial evidence in support of this assertion, including the presence of calcareous relics and early diagenetic siderite. ii) Intrasedimentary concretional growth as demonstrated by Hallimond (1951), Hemingway (1974), followed by Salama et al. (2014), Baioumy et al. (2017), and Garnit et al. (2017). Supporters of this theory have employed various methods to validate it, chiefly the presence of radial-fibrous concentric layers and the identification of authigenic minerals, such as siderite. iii) The extrasedimentary mechanical accretion of ooids (Bhattacharya & Kakimoto, 1982; Van Houten & Purucker, 1984; Kearsley, 1989). This one is supported by evidence such as well-rounded spherical ooids and the presence of sedimentary structures. iv) Dahanayake & Krumbein (1986) proposed the theory of primary biological accretion, which Burkhalter (1995) followed. The theory is supported by the presence of ferruginous stromatolitic microbialites that contain microbial laminae composed of fossilized leptothrix-like bacterial filaments (El Aref et al., 2006b; Salama et al., 2013, 2014). v) Siehl and Thein (1989) were the first to suggest that iron ooids or pisoids were derived from lateritic soils. This proposition was based on the absence of aluminium substitution and other evidence, which contradicted alternative theories. vi) Harder1989 proposed

* Corresponding author e-mail: Hakim.bouchair@univ-jijel.dz

crystallisation from precursor iron oxyhydroxide gels based on experimental or theoretical evidence that ferruginous gels can act as precursors to mineral phases, especially under early diagenetic conditions (low temperature and pressure).

In the African continent, ooidal ironstone deposits represent an important source of iron (McGregor et al., 2010), over 100 deposits are spread over six countries almost located in the north African basin (i.e. Algeria, Tunisia, Sudan, Morrocco, Libya, Egypt, and Nigeria), ranging in age from the Paleozoic (Ordovician to Devonian), Mesozoic (Jurassic and Cretaceous) to less commonly cenozoic (Petranek and Van Houten, 1997). In North Africa, only three Eocene ooidal ironstone occurrences have been inventoried: the Djebel Ank ooidal ironstone in central Tunisia, the Bahariya Depression in the Western desert of Egypt, and the Aïn Babouche in northeastern Algeria (Petranek and Van Houten, 1997; El Aref et al., 1999, 2006a, 2006b). The latter is considered "an uneconomic deposit", although it is currently mined, and the ore is used by cement factories in the region.

The Aïn Babouche ooidal iron deposit, hosted within Eocene formations, is the only deposit of this type currently mined in the Tebessa region. While the Tunisian Djebel Ank deposit, located approximately 160 km southeast, is equivalent to the Aïn Babouche deposit, as it is also hosted in Eocene formations (Garnit et al., 2017).

The purpose of the present study is to characterise the petrography, mineralogy, and geochemistry of the Eocene ooidal ironstones from the Aïn Babouche deposit in order to understand the sedimentation processes, depositional environment and diagenetic processes that prevailed during ironstone formation. It is hoped that this work can serve as a reference for studies of other ironstone deposits in different regions.

2. Geological background

The Aïn Babouche deposit is located in the north-east of Algeria, at a distance of 56 km south-west of the city of Tebessa and about 10 km west of the town of Telidjene (Figure 2). The Tebessa region is situated within the eastern Saharan Atlas, south of the Tell Atlas. It is separated from the Saharan platform to the south by the South Atlas Front, a structural alignment that extends over more than 1000 km. This alignment consists of a Palaeozoic basement covered by Meso-Cenozoic sediments (Figure 1). The main geological features of the Tebessa region include subsidence, diapirism, folding, faulting, and grabens. The sedimentary sequence thickness from the Barremian to the Quaternary is roughly 6 km, whereas bathymetric estimations do not surpass a few hundred meters (Dubourdieu, 1956).

The most ancient geological formations that outcrop in the Aïn Babouche sector are constituted of evaporitic rocks from the Triassic period mainly consisting of gypsum, variegated clays, cargneules, and dolomites. These rocks outcrop particularly to the NW and SE of the Aïn Babouche syncline in the Hamimat Guibeur and Hamimat Meskouta diapirs, respectively (Figure 2). Jurassic formations are absent from the outcrop. However, Vila (1992) reported the presence of exogenous Jurassic shreds of reduced size in the Triassic formations of the two diapirs.

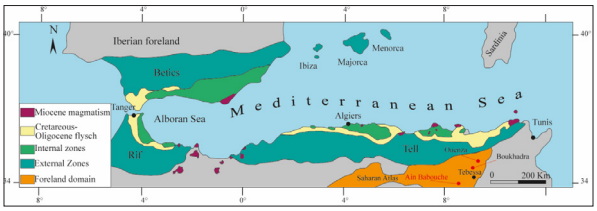

Figure 1. Map showing different domains of the Western Mediterranean Alpine orogen (modified from Durand Delga et Fontboté 1980; Vila, 1980; Etheve et al., 2016)

The Lower Cretaceous formations are limited to the central part of the Ain Telidjene anticline (Figure 2), represented by iron-bearing sandstones and dolomites. Limestones and dolomites, phosphate-bearing marls and brecciated limestones are often overlain by marly limestones.

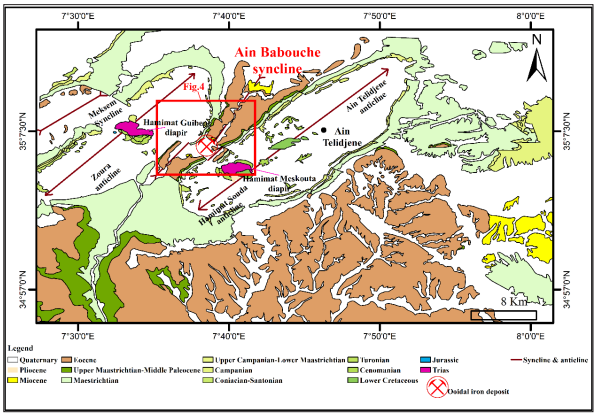

Figure 2. Geological sketch map showing the Aïn Babouche syncline among the so-called NE-SW "Atlasic folds" of the Northeastern Saharan Atlas of Algeria (Vila, 1992).

As stated by Vila (1992), the Upper Cretaceous formations are characterised by an alternation of gypsum marls and limestone. The Cretaceous successions consist mainly of limestones in the lower part and an alternation of limestones, marl and phosphatic rocks in the upper part (Figure 3). The Palaeocene formations consist of marls from the Dano-Montian period, with sedimentary continuity with those from the end of the Maastrichtian period. The Ypresian contains a series of limestones that include many multiform black or brown flints. They are rich in lumachellics shell debris and have a sparse cement with little phosphate debris.

Shown in Figure 4, stratiform ooidal ironstone layers are confined within the Lutetian series of partially ferrugenated marls, sandstones, and mudstone, topped by limestones and gypsum. Based on our geological cross-section and field observations (Figure 4), the mineralized zone consists of numerous layers of compact ooidal ironstones, totaling 11 layers. Due to their diminutive thickness, the ironstones mentioned above have been categorized into four primary layers in the cross-section. The stratigraphic sequence of the mineralised zone begins with an alternation of marls and ironstone, with a thickness range from 10-50 cm. The first levels of marls contain abundant debris of ostracodes, including several *NONIONELLASP AND VIRGULINA GR. DANVILLENSIS HOWE & WALLACE*, as well as *CAVERNOCYTHEREIS (LOXOCONCHA) CAVERNOSA*

(APOSTOLESCU & MAGNE). Based on the debris, Vila (1992) dated the series that contains the ooidal ironstones to the upper-middle Lutetian period. Thereafter, an alternation of thin layers of ironstone (5 to 10 cm) with layers of marl. The sequence concludes with two two-layer measuring 4 m in thickness. The ironstone layers show various sedimentary structures, includingcross-beddings, graded bedding, and channels (Figure 5). The cross-bedding is composed of bands with a thickness varying from 1.5 to 3 cm, separated by millimetre-sized laminae, consisting of consolidated iron oxide. The transition between the various formations exhibits no structures indicative of substantial modification. There are no structures of the emersion surface type, hardened surface, stratigraphic gap, or discordance.

The Miocene rocks consist mainly of siliceous conglomerates and a red sandy-clay series with rare carbonate elements (Figures 3 and 4).

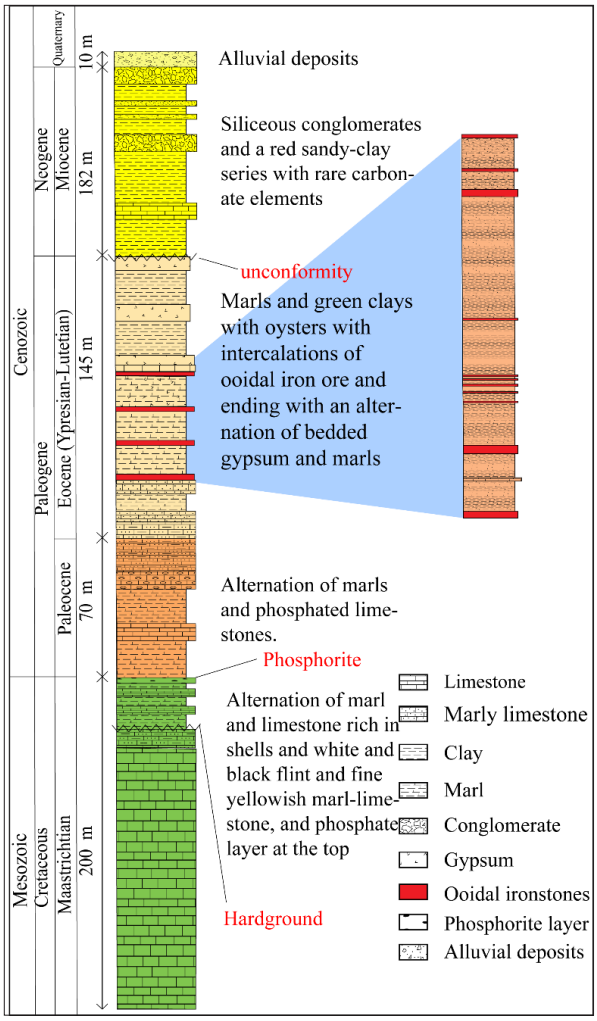

Figure 3. Litho-stratigraphic column of Djebel Dahar series (SE side of the Aïn Babouche syncline). Based on field and petrographical data, the chronological sequence was established by Vila (1992).

The Aïn Babouche region is marked by several folds and fault structures, some of which exhibit Triassic evaporitic rocks emplaced through multiphase diapiric activities (Figures 2 and 4). The fold structures consist of narrow synclines and wide anticlines with a NE–SW direction. They were formed during the Atlasic phase of the Upper Eocene, which affected the Saharan Atlas (Dubourdieu, 1956). The narrow Aïn Babouche syncline is located between the wide Zoura in the northwest side and the Aïn Telidjene anticline in the southeast side (Figure 4). The axis of the syncline (~10 x 3.5 km) aligns with the stream bed of the Wadi Babouche, trending NE–SW to the northeastern part, ENE–WSW to the central part, and NE–SW to the south-western part. The shift of directions is due to NW–SE faults that subdivide the syncline into three segments (Figure 4).

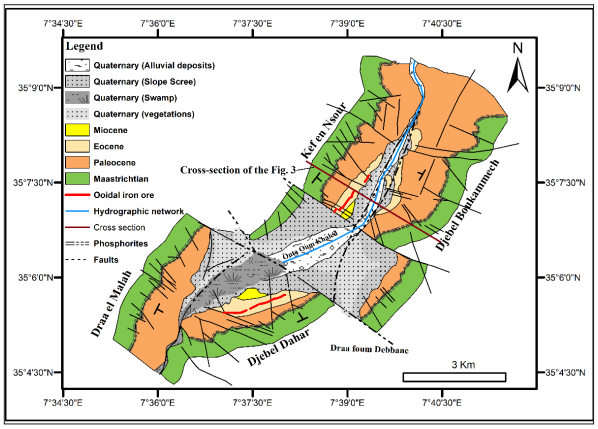

Figure 4. Geological map of the Aïn Babouche syncline showing the arrangement of the main iron ore outcrops within the different geological formations (Sonarem-Rudis, 1968; Keddar, 1985). (Extension of the ore body and Miocene formations were determined by the authors based on field observations and petrographical data).

3. Material and Methods

Sampling and field descriptions were carried out on the Aïn Babouche sedimentary series from both sides of the Aïn Babouche syncline. “Bed-by-bed” 37 samples were collected and described. Thin sections (90) and polished sections (20) were prepared in the geological engineering laboratory at the University of Jijel and in the laboratory of the geology department at the University of Annaba. They were examined using a Zeiss polarising and reflected light microscope, respectively.

X-Ray diffraction analysis (XRD) was performed at the Physitek Analysis and Equipment Laboratory using five bulk samples on a Smart Lab SE automated multipurpose X-ray diffractometer using Cu Kα radiation (λ = 1.5406 Å) with an accelerating voltage of 40 kV, a filament current of 40 mA, and a scan range between 5 and 70. Data were interpreted using X’Pert HighScore Plus software. Major element concentrations were also measured at Physitek Laboratory using an Epsilon 4 X-ray fluorescence spectrometer, operated at a tube voltage of 50 kV and a current of 1 mA.

Trace element (TE) analyses were carried out on eight polished sections, using the Laser Ablation Inductively Coupled Plasma Mass Spectrometry (LA-ICP-MS) at the Department of Earth Sciences “A. Desio” of the University of Milan, using an Analyte excite 193 nm ArF excimer laser coupled with an iCAP-RQ mass spectrometer. The operating conditions were 1 J/cm² fluence, a 65 µm spot size, and a 6 Hz repetition rate. The acquisition time was 60 seconds on the sample and 40 seconds on the background. Data reduction was performed using the software GLITTER (Griffin et al., 2008), with FeO wt% concentrations from the electron probe

micro-analyzer (EPMA) serving as an internal standard. The international reference material GSD-1g (Jochum et al., 2011) was used as the primary standard, and the reference glasses NIST 610, BCR-2g, and BHVO-2g (Jochum et al., 2011) were used to monitor accuracy.

Scanning electron microscopy (SEM), coupled with energy-dispersive X-ray spectroscopy (EDS) analysis, was performed on five polished and thin sections using a scanning electron microscope Ultra High-Resolution SEM (UHR-SEM) - ZEISS CrossBeam 350, coupled with an EDX spectrometer - EDAX OCTANE Elite Plus - Silicon drift type. The instrumental conditions set for the EDX analysis were as follows: HV, 15 keV; and probe current, 100 pA. The analyses SEM analyses were carried out at CM2 (Center of Microscopy and Microanalysis) – Department DiBEST (Biology, Ecology and Earth Sciences) of the University of Calabria, 87036 Arcavacata di Rende, Italy.

4. Results

4.1. Petrography

Petrographic examinations show that the ooidal ironstones of Ain Babouche Area are composed of more than 70% of ooids and granules as the main constituents of ironstones. Other grains are detritals, such as quartz (20%), phosphate (5%), glauconite, and other organic debris, which account for a small percentage. These components are set in a ferruginous clayey matrix and cemented by calcite cement.

The space between the ooids is filled by many grains; Quartz occupied the most space (Figure 6d), with rare apatite (Figure 8a), debris of carbonate organisms, including teeth probably belonging to “Selacians”, and the glauconite mentioned by Keddar (1985). In the flank of Kef en Nsour, the grains constituting iron ore are contiguous, unlike at Djebel Dahar, where they are spaced out from each other. The cement nature of Kef en Nsour ironstone is ferruginous or clayey, which explains the crumbly texture of the ore. In contrast, at Djebel Dahar, the deposit is larger due to the presence of carbonate cement.

Ooids are generally spherical, with a variable size (max 2 mm in diameter), and have a smooth outer surface under a reflected light microscope. The cores of the ooids are composed of goethite, while the concentric cortex consists of alternating colours between light and dark grey, corresponding to goethite and limonite, respectively (Figures 6 and 9). Each ooid typically has 2 to 10 concentric layers, with a thickness ranging from 50 µm to 200 µm. Most laminations are α-type (Figure 6a), which tend to regularise the morphology of the nucleus. In revanche, the β-type ooid is present in small quantities (Figure 6c) and tends to preserve the original morphology of the nucleus.

In addition to the ooids, granules are ubiquitously present in the iron ore. Granules are grains with the same composition as ooids but without the enveloping structures. In our case, they are mainly goethitic in composition and similar in size and shape to ooids (Figure 6d). The XRD analysis reveals that all the ooids and granules of the two flanks of the syncline of Ain Babouche (Kef en Nsour and Djebel Dahar) are both mainly composed of goethite (Figure 7).

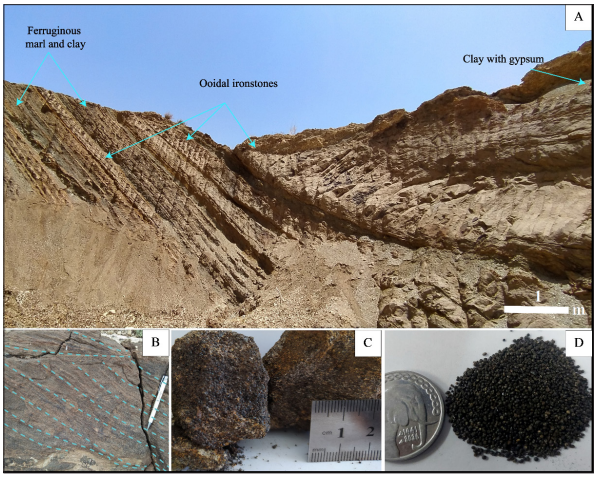

Figure 5. a) Field photos and macrophotographs illustrating the occurrence of two types of iron ore (ooidal ironstones and ferruginous marl and clay) at the scale of the outcrop. **b)** Ironstone layers with Cross-beddings. **c)** Ooidal ironstones. **d)** Crumbly sample ground by hand.

The nuclei of most ooids are typically rounded, which can be attributed to multiple phases of reworking. However, they rarely exhibit xenomorphic shapes (Figure 6a). Their diameter varies between 0.01 mm and 0.4 mm. Ooids typically consist of a single nucleus, although they may have up to four. Their composition might include quartz (Figure 8c), ooid fragments (Figure 6b), goethite fragments, and grains formed from a combination of several elements (quartz, goethite).

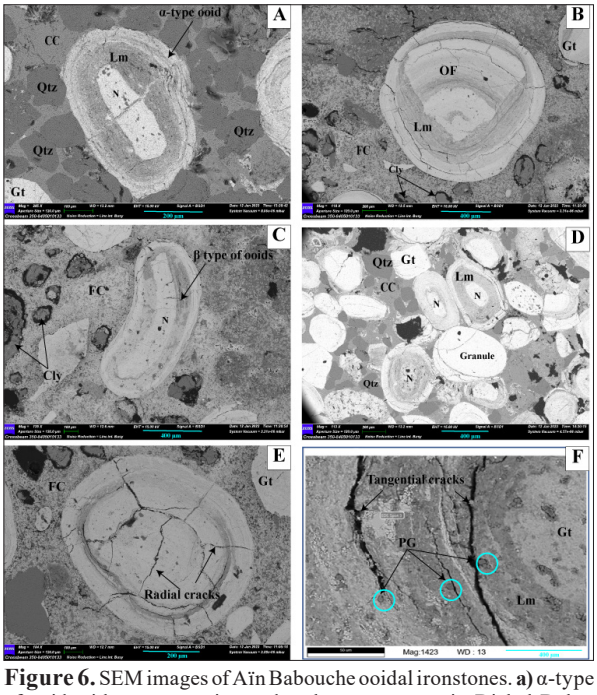

Figure 6. SEM images of Aïn Babouche ooidal ironstones. **a)** α-type of ooid with quartz grains and carbonate cement in Djebel Dahar ironstones. **b)** Ooid fragment as nucleus and clay grains cemented with a ferruginous cement in Kef en Nsour ironstones. **c)** β-type ooid with clay grains cemented with a ferruginous cement in Kef en Nsour ironstones. **d)** Ooids, granules, and quartz cemented with carbonate cement in Djebel Dahar ironstones. **e)** Ooid represents the radial type of cracks in Kef en Nsour ironstones **f)** The concentric layers of ooid contain phosphate grains. (Lm: limonite. Gt: Goethite Qtz: quartz. Ap: Apatite. Cly: Clay. PG: Phosphate grains. N: nucleus. CC: carbonate cement. FC: ferruginous cement. OF: ooid fragment)

Iron ooids have been identified as being affected by two distinct categories of cracks. (1) The most prevalent group of fractures is the early group, which is frequently oblique to parallel with the layers of the rim (Figure 8b). (2) The second group of cracks is radial to the various envelopes of the ooids. In certain instances, these cracks may divide the ooids into fragments, some of which serve as nuclei, leading to the formation of new layers of ooids around them (Figure 6b).

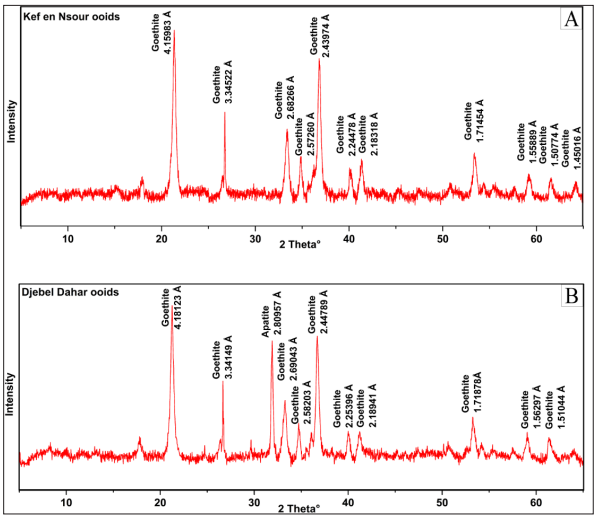

Figure 7. X-Ray diffractograms of two samples of ooidal ironstones (Ooids) showing the presence of goethite and Apatite minerals inside the ooids

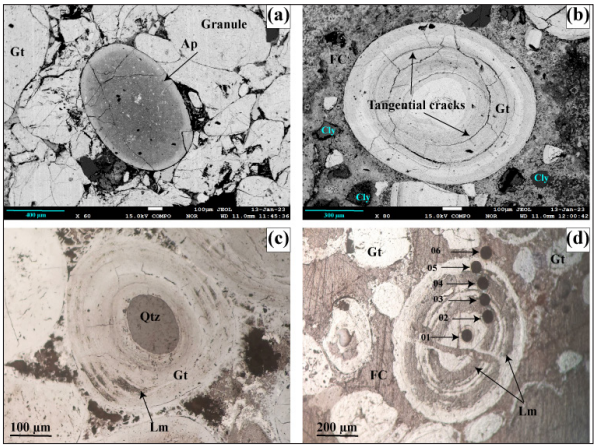

Figure 8. EMPA microphotographs of polished sections: **a)** Apatite grain with goethitic granules in Kef en Nsour ooidal ironstones. **b)** Ooid showing the tangential type of cracks in Kef en Nsour ooidal ironstones (Reflected light observation). **c)** Ooid with quartz nucleus. **d)** Ooid showing the LA-ICP-MS points analyses of the ooidal ironstone sample

4.3. Geochemistry

4.3.1. Major oxide elements

The concentrations of major oxides in the ooidal ironstones and the host rocks from Kef en Nsour and Djebel Dahar are shown in Table 1. In the iron ore, FeO is the most abundant, with an average (av.) content of (63.09 wt % FeO), followed by SiO_2 (av. 10.46 wt %) and Al_2O_3 (av. 3.64 wt %).

Table 1. Major oxides concentration (wt.%) of ooidal ironstones and host rocks of Kef en Nsour and Djebel Dahar (Aïn Babouche) measured by XRF (OI: Ooidal Ironstones, HR: Host Rocks; bdl = below detection limit)

Area	Samples	Rock type	SiO_2	Al_2O_3	FeO	CaO	MgO	MnO	K_2O	P_2O5	TiO_2
Djebel Dehar	DD01	OI	8.32	3.33	65.07	3.71	1.49	1.29	0.17	3.07	bdl
	DD06	OI	6.23	3.50	65.60	3.83	1.26	1.07	0.12	2.80	0.11
Kef en Nsour	ABW08	OI	9.05	3.40	63.45	1.33	0.76	0.87	0.13	1.92	bdl
	ABW09	OI	12.37	3.68	67.30	2.42	1.16	0.87	0.27	2.64	0.12
	ABW10	OI	8.13	3.29	61.07	0.49	0.96	0.10	0.13	1.17	0.09
	ABW10b	HR	50.12	7.58	5.24	1.57	0.27	bdl	1.31	0.18	0.75
	ABW11	OI	17.91	4.36	53.63	2.14	0.76	1.21	0.33	2.06	bdl
	ABW12	OI	13.22	3.59	58.42	6.35	1.23	1.41	0.23	5.13	0.15
	KN08	OI	8.47	3.99	70.22	0.92	1.16	0.92	0.12	1.72	bdl

The CaO concentrations (average 2.64 wt%), had a positive correlation with P2O5 (average 2.56 wt%), as expressed by a correlation coefficient of 0.98. The MgO content in ores varies from 0.76% to 1.49% (av. 1.09%). MnO content averages between 0.1% and 1.41%. TiO_2 and K_2O occur in very low proportions, with averages of 0.06% and 0.19%, respectively.

4.3.2. Trace elements

The trace element concentrations of the ooidal ironstones from Aïn Babouche were determined by LA-ICP-MS (Table 2). V and Zn recorded the highest concentrations among the trace elements, with an average of 682.88 ppm and 562.13 ppm, respectively. The average concentrations (ppm) of the other trace elements in descending order are Ni (332.45), Co (195.6), Cr (159.57), As (113.8), Ba (102.46), Sr (55.11), Pb (55.66), Y (50.09), Zr (35.85), Cu (10.17), Mo (9.5), U (9.24), Sc (8.06), Rb (7.92), Th (4.76), Nb (3.68), Sn (0.95), Sb (0.76), Hf (0.62), and Ta (0.12). The ooids of the two sides of the syncline (Kef en Nsour and Djebel Dahar) contain almost the same concentrations.

Upon normalization to the upper continental crust (UCC) as outlined by Taylor and McLennan, (1985), the concentrations indicate that V, Co, Ni, Zn, As, Mo, Ba, Pb, and Zn exhibit enrichment relative to the UCC. In contrast, Rb, Sr, Zr, Nb, Sn, Hf, and Ta demonstrate depletion (Figure 9). The same trends are observed in the ooidal ironstones on both the northwest flank (Kef en Nsour) and the southeast flank (Djebel Dahar). The same characteristics are observed in both the nuclei and the envelopes of the ooids.

Trace elements analysis of the Aïn Babouche ooidal iron deposit reveals significant similarities with regional and global ooidal iron deposits, including Djebel Ank (Tunisia, Garnit et al., 2017), Aswan (Egypt, Baioumy et al., 2017), and Bakchar (Siberia, Rudmin et al., 2019), as illustrated in Figure

10b. The slight differences include Sr depletion within Aïn Babouche ooids, whereas the ooids from Djebel Ank have higher contents of U and Mo. Additionally, samples from the Bakchar deposit exhibit higher concentrations of V and Ba, while showing lower contents of Co and Ni (Figure 9b).

Table 2. Aïn Babouche trace elements analysis of ooidal ironstones determined by LA-ICP-MS (values are the average of the measured points from the nucleus to the concentric layers for each sample)

	Djebel Dahar				Kef En Nsour			
Element (ppm)	STI04	DD01	DD06	STI01	ABW8	ABW9	ABW11	ABW12
Sc	8.42	8.07	7.75	8.61	7.79	8.20	7.36	8.29
V	798.97	606.85	713.43	806.66	594.46	569.24	644.36	729.10
Cr	151.56	87.08	208.37	187.58	159.69	124.51	206.13	151.66
Co	186.16	165.39	135.91	206.67	153.51	137.54	405.54	174.08
Ni	326.92	312.96	226.02	346.97	274.75	275.64	614.64	281.77
Cu	7.97	10.33	14.61	10.52	7.96	5.87	16.49	7.68
Zn	505.28	504.00	635.75	573.30	390.39	620.79	611.86	655.70
As	98.27	109.86	156.50	115.70	112.28	118.41	115.42	83.98
Rb	6.11	4.79	7.03	7.44	7.71	6.03	17.01	7.27
Sr	19.84	21.30	65.92	27.29	30.70	35.73	203.83	36.29
Zr	37.29	33.37	35.91	40.02	41.40	29.32	35.40	34.10
Nb	3.38	2.53	3.51	3.23	2.94	2.80	8.58	2.53
Mo	27.62	4.11	3.34	28.30	3.70	2.44	4.14	2.74
Sn	0.83	0.53	1.13	0.92	0.76	0.51	2.01	0.96
Sb	0.81	0.71	0.80	0.72	0.60	0.52	1.12	0.88
Ba	68.47	61.74	90.37	217.41	50.41	63.27	222.64	45.37
Hf	0.82	0.36	0.70	0.65	0.70	0.45	0.70	0.63
Ta	0.14	0.10	0.10	0.12	0.12	0.09	0.28	0.08
Pb	42.30	40.71	75.68	57.05	60.40	59.96	67.07	42.15
Th	4.56	2.58	5.72	5.65	4.97	3.32	5.54	5.83
U	10.67	7.73	11.18	10.28	13.41	7.34	7.25	6.13

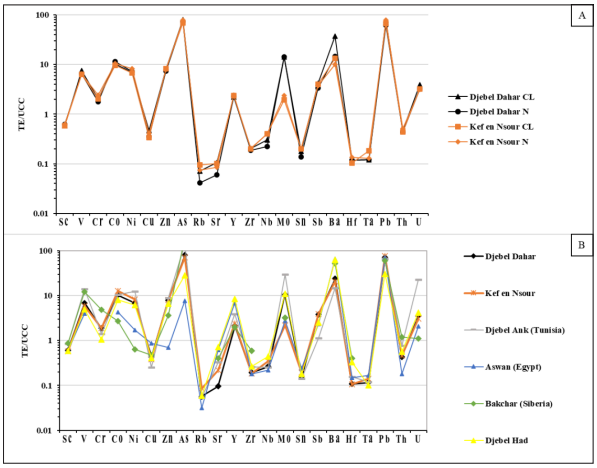

Figure 9. a) UCC-normalized trace elements of Aïn Babouche ooids nucleus (N) and the concentric layers (N). **b)** UCC-normalized trace elements of Aïn Babouche Fe ooids compared to Djebel Had deposit (Diab et al., 2020), Djebel Ank deposit (Garnit et al., 2017), Aswan deposit (Baioumy et al., 2017), and Bakchar deposit (Rudmin et al., 2019). Depleted values below 0.5 and those greater than two are enriched

The high content of Ni+Co and the low content of As+Cu+Mo+Pb+V+Zn mean that both Kef en Nsour and Djebel Dahar ooidal ironstone are within the hydrogenous fields of the binary diagram of trace elements. (Nicholson, 1992).

4.3.3 Rare earth elements

The total REE+Y content ranges between 104 and 362 ppm, with an average of 242 ppm (Table 3). The Kef en Nsour's average value of the total REE+Y (264 ppm) is slightly higher than that of Djebel Dahar's (220 ppm). The average value of the total REE+Y of 19 points analysed in the nucleus (244 ppm) is almost the same as the points in the concentric layers (221 ppm).

The patterns of REE values of Aïn Babouche ooidal ironstones normalised against post-Archean Australian shale (PAAS) (Taylor and McLennan, 1985) show a slight enrichment in HREE and MREE compared to LREE. The ores of the two flanks of the synclinal structure (Kef en Nsour to the NW and Djebel Dahar to the SE) show similar REE patterns (Figure 10a). In addition, similar REE patterns are also expressed in the nucleus and in the rim of the ooids analysed (Figure 10a).

The average ∑REE-Y values of Djebel Had (967 ppm), Aswan (631 ppm) (Baioumy et al., 2017), Djebel Ank (464 ppm) (Garnit et al., 2017), and Bakchar (399 ppm) (Rudmin et al., 2019) are all higher than the values of Aïn Babouche ironstone (242 ppm).

Figure 12 shows the patterns of REE values normalised against PAAS (Taylor and McLennan, 1985) of ooidal

ironstones of Aïn Babouche (Algeria), Djebel Had (Algeria, Diab et al., 2020), Djebel Ank (Tunisia, Garnit et al., 2017), Aswan (Egypt, Baioumy et al., 2017), and Bakchar (Siberia, Rudmin et al., 2019). Ironstones of Aïn Babouche have the same REE-Y signature as those of Djebel Ank and Aswan against PAAS. North African ooidal ironstones (Djebel Had, Djebel Ank, and Aswan) are slightly more enriched with heavy REE, unlike Bakchar ironstones, which are more enriched with light REE (Figure 10b). The North African ironstones also stand out from those of Bakchar by the presence of a positive cerium anomaly, which is absent in those of Bakchar.

Table 3. Aïn Babouche REE of ooidal ironstones determined by LA-ICP-MS analysis (values are the average of the measured points from the nucleus to the concentric layers for each sample)

	Djebel Dahar				Kef En Nsour			
Element (ppm)	STI04	DD01	DD06	STI01	ABW8	ABW9	ABW11	ABW12
La	23.59	33.39	9.37	22.13	34.05	18.81	23.72	10.52
Ce	93.13	101.60	29.92	92.77	109.22	61.46	174.43	34.15
Pr	7.58	8.90	3.63	7.54	11.54	6.11	9.66	4.18
Nd	29.83	34.64	14.74	30.10	49.37	24.79	43.94	16.64
Sm	6.99	7.94	4.67	7.77	12.30	6.52	11.34	5.03
Eu	1.95	1.97	1.42	2.11	3.34	1.79	3.16	1.51
Gd	8.75	7.60	5.86	8.52	14.70	8.04	12.17	7.06
Tb	1.63	1.33	1.21	1.68	2.41	1.24	2.18	1.30
Dy	10.78	8.26	7.70	11.38	16.52	9.32	12.32	9.05
Y	53.81	43.39	35.18	54.30	74.68	46.31	53.05	40.06
Ho	2.29	1.61	1.58	2.35	3.52	1.78	2.23	1.75
Er	7.26	5.65	4.41	6.59	9.79	5.52	6.56	5.35
Tm	1.06	0.84	0.77	1.06	1.32	0.84	0.94	0.83
Yb	7.11	6.28	4.78	6.80	9.15	5.66	6.12	5.59
Lu	1.01	0.85	0.75	0.94	1.24	0.75	0.86	0.64
∑REE-Y	256.77	264.25	104.99	256.06	353.13	198.94	362.68	143.67
LREE	171.82	196.04	58.01	170.95	234.51	127.53	278.42	79.09
HREE	84.95	68.21	46.97	85.11	118.62	71.42	84.26	64.58
Ce/Ce*	1.58	1.35	1.14	1.62	1.25	1.30	2.55	1.14
Eu/Eu*	1.16	1.18	1.27	1.21	1.16	1.16	1.26	1.18
Y/Y*	0.76	0.84	0.92	0.78	0.81	0.88	0.78	0.78
$Y_{(N)}/Ho_{(N)}$	0.87	1.00	0.83	0.85	0.78	0.97	0.88	0.85

The cerium anomaly Ce/Ce* = 2 $Ce_N/(La_N + Pr_N)$ was calculated according to De Baar et al. (1983). The europium anomaly was calculated as (Eu/Eu*) = $Eu_N/(Sm_N \times Gd_N)^{½}$ (Taylor and McLennan, 1985), and the yttrium anomaly as Y/Y* = $2Y_N/(Dy_N + Ho_N)$ (Fazio et al., 2007), where N is the normalised value. The ooidal ironstones of the Aïn Babouche deposit are characterised by a positive cerium anomaly for which Ce/Ce* varies from 1.14 to 2.55 and also a slight positive europium anomaly where Eu/Eu* is between 1.16 and 1.27. We note the presence of a slight negative yttrium anomaly where Y/Y* shows values between 0.76 and 0.92.

In the two discrimination diagrams of Bau et al., (2014) (Ce/Ce* vs Y_N/Ho_N) and (Ce/Ce* vs Nd), which are generally used for the discrimination between different genetic origins of ooidal ironstones, the samples from the iron ore of the Aïn Babouche deposit are plotted in the hydrogenous fields (Figure 13).

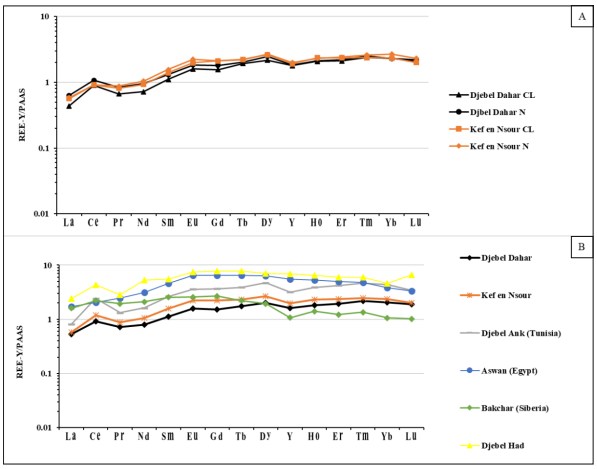

Figure 10. a) PAAS-normalized REE-Y of Aïn Babouche ooids nucleus and the concentric layers. **b)** PAAS-normalized REE-Y of Aïn Babouche iron ooids compared to Djebel Had deposit (Diab et al., 2020), Djebel Ank deposit (Garnit et al., 2017), Aswan deposit (Baioumy et al., 2017) and Bakchar deposit (Rudmin et al., 2019). Normalising factors inspired by Taylor and McLennan (1985).

4.3.4. Mineralogical and chemical variation in the ooids and their matrix

Maps of chemical element distribution (SEM-EDS) with punctual microanalyses are used in addition to EMPA analysis to confirm the microscopic observations of polished and thin sections. Iron is present in most of the ooids, granules, and some areas of the matrix (Figure 11c).

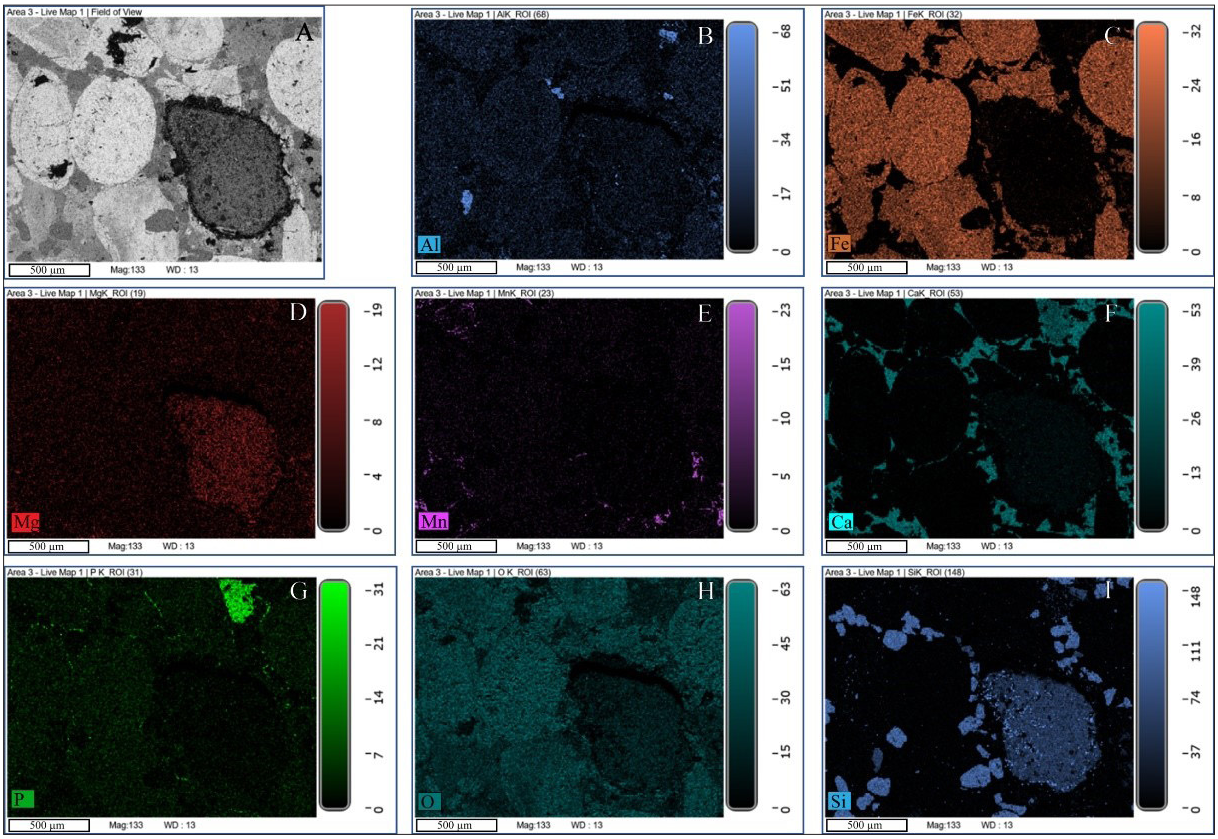

Figure 11. SEM-EDS maps of chemical element distribution

Al is particularly present in localised zones between oolitic grains, while Si is present only in quartz grains and in the grain to the right of Figure 10 a-i. The latter also contains an intermediate concentration of Mg and Al and is depleted in P and O (Figure 11b-d-g-h-i). Mn appears only in some small areas (Figure 11e). The concentration of P IS 0.9%. This element spreads across almost the entire area with low concentrations; however, in a small grain, it shows a high concentration (Figure 11g). Ca concentrations appear only in the matrix (Figure 11f).

5. Discussion

5.1. Petrography

The petrographic observation of Ain Babouche ooidal ironstones demonstrates the association of these iron ores with terrigenous and detrital minerals, including clay, quartz and apatite. This observation lends support to the hypothesis that the iron originated from a continental source. Sedimentary structures, such as metric cross-bedding, grading, and channelized facies, observed in the compact ooidal ironstones of Djebel Dahar (Figure 5b), argue for a relatively agitated shallow marine environment (e.g., Mutrux et al., 2008). This assertion is further substantiated by the observed correlation between the nucleus and the rim of the ooids, with the preponderance of α-type laminations (Figure 6a), suggesting that these ooids have formed in an agitated marine environment (Purser, 1980). In revanche, the β-type ooid is present in small quantities (Figure 6c), indicating formation in sheltered marine environments and non-marine caves (Purser, 1980). The nuclei of ooids are typically rounded, as Figure 6c shows, a consequence of multiple stages of reworking, and the majority of ooids exhibit a spherical to ellipsoidal shape, a result of the combined effects of accretion and corrosion (Scholle & Ulmer, 2003). Oblique cracks, parallel to the layers of the rim, are probably the result of compaction and retraction of ooids. The fragmented oolites indicate intense reworking and attest to an intensely agitated coastal palaeomilieu (Keddar, 1985). The presence of ooid fragments, sometimes constituting the nucleus of new ooids in the ironstones of Aïn Babouche, indicates intense reworking and serves as evidence of a shallow, intertidal, agitated environment. The angular shape of these fragments indicates that ooids have not been subjected to prolonged transportation.

Moreover, hydrothermal ooidal ironstones deposits are characterised by the presence of sulfide minerals, such as pyrite, chalcopyrite, sphalerite, galena, along with barite (Rudmin et al., 2019). Interestingly, our mineralogical examination reveals the absence of these minerals in the Ain Babouche ooidal ironstone, which allows us to distinguish it from hydrothermal ooidal ironstone deposits, as well as the metasomatic iron deposits of Ouenza and Boukhadra, located 100 km further north of Tebessa. The latter, as determined through stable isotope analysis and fluid inclusions (Bouzenoune et al., 1997; Bouzenoune et al., 2006;

Ait Abdelouahab et al., 2011; Bouzenoune, 2022), originate from the conversion of carbonate host rocks into iron ore, occurring at approximately 120 °C, with mineralising fluid salinities around 22% equivalent NaCl.

5.2. Geochemistry

In the Si-Al discrimination diagram of Choi and Hariya (1992) (Figure 12a), the Aïn Babouche iron ooids samples plot within the hydrogenous field, which is quite similar to Djebel Ank (Tunisia), Djebel Had (Algeria), and the Aswan deposit (Egypt), indicative of the same origin and formation process. This similarity is well supported in the diagram of Nicholson (1992) (Figure 12b), where all the Ain Babouche ironstone samples fall within the field of hydrogenous origin ores.

The strong positive correlation between CaO and P_2O_5 (i.e. 0.98), indicates that they originate from the same mineral phase, most likely apatite, which was also identified using SEM observations and elemental analyses (Figures 6f, 9a, and 10g). Moreover, the positive correlation between SiO_2 and Al_2O_3 confirms the presence of clay.

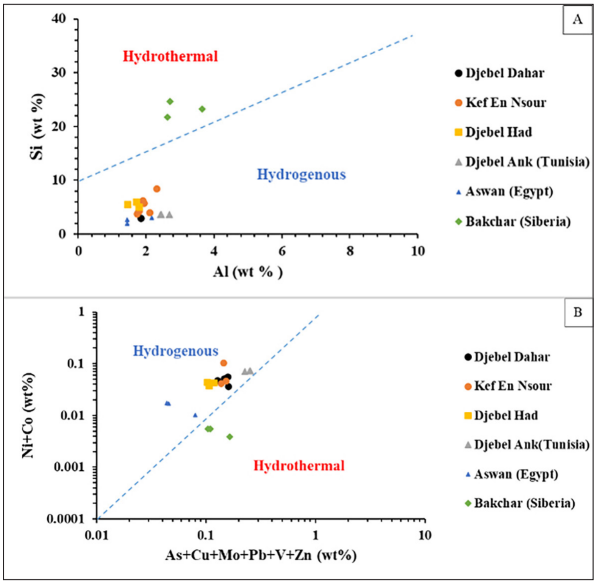

Figure 12. Cross plots between **a)** Si and Al by Choi and Hariya (1992); **b)** (Ni + Co) and (As + Cu + Mo + Pb + V + Zn) (Nicholson, 1992). Aïn Babouche values are compared to Djebel Had deposit (Diab et al., 2020), Djebel Ank deposit (Garnit et al., 2017), Aswan deposit (Baioumy et al., 2017) and Bakchar deposit (Rudmin et al., 2019)

Plotting the REEs in the two discrimination diagrams of Bau et al. (2014): Ce/Ce* vs. Nd and Ce/Ce* vs. YN/HoN (Figure 13a-b) reflects the hydrogenous origin of the iron in the studied deposits. The average value of the total REE+Y of 19 points analysed in the nucleus (244 ppm) is almost equivalent to the points in the concentric layers (221 ppm), suggesting no significant geochemical difference between the two mineralogical phases from which the nucleus is composed. In both cases, these phases consist of goethite. This similarity in composition is indicative of the identical genesis conditions of the ironstones on the two flanks of the syncline and also reflects the same origin for the two minerals (goethite) that constitute the nucleus and the cortex of the ooids.

Redox reactions likely control variations in cerium as Ce has two oxidation states, Ce^{3+} and Ce^{4+}. However, Ce^{4+} is almost never present in aqueous solutions unless strongly complexed in oxidising conditions (De Baar et al., 1983). The positive cerium anomaly and the negative yttrium anomaly in the ooidal ironstones of Aïn Babouche argue for environmental conditions rich in oxygen that prevailed in the Eocene Sea in which they were deposited. Under such oxidizing conditions, Ce^{3+} oxidizes and transforms into Ce^{4+}, which precipitates by being incorporated into different minerals such as the goethite ooids. It is important to acknowledge that the majority of authors who examined the ooidal ironstones of North Africa obtained analogous results and adopted the same interpretations (Salama et al., 2012; Garnit et al., 2017; Diab et al., 2020).

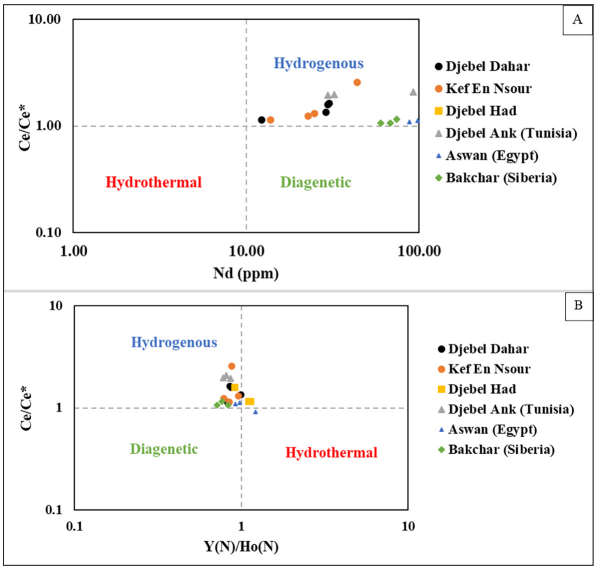

Figure 13. a) Ce/Ce* vs Nd discrimination diagrams. **b)** Ce/Ce* vs Y(N)/Ho(N) discrimination diagrams Bau et al., (2014). Aïn Babouche values are compared to Djebel Had deposit (Diab et al., 2020), Djebel Ank deposit (Garnit et al., 2017), Aswan deposit (Baioumy et al., 2017) and Bakchar deposit (Rudmin et al., 2019)

The study of Ain Babouche ooidal ores using SEM revealed that ooids are devoid of any discernible precursor carbonate or clay minerals, suggesting that goethite formation is not attributable to replacement processes. Furthermore, observations indicated that calcite was exclusively present as cement between the ooids and the granules, with no indication of replacement by iron-bearing minerals (Figure 6d). The presence of Al is particularly evident in localised zones between oolitic grains, suggesting the possibility of clay minerals. Conversely, Si is present only in quartz grains and in the grain located to the right of Figure 10a. The observed concentrations of Mg and Al in certain grains indicate the presence of clay minerals (Figure 11b-d-g-h-i). These findings collectively support the hypothesis of a continental source of iron, characterised by terrigenous and detrital minerals. The presence of Mn is only observed in specific areas, which may be indicative of rare grains of manganese minerals such as cryptomelane and psilomelane, as reported by Diab et al. (2020) in the Aïn Babouche deposit and by Garnit et al. (2017) in the Djebel Ank deposit (Figure 11e). The presence of elevated phosphorus concentrations in small grains is indicative of apatite (Figure 11g).

5.3. Depositional environment

The depositional environment of the North African Eocene ooidal ironstones is believed to be a shallow intertidal setting. This interpretation is mainly supported by the presence of sedimentary structures such as cross-bedding, the size and shape of grains, and petrographic features such as the presence of authigenic minerals (El Aref et al., 2006a; Salama et al., 2012; Garnit et al., 2017; Diab et al., 2020), and the presence of some microbial structures that develop in calm water conditions (El Aref et al., 2006b).

The border region between Algeria and Tunisia is situated on an epineritic platform, where the island of Kasserine developed from the late Cretaceous to the Miocene (Chabou-Mostefai et al., 1978; Zaïer et al., 1998). Significant phosphorite deposits, currently being exploited in Algeria and Tunisia, were formed around this island during the late Palaeocene to Early Eocene in a shallow intertidal depositional environment (Kechiched et al., 2016; Dassamiour et al., 2021). The Eocene ironstone deposits of Aïn Babouche (Algeria) and Djebel Ank (Tunisia) were formed under these palaeogeographic conditions. They are located to the west and south of the island, respectively. The high phosphate contents in the ironstones at Aïn Babouche likely originate from nearby phosphorite deposits situated approximately 50 km to the southeast (Djebel Onk phosphate deposits) and northeast (Kouif and Djebel Dyr phosphate deposits) of the Aïn Babouche ironstone deposit.

The presence of sedimentary structures such as metric cross-bedding and channelized facies indicates a marine environment that was likely to be shallow and agitated. The presence of laminations (alpha type with some beta type) indicates agitation, as do spherical to ellipsoidal shapes (due to accretion/corrosion). Ooid fragments sometimes form the nucleus of new ooids, showing intense reworking and confirming a shallow, agitated intertidal environment.

5.4. Source of iron

In the genetic models employed in the studies that addressed the Cenozoic ooidal iron deposits, three primary sources of iron were suggested: a continental source by alteration of pre-existing rocks, a hydrothermal source involving iron-rich fluids, and a mixed source with continental weathering and hydrothermal contribution (Young, 1989; Salama et al., 2012; Baioumy et al., 2017; Garnit et al., 2017; Rudmin et al., 2019; Diab et al., 2020).

The most common conclusion of previous studies is that the continental source is the most probable. For the Djebel Ank ironstone deposit, Garnit et al., (2017) posit a continental source for several reasons, including the relatively high content of phosphorus (up to 2%) and the low TiO_2/Al_2O_3 ratio (0.2–0.3). The authors considered that phosphorus and iron are usually believed to be transported to the basin of deposition after being leached from a continental source. Similarly, at the Djebel Had deposits, Diab et al. (2020) believe that iron is leached from the adjacent metasomatic continental formations associated with diapirism. However, they do not give any information on these metasomatic rocks. The authors approve their conclusion on indirect arguments, including mineralogical evidence, such as the presence of piemontite and pyrochlore in the ironstones, and geochemical evidence, such as the abundance of As, Zn, and Ag and the low content of Eu, which rules out a hydrothermal source of iron.

Many studies have considered a hydrothermal source of the iron of the ooidal ironstones (Villain, 1902; Schweigart, 1965; Kimberley, 1989; Rudmin et al., 2019). This hypothesis suggests that the precipitation of iron occurs from Fe-rich fluid flux or hydrothermal fluid with or without the intervention of volcanic events. The main arguments used to support this hypothesis include the concentrations of trace elements such as Pb, Cu, Zn, As, Bi, Ti, Cr, Mo, Li, and B that concentrate only in hydrothermal fluids (Schweigart, 1965); REE such as positive anomalies of Eu; and some mineralogical evidence, such as the presence of authigenic minerals. In contrast, several authors (Salama et al., 2012; Baioumy et al., 2017; Garnit et al., 2017) consider a hydrogenous source of iron based on trace elements and REE discrimination diagrams. The dehydration and crystallization of this gel yields iron hydroxide. In the case of ironstones from the Aïn Babouche deposit, and with reference to the results obtained in this study, it would appear that most of the results, and in particular the geochemical data, point to a hydrogenous origin for the ores from this deposit. Moreover, a mixed source of iron has been proposed by Baiyoumi et al. (2014) and Rudmin et al. (2019), combining hydrothermal and continental sources.

The hypothesis of a continental source for the iron in the ores from the Aïn Babouche deposit is supported by the deposition of ooids in a shallow, agitated marine environment near continental margins, alongside the association of these iron ores with terrigenous and detrital minerals, including clay and quartz, in addition to their geochemical characteristics. However, the palaeogeography of the Eocene period does not allow us to identify any rocks likely to have supplied, through supergene alteration, such large quantities of iron as would be required to form a deposit of around 10 million tonnes, such as that at Aïn Babouche.

On the other hand, the mobilization of iron from ante-Eocene sedimentary series, dominated by clay and marl by relatively saline hydrothermal fluids and its introduction into the marine environment, remains plausible. The Hamimat Guibeur and Hamimat Meskouta diapirs, located respectively to the northwest and southeast of the Aïn Babouche deposit (Figure 2), would play a significant role in providing the heat and salinity, enabling the basinal fluids to acquire the capacity to dissolve the iron contained in the ante-Eocene sedimentary series and creating a favourable geo-tectonic context for the circulation of hydrothermal fluids (Bouzenoune et al., 1995; Bouzenoune, 2024). It is also interesting to note that the structure of the Aïn Babouche deposit is strongly compartmentalised by tectonic accidents in an NW–SE direction (Figure 4) and that the three main outcrops of diapiric Triassic evaporites are aligned along one of these strike-slip tectonic accidents with a sinistral component (Draa Foum Debbane strike-slip fault, Figure 4). This accident was also considered as a portion of a long

lineament (Gafsa fault or Khenchela–Tripolitania lineament) along which the deposits of Aïn Babouche and Djebel Ank are located, as well as other deposits (Nicolini, 1967; Vila, 1992).

5.5. Formation of ooidal ironstones

The formation of the iron ooids that constitute ironstone-type deposits has been the subject of numerous scientific studies, and various mechanisms have been proposed to explain the genesis of these ooids (Sorby, 1856; Hemingway, 1974; Kimberley, 1979; Van Houten and Purucker, 1984; Harder, 1989; Siehl and Thein, 1989; El Aref et al., 2006b; Salama et al., 2012; Garnit et al., 2017; Rudmin et al., 2019). One of the most frequently invoked mechanisms is that proposed by Sorby (1856), which stipulates the transformation of carbonate ooids into iron ooids following the percolation of iron-rich fluids into the surrounding rocks. This mechanism has also been used to explain the genesis of the ooids in the Djebel Had deposit, which is part of the Aïn Babouche deposit (Diab et al., 2020). The results obtained from the study of the Kef en Nsour and Djebel Dahar ores showed that calcite was observed only as a cement between the ooids and granules, with no trace of possible replacement by iron-bearing minerals (Figure 6d). In addition, SEM observation of the ooids showed no trace of any precursor carbonate or clay minerals at the expense of the goethite that may have been formed by replacement. Microchemical analyses of the ooids showed relatively low Ca and Al contents (average of 0.26 wt % and 1.65 wt %, respectively), reflecting the absence of carbonate or clay minerals together with the non-existence of calcareous ooids in the surrounding area indicative of possible precursors replaced by goethite.

The spherical shape of ooids is a result of the combined effect of accretion and corrosion, in addition to the presence of ooid cracks, ooid fragments, and rounded nuclei, which are characteristics of multiple stages of reworking. The concentric laminae provide support for accretionary growth. Furthermore, the existence of modern analogue like the ongoing formation of iron ooids on the island of Panarea in Italy (Di Bella et al., 2019) and the unconsolidated submarine deposit of iron ooids and pisoids on the volcanic island of Mahengetang, Indonesia (Heikoop et al., 1996), can provide physical evidence of the chemical precipitation of iron around seafloor particles and that can be observed almost in real time.

In summary, Whether the source of the iron is continental, hydrothermal, or mixed, once introduced into the marine environment, the iron undergoes oxidation from the soluble and mobile ferrous state (Fe^{2+}) to the ferric state (Fe^{3+}), leading to precipitation. Oxidising conditions, expressed by the positive cerium anomaly, result from exchanges between the atmosphere and marine waters, producing an increase in the quantity of dissolved oxygen and, consequently, the oxidation of Fe^{2+} to Fe^{3+} and its precipitation in the form of a ferrihydrite gel. In the case of the introduction of bivalent iron (Fe^{2+}) dissolved in the marine environment in the form of $FeCl_2$ from basinal brines and continental supplies, the iron hydroxide gel (ferrihydrite) that precipitates following the oxidation of the bivalent iron is transformed into much more stable phases such as goethite and hematite (Pedersen et al., 2005; Benderev et al., 2022). The stable goethite precipitate directly around seafloor particles in a shallow, agitated marine environment.

6. Conclusion

This study investigates the petrographic, mineralogical, and geochemical characteristics of the ooidal ores of the Aïn Babouche deposit. The following conclusions arise:

Sedimentary structures such as cross-bedding, grading, and channelized facies, as well as the fragmented state of the ooids whose fragments constitute the nuclei of other, more recent ooids, argue for a shallow and relatively agitated marine environment. The geochemistry of the major elements and the trace elements in the ironstones indicates the hydrogenous origin of the iron. Two potential sources of iron have been suggested. The iron could be leached from a continental source, or the iron could come from basinal brines. A mixed source is also plausible.

The genesis of the ooids of Aïn Babouche was eceded by the saturation of iron in water, which was achieved by the fluvial flow of continental origin and/or by leaching of the ante-Eocene series by basinal brines. Subsequently, iron (Fe^{2+}) oxidizes and precipitates as a low-crystalline ferrihydrite gel, which is transformed by oxidation into more stable phases that precipitate around solid particles in a shallow, agitated marine environment.

References

Ait Abdelouahab, Dj., Bouzenoune, A., Préat, A. (2011). Les isotopes stables du carbone et de l'oxygène des carbonates (calcaires et sidérites) du gisement de fer de Boukhadra (Algérie nord orientale). Bulletin du Service Géologique National 22 : 381-395.

Baioumy, H., Omran, M., Fabritius, T. (2017). Mineralogy, geochemistry and the origin of high-phosphorus oolitic iron ores of Aswan, Egypt. Ore Geology Reviews 80: 185-199. https://doi.org/10.1016/j.oregeorev.2016.06.030

Bau, M., Schmidt, K., Koschinsky, A., Hein, J., Kuhn, T., Usui, A. (2014). Discriminating between different genetic types of marine ferro-manganese crusts and nodules based on rare earth elements and yttrium. Chemical Geology 381: 1-9. https://doi.org/10.1016/j.chemgeo.2014.05.004

Benderev, A., Trayanova, M., Tarassov, M., Tarassova, E. (2022). Conditions and processes of precipitation of iron compounds upon discharge of high-mineralised artesian water from artesian borehole R-30, Staro Oryahovo, Bulgaria. Environ Geochem Health 44: 2235-2251.https://doi.org/10.1007/s10653-021-01107-6

Bhattacharya, D.P., Kakimoto, P.K. (1982). Origin of ferriferous ooids: an SEM study of ironstone ooids and bauxite pisoids. Journal of Sedimentary Petrology 52: 849-857.

Bouzenoune, A., Rouvier, H., Thibieroz, J. (1995). Trias de l'Ouenza : context diapirique, zonation minéralogique et conséquences métallogéniques. Bulletin du Service Géologique de l'Algérie 6 : 3-24.

Bouzenoune, A., Rouvier, H., Thibieroz, J. (2006). Chronologie relative et conditions de mise en place des minéralisations du massif de l'Ouenza (Algérie NE). Bulletin du Service Géologique de lɔAlgérie 17 : 3-27.

Bouzenoune, A. (2022) Salt Tectonics and Mineralization Processes in NE Algeria. In: Meghraoui, M., Sundararajan, N.,

Banerjee, S., et al. (Eds.), Advances in Geophysics, Tectonics and Petroleum Geosciences. Springer International Publishing, Cham, pp. 623–626 https://doi.org/10.1007/978-3-030-73026-0_138

Bouzenoune, A. (2024). Petrographic and Geochemical Particularities of the NE Algerian Salt Domes and Associated «Cap-Rocks,» in: Khomsi, S., Bezzeghoud, M., Banerjee, S., Eshagh, M., Benim, A.C., Merkel, B., Kallel, A., Panda, S., Chenchouni, H., Grab, S., Barbieri, M. (Eds.), Selected Studies in Geophysics, Tectonics and Petroleum Geosciences, Advances in Science, Technology & Innovation. Springer Nature Switzerland, Cham, pp. 205–208. https://doi.org/10.1007/978-3-031-43807-3_43

Bouzenoune, A., Lécolle, P. (1997). Petrographic and geochemical arguments for hydrothermal formation of the Ouenza siderite deposit (NE Algeria). Mineralium Deposita 32 : 189-196. https://doi.org/10.1007/s001260050084

Burkhalter, R.M. (1995) Ooidal ironstones and ferruginous microbialites: origin and relation to sequence stratigraphy (Aalenian and Bajocian, Swiss Jura mountains). Sedimentology 42 : 57-74.

Chabou-Mostefai, S., Devolve, J.J., Fuchs, Y., Menant, G., Reviere, M. (1978). Sur les niveaux à célestite de Tunisie centrale et du Sud-constantinois. Sciences de la Terre 22 : 291-300.

Choi, J.H., Hariya, Y. (1992). Geochemistry and depositional environment of Mn oxide deposits in the Tokoro Belt, northeastern Hokkaido, Japan. Economic Geology 87: 1265-1274. https://doi.org/10.2113/gsecongeo.87.5.1265

Dahanayake, K., Gerdes, G., Krumbein, W.E. (1985). Stromatolites, oncolites and oolites biogenically formed in situ. Naturwissenschaften 72: 513-518.

Dassamiour, M., Mezghache, H., Raji, O., Bodinier, J.-L. (2021). Depositional environment of the Kef Essennoun phosphorites (northeastern Algeria) as revealed by P2O5 modeling and sedimentary data. Arabian Journal of Geosciences 14: 1-17. https://doi.org/10.1007/s12517-021-07400-z

De Baar, H.J.W., Bacon, M.P., Brewer, P.G. (1983). Rare-earth distributions with a positive Ce anomaly in the Western North Atlantic Ocean. Nature 301 : 324-327. https://doi.org/10.1038/301324a0

Di Bella, M., Sabatino, G., Quartieri, S., Ferretti, A., Cavalazzi, B., Barbieri, R., Foucher, F., Messori, F., Italiano, F. (2019). Modern Iron Ooids of Hydrothermal Origin as a Proxy for Ancient Deposits. Scientific Reports 9, 7107. https://doi.org/10.1038/s41598-019-43181-y

Diab, H., Chouabbi, A., Chi Fru, E., Nacer, J.-E., Krekeler, M. (2020). Mechanism of formation, mineralogy and geochemistry of the ooidal ironstone of Djebel Had, northeast Algeria. Journal of African Earth Sciences 162: 103736. https://doi.org/10.1016/j.jafrearsci.2019.103736

Dubourdieu, G. (1956). Etude Géologique de la Région de l'Ouenza (Confins Algéro-Tunisiens). Paris University, France.

Durand-Delga, M. and Fontboté, J.M. (1980). Le cadre structural de la Méditerranée occidentale. In: Aubouin, J., Debelmas, J., and Latreille, M. (Eds.), Géologie des chaînes alpines issues de la Téthys, Colloque No. 5, 26th International Geological Congress, Paris, Mémoires du Bureau de Recherches Géologiques et Minières 115: 67-85.

El Aref, M.M., El Sharkawi, M.A., Khalil, M.A. (1999). Geology and genesis of the strata-bound and Stratiform Cretaceous–Eocene iron ore deposits of the Bahariya region,Western Desert, Egypt. GAW 4th Int. Conf., Cairo Univ., Egypt, pp. 450-475.

El Aref, M.M., Mesaed, A.A., Khalil, M.A., Salama, W.S. (2006a). Stratigraphic setting, facies analyses and depositional environments of the Eocene ironstones of Gabal Ghorabi mine area, El Bahariya Depression, Western Desert, Egypt. Egyptian Journal of Geology 50: 29-57.

El Aref, M.M., Mesaed, A.A., Khalil, M.A., Salama, W.S. (2006b). Microbialite morphostructures and biogenic accretion mechanism of the Eocene ironstones of Gabal Ghorabi mine area, El Bahariya Depression, western Desert, Egypt. Egyptian Journal of Geology 50: 59-81.

Etheve, N., de Lamotte, DF., Mohn, G., Martos, R., Roca, E., Blanpied, C. (2016). Extensional vs. contractional Cenozoic deformation in Ibiza (Balearic Promontory, Spain): integration in the West Mediterranean back-arc setting. Tectonophysics 682: 35–55.

Fazio, A.M., Scasso, R.A., Castro, L.N., Carey, S. (2007). Geochemistry of rare earth elements in early-diagenetic miocene phosphatic concretions of Patagonia, Argentina: Phosphogenetic implications. Deep Sea Research Part II 54: 1414-1432. https://doi.org/10.1016/j.dsr2.2007.04.013

Garnit, H., Bouhlel, S. (2017). Petrography, mineralogy and geochemistry of the Late Eocene oolitic ironstones of the Jebel Ank, Southern Tunisian Atlas. Ore Geology Reviews 84: 134-153. https://doi.org/10.1016/j.oregeorev.2016.12.026

Griffin, W.L., Powell, W.J., Pearson, N.J., O›Reilly, S.Y. (2008). GLITTER: data reduction software for laser ablation ICP-MS: laser Ablation-ICP-MS in the earth sciences. Mineralogical Association of Canada Short Course Services 40: 204-207.

Gross, G.A. (1965). Geology of iron deposits in Canada, V 1., Geological Survey of Canada, Canada.

Hallimond, A.F. (1951). Problems of the Sedimentary Iron Ores. Proceedings of the Yorkshire Geological Society 28: 61-66.

Harder, H. (1989). Mineral genesis in ironstones: a model based upon laboratory experiments and petrographic observations. Geological Society, London, Special Publications 46: 9-18. https://doi.org/10.1144/GSL.SP.1989.046.01.04

Hemingway, J.E. (1974). Jurassic, in: The Geology and Mineral Resources of Yorkshire, edited by Raynor, D.H., Hemingway, J.E. Yorkshire Geological Society, London. pp.161-223.

Heikoop, J.M., Tsujita, C.J., Risk, M.J., Tomascik, T., Mah, A.J. (1996). Modern iron ooids from a shallow-marine volcanic setting: Mahengetang, Indonesia. Geology 24: 759. https://doi.org/10.1130/0091-7613(1996)024<0759:MIOFAS>2.3.CO;2

Jochum, K.P., Weis, U., Stoll, B., Kuzmin, D., Yang, Q., Raczek, I., Jacob, D.E., Stracke, A., Birbaum, K., Frick, D.A., Günther, D., Enzweiler, J. (2011). Determination of Reference Values for NIST SRM 610–617 Glasses Following ISO Guidelines. Geostandard Geoanalytic Research 35: 397-429. https://doi.org/10.1111/j.1751-908X.2011.00120.x

Kearsley, A.T. (1989). Iron-rich ooids, their mineralogy and microfabric: clues to their origin and evolution. Geological Society, London, Special Publications 46: 141-164. https://doi.org/10.1144/GSL.SP.1989.046.01.14

Kechiched, R., Laouar, R., Bruguier, O., Laouar-Salmi, S., Ameur-Zaimeche, O., Foufou, A. (2016). Preliminary Data of REE in Algerian Phosphorites: A Comparative Study and Paleo-redox Insights. Procedia Engineering 138: 19-29. https://doi.org/10.1016/j.proeng.2016.02.048

Keddar, B. (1985). Etude géologique et gitologique de l›indice de fer oolithique d›Aïn Babouche (Chéria, W. de Tébessa). M.Sc. Thesis, Université des Sciences et de la Technologie Houari Boumedienne, Alger.

Kimberley, M.M. (1979). Origin of oolitic iron formations. Journal of Sedimentary Petrology 49: 111-131. https://doi.org/10.1306/212F76D0-2B24-11D7-8648000102C1865D.

Kimberley, M.M. (1989). Exhalative origins of iron formations. Ore Geology Reviews 5: 13-145. https://doi.org/10.1016/0169-1368(89)90003-6

McGregor, F., Ramanaidou, E., Wells, M. (2010). Phanerozoic ooidal ironstone deposits – generation of potential exploration targets. Applied Earth Science 119: 60-64. https://doi.org/10.1179/037174510X12853354810660

Mutrux, J., Maher, H., Shuster, R., & Hays, T. (2008). Iron ooid beds of the Carolinefjellet Formation, Spitsbergen, Norway. Polar Research, 27(1), 28–43. doi:10.1111/j.1751-8369.2007.00039.x.

Nicholson, K. (1992). Contrasting mineralogical-geochemical signatures of manganese oxides; guides to metallogenesis. Economic Geology 87: 1253-1264. https://doi.org/10.2113/gsecongeo.87.5.1253

Nicolini, P. (1967). Remarques comparatives sur quelques éléments sédimentologiques et paléogéographiques liés aux gisements de fer oolithiques du Djebel Ank (Tunisie) et de Lorraine (France). Mineral. Deposita 2: 95-101. https://doi.org/10.1007/BF00206582

Pedersen, H.D., Postma, D., Jakobsen, R., Larsen, O. (2005). Fast transformation of iron oxyhydroxides by the catalytic action of aqueous Fe(II). Geochimica et Cosmochimica Acta 69: 3967-3977. https://doi.org/10.1016/j.gca.2005.03.016

Petranek, J., van Houten, F.B. (1997). Phanerozoic ooidal ironstones. Czech Geological Survey 7: 1-71.

Purser, B.H. (1980). Sédimentation et diagenèse des carbonates néritiques récents. Les éléments de la sédimentation et de la diagenèse. Tome 1., Editions technip, Paris.

Rudmin, M., Mazurov, A., Banerjee, S. (2019). Origin of ooidal ironstones in relation to warming events: Cretaceous-Eocene Bakchar deposit, southeast Western Siberia. Marine and Petroleum Geology 100: 309-325. https://doi.org/10.1016/j.marpetgeo.2018.11.023

Salama, W., El Aref, M.M. and Gaupp, R. (2013) Mineral evolution and processes of ferruginous microbialite accretion – an example from the Middle Eocene stromatolitic and ooidal ironstones of the Bahariya Depression, Western Desert, Egypt. Geobiology 11: 15-28. https://doi.org/10.1111/gbi.12011

Salama, W., El Aref, M., Gaupp, R. (2012). Mineralogical and geochemical investigations of the Middle Eocene ironstones, El Bahariya Depression, Western Desert, Egypt. Gondwana Research 22: 717-736. https://doi.org/10.1016/j.gr.2011.11.011

Salama, W., El Aref, M., Gaupp, R. (2014). Facies analysis and palaeoclimatic significance of ironstones formed during the Eocene greenhouse. Sedimentology 61: 1594-1624. https://doi.org/10.1111/sed.12106

Scholle, P.A. & Ulmer-Scholle, D.S. (2003). GRAINS: Non-skeletal Grains: Ooids, Pisoids, and Other Coated Grains. In: A Color Guide to the Petrography of Carbonate Rocks: Grains, textures, porosity, diagenesis. AAPG Memoir 77. https://doi.org/10.1306/M77973

Schweigart, H. (1965). Genesis of the iron ores of the Pretoria series, South Africa. Economic Geology 60: 269-298. https://doi.org/10.2113/gsecongeo.60.2.269

Siehl, A., Thein, J. (1989). Minette-type ironstones. Geological Society, London, Special Publications 46 : 175-193. https://doi.org/10.1144/GSL.SP.1989.046.01.16

Sonarem-Rudis. (1968). Recherches géologiques à Ain Babouche (Gisement de fer) effectuées en 1968. Sonarem, Algiers.

Sorby, H.C. (1849). On the Origin of the Cleveland Hill Ironstone. PYGS 3: 457-461. https://doi.org/10.1144/pygs.3.457

Taylor, S.R., McLennan, S.M. (1985). The Continental Crust: its Composition and Evolution. Blackwell Scientific Publications, Oxford.

Van Houten, F.B., Purucker, M.E. (1984). Glauconitic peloids and chamositic ooids - favorable factors, constraints, and problems. Earth-Science Reviews 20 : 211-243. https://doi.org/10.1016/0012-8252(84)90002-3

Vila, J.M. (1992). Carte géologique de l›Algérie à 1/50 000, feuille n° 265, Aïn Télidjène avec notice détaillée. Publication du Service de la Carte Géologique de l'Algérie, Boumerdes, Algeria 27pp.

Villain, F. (1902). Le gisement de minerai de fer oolithique de la Lorraine. Dunod, Paris.

Young, T.P. (1989). Phanerozoic ironstones: an introduction and review. Geological Society, London, Special Publications 46:9-25. https://doi.org/10.1144/GSL.SP.1989.046.01.02

Zaïer, A., Beji-Sassi, A., Sassi, S., Moody, R.T.J. (1998). Basin evolution and deposition during the Early Paleogene in Tunisia. Geological Society, London, Special Publications 132, 375–393. https://doi.org/10.1144/GSL.SP.1998.132.01.21

JJEES

JJEES (2025) 16 (4): 365-390
ISSN 1995-6681

Jordan Journal of Earth and Environmental Sciences

Spatiotemporal Dynamics in selected Physicochemical Properties, Metals, and Total petroleum hydrocarbons contents in Crude oil impacted Soil in Part of the Niger Delta Region of Nigeria

Grace E Obi-Iyeke*

Department of Botany, Delta State University, Abraka, Nigeria

Received on January 12, 2025, Accepted on May 6, 2025

Abstract

The Niger Delta of Nigeria has witnessed several oil spillages arising from oil production and transportation and oil pipeline vandalism. These activities might have caused continuous and remarkable changes in the structure and function of the ecosystem with resultant environmental impacts. Thus, this study aims to evaluate the spatio-temporal and seasonal changes in some physicochemical properties, metals, and total petroleum hydrocarbons contents in crude oil contaminated soils in part of the Niger Delta of Nigeria. Soil samples were collected from seven locations at a crude oil spillage site in Amukpe. Soil samples were analysed using standard chemical methods. The order of mean concentrations of the heavy metals in mg kg^{-1} in the soil samples for dry seasons in descending orders were Fe (981) > Zn (270) > Pb (>74.1) > Mn (58.71) > Cu (48.2) > Cr (21.83) > Ni (12.6) > V (3.3) > Cd (0.41) > (0.04), and those of the wet season were Fe (1017) > Zn (230) > Pb (69.9) > Mn (51.6) > Cu (43) > Cr (19) > Ni (10.7) > Cd (0.83) > As (0.31). The concentrations of metals in this study were higher than their respective FAO/WHO permissible limits. Heavy metal enrichment factors follow the order Pb>Cd>Zn>Cu>Cr>Ni>Mn>As>V. The enrichment factor (EF) of Pb, Cu, Cd, Zn, and Cr were greater than 10 indicating anthropogenic origin. The result of correlation and principal component analysis indicates that there was a strong positive correlation between TPH and metals which indicate that TPH and metals from the same anthropogenic source, such as oil spillage and associated activities.The clean-up of the impacted site is recommended in order to restore the soil's fertility for productive agricultural activities which are the major source of economic survival of the inhabitants in the study area.

Keywords: *Amukpe; Contamination; Geoaccumulation index; Enrichment factor; Pollution load index*

1. Introduction

The most visible activities in Nigeria's Niger Delta are oil exploration and exploitation, which are accompanied by a growing problem with oil contamination (Ogri, 2001). According to Yakubu (2007), oil pollution can have catastrophic effects, which is why Nigeria has seen several oil blowout disasters. Such blowouts and pipeline leakages have all resulted in pollution of land, freshwater swamps and the marine environment (Nwachukwu et al., 2010). Currently, there are eleven oil Corporations operating approximately 159 oil fields and 1,481 oil wells in the Niger Delta region of Nigeria (Wegwu et al., 2011). According to available data, the Niger Delta region of Nigeria is more susceptible to oil spills than any other place in the world, with an average of 273 oil spills occurringbetween 1983 and 2005, resulting in around 115,000 barrels of crude oil valued at US$5.64 million annually (Agbogidi et al., 2009). Some notable recent oil spills recorded in Nigeria include Assa-Rumekpe pipeline at Elele Alumini (2014), Nkpoku-Bomu pipeline at Ekporo (2014), Nembe creek pipeline at Elem-Kalabari (2014), Bomu-Bonny pipeline at Dere (2013), Amukpe trunk line at Amukpe (2011), and Nun-river Kolo creek at Oporoma (2013) (Shell Petroleum Development Company (SPDC), 2014). It appears that the amount of attention paid to oil spills on a global scale varies significantly depending on where they occur. For example, the 1989 Exxon Valdez oil spill (260,000 barrels) is highly referenced, likely because it happened in the United States. Still, there are many spills in developing nations that are larger, based on volume spilled and sensitivity of impact, than the aforementioned Exxon Valdez oil spill, but they are rarely used as benchmarks. Given that their regular sources of sustainable livelihoods—farming and fishing—are constantly disrupted, these spills and other environmental hazards related to the region's oil production have a significant impact on residents' fundamental right to exist (Agbogidi et al., 2009). Crude oil inundates the soil, a key component of agricultural productivity and a significant source of income for the communities that produce it, when it is accidentally released onshore for a variety of reasons, such as malfunctioning production machinery, operational errors, or deliberate damage to production facilities (Nkwocha and Duru, 2010; Yakubu, 2007; Odjuvwuederhie et al., 2006). Available records indicate that there is inadequate data to formulate or implement appropriate policies to manage some of the challenges of oil spillage, as most towns affected by crude oil spillage have not received any notable attention

* Corresponding author e-mail: ekyobiiyeke@gmail.com

(Osuji et al., 2004; NEST, 1991). One such area is Amukpe, in Sapele Local Government Area of Delta State, the host community of Shell BP's oil well No. 25. This area has witnessed several oil spillages arising from oil production and transportation, as well as oil pipeline vandalism (SPDC, 2014). These activities have caused continuous and remarkable changes in the structure and function of the ecosystem with resultant environmental impacts. The desire to provide information on the effects of oil spillage on soil, food crops, and plant diversity in Amukpe becomes imperative, as their environment and socio-economic life have been threatened by the impact of the spillage. Thus, the aim of this study is to investigate the spatiotemporal dynamics of some physicochemical properties, metals and total petroleum hydrocarbons contents in crude oil- impacted soils from Amukpe in the Niger Delta of Nigeria.

2. Materials and Methods

2.1 Description of Study Area

The study area is Amukpe, located within Longitude E 5° '42' 55.76"and Latitude N 5° 51'38.75"with elevation above sea level being 11meters. The area has a tropical equatorial climate. The area has an average annual rainfall of 1900 mm, with a temperature range of 23 °C to 37 °C and a relative humidity range of 75% to 89% (Erhayimwen et al., 2024; Tesi et al., 2020). The vegetation is typical of the rainforest except for drainage streams where swampy areas exist (Erhayimwen et al., 2024; Jaboro and Omonigho, 2019). The rich, silty soil, coupled with salt- and freshwater bodies, provided the necessary incentives for the people whose main occupations are farming and fishing (Obi-Iyeke, 2022). Amukpe is part of the Oben/ Sapele/Amukpe oil and gas field, which is operated by the Nigerian Petroleum Development Company. Amukpe has a flow station, a Liquid Treatment Facility, and crude storage tanks. Amukpe also hosts the commercial farm holding, which is an integrated farm registered as a company limited by the Delta State Government, modelled after the Songhai-Parakou of the Republic of Benin. The crude oil exploration has resulted in incidents of oil spillage in the study area. The study area map is shown in Figure 1.

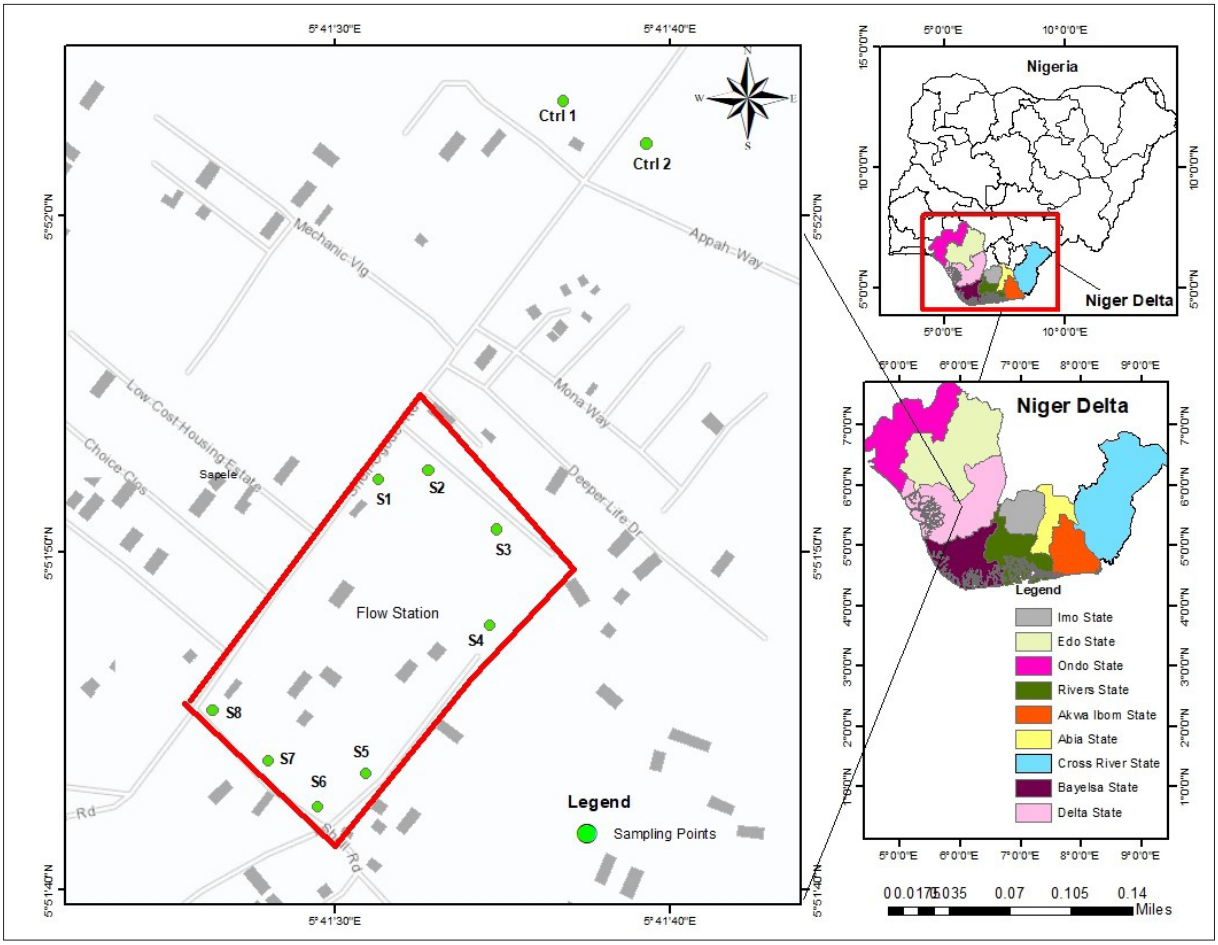

Figure 1. Map of the study area

2.2 Soil Sample Collection

Soil sampling was done according to the FAO (2006) method. Eight (8) soil samples were collected from crude oil-impacted locations in the study area while two (2) soil samples were collected from a non-impacted area which served as control samples. Sampling points were geo-referenced using geographical positioning system (GPS) to ensure consistency and are shown in Figure 1 and Table 1. The soil samples were collected at depths 0-15 cm and 15-30 cm using a stainless steel auger after foreign materials such as roots, gravel, pebbles, leaves and stones were removed. At each sampling point, three different samples were collected and pooled together. Thereafter, a single representative or composite sample was collected by

quartering and compartmentalization. Sampling was carried out during the dry season (January) and then the wet season (June) for two years. Soil samples for metal analysis were stored in polythene bags, while those for total petroleum hydrocarbons were stored in aluminum foil and kept in an ice chest. Samples were correctly labeled and transported to the laboratory. In the laboratory, the soil samples were air dried in the dark, sieved through a 2 mm mesh, and stored at -4 °C until analysis.

Table 1. Sample coordinates in decimal degrees

Sampling ID	Latitude	Longitude	Activities
S1	N 5.864468	E 5.692029	Farmland
S2	N 5.864559	E 5.692442	Farmland
S3	N 5.864057	E 5.693007	Farmland
S4	N 5.863282	E 5.692946	Farmland
S5	N 5.862064	E 5.691922	Farmland
S6	N 5.861775	E 5.691524	Farmland
S7	N 5.862156	E 5.691111	Farmland
S8	N 5.862582	E 5.690637	Farmland
Ctrl 1	N 5.867602	E 5.693558	Farmland
Ctrl 2	N 5.867237	E 5.694246	Farmland

2.3 Physicochemical Characterization of Soil Samples

Physical analysis was conducted on the composite soil samples, consisting of five random samples from each plot for the two profile layers (0-15cm and 15-30cm). Control samples were also collected 5km away from the polluted site, in the direction opposite to the drainage, with similar vegetation, using the same procedures. The background samples were collected 1000 m away from the polluted site. Particle size analysis was done by the Bouyoucas Method (1962). Total organic carbon was measured using the wet oxidation digestion method of Walkley and Black (1959). The exchangeable cations were extracted by the ammonium acetate extraction method (He et al., 2005). Available phosphorus was determined by the molybdenum blue colour method (Osuji et al., 2006). Nitrogen was determined by the modified Kjeldahl method (Bakker et al., 2000). A pH meter (Orion Digital pH / millivoltmeter 611) was used to determine the pH of the soil, following the procedures of Oluyemi et al. (2008). Total petroleum hydrocarbon (TPH) was determined using the method of Mihaly-Cozmuta et al. (2005).

2.4 Heavy metal analysis of the soil samples

Five grams of the air-dried soil sample were digested in an acid mixture prepared from 20 mL HNO_3, 10 mL HCl, and 2 mL HF. The digest was placed on a hot plate (130 ^oC) for 2 hours with constant stirring. The filtered solution was made up to 100 mL with distilled water. The solution was analyzed for heavy metals (Fe, Zn, Cr, Cd, Cu, Pb and Mn) using Flame Atomic Absorption Spectrophotometry (AAS) (PerkinElmer Analyst 200). Vanadium was analyzed using a nitrous oxide flame, whereas arsenic was analyzed by hydride generation AAS. The AAS was fitted with D2 background correction devices. All samples were analyzed in triplicate.

2.5 Data Analysis

Data collected were subjected to analysis of variance (ANOVA) and the means were compared using ' 'Duncan's new multiple range test (DNMRT) at $p < 0.05$ levels of significance. The Pearson correlation coefficient was used to assess the relationships between the metals in soil samples from polluted and unpolluted sites, while principal component analysis was applied to identify the sources of metals.

2.6 Determination of the extent of pollution

The extent of pollution and ecological risk was evaluated using variouspollution indices including the contamination/ pollution index, pollution load and geo-accumulation index.

Contamination / pollution index: The contamination/ pollution index was computed using the equation:

$$\text{CPI} = \frac{Concentration\ of\ metals\ in\ soil}{DPR\ Target\ value} \quad (1)$$

Geoaccumulation index (Igeo): The geoaccumulation index was calculated by the equation:

$$\text{Igeo} = \text{Log}\,2\frac{C_n}{1.5B_n} \quad (2)$$

Enrichment factor (EF): The enrichment factor of metals in the soil was calculated following the equation:

$$\text{EF} = \frac{Cn\ (test\ element)}{Cn\ (Reference)} \div \frac{Bn\ (test\ element)}{Bn\ (Reference)} \quad (3)$$

Pollution load index: Pollution load index (PLI) was estimated using the equation:

$$\text{PLI} = \sqrt[n]{CF1 \times CF2 \times CF3 \times CF4} \times \ldots CFn \quad (4)$$

The definition and values of variables in equations (1) to (4) are as given in Tesi et a. (2020) and Iwegbue et al. (2018).

3. Results and Discussion

3.1 Soil physicochemical characteristics

The results of some physicochemical properties, including particle size distribution, pH, electrical conductivity, nitrate, phosphate, and total petroleum hydrocarbon contents in the crude oil-impacted soils for the two sampling years are presented in Table 1.

Table 1. Some physicochemical properties of soils of the study area

Sites	Depth	pH				TOC (%)				EC (µ∫/cm)			
		2013		2014		2013		2014		2013		2014	
		D	W	D	W	D	W	D	W	D	W	D	W
1	0-15cm	6.06±0.05^{c}	6.14±0.04^{d}	6.52±0.43^{b}	6.54±0.04^{d}	1.80±0.09^{d}	1.60±0.12^{c}	1.72±0.03^{b}	1.51±0.39^{d}	62.7±0.05^{c}	60.9±0.06^{b}	58±0.05^{c}	42.4±2.05^{d}
	15-30cm	6.76±0.17^{b}	6.9±0.67^{d}	6.79±0.57^{b}	6.99±0.61^{c}	1.52±1.05^{d}	1.46±1.04^{c}	1.51±0.00^{b}	1.31±0.05^{e}	54.4±0.70^{d}	42.1±1.90^{d}	57±0.21^{c}	41.7±0.03^{d}
2	0-15cm	5.89±1.40^{d}	6.03±0.05^{d}	5.99±0.00^{c}	6.75±1.40^{c}	2.1±0.00^{c}	1.94±0.05^{c}	1.84±0.40^{b}	1.86±0.20^{d}	61.8±0.00^{c}	57.4±0.03^{c}	57.8±0.05^{c}	52.8±0.19^{c}
	15-30cm	6.21±0.52^{c}	6.84±1.03^{b}	6.56±0.25^{b}	6.93±0.75^{c}	1.8±0.04^{d}	1.73±0.48^{c}	1.76±1.42^{b}	1.37±0.03^{e}	49±0.48^{e}	49.6±0.18^{d}	48.7±0.01^{d}	43±0.05^{d}
3	0-15cm	6.06±0.60^{c}	5.97±0.09^{e}	6.74±0.39^{b}	5.98±0.00^{e}	3.1±0.18^{b}	3.8±1.36^{a}	2.9±0.01^{a}	3.3±0.15^{b}	49.3±0.06^{e}	53±0.04^{c}	49.3±1.07^{d}	53±1.13^{c}
	15-30cm	6.74±0.65^{b}	6.43±1.05^{c}	6.94±0.01^{b}	6.75±1.28^{c}	2.9±0.05^{c}	3.0±0.00^{a}	1.6±0.50^{c}	1.8±2.30^{e}	36.1±0.10	35±0.16^{e}	36.1±0.90^{e}	35±0.02^{e}
4	0-15cm	5.67±1.54^{d}	6.46±0.13^{d}	5.93±0.05^{c}	6.97±0.05^{c}	2.3±0.42^{c}	3.5±5.75^{a}	2.3±0.07^{a}	2.6±0.00^{c}	72.8±0.00^{b}	67±0.00^{b}	72.8±0.05^{b}	67±0.00^{b}
	15-30cm	6.39±3.00^{c}	6.83±1.76^{c}	6.84±1.03^{b}	6.91±0.31^{c}	2.4±0.03^{c}	2.9±0.13^{b}	2.1±0.14^{a}	2.1±1.02^{c}	64±0.35^{c}	58.2±0.03^{c}	64±0.14^{b}	58.2±1.05^{c}
5	0-15cm	5.94±0.95^{d}	6.05±0.94^{d}	6.98±0.05^{b}	6.99±1.52^{c}	1.61±0.00^{d}	1.83±0.00^{c}	1.83±0.70^{b}	1.87±0.44^{d}	51±0.92^{d}	46.4±0.12^{d}	51±1.80^{c}	46.4±0.00^{d}
	15-30cm	6.03±2.17^{c}	6.74±2.01^{b}	7.02±0.09^{a}	7.2±0.93^{b}	1.51±0.72^{d}	1.63±0.25^{c}	1.21±0.20^{c}	1.01±0.05^{e}	38.2±0.04^{f}	31±0.07^{e}	38.2±0.04^{e}	31±0.48^{e}
6	0-15cm	6.09±0.52^{c}	6.06±0.00^{d}	6.64±0.10^{b}	6.34±0.04^{d}	1.37±0.13^{d}	1.48±0.34^{d}	1.07±0.71^{c}	1.32±0.00^{e}	53.1±0.10^{d}	52±0.31^{c}	53.1±0.00^{c}	52±0.05^{c}
	15-30cm	6.71±1.64^{b}	6.57±0.17^{c}	6.79±0.57^{b}	6.72±0.57^{c}	1.61±0.00^{d}	1.32±1.30^{d}	0.91±1.09^{d}	0.81±0.04^{f}	42.9±0.00^{e}	38.9±0.09^{e}	42.9±2.01^{d}	38.9±1.04^{e}
7	0-15cm	4.9±1.57^{e}	5.7±0.45^{f}	5.34±1.04^{d}	5.93±2.48^{e}	3.73±0.01^{a}	3.46±0.04^{a}	2.41±0.00^{a}	3.71±0.05^{a}	86.1±2.08^{a}	72.5±0.05^{a}	86.1±0.17^{a}	72.5±0.18^{a}
	15-30cm	5.1±0.05^{e}	6.08±2.71^{d}	5.82±0.00^{c}	6.45±0.64^{d}	3.24±0.25^{b}	3.21±0.21^{a}	2.41±0.68^{a}	2.8±0.36^{c}	48.3±0.18^{e}	44±0.03^{d}	48.3±0.04^{d}	44±2.53^{d}
8	0-15cm	6.04±0.63^{c}	6.18±0.03^{d}	6.73±0.50^{b}	6.93±0.01^{c}	2.1±0.041^{c}	2.1±0.01^{b}	1.9±0.21^{c}	1.0±0.00^{e}	32.5±1.04^{f}	31±0.00^{e}	32.5±0.38^{e}	31±0.19^{e}
	15-30cm	6.56±0.98^{b}	6.03±0.51^{d}	6.81±0.07^{b}	6.98±1.00^{c}	1.9±0.00^{d}	1.8±0.05^{d}	0.7±0.53^{e}	0.8±0.71^{g}	23±0.05^{g}	20.6±0.02^{f}	23±0.45^{f}	20.6±0.05^{f}
Control 1	0-15cm	7.01±0.00^{b}	7.06±0.07^{b}	7.13±0.03^{a}	7.06±0.00^{b}	0.7±0.05^{f}	0.61±0.03^{e}	0.51±0.03^{d}	0.61±0.05^{f}	21.9±0.00^{g}	18.5±0.04	22±0.05^{f}	17±0.04^{h}
	15-30cm	7.56±0.11^{a}	7.73±1.34^{a}	7.21±0.51^{a}	7.62±1.30^{a}	0.81±0.63^{e}	0.71±1.00^{e}	0.74±0.50^{d}	0.80±0.00^{f}	17.8±2.01^{h}	17±0.04^{h}	18.6±1.46^{g}	18.3±0.56^{g}
Control 2	0-15cm	6.94±0.00^{a}	7.01±2,04^{b}	6.89±0.32^{b}	7.01±0.00^{b}	0.92±0.01^{e}	0.83±0.04^{e}	0.88±1.34^{d}	0.67±1.46^{f}	22.7±0.16^{g}	21.7±1.03^{f}	22.9±0.61^{f}	22±0.01^{f}
	15-30cm	7.25±0.10^{a}	7.53±1.80^{a}	7.04±1.60^{a}	7.27±0.52^{b}	0.83±1.07^{e}	0.81±0.00^{e}	0.37±0.56^{d}	0.34±0.29^{g}	20.3±0.05^{g}	19.9±0.05^{g}	21.1±0.00^{f}	21.5±0.06^{f}

W=Wet season; D=Dry season; Means with different alphabets within the same column are significantly different at $P \leq 0.05$ using Duncan's Multiple Range Tests

Continuing from Table 1. Some physicochemical properties of soils of the study area

		Nitrate (mg kg^{-1})				Phosphate (mg kg^{-1})				CEC (mg kg^{-1})			
		2013		2014		2013		2014		2013		2014	
		D	W	D	W	D	W	D	W	D	W	D	W
1	0-15cm	28.5±0.07^{c}	26.6±3.10^{f}	31.4±3.05^{d}	29.8±0.57^{e}	12.4±0.73^{g}	11.9±3.61^{h}	14.6±0.02^{f}	14±0.04^{f}	22.1±0.05^{c}	20.1±3.01^{b}	23.8±2.40^{d}	22.4±0.00^{e}
	15-30cm	32.9±0.05^{b}	34.3±0.16^{c}	34.9±0.09^{c}	35.2±6.01^{c}	14±1.90^{e}	13.6±0.03^{f}	15.9±1.60^{e}	15±1.21^{e}	20.1±4.00^{d}	21.5±0.09^{b}	19.4±0.05^{e}	20.6±3.10^{e}
2	0-15cm	29±1.13^{c}	29.8±2.50^{e}	29.5±2.10^{e}	30±1.93^{d}	13.8±0.05^{f}	12±0.05^{g}	14.7±2.48^{f}	14±0.05^{f}	33.4±1.10^{b}	31.4±4.00^{a}	30.4±1.00^{b}	28.7±0.41^{b}
	15-30cm	33.6±0.93^{b}	34.9±0.04^{c}	34.9±0.50^{c}	36±0.06^{c}	16±2.74^{c}	14.6±0.38^{e}	17±0.05^{c}	16.7±4.79^{d}	28.1±3.02^{b}	29.4±0.01^{a}	30.1±0.09^{b}	22.7±0.05^{de}
3	0-15cm	25.4±3.60^{d}	27.5±2.58^{f}	25.4±2.93^{f}	28.7±0.13^{e}	12.7±0.59^{g}	13±2.00^{f}	14.6±2.53^{f}	16.9±0.05^{d}	18.3±0.16^{d}	20.4±0.95^{b}	20.8±0.40^{d}	21.4±2.77^{e}
	15-30cm	30.4±0.94^{b}	31.7±5.90^{d}	30.4±0.04^{d}	35.1±2.46^{c}	14±3.02^{e}	13.8±3.15^{f}	16.1±0.05^{d}	14.7±2.01^{f}	18.3±0.50^{d}	20.4±0.01^{b}	22.3±3.28^{d}	20.4±0.18^{e}
4	0-15cm	28.5±0.01^{c}	26±1.01^{f}	29.5±0.92^{e}	27±0.05^{e}	12±0.01^{g}	12.1±0.02^{g}	11.1±0.34^{i}	13.8±0.00^{g}	27.4±4.20^{b}	30.1±0.41^{a}	26.3±0.05^{c}	23.4±0.55^{d}
	15-30cm	34.2±4.00^{b}	30±2.00^{d}	32.3±3.78^{cd}	30±0.29^{d}	13.4±1.93^{f}	13.6±0.00^{f}	15.3±0.05^{e}	14.7±0.25^{f}	21.5±0.00^{cd}	32.1±3.59^{a}	20.1±1.00^{d}	23.4±1.20^{d}
5	0-15cm	32.6±1.72^{c}	30.3±1.10^{d}	34.7±0.03^{bc}	31.3±0.04^{d}	15.7±5.20^{d}	14.7±3.46^{e}	18±2.00^{b}	16.9±1.63^{d}	28.7±1.03^{b}	29.8±0.02^{a}	27.3±0.30^{c}	26.4±0.06^{c}
	15-30cm	38.7±2.00^{b}	36.5±0.04^{c}	37.1±2.71^{b}	37.2±0.92^{c}	16.9±0.06^{c}	15±1.03^{d}	18±1.04^{b}	18.7±0.05^{b}	24.4±0.01^{c}	26.4±5.34^{b}	25.2±2.90^{c}	26.1±0.30^{c}
6	0-15cm	26.3±0.18^{e}	29.8±3.50^{d}	28.3±1.39^{e}	31±4.01^{d}	11.5±2.80^{h}	12±4.10^{g}	13.6±2.85^{g}	15±3.04^{e}	15.3±4.10^{e}	15.3±0.01^{c}	17.8±0.03^{f}	15.7±0.01^{f}
	15-30cm	31.6±0.05^{b}	31.1±1.03^{d}	32±2.78^{cd}	36.4±0.64^{c}	12.9±0.03^{g}	13.4±0.35^{f}	12.9±0.30^{h}	17.6±1.90^{c}	16.4±0.34^{e}	13.2±0.05^{d}	16.3±0.00^{f}	12.3±2.45^{g}
7	0-15cm	25.7±3.80^{e}	26.2±0.05^{f}	24.4±0.43^{f}	29.4±5.10^{e}	11.1±0.46^{h}	10.3±1.48^{i}	13.5±3.96^{g}	12.9±0.00^{h}	38.4±0.52^{a}	29.1±1.46^{a}	36.8±1.56^{a}	32.4±0.00^{a}
	15-30cm	28.9±0.64^{c}	29±2.83^{e}	28.9±0.05^{e}	32.8±0.02^{d}	12.9±3.70^{g}	12.9±2.80^{g}	15±0.73^{e}	13.81±0.52^{g}	38.3±3.11^{a}	20.1±0.00^{b}	33.7±0.05^{a}	20.6±1.10^{e}
8	0-15cm	30.6±0.05^{b}	31.7±0.07^{d}	33.9±2.69^{c}	34.2±2.18^{c}	13±1.40^{f}	13.4±0.05^{f}	14.3±0.05^{f}	14.2±1.04^{f}	19.8±0.44^{d}	16.8±0.21^{c}	21.4±0.62^{d}	22.3±0.44^{e}
	15-30cm	35.7±1.93^{b}	33.9±4.10^{d}	35.4±0.48^{b}	35.5±0.03^{c}	14.7±0.06^{e}	14±0.20^{e}	16±0.03^{d}	13.1±0.02^{g}	16.1±0.50^{e}	16.6±2.00^{c}	16.0±0.07^{f}	13.0±0.00^{g}
Control 1	0-15cm	42.3±0.26^{a}	40.6±0.02^{b}	43.7±5.01^{a}	41.6±0.72^{b}	17.3±0.34^{b}	15±0.74^{d}	18.6±0.05^{b}	17.8±0.70^{c}	10.3±0.01^{f}	7.8±0.02^{f}	7.3±0.00^{h}	7.00±0.97^{i}
	15-30cm	46.7±3.40^{a}	45±1.46^{a}	47±0.15^{a}	47.4±0.00^{a}	18±1.05^{a}	16.8±2.03^{c}	19.7±3.19^{a}	18.1±0.05^{b}	10.7±0.00^{f}	9.80±1.41^{e}	8.60±3.10^{g}	8.20±2.40^{h}
Control 2	0-15cm	43.2±0.18^{a}	39.5±0.05^{b}	44.6±0.02^{a}	40±1.78^{b}	15.3±0.00^{d}	17±0.00^{b}	17.9±0.03^{c}	18.5±0.00^{b}	8.7±1.53^{f}	7.20±0.00^{f}	7.30±2.41^{h}	6.80±0.01^{i}
	15-30cm	45.9±0.05^{a}	42.6±2.48^{b}	45.7±0.97^{a}	43±5.02^{b}	17.5±1.94^{b}	18.4±1.02^{a}	19.7±0.50^{a}	19.1±0.52^{a}	9.8±0.91^{f}	10.3±2.11^{e}	9.4±0.01^{g}	8.50±0.00^{h}

W=Wet season; D=Dry season; Means with different alphabets within the same column are significantly different at $P \leq 0.05$ using Duncan's Multiple Range Tests

Continuing from Table 1. Some physicochemical properties of soils of the study area

		Clay (%)				Silt (%)				Sand (%)			
		2013		2014		2013		2014		2013		2014	
		D	W	D	W	D	W	D	W	D	W	D	W
1	0-15cm	11.6^{e}	12^{d}	12.6^{e}	12.9^{d}	14.2^{f}	13.6^{f}	14.9^{e}	14^{e}	41.7^{d}	38.2^{e}	38^{f}	33.3^{h}
	15-30cm	13.4^{c}	13.8^{c}	14.3^{c}	14^{b}	15^{e}	14.3^{e}	15^{d}	15.2^{d}	38.9^{e}	34.6^{f}	36.5^{g}	32.9^{h}
2	0-15cm	12.7^{d}	13.6^{c}	12.8^{e}	14.4^{b}	18.4^{b}	18.1^{a}	17^{b}	19^{a}	38.7^{e}	42.1^{c}	38^{f}	35.6^{g}
	15-30cm	13.7^{c}	13.1^{c}	14.4^{c}	13.9^{c}	19.6^{a}	18.9^{a}	18.5^{a}	19^{a}	41^{d}	36.7^{f}	35^{h}	33^{h}
3	0-15cm	10.1^{f}	12.1^{d}	11.5^{f}	12.9^{d}	12.4^{h}	12.8^{g}	13^{f}	13.2^{f}	38.4^{e}	31^{g}	34.6	29.7^{j}
	15-30cm	11.9^{e}	12.4^{d}	12.7^{e}	13.4^{c}	13^{g}	11.1^{h}	14^{e}	14.4^{e}	35.1^{f}	28.7^{h}	31.6	26^{l}
4	0-15cm	10^{f}	8.2^{g}	10^{g}	9^{f}	14.3^{f}	12.3^{g}	14.1^{e}	13^{f}	54.6^{a}	55.3^{a}	46.3^{c}	46.9^{c}
	15-30cm	11.7^{e}	10^{f}	12^{e}	11.2^{e}	14.8^{f}	13.1^{f}	15.3^{d}	13.9^{f}	49.1^{b}	51.6^{b}	42.6^{d}	48.1^{b}
5	0-15cm	11.3^{e}	10.4^{f}	12.5^{e}	11.6^{e}	17.5^{c}	15.8^{d}	18^{a}	16.2^{c}	42.1^{d}	38.6^{e}	38.8^{f}	31^{i}
	15-30cm	12.8^{d}	11.7^{e}	13.3^{d}	12^{d}	18.1^{b}	12.2^{g}	18.9^{a}	13.7^{f}	41^{d}	39.3^{e}	34.5^{i}	32^{i}
6	0-15cm	10.8^{f}	11.7^{e}	11^{f}	12.1^{d}	15.2^{e}	14.4^{e}	16.1^{c}	14.2^{e}	48.3^{b}	42.5^{c}	42.1^{d}	39.8^{e}
	15-30cm	11.5^{e}	11^{e}	12.5^{e}	13.1^{c}	15.1^{e}	14^{e}	15.9^{d}	15.4^{d}	45.1^{c}	40.1	40.4^{e}	38.2^{e}
7	0-15cm	9.7^{g}	11.6	10.4^{g}	11.1^{e}	13.6^{g}	12^{g}	13.8^{f}	12.6^{g}	58.3^{a}	52.4^{b}	57^{a}	51.9^{a}
	15-30cm	10.7^{f}	12.4^{d}	12^{e}	12.9^{d}	18.9^{b}	12.8^{g}	15^{d}	13.2^{f}	50.6^{b}	51.7^{b}	51.4^{b}	48.9^{b}
8	0-15cm	12.5^{d}	11.6^{e}	13.2^{d}	11.8^{e}	16.8^{d}	15.8^{d}	16.4^{c}	15.5^{d}	45.7^{c}	42.6^{c}	40.7^{e}	40.3^{d}
	15-30cm	13.1^{c}	12.9^{d}	14.5^{c}	13^{c}	16.6^{d}	16.4^{c}	17^{b}	16.9^{c}	42^{d}	40.9^{d}	37.9^{f}	37.4^{f}
Control 1	0-15cm	14^{b}	13.2^{c}	15.6^{b}	13.2^{c}	15.3^{e}	16.3^{c}	15.9^{d}	16.1^{c}	30.6^{g}	28.3^{h}	29.1^{j}	25.1^{l}
	15-30cm	15^{a}	15^{a}	16^{a}	15^{a}	15.5^{e}	17^{b}	15.8^{d}	17.1^{b}	26.3^{h}	24^{i}	28.4^{k}	22.7^{m}
Control 2	0-15cm	13.8^{c}	13.4^{c}	14.8^{c}	13.4^{c}	17.5^{c}	14.8^{c}	17.1^{b}	15.3^{d}	31^{g}	38.3^{h}	29.5^{j}	32.1^{i}
	15-30cm	14.5^{b}	14.6^{b}	16.5^{a}	14.6^{b}	18^{b}	15.4^{d}	18.3^{a}	15.9^{d}	27.1^{h}	26.9^{i}	28.8^{k}	27.2^{k}

W=Wet season; D=Dry season; Means with different alphabets within the same column are significantly different at $P \leq 0.05$ using Duncan's Multiple Range Tests

The pH value for the crude oil-impacted soil ranged from 4.9 to 7.2 across the two sampling years. The results obtained from this study indicated that the pH values in the crude oil-impacted soils were acidic to near-neutral in nature, which corresponds to the typical pH of anaerobic soils in the Niger Delta. The pH values, reported in this study, were within the range of 6.0 to 7.5, as set by FAO (2011) for agricultural soils. The pH recorded in the study also corresponds to pH value previously reported for Niger Delta soils (Nkwocha and Duru, 2010; Abii and Nwosu, 2009; Iwegbue et al., 2009; Iwegbue et al., 2006. pH is an important soil property, having great effect on solute concentration and sorption/ adsorption of contaminants in soils (Ambo et al., 2013). High pH value might reduce the mobility of some metal species down the soil strata, while low pH value usually enhances metal distribution and transport in soil (Ogboi, 2012; Osuji and Nwoye, 2007). The pH values in this study agree with the results obtained by Ideriah et al. (2013) from soil in the Niger Delta region and with those reported by Wegwu et al. (2011) in a post-impact assessment of a crude oil-spilled site four years after the recorded incidence. When evaluating the movement of most metals, soil pH is crucial because precipitation as insoluble organic complexes, carbonates,, and hydroxides,as well asd enhanced sorption tooxide surfaces,s reduces mobility as the soil pH rises (Osuji and Udoetok, 2008). As the pH value decreases, the concentration of soluble metals increases (Abii and Nwosu, 2009). The acidic or alkaline status of the soil determines the availability of many nutrients for plant growth. pH thus plays a key role in soil microbial reactions (Edema et al., 2009).

Total organic matter (TOC) in the sampled plots ranged from 0.37 to 3.8%. The total organic matter at the polluted site was significantly higher ($p < 0.05$) than that of the control site. The amount of organic matter in soils affects numerous chemical and physical processes. It is a key indicator of the soil as a rooting environment, even though soil organic carbon is not necessary for plant growth (Tesi et al., 2020).

The electrical conductivity (EC) varied between 17 and 86.1µS cm^{-1}. The highest EC value was observed at Site 7 during both sampling periods. The electrical conductivities of the impacted soils were significantly higher ($p < 0.05$) than those of the control sites.

Cation exchange capacity (CEC) in the sampled plots ranged from 6.80 to 38.4 mg kg^{-1}. The cation exchange capacity at the polluted site was significantly higher ($p < 0.05$) than that of the control site. Additionally, there was significant variation in responses to sites and depth. The higher values of CEC were observed at sites 7, 4, and 1 in comparison to other sites. A similar range of CEC (9.41-48.31 mg kg-1) was reported by Iwegbue et al. (2013) in the soil surrounding cassava processing mills in southern Nigeria. The values of CEC obtained in this study were significantly higher than those reported in soils from an oil field in the Niger Delta, Nigeria, by Iwegbue et al. (2006). The soil's ability to absorb metals is correlated with its CEC. The more exchange sites on the soil minerals that are accessible for metal retention, the higher the CEC value.

The concentrations of nitrate in the crude oil-impacted soil were lower than the levels found in the control sites, ranging from 24.4 to 47.4 mg kg^{-1} for the two sampling periods. The phosphate concentration in the soil impacted by crude oil varied from 10.3 to 18.7 mg kg^{-1}. There were no significant spatial and seasonal changes in the levels of phosphate in these soils. The concentration of nitrates and phosphates was very low and coupled with the fact that the spill was an extensive one that has lasted for about 3 years (in a low oxygen state). Metabolic activities have depleted the nitrates and phosphates in the soil, which may retard hydrocarbon degradation. Soil N and P levels were lower at the two depths in the polluted plots than in the control sites. The reduction in phosphorus could be attributed to the effect of the oil spill on the soil, which affected the activity of the enzyme phosphatase and, therefore, inhibited the release of phosphorus from the organic materials in the soil. The acidic/ alkaline status of the soil determines the availability of many nutrients for plant growth. pH thus plays a key role in soil microbial reactions (Edema et al., 2009). It has been noted that contamination from crude oil lowers the soil's nutritional content (Nwadinigwe and Onyeidu, 2012). Osuji and Nwoye (2007) reported that the soil ecosystem is limited by organic matter, such that the presence of nitrogen-free substrates (crude oil), N and P become limiting. The low levels of phosphorus and nitrogen is indicative of a stressed environment.

Analysis of the soil samples showed that the proportion of soil particles varied as follows: sand (22.7%-58.3 %), clay (8.2%-16.5 %), and silt (12.0%-19.6%). The particle size pattern indicates the dominance of the sand fraction. The clay fraction of the soil was less than 18%. There is a significant spatial variation in particle size distribution. The sand fraction forms the predominant fraction at all sites and depths, while the clay fraction is low compared to the sand and silt. The sandy loam nature of the soil may have been responsible for an extensive vertical and horizontal migration of oil in the environment. This observation agrees with that of Akani et al. (2009), who reported that the sandy–loam nature of soils enhances oil migration in crude oil-polluted soil. There is no regular trend in particle size distribution with depth.

3.2 Metals and TPH concentrations in the soils

The results of the heavy metal and TPH analyses of the examined soils for the two sampling years are presented in Table 2. The results showed that impacted sites generally had higher concentrations of metals than the control site. The concentrations of metals in the crude oil-impacted soil were several times higher than those of the uncontaminated control sites throughout the different sampling seasons and periods, except for vanadium. This result indicates that the crude oil spillage had a significant impact on the environment due to the presence of metals. The spatial difference in the concentrations of crude oil-impacted soil is related to the background concentration of metals, topography, surface processes, and the magnitude of the crude oil spillage's impact.

Table 2. Seasonal variation of metals concentrations (mg kg-1 dry weight) in soils of the study area

Sites	Depth	As				Cd				Pb				Cr			
		2013		2014		2013		2014		2013		2014		2013		2014	
		D	W	D	W	D	W	D	W	D	W	D	W	D	W	D	W
1	0-15cm	1.02	0.75	0.94	0.74	1.6	1	1.43	1.1	88.0	81.0	75.7	72.2	33.7	26.4	15.5	20.5
	15-30cm	0.36	0.21	0.03	0.01	0.8	0.96	0.21	0.52	49.0	40.0	38.9	38.8	24.1	21.7	15.6	17.9
2	0-15cm	1.04	0.68	0.45	0.28	0.6	0.52	0.64	0.83	94.0	89.0	82.9	65.8	21.4	18.7	18.3	19.0
	15-30cm	0.2	0.15	0.04	0.05	0.2	0.06	0.83	0.02	56.0	69.0	50.5	44.3	20.9	18.9	18.0	16.0
3	0-15cm	0.93	0.56	0.83	0.46	0.6	0.48	0.57	0.97	96.0	91.0	70.2	72.7	18.6	19	16.8	14.6
	15-30cm	0.07	0.09	0.02	0.01	0.2	0.16	0.21	0.24	42.0	44.0	38.5	28.5	13.5	15.8	15.1	10.4
4	0-15cm	0.36	0.56	0.3	0.45	2.8	2.08	2.2	2.43	107	98.0	94.2	72.0	34.8	28.3	27.6	22.1
	15-30cm	0.05	0.01	0.06	0.01	1.2	1.13	1.32	1.17	86.0	47.0	72.8	33.3	30.7	22.6	29.8	23.7
5	0-15cm	0.64	0.32	0.91	0.74	1.5	1.16	1.21	1.02	89.0	97.0	68.0	81.3	16.7	13.9	14.5	11.1
	15-30cm	0.08	0.05	0.04	0.03	0.1	1.02	0.56	0.83	38.0	42.0	29.6	35.7	16	11.7	10.3	9.7
6	0-15cm	0.72	0.64	0.74	0.75	1.3	0.86	1.29	0.48	92.0	85.0	78.6	69.5	22.4	20	19.0	16.9
	15-30cm	0.08	0.03	0.05	0.02	0.6	0.62	0.4	0.13	48.0	58.0	32.7	42.4	19.6	18.7	19.0	17.3
7	0-15cm	0.83	0.31	0.43	0.83	2.4	1.74	2.04	1.05	126	116	93.0	94.5	29.7	24.4	22.5	20.1
	15-30cm	0.06	0.06	0.05	0.064	0.6	0.52	0.31	0.1	723	48.0	54.7	41.6	20	21.7	20.2	19.2
8	0-15cm	0.42	0.49	0.53	0.95	0.9	0.76	0.13	0.51	66.0	68.0	46.1	41.6	14.9	15.6	11.0	13.8
	15-30cm	0.05	0.02	0.03	0.06	0.4	0.23	0.26	0.17	37.0	44.0	24.7	27.4	11.8	9.43	9.5	12.0
Control 1	0-15cm	0.03	0.02	0.05	0.04	0.01	0.05	0.05	0.09	23.0	23.0	21.1	20.3	0.78	ND	0.94	0.02
	15-30cm	ND	0	0.006	ND	0.02	0.03	0.03	0.01	16.0	7.8	13.4	15.0	0.1	1.31	0.06	ND
Control 2	0-15cm	0.06	0.02	0.01	0.02	0.09	0.12	0.09	0.11	20.0	16.0	23.5	22.8	0.34	0.1	0.15	0.10
	15-30cm	0.01	ND	ND	ND	0.02	0.04	0.06	0.04	19.0	16.0	14.9	13.0	0.98	0.56	0.20	0.01

W=Wet season; D=Dry season

Continuing from Table 2. Seasonal variation of metals concentrations (mg kg-1 dry weight) in soils of the study area

Sites	Depth	Ni				Cu				V				Mn			
		2013		2014		2013		2014		2013		2014		2013		2014	
		D	W	D	W	D	W	D	W	D	W	D	W	D	W	D	W
1	0-15cm	11	8.94	9.75	7.18	54.0	47.0	41.5	39.0	5.61	2.31	3.97	2.01	58.7	56.9	50.0	48.5
	15-30cm	9.6	7.93	6.13	6.98	24.0	21.0	19.5	18.6	4.21	0.94	3.04	2.41	50.2	53.5	43.7	42.3
2	0-15cm	13.7	11.9	10.45	10.54	42.0	40.0	39.7	43.0	7.32	3.59	7.16	2.23	67.4	53.7	53.6	51.4
	15-30cm	10.5	9.02	8.89	7.93	32.0	29.0	19.9	25.7	4.23	0.36	4.04	0.52	46.7	25.7	37.0	32.5
3	0-15cm	9.8	6.94	7.23	5.87	77.0	70.0	54.2	54.7	3.44	1.89	3.01	1.73	63.5	66.8	56.2	52.0
	15-30cm	9.34	5.61	8.75	3.42	33.0	27.0	31.0	24.5	1.32	0.6	2.76	1.42	64.3	60.3	42.1	35.9
4	0-15cm	16.5	11.6	12.3	9.65	62.0	59.0	41.6	39.1	5.82	3.26	3.42	2.41	96.4	98.6	57.0	68.7
	15-30cm	10.9	11.8	9.05	10.65	46.0	36.0	29.9	17.9	2.34	1.42	3.06	0.95	63.9	60.4	40.4	48.0
5	0-15cm	9.72	9.01	7.95	8.63	94.0	88.0	58.7	61.1	1.06	0.96	1.01	1.04	56.4	58.7	45.0	42.1
	15-30cm	8.16	8.82	8.04	7.93	47.0	35.0	23.4	33.1	0.01	0.2	0.82	0.36	48.8	49.2	30.5	28.6
6	0-15cm	23.7	20.1	18.64	17.34	59.0	43.0	30.8	28.0	1.7	2.14	1.95	1.64	58.7	48.9	42.9	40.7
	15-30cm	20.6	16.7	15.45	13.52	34.0	34.0	17.6	12.8	0.89	0.31	1.21	0.96	40.4	38.6	27.2	31.3
7	0-15cm	17.4	15.7	13.04	10.63	49.0	41.0	29.5	19.5	5.03	5.09	3.12	2.94	98.7	64.6	61.0	54.7
	15-30cm	15.4	14.2	10.62	11.49	38.0	31.0	15.9	9.4	4.86	3.94	3.31	3.01	54.9	38.8	45.6	29.3
8	0-15cm	7.41	7.09	8.64	8.31	52.0	46.0	42.0	33.3	3.01	2.54	2.41	1.06	39.6	30.0	42.3	32.1
	15-30cm	7.03	6.44	7.97	7.52	29.0	33.0	27.8	11.8	1.97	0.95	0.85	1.23	31.0	20.4	26.7	18.5
Control 1	0-15cm	1.21	0.12	1.14	0.18	10.0	13.0	9.6	11.4	0.18	0.26	0.11	0.47	13.6	9.9	11.8	7.1
	15-30cm	2.09	0.91	1.01	0.9	12.0	12.0	9.2	10.8	0.0	0.23	0.003	0.13	8.4	6.7	6.6	4.4
Control 2	0-15cm	0.47	0.42	0.09	0.49	11.0	11.0	10.3	11.6	0.26	0.19	0.07	0.19	15.2	11.4	12.3	8.6
	15-30cm	1.18	1.06	1.02	1.01	9.0	7.9	8.3	8.6	0.04	0.07	ND	0.04	9.6	5.0	6.7	3..23

W=Wet season; D=Dry season

Continuing from Table 2. Seasonal variation of metals concentrations (mg kg-1 dry weight) in soils of the study area

Sites	Depth	Zn				Fe				TPH			
		2013		2014		2013		2014		2013		2014	
		D	W	D	W	D	W	D	W	D	W	D	W
1	0-15cm	262	248	209	202.1	1031	968	956	764	128	113	106	98.7
	15-30cm	211	197	196	183.3	976	697	634	514	79	67	75.5	59.0
2	0-15cm	218	206	185	179.9	1207	1184	994	974	137	105	92.1	75.9
	15-30cm	221	212	154	146.4	1053	3988	630	605	82	69	54.1	47.0
3	0-15cm	249	203	192	178	843	706	594	474	175	138	125	110
	15-30cm	236	187	185	160.5	758	643	502	387	91	99	78.3	67.2
4	0-15cm	437	352	286	235.4	1463	1127	1194	1014	219	201	155	133
	15-30cm	454	329	224	194	1211	948	1005	922	99	93.1	89.5	76.9
5	0-15cm	214	202	195	175.6	764	678	646	532	113	101	89.7	84.9
	15-30cm	219	207	186	159.8	501	587	574	398	69	63	43.1	39.1
6	0-15cm	226	196	188	164.9	1125	797	973	903	154	139	128	94.4
	15-30cm	233	206	151	148.5	853	534	730	848	83.5	79	71.9	58.2
7	0-15cm	449	327	327	272.8	1583	1252	1208	994	231	215	138	115
	15-30cm	433	354	274	238	1144	977	972	682	97.7	93	92.5	81.0
8	0-15cm	133	120	104	84.75	698	683	627	601	108	96	68.0	51.8
	15-30cm	129	128	87	72.63	487	503	483	548	58.3	52	38.3	30.7
Control 1	0-15cm	33.1	30.6	28	32.75	79	69	54	56	12.9	11.6	10.3	13.9
	15-30cm	32.6	31.3	19	24.02	74	57	50	42	8.01	7.93	6.7	9.5
Control 2	0-15cm	27.3	25.4	26	20.57	82	84	65	59	9.35	10.2	8.4	12.7
	15-30cm	28.9	22.8	21	18.42	64	73	56	44	9.03	9.64	7.7	11.2

W=Wet season; D=Dry season

In this study, higher concentrations of metals were observed in the dry season than in the wet season, which may be influenced by the leaching action of rainwater during the wet season. Moreover, the elevated levels of metal during the dry season may be related to the fact that atmospheric deposition of metal-contaminated dust is highest during the dry season. This result is similar to that of Nwadinigwe et al. (2014) and Nwajei (2011), who also reported a higher concentration of metal during the dry than during the wet season. In this study, the distribution patterns of metals followed the order Fe > Zn > Mn > Pb > Cu >Cr>Ni> V > Cd > As in both seasons.

The concentrations of As ranged from 0.01 to 1.04 mg kg^{-1} at all sites and depths and were lower than the DPR target value of 1.0 mg kg^{-1} for As in soil (DPR, 2018). The concentration of As found in the impacted sites was higher than that found in the soils of oil fields in Nigeria (Iwegbue et al., 2006).

The concentration of Cd ranged from 0.02 to 2.8 mg kg-1 at all sites and depths. The Cd contents found in these oil-impacted soils were above the DPR target value of 0.8 mg kg-1 for Cd in soil. The Cd levels found in this study were comparable to the range of 0.05-3.01 mg kg^{-1} (Iwegbue et al., 2009), < 0.2 mg kg^{-1} (Osuji and Onojake, 2005), 2.2-11.0 mg kg^{-1} (Fatoba et al., 2015), 0.10-0.18 mg kg^{-1} (Bada and Olarinre, 2012), and 0.001-0.20 mg kg^{-1} (Nwaichi et al., 2016) previously reported for crude oil-impacted soils in the Niger Delta of Nigeria.

The concentrations of Pb in the crude oil impacted sites varied from 24.7 to 723 mg kg^{-1}. The concentrations of Pb decreased with depth during the two sampling periods. There were significant ($P \leq 0.05$) spatial and seasonal differences in the concentrations of Pb in crude oil-impacted sites. The results of these studies indicated that the topsoil had a higher concentration of Pb than the subsoil, which may be attributed to the fact that most anthropogenic activities are typically restricted to the surface horizons. The concentration of Pb reported in this study exceeded the permissible limit of 0.35 mg kg^{-1} set by FAO/WHO (2011). The concentrations of Pb in the majority of the sites exceeded the 85 mg kg^{-1} maximum allowable concentration of Pb in soil (DPR, 2018). Pb concentrations in the range of 14.32 to 37.98 were found in soil contaminated with crude oil at Aboh-Abalagada, Delta State (Iwegbue et al., 2009). Osuji and Onojake (2004) reported Pb levels of 10.0 to 10.8 mg kg-1 in soil samples collected 6 months after the Ebocha-8 oil spill in River State. Iwegbue et al. (2006) reported Pb levels of 2.0 to 58.0 mg kg-1 in soils of an oil field in Delta State, Nigeria. The concentrations of Pb in soil profiles collected within a 30m distance of crude oil-contaminated sites were found to be 0.08 to 0.44 mg kg^{-1}. The concentrations of Pb observed in these sites were higher than the concentration of Pb previously reported for some crude oil contaminated sites in the Niger Delta (Iwegbue et al., 2009; Iwegbue et al., 2006) but were similar to those values found in rural/urban soils under different land uses (Iwegbue, 2014) and in the vicinity of Shell Petroleum Development Company operating area (Nwajei, 2009). Pb concentrations above regulatory control limits call for concern, given the toxicity and health effects associated with human exposure to Pb. Therefore, these sites need remediation to reduce the risk of human exposure to Pb.

The concentrations of Cr in the crude oil impacted site range from ND to 34.8 mg kg^{-1}. The concentrations of Cr in the impacted sites were significantly higher ($P \leq 0.05$) than those in the control sites. Particularly when exposed to moderate redox settings at a pH close to neutral, chromium exhibits little mobility. The adsorption of Cr^{6+} diminishes as the pH rises. Cr^{6+}, however, is harmful to biological systems (Hu et al., 2011). The concentrations of Cr in the crude oil-impacted sites were higher than the control site which suggests the impact of the oil spillage. The concentration of Cr reported in this study was higher than the permissible limit of 0.5 mg kg^{-1} set by FAO/WHO (2011). The concentrations of Cr observed in these sites were below the maximum permissible limit of 100 mg kg^{-1} specified by the DPR (2018). Iwegbue et al. (2006) reported Cr levels in the range of 1.0 to 62.0mg kg^{-1} in the soil of an oil field in the Niger Delta. Similarly, Iwegbue et al. (2009) found Cr concentrations of 2.19 to 44.07mg kg^{-1} in Delta State. Ikhajiagbe et al. (2014) found Cr concentrations, ranging from 0.09 to 2.19 mg kg^{-1} in waste oil-polluted sites in the Benin metropolis. The concentrations of Cr in the present study correspond to the range reported for the crude oil impact zone in the Niger Delta (Iwegbue et al., 2006), but were lower than those reported for waste oil-impacted sites (Ikhajiagbe et al., 2014).

The concentration of Ni varied between 3.42 and 23.7 mg kg^{-1}. There are no significant seasonal or temporal changes in the concentrations of Ni in the crude oil-impacted soil. There is a significant difference ($P \leq 0.05$) in the concentrations of Ni observed between the control sites and those of the impacted sites. The concentration of Ni obtained in this study was above the maximum permissible limit set by FAO/WHO (0.20 mg kg^{-1}). The concentration of Ni observed in the crude oil-impacted sites was below the Department of Petroleum Resources' maximum allowable limit of 35 mg kg-1 for Ni in soil. A wide concentration range of nickel (Ni) has been reported for crude oil-impacted soils in the Niger Delta. Iwegbue et al. (2009) found Ni concentrations of 11.87 to 42.25mg kg^{-1} in crude oil-impacted soils. Osuji and Onojake (2004) reported Ni concentration in the range of 12.6 to 12.8mg kg^{-1} in soil samples collected 6 months after the Ebocha-8 oil spillage in the Niger Delta.

The concentrations of Cu in the crude oil impacted site range from 0.01 to 61.1 mg kg^{-1}. Higher concentrations of Cu were observed during the dry season than during the wet season. The concentration of Cu obtained in this study were above the maximum permissible limit set by FAO/WHO (0.20 mg kg^{-1}). The concentrations of Cu in the majority of sites during the first sampling period exceeded the 36 mg kg^{-1} maximum allowable limit for Cu set by the Department of Petroleum Resources in soil (DPR, 2018). A wide range of Cu in soils has been reported in the literature. Osuji and Onojake (2004) reported lower Cu levels in the range of 4.1 to 5.2 mg kg-1 in soil samples collected six months after the Ebocha–8 oil spillage in the Niger Delta, Nigeria. The concentrations of Cu found in this study were higher than those previously

reported for crude oil-impacted sites in the Niger Delta (Ideriah et al., 2013) but similar to the Cu concentration reported in soil in the Niger Delta (Aniekan et al., 2014). The concentrations of Cu in most of the samples were above the permissible limits of 36 mg kg^{-1} set by DPR (2018).

The concentrations of V in the crude oil impacted soil ranged from ND to 7.32 mg kg^{-1}. The mean concentration of manganese at the studied site ranged from 3.23 to 98.7 mg kg^{-1} for the two sampling years. There is no guide specifying the permissible limit of vanadium in soil by the Nigerian regulatory authorities. However, the concentration of vanadium observed in these sites was generally higher in comparison with vanadium concentration observed in farm land in Ibeno (Nwandinigwe et al., 2014b), crude oil impacted sites (<0.2mgkg^{-1}) in Nigeria (Osuji and Onoyake, 2004) but was comparable to vanadium levels reported for an oil field in the Niger Delta (Iwegbue et al., 2006).

High contents of Mn in soils are of concern due to the high mobility of Mn. It can be easily mobilized and contaminate water sources, such as surface and groundwater. Its precipitation and oxidation are more effective at higher pH values (Lloyd and Solomon, 2002). The concentrations of Mn in the crude oil impacted site range from 18.5 to 98.7 mg kg^{-1}. The concentration of Mn reported in this study exceeded the permissible limit of 0.2 mg kg^{-1} set by FAO/WHO (2011). However, the content of Mn in the soils was lower than the CAV of 850 mg kg^{-1}. Nwadinigwe et al. (2014b) reported the mean concentrations of Mn in soil from farmland in Ibeno, Nigeria, as 9.66 to 10.37 mg kg^{-1}. Iwegbue et al. (2006) reported Mn concentrations in the range of 12.3 to 539.4 mg kg-1 in crude oil-impacted soil in Delta State. The concentrations of Mn observed in these sites were similar to the range reported for crude oil-impacted soil (2009) and in soil in the vicinity of Shell Development Company, Delta State (Nwajei, 2009).

The concentration of Zn during the study period varied from 18.42 to 454 mg kg^{-1}. There are significant differences ($P \leq 0.05$) in the spatial and seasonal characteristics of Zn in the impacted soils. The concentrations of Zn were higher than during the dry season than in the wet season and also higher in the first sampling year than in the second sampling year. Although zinc is essential for humans, animals, and plants, prolonged exposure to soil contaminated with zinc can cause a variety of toxicities and health problems, including anemia (Chibowski, 2000). The concentrations of Zn in all sites were above the regulatory control limit of Zn in soil, except for site 8 and control sites. The concentration of Zn reported in this study was higher than the permissible limit of 2.0 mg kg^{-1} set by FAO/WHO (2011) and also higher than the values (4.47 to 49.55 mg kg^{-1}) reported by Iwegbue et al. (2006) in crude oil contaminated soil at Abalagada in Delta State and Nwadinigwe et al. (2014b) who reported mean Zn concentrations of 0.066 mg kg^{-1} in soil samples in farm lands in Ibeno coastal area, Nigeria.

Fe in the sites varied from 42 to 1583 mg kg^{-1} for the sampling years. The concentration of Fe in the surface horizon was higher than that of the subsoil (15- 30 cm). There was a significant reduction in the mean concentration of Fe during the second sampling year. Iron has no specified permissible limit in soil in the legislation of most countries. The concentration of Fe reported in this study exceeded the allowable limit of 5.0 mg kg^{-1} set by FAO/WHO (2011). However, the crustal abundance value for Fe is 4.7% (47000 mg kg^{-1}). The levels of Fe observed at the crude oil-impacted sites were far below the crustal abundance values. A wide concentration range of Fe has been reported in the literature for contaminated soils. For example, Iwegbue (2014) reported Fe concentrations of 4388.2 to 31891 mg kg-1 under different land uses in the Niger Delta. Similarly, Iwegbue et al. (2015) reported Fe concentrations ranging from 58.0 to 257mg kg^{-1} in soils around asphalt plants in Delta State. Nwadinigwe et al. (2014b) found mean Fe levels between 12.09 and 15.5 mg kg-1 in soils of cropland in the Ibeno coastal area, Nigeria.

The quantifiable quantity of petroleum-based hydrocarbons in an environmental medium is known as total petroleum hydrocarbon, or TPH. It represents a large family of substances that originated from crude oil (Tse and Nwankwo, 2013). Total petroleum hydrocarbon (TPH) varied from 6.7 to 231 mg kg^{-1}. Significant and apparent variability exists when the concentration of TPH on various sites and profiles is compared. The concentration of TPH decreased with depth in all sites. This signifies that higher TPH accumulates in the topsoil in relation to the subsoil. TPH was significantly ($P<0.05$) higher at the polluted sites compared with the control site within the two sampling years. The high TPH content in polluted sites confirms the presence of petroleum pollution. The level of TPH in the dry season was higher than in the wet season. This difference could be due to the higher temperature values in the dry season, which resulted in the melting of the sunken oil, causing it to resurface again at sites. The significant reduction in the concentration of TPH and heavy metals, during the second sampling year, may be attributed to the biodegradation process which is controlled not only by its speciation, changes in pH and salinity but also by unknown factors (Essiett et al., 2010). A similar range of mean TPH (104.5 mg kg^{-1}) has been reported in soils impacted with crude oil in the Niger Delta (Iwegbue et al., 2007). Higher TPH content (317.43 mg kg^{-1}) was also observed in Nigeria from Niger Delta soils (Aniekan et al., 2014); 1276 mg kg^{-1} observed in crude oil spill site in Kpean community in Rivers State, Nigeria (Gighi et al., 2012), and 5251.99 mg kg^{-1} recorded in soils impacted with petroleum in Olomoro, Delta State, Nigeria by Idodo-Umeh and Ogbeibu (2010). Although the initial concentration of hydrocarbon at the time of spillage was not known, natural degradation of the spilled oil by microbes over the period might have also affected the result of the amount of TPH recorded.y

3.3 Assessment of the extent of pollution

3.3.1 Contamination/Pollution Index

The contamination/pollution index (CPI) indicates the relationship between the measured concentration of metals in the soil and the background concentration (Lacutusu, 2002). The computed CPIs are shown in Tables 3 and 4. The CPI of metals in the crude oil impacted soils indicates that the majority of the studied metals (Fe, Zn, Cu, Cr, V, Pb, and Ni) had CPI values greater than 16 in all sites and depths, indicating excessive pollution, while the CPI for As and Mn were < 1, indicating slight contamination.

Table 3. Contamination/pollution index of metals for the first sampling year

Location	Depth	Pb		Cu		Cd		Mn		Fe		Zn		Ni		Cr		V		As	
		D	W	D	W	D	W	D	W	D	W	D	W	D	W	D	W	D	W	D	W
1	0-15cm	149	137	360	313	400	250	0.28	0.27	14.2	13.3	728	689	57.9	47.1	37.9	29.7	4.68	1.93	0.13	0.10
	15-30cm	83	68	160	140	200	240	0.24	0.26	13.4	9.6	586	547	50.5	41.7	27.1	24.4	3.51	0.78	0.05	0.03
2	0-15cm	159	151	280	267	150	130	0.32	0.26	16.6	16.3	606	572	72.1	62.6	24.0	21.0	6.10	2.99	0.14	0.09
	15-30cm	95	117	213	193	50	15	0.22	0.12	14.5	54.8	614	589	55.3	47.5	23.5	21.2	3.53	0.30	0.03	0.02
3	0-15cm	163	154	513	467	150	120	0.31	0.32	11.6	9.7	692	564	51.6	36.5	20.9	21.3	2.87	1.58	0.12	0.07
	15-30cm	71	75	220	180	50	40	0.31	0.29	10.4	8.8	656	519	49.2	29.5	15.2	17.8	1.10	0.50	0.01	0.01
4	0-15cm	181	166	413	393	700	520	0.46	0.47	20.1	15.5	1214	978	86.8	61.1	39.1	31.8	4.85	2.72	0.05	0.07
	15-30cm	146	80	307	240	300	283	0.31	0.29	16.6	13.0	1261	914	57.4	62.1	34.5	25.4	1.95	1.18	0.01	0.00
5	0-15cm	151	164	627	587	375	290	0.27	0.28	10.5	9.3	594	561	51.2	47.4	18.8	15.6	0.88	0.80	0.08	0.04
	15-30cm	64	71	313	233	25	255	0.23	0.24	6.9	8.1	608	575	42.9	46.4	18.0	13.1	0.01	0.17	0.01	0.01
6	0-15cm	156	144	393	287	325	215	0.28	0.24	15.5	11.0	628	544	124.7	105.8	25.2	22.5	1.42	1.78	0.09	0.08
	15-30cm	81	98	227	227	150	155	0.19	0.19	11.7	7.3	647	572	108.4	87.9	22.0	21.0	0.74	0.26	0.01	0.00
7	0-15cm	214	197	327	273	600	435	0.48	0.31	21.8	17.2	1247	908	91.6	82.6	33.4	27.4	4.19	4.24	0.11	0.04
	15-30cm	1225	81	253	207	150	130	0.26	0.19	15.7	13.4	1203	983	81.1	74.7	22.5	24.4	4.05	3.28	0.01	0.01
8	0-15cm	112	115	347	307	225	190	0.19	0.14	9.6	9.4	369	333	39.0	37.3	16.7	17.5	2.51	2.12	0.05	0.06
	15-30cm	63	75	193	220	100	58	0.15	0.10	6.7	6.9	358	356	37.0	33.9	13.3	10.6	1.64	0.79	0.01	0.00

Table 4. Contamination/pollution index of metals in the second sampling year

Location	Depth	Pb		Cu		Cd		Mn		Fe		Zn		Ni		Cr		V		As	
		D	W	D	W	D	W	D	W	D	W	D	W	D	W	D	W	D	W	D	W
1	0-15cm	128	122	277	260	358	275	0.24	0.23	13.1	10.5	581	561	51.3	37.8	17.4	23.1	3.31	1.68	0.12	0.10
	15-30cm	66	66	130	124	53	130	0.21	0.20	8.7	7.1	546	509	32.3	36.7	17.6	20.1	2.53	2.01	0.00	0.00
2	0-15cm	140	112	265	287	160	208	0.26	0.25	13.7	13.4	513	500	55.0	55.5	20.6	21.3	5.97	1.86	0.06	0.04
	15-30cm	86	75	132	171	208	5	0.18	0.16	8.7	8.3	427	407	46.8	41.7	20.2	18.0	3.37	0.43	0.01	0.01
3	0-15cm	119	123	361	365	143	243	0.27	0.25	8.2	6.5	533	495	38.1	30.9	18.8	16.4	2.51	1.44	0.11	0.06
	15-30cm	65	48	206	163	53	60	0.20	0.17	6.9	5.3	514	446	46.1	18.0	16.9	11.7	2.30	1.18	0.00	0.00
4	0-15cm	160	122	277	260	550	608	0.27	0.33	16.4	13.9	795	654	64.9	50.8	31.1	24.8	2.85	2.01	0.04	0.06
	15-30cm	123	56	199	119	330	293	0.19	0.23	13.8	12.7	621	539	47.6	56.1	33.4	26.6	2.55	0.79	0.01	0.00
5	0-15cm	115	138	391	407	303	255	0.22	0.20	8.9	7.3	541	488	41.8	45.4	16.3	12.4	0.84	0.87	0.12	0.10
	15-30cm	50	61	156	220	140	208	0.15	0.14	7.9	5.5	518	444	42.3	41.7	11.6	10.9	0.68	0.30	0.01	0.00
6	0-15cm	133	118	206	187	323	120	0.21	0.20	13.4	12.4	521	458	98.1	91.3	21.3	19.0	1.63	1.37	0.10	0.10
	15-30cm	55	72	117	85	100	33	0.13	0.15	10.0	11.7	421	413	81.3	71.2	21.4	19.5	1.01	0.80	0.01	0.00
7	0-15cm	158	160	197	130	510	263	0.29	0.26	16.6	13.7	907	758	68.6	55.9	25.2	22.6	2.60	2.45	0.06	0.11
	15-30cm	93	70	106	62	78	25	0.22	0.14	13.4	9.4	762	661	55.9	60.5	22.7	21.6	2.76	2.51	0.01	0.01
8	0-15cm	78	71	280	222	33	128	0.20	0.15	8.6	8.3	288	235	45.5	43.7	12.4	15.4	2.01	0.88	0.07	0.12
	15-30cm	42	46	185	79	65	43	0.13	0.09	6.6	7.5	243	202	41.9	39.6	10.7	13.5	0.71	1.03	0.00	0.01

The CPI values for the metals did not show a remarkable seasonal difference. However, the CPI value for the metals during the second sampling year was lower than that obtained in the first sampling period. A similar range of CPI has been reported in contaminated environmental media (Etchie et al., 2011), while higher CPI values have been reported in polluted sediments (Fagbote and Olanipekun, 2010) and at an industrial contaminated site in Pakistan (Malik et al., 2010).

3.3.2 Geoaccumulation index (I_{geo})

The I_{geo} values of the metals in the soils are shown in Tables 5 and 6 for the first and second sampling years, respectively. The Igeo sequence was as follows: Zn > Cu > Cd > Pb > Ni > Cr > Fe > V > As > Mn for both years. The Igeo of Cu, Cd, Zn, Ni, and Pb falls into Igeo class 7 (i.e.,> 5) in both years, which indicates that the soils were extremely polluted with Cu, Cd, Zn, Ni, and Pb. However, the Igeo values of As, V, and Mn fall into Igeo class 1 (i.e., < 0), indicating that the soils were not polluted with As, V, and Mn at any site or depth in either year.

3.3.3 Enrichment factor

The computed enrichment factors (Er) for the studied metals are displayed in Tables 7 and 8. Heavy metal enrichment factors follow the order Pb>Cd>Zn>Cu>Cr>Ni>Mn>As>V for the two sampling years. Generally, the EF of metals was higher in the dry season than in the wet season. Also, higher EFS were obtained for the metals in the first sampling year compared with the second sampling year. As the EF values increase, the contributions of the anthropogenic origins also increase. Metal enrichment in these soils may be due to oil spills and related anthropogenic activities in this area.

3.3.4 Pollution load index (PLI)

PLI provides a comparative means of assessing site quality, where a value of PLI < 1 denotes perfection; PLI = 1 presents a baseline level of pollutant; and PLI > 1 indicates deteriorating site quality. The computed PLI for this study is shown in Tables 9 and 10. The pollution load index in the first year ranged from 5.72 to 30.8 and 0.00 to 24.8 for dry and wet seasons, respectively. While the PLI for the second year ranged from 6.48 to 21.7 and 6.02 to 19.6, corresponding to the dry and wet seasons, respectively. The PLI of most sites and depths was more than 1, indicating deteriorating site quality. The result of the pollution load index (PLI) also indicates that site 7 with PLI mean value of 30.8 and 23.1 for dry and wet season, respectively, in the first sampling year has the highest heavy metal load. In contrast, site 8 with a PLI mean value of 9.01 and 0.00 for the dry and wet seasons, respectively, the first sampling year recorded the least metal load.

3.3.5 Correlation Analysis

The ‘ ‘Pearson’s correlation coefficients of metals and TPH studied are shown in Tables 11 and 12. The results of the correlation analysis showed similar patterns between the parameters investigated in this study for the first and second years. In both years, a negative correlation was observed between pH and metals. This observation indicates that pH has no effect on metals in the soils. However, there was a strong positive correlation between TPH and metals in both years which indicate that TPH and metals originate from the same anthropogenic source, such as oil spillage and associated activities. Also, there was positive strong correlation between Cu/Pb, Cd/Pb, Mn/Cd, Fe/Pb, Fe/Mn, Zn/Cd, Zn/Mn, Zn/Fe, Cr/Pb, Cr/Cd, Cr/Mn, Cr/Fe, Cr/Zn, V/Pb, V/Fe, V/Zn, V/Mn, As/Pb, As/Cu, and As/Mn. The correlation pattern of these metals in this study, observed in both years, suggests that they exist in the soils in the Fe and Mn oxide phases. This result agrees with that of Osam et al. (2011) who reported a positive correlation between TPH and metals at an oil-polluted site in Omoko, Nigeria.

Table 5. Geoaccumulation index of metals during the first sampling year

Location	Depth	Pb		Cu		Cd		Mn		Fe		Zn		Ni		Cr		V		As	
		D	W	D	W	D	W	D	W	D	W	D	W	D	W	D	W	D	W	D	W
1	0-15cm	6.64	6.52	7.91	7.71	8.06	7.38	-2.41	-2.45	3.24	3.15	8.92	8.84	5.27	4.97	4.66	4.31	1.64	0.36	-3.50	-3.94
	15-30cm	5.79	5.50	6.74	6.54	7.06	7.32	-2.63	-2.54	3.16	2.68	8.61	8.51	5.07	4.80	4.17	4.02	1.23	-0.94	-5.00	-5.8
2	0-15cm	6.73	6.65	7.55	7.47	6.64	6.44	-2.21	-2.54	3.47	3.44	8.66	8.58	5.59	5.38	4.00	3.81	2.02	1.00	-3.47	-4.08
	15-30cm	5.98	6.29	7.15	7.01	5.06	3.32	-2.74	-3.60	3.27	5.19	8.68	8.62	5.20	4.98	3.97	3.82	1.23	-2.32	-5.85	-6.27
3	0-15cm	6.76	6.68	8.42	8.28	6.64	6.32	-2.29	-2.22	2.95	2.69	8.85	8.56	5.10	4.61	3.80	3.83	0.93	0.07	-3.63	-4.36
	15-30cm	5.57	5.64	7.20	6.91	5.06	4.74	-2.28	-2.37	2.80	2.56	8.77	8.44	5.03	4.30	3.34	3.57	-0.45	-1.59	-7.37	-7.0
4	0-15cm	6.92	6.79	8.11	8.04	8.87	8.44	-1.69	-1.66	3.75	3.37	9.66	9.35	5.86	5.35	4.70	4.41	1.69	0.86	-5.00	-4.36
	15-30cm	6.60	5.73	7.68	7.32	7.64	7.56	-2.29	-2.37	3.47	3.12	9.72	9.25	5.26	5.37	4.52	4.08	0.38	-0.34	-7.85	-10.2
5	0-15cm	6.65	6.78	8.71	8.61	7.97	7.60	-2.47	-2.41	2.81	2.64	8.63	8.55	5.09	4.98	3.65	3.38	-0.76	-0.91	-4.17	-5.17
	15-30cm	5.42	5.57	7.71	7.28	4.06	7.41	-2.68	-2.66	2.20	2.43	8.66	8.58	4.84	4.95	3.58	3.13	-7.49	-3.17	-7.17	-7.85
6	0-15cm	6.70	6.59	8.04	7.58	7.76	7.16	-2.41	-2.67	3.37	2.87	8.71	8.50	6.38	6.14	4.07	3.91	-0.08	0.25	-4.00	-4.17
	15-30cm	5.76	6.03	7.24	7.24	6.64	6.69	-2.95	-3.01	2.97	2.29	8.75	8.58	6.18	5.87	3.88	3.81	-1.02	-2.54	-7.17	-8.59
7	0-15cm	7.15	7.03	7.77	7.51	8.64	8.18	-1.66	-2.27	3.86	3.52	9.70	9.24	5.93	5.78	4.48	4.19	1.48	1.50	-3.80	-5.22
	15-30cm	9.68	5.76	7.40	7.11	6.64	6.44	-2.51	-3.01	3.39	3.16	9.65	9.36	5.76	5.64	3.91	4.02	1.43	1.13	-7.59	-7.59
8	0-15cm	6.22	6.26	7.85	7.68	7.23	6.99	-2.97	-3.38	2.68	2.65	7.95	7.80	4.70	4.64	3.48	3.55	0.74	0.50	-4.78	-4.56
	15-30cm	5.39	5.64	7.01	7.20	6.06	5.26	-3.33	-3.93	2.16	2.20	7.90	7.89	4.62	4.50	3.14	2.82	0.13	-0.92	-7.85	-9.17
Mean		**6.39**	**6.29**	**7.74**	**7.58**	**7.42**	**7.11**	**-2.41**	**-2.59**	**3.17**	**3.22**	**8.97**	**8.74**	**5.47**	**5.23**	**4.03**	**3.83**	**0.87**	**0.07**	**-4.85**	**-5.22**

Table 6. Geoaccumulation index of metal during the second sampling year

Location	Depth	Pb		Cu		Cd		Mn		Fe		Zn		Ni		Cr		V		As	
		D	W	D	W	D	W	D	W	D	W	D	W	D	W	D	W	D	W	D	W
1	0-15cm	6.42	6.35	7.53	7.44	7.90	7.52	-2.64	-2.68	3.13	2.81	8.60	8.55	5.10	4.66	3.54	3.94	1.14	0.16	-3.62	-3.96
	15-30cm	5.46	5.45	6.44	6.37	5.13	6.44	-2.83	-2.88	2.54	2.24	8.51	8.41	4.43	4.61	3.55	3.74	0.76	0.42	-8.59	-10.2
2	0-15cm	6.55	6.22	7.46	7.58	6.74	7.11	-2.54	-2.60	3.19	3.16	8.42	8.38	5.20	5.21	3.78	3.83	1.99	0.31	-4.68	-5.36
	15-30cm	5.83	5.65	6.47	6.84	7.11	1.74	-3.07	-3.26	2.53	2.47	8.15	8.08	4.96	4.80	3.75	3.58	1.17	-1.79	-8.17	-7.85
3	0-15cm	6.31	6.36	7.91	7.93	6.57	7.34	-2.47	-2.58	2.45	2.12	8.47	8.37	4.67	4.36	3.65	3.46	0.74	-0.06	-3.80	-4.65
	15-30cm	5.44	5.01	7.11	6.77	5.13	5.32	-2.89	-3.12	2.20	1.83	8.42	8.22	4.94	3.59	3.50	2.96	0.62	-0.34	-9.17	-10.2
4	0-15cm	6.73	6.35	7.53	7.44	8.52	8.66	-2.45	-2.18	3.45	3.22	9.05	8.77	5.44	5.08	4.37	4.05	0.93	0.42	-5.27	-4.68
	15-30cm	6.36	5.23	7.06	6.32	7.78	7.61	-2.95	-2.70	3.20	3.08	8.70	8.49	4.99	5.22	4.48	4.15	0.77	-0.92	-7.59	-10.2
5	0-15cm	6.27	6.52	8.03	8.09	7.66	7.41	-2.79	-2.89	2.57	2.29	8.50	8.35	4.80	4.92	3.44	3.05	-0.83	-0.79	-3.66	-3.96
	15-30cm	5.06	5.34	6.70	7.20	6.54	7.11	-3.35	-3.44	2.40	1.87	8.43	8.21	4.82	4.80	2.95	2.86	-1.13	-2.32	-8.17	-8.59
6	0-15cm	6.47	6.30	7.10	6.96	7.75	6.32	-2.86	-2.94	3.16	3.05	8.44	8.26	6.03	5.93	3.83	3.66	0.12	-0.13	-3.96	-3.94
	15-30cm	5.21	5.58	6.29	5.83	6.06	4.44	-3.52	-3.32	2.74	2.96	8.13	8.10	5.76	5.57	3.83	3.70	-0.57	-0.91	-7.85	-9.17
7	0-15cm	6.72	6.74	7.04	6.44	8.41	7.45	-2.35	-2.51	3.47	3.19	9.24	8.98	5.52	5.22	4.07	3.91	0.79	0.71	-4.75	-3.80
	15-30cm	5.95	5.55	6.15	5.38	5.69	4.06	-2.77	-3.41	3.15	2.64	8.99	8.78	5.22	5.33	3.92	3.85	0.88	0.74	-7.85	-7.49
8	0-15cm	5.70	5.56	7.55	7.21	4.44	6.41	-2.88	-3.28	2.52	2.46	7.59	7.29	4.92	4.87	3.05	3.36	0.42	-0.76	-4.44	-3.60
	15-30cm	4.80	4.95	6.95	5.72	5.44	4.82	-3.54	-4.07	2.14	2.33	7.34	7.07	4.81	4.72	2.84	3.17	-1.08	-0.55	-8.59	-7.59
Mean		**6.07**	**5.93**	**7.18**	**7.04**	**7.15**	**6.93**	**-2.83**	**-2.92**	**2.87**	**2.68**	**8.51**	**8.34**	**5.16**	**5.02**	**3.73**	**3.63**	**0.64**	**-0.15**	**-5.08**	**-4.89**

Table 7. Enrichment factor of As, Cd, Pb, Cr and Ni during the study period

		As				Cd				Pb				Cr				Ni			
		2013		2014		2013		2014		2013		2014		2013		2014		2013		2014	
	Depth	D	W	D	W	D	W	D	W	D	W	D	W	D	W	D	W	D	W	D	W
1	0-15cm	3.58	2.8	3.55	3.5	248	162	234	226	201	196	186	222	17.1	14.2	8.48	14	7.44	6.38	7.05	6.5
	15-30cm	1.33	1.09	0.17	0.07	130	216	52	158	119	136	144	177	12.9	16.3	12.9	18.1	6.8	7.87	6.68	9.38
2	0-15cm	3.12	2.08	1.64	1.04	72.7	68.8	101	133	182	177	196	159	9.2	8.2	9.6	10.2	7.85	6.95	7.27	7.48
	15-30cm	0.69	0.14	0.23	0.3	28.3	2.4	207	5	124	40	188	172	10.4	2.5	14.9	13.8	6.89	1.56	9.76	9.06
3	0-15cm	3.99	2.87	5.05	3.51	113	106	150	320	267	301	277	360	11.6	14	14.7	16.1	8.09	6.79	8.41	8.55
	15-30cm	0.33	0.51	0.14	0.09	49.6	39	65.5	97.1	129	160	180	173	9.3	12.8	15.7	14	8.51	6.03	12	6.1
4	0-15cm	0.89	1.8	0.91	1.6	296	289	289	376	171	206	185	167	12.4	13.1	12.1	11.4	7.8	7.11	7.15	6.58
	15-30cm	0.15	0.04	0.23	0.04	150	187	206	199	167	117	170	85	13.2	12.4	15.5	13.4	6.22	8.6	6.22	7.98
5	0-15cm	3.03	1.71	5.15	5.03	314	268	293	300	275	335	247	359	11.4	10.7	11.7	10.8	8.79	9.18	8.5	11.2
	15-30cm	0.58	0.31	0.23	0.27	215	272	153	327	176	168	121	211	16.7	10.4	9.38	12.8	11.2	10.4	9.68	13.8
6	0-15cm	2.31	2.9	2.75	3	182	169	208	83.3	193	250	190	181	10.4	13.1	10.2	9.8	14.6	17.4	13.2	13.3
	15-30cm	0.34	0.2	0.25	0.09	108	182	85.9	24	134	253	105	118	12	18.3	13.6	10.7	16.7	21.6	14.6	11
7	0-15cm	1.9	0.9	1.29	3.02	234	218	264	165	188	219	181	223	9.8	10.2	9.7	10.5	7.6	8.67	7.46	7.39
	15-30cm	0.19	0.22	0.02	0.34	87.6	83.4	50	23	149	117	132	143	9.1	11.6	10.8	14.7	9.3	10.1	7.55	11.6
8	0-15cm	2.17	2.59	3.06	5.71	209	174	32.5	133	220	234	173	163	11.2	11.9	9.2	11.9	7.33	7.18	9.53	9.55
	15-30cm	0.37	0.14	0.22	0.4	132	71.6	84.4	48.6	179	205	120	118	12.7	9.8	10.3	11.5	9.98	8.85	11.4	9.49
	MIN	0.15	0.04	0.02	0.04	28.3	2.36	32.5	5.18	119	40	105	84.8	9.1	2.5	8.48	9.77	6.22	1.56	6.22	6.1
	MAX	3.99	2.9	5.15	5.71	314	289	293	376	275	335	277	360	17.1	18.3	15.7	18.1	16.7	21.6	14.6	13.8
	MEAN	1.56	1.27	1.56	1.75	161	157	155	164	180	195	175	189	11.8	11.9	11.8	12.7	9.07	9.04	9.16	9.31

Table 8. Enrichment factor of Cu, V, Mn and Zn during the study period

		Cu				V				Mn				Zn			
		2013		2014		2013		2014		2013		2014		2013		2014	
Sites	Depth	D	W	D	W	D	W	D	W	D	W	D	W	D	W	D	W
1	0-15cm	54.6	50.2	45.4	53.4	1.97	0.86	1.5	0.95	3.15	3.25	2.89	3.51	126	127	108	131
	15-30cm	25.4	31.3	32.1	37.7	1.56	0.49	1.73	1.69	2.84	4.24	3.81	4.54	107	140	153	176
2	0-15cm	36.6	35.8	41.7	46.1	2.19	1.1	2.6	0.83	3.09	2.51	2.98	2.92	89.4	86.4	91.9	91.3
	15-30cm	31.6	7.8	33	44.3	1.45	0.03	2.32	0.31	2.45	0.36	3.25	2.97	104	26.3	121	120
3	0-15cm	94.9	104	95.3	120	1.48	0.97	1.83	1.32	4.16	5.23	5.23	6.07	146	143	160	186
	15-30cm	45	45.1	64.4	66	0.63	0.34	1.99	1.33	4.69	5.18	4.63	5.13	154	143	182	205
4	0-15cm	44.5	54.3	36.4	40.2	1.44	1.05	1.04	0.86	3.64	4.84	2.64	3.75	148	154	119	115
	15-30cm	39.4	40	31.1	20.3	0.7	0.54	1.1	0.37	2.92	3.52	2.22	2.88	185	172	110	104
5	0-15cm	128	135	94.9	120	0.5	0.51	0.57	0.71	4.08	4.79	3.85	4.37	139	147	149	163
	15-30cm	97.2	62.1	42.6	86.8	0.01	0	0.52	0.33	5.37	4.63	2.94	3.98	216	174	160	199
6	0-15cm	54.4	57.3	33.1	32.4	0.55	0.97	0.72	0.66	2.89	3.4	2.44	2.49	99.4	122	95.3	90.4
	15-30cm	41.7	66.7	25.2	15.7	0.38	0.21	0.6	0.41	2.62	4	2.06	2.04	135	191	103	86.7
7	0-15cm	32.8	34.2	25.5	20.5	1.15	1.47	0.93	1.07	3.45	2.85	2.79	3.04	140	129	134	136
	15-30cm	34.7	33.7	17.1	14.3	1.54	1.46	1.23	1.59	2.65	2.2	2.6	2.37	187	179	140	173
8	0-15cm	77.3	70.8	70	57.9	1.56	1.34	1.39	0.64	3.14	2.43	3.73	2.95	94.2	87.2	81.8	69.7
	15-30cm	63.3	68.5	60.2	22.5	1.46	0.68	0.64	0.81	3.52	2.25	3.06	1.87	131	127	89.5	65.6
	MIN	25.4	7.8	17.1	14.3	0.01	0	0.52	0.31	2.45	0.36	2.06	1.87	89	26	81.8	65.6
	MAX	128.5	135	95.3	120	2.19	1.47	2.6	1.69	5.37	5.23	5.23	6.07	216	191	182	205
	MEAN	56.4	56.1	46.7	49.9	1.16	0.75	1.29	0.87	3.42	3.48	3.2	3.43	138	134	125	132

Table 9. Pollution Load Index of metals during the first sampling year

Location	Depth	DRY SEASON											WET SEASON										
		Pb	Cu	Cd	Mn	Fe	Zn	Ni	Cr	V	As	PLI	Pb	Cu	Cd	Mn	Fe	Zn	Ni	Cr	V	As	PLI
1	0-15cm	149	360	400	0.28	14.2	728	57.9	37.9	4.68	0.13	**24.7**	137	313	250	0.27	13.3	689	47.1	29.7	1.93	0.1	**19.3**
	15-30cm	83	160	200	0.24	13.4	586	50.5	27.1	3.51	0.05	**16.1**	68	140	240	0.26	9.6	547	41.7	24.4	0.78	0.03	**12.2**
2	0-15cm	159	280	150	0.32	16.6	606	72.1	24	6.1	0.14	**22.4**	151	267	130	0.26	16.3	572	62.6	21	2.99	0.09	**18.4**
	15-30cm	95	213	50	0.22	14.5	614	55.3	23.5	3.53	0.03	**13.9**	117	193	15	0.12	54.8	589	47.5	21.2	0.3	0.02	**9.77**
3	0-15cm	163	513	150	0.31	11.6	692	51.6	20.9	2.87	0.12	**20.3**	154	467	120	0.32	9.7	564	36.5	21.3	1.58	0.07	**16.3**
	15-30cm	71	220	50	0.31	10.4	656	49.2	15.2	1.1	0.01	**10.3**	75	180	40	0.29	8.8	519	29.5	17.8	0.5	0.01	**8.46**
4	0-15cm	181	413	700	0.46	20.1	1214	86.8	39.1	4.85	0.05	**29.4**	166	393	520	0.47	15.5	978	61.1	31.8	2.72	0.07	**24.8**
	15-30cm	146	307	300	0.31	16.6	1261	57.4	34.5	1.95	0.01	**17.9**	80	240	283	0.29	13	914	62.1	25.4	1.18	0	**0**
5	0-15cm	151	627	375	0.27	10.5	594	51.2	18.8	0.88	0.08	**18.2**	164	587	290	0.28	9.3	561	47.4	15.6	0.8	0.04	**15.8**
	15-30cm	64	313	25	0.23	6.9	608	42.9	18	0.01	0.01	**5.72**	71	233	255	0.24	8.1	575	46.4	13.1	0.17	0.01	**9.31**
6	0-15cm	156	393	325	0.28	15.5	628	125	25.2	1.42	0.09	**21.6**	144	287	215	0.24	11	544	105.8	22.5	1.78	0.08	**18.4**
	15-30cm	81	227	150	0.19	11.7	647	108	22	0.74	0.01	**12.1**	98	227	155	0.19	7.3	572	87.9	21	0.26	0	**0**
7	0-15cm	214	327	600	0.48	21.8	1247	91.6	33.4	4.19	0.11	**30.8**	197	273	435	0.31	17.2	908	82.6	27.4	4.24	0.04	**23.1**
	15-30cm	1225	253	150	0.26	15.7	1203	81.1	22.5	4.05	0.01	**21**	81	207	130	0.19	13.4	983	74.7	24.4	3.28	0.01	**14.2**
8	0-15cm	112	347	225	0.19	9.6	369	39	16.7	2.51	0.05	**14.7**	115	307	190	0.14	9.4	333	37.3	17.5	2.12	0.06	**13.8**
	15-30cm	63	193	100	0.15	6.7	358	37	13.3	1.64	0.01	**9.01**	75	220	58	0.1	6.9	356	33.9	10.6	0.79	0	**0**
Mean		**125**	**320**	**258**	**0.28**	**13.5**	**750**	**66.3**	**24.5**	**2.75**	**0.05**	**19.1**	**117**	**287**	**208**	**0.25**	**14**	**639**	**56.3**	**21.3**	**1.58**	**0.04**	**16.1**

Table 10. Pollution Load Index of metals during the second sampling year

Location	Depth	DRY SEASON											WET										
		Pb	Cu	Cd	Mn	Fe	Zn	Ni	Cr	V	As	PLI	Pb	Cu	Cd	Mn	Fe	Zn	Ni	Cr	V	As	PLI
1	0-15cm	128	276.9	357.5	0.241	13.1	580.6	51.3	17.45	3.31	0.12	**19.6**	122.4	260.2	275	0.23	10.5	561.3	37.79	23.07	1.68	0.1	**16.7**
	15-30cm	65.8	129.7	52.5	0.21	8.71	545.8	32.3	17.57	2.53	0	**8.71**	65.68	123.9	130	0.2	7.07	509.2	36.74	20.07	2.01	0	**8.27**
2	0-15cm	140	264.8	160	0.258	13.7	512.6	55	20.61	5.97	0.06	**18.3**	111.6	286.7	207.5	0.25	13.4	499.6	55.47	21.31	1.86	0.04	**15.6**
	15-30cm	85.6	132.5	207.5	0.178	8.65	427.1	46.8	20.17	3.37	0.01	**11**	75.08	171.2	5	0.16	8.32	406.5	41.74	17.99	0.43	0.01	**6.11**
3	0-15cm	119	361.3	142.5	0.271	8.17	532.6	38.1	18.82	2.51	0.11	**16.4**	123.2	364.7	242.5	0.25	6.52	494.6	30.89	16.45	1.44	0.06	**14.4**
	15-30cm	65.2	206.5	52.5	0.203	6.9	513.7	46.1	16.94	2.3	0	**8.66**	48.27	163.2	60	0.17	5.32	445.9	18	11.71	1.18	0	**6.02**
4	0-15cm	160	277.3	550	0.274	16.4	794.6	64.9	31.06	2.85	0.04	**21.3**	122.1	260.4	607.5	0.33	13.9	653.9	50.79	24.8	2.01	0.06	**18.7**
	15-30cm	123	199.4	330	0.195	13.8	621.4	47.6	33.43	2.55	0.01	**14.6**	56.41	119.5	292.5	0.23	12.7	538.8	56.05	26.57	0.79	0	**9.29**
5	0-15cm	115	391.3	302.5	0.217	8.88	540.9	41.8	16.31	0.84	0.12	**15.8**	137.7	407.1	255	0.2	7.32	487.6	45.42	12.43	0.87	0.1	**14.7**
	15-30cm	50.1	156.1	140	0.147	7.89	517.6	42.3	11.6	0.68	0.01	**8.06**	60.53	220.4	207.5	0.14	5.47	443.8	41.74	10.92	0.3	0	**7.4**
6	0-15cm	133	205.5	322.5	0.207	13.4	520.9	98.1	21.3	1.63	0.1	**18.3**	117.8	186.9	120	0.2	12.4	458.1	91.26	18.97	1.37	0.1	**15.2**
	15-30cm	55.4	117.2	100	0.131	10	420.8	81.3	21.39	1.01	0.01	**9.15**	71.88	85	32.5	0.15	11.7	412.6	71.16	19.46	0.8	0	**7.27**
7	0-15cm	158	196.7	510	0.294	16.6	907.4	68.6	25.24	2.6	0.06	**21.7**	160.2	130.1	262.5	0.26	13.7	757.7	55.95	22.55	2.45	0.11	**19.6**
	15-30cm	92.8	106.2	77.5	0.22	13.4	762.3	55.9	22.65	2.76	0.01	**11.5**	70.44	62.4	25	0.14	9.38	661.2	60.47	21.62	2.51	0.01	**8.75**
8	0-15cm	78.1	280.1	32.5	0.204	8.62	287.9	45.5	12.4	2.01	0.07	**11.1**	70.56	222.1	127.5	0.15	8.26	235.4	43.74	15.45	0.88	0.12	**11.6**
	15-30cm	41.9	185.3	65	0.129	6.63	242.5	41.9	10.72	0.71	0	**6.48**	46.44	78.8	42.5	0.09	7.53	201.8	39.58	13.52	1.03	0.01	**6.24**
Mean		**101**	**218**	**212.5**	**0.211**	**10.9**	**545.6**	**53.6**	**19.89**	**2.34**	**0.04**	**15.2**	**91.27**	**196.7**	**182.5**	**0.2**	**9.59**	**485.6**	**48.63**	**18.54**	**1.35**	**0.05**	**13.4**

A similar correlation pattern among metals in soils in the Niger Delta, Nigeria, was reported by Aniekan et al. [43].

Table 11. Correlation Analysis First Sampling Year, 2013

	Pb	Cu	Cd	Mn	Fe	Zn	Ni	Cr	V	As	TPH	pH
Dry season												
Pb	1.00	0.60*	0.76**	0.80**	0.78**	0.59*	0.44	0.66*	0.55*	0.70**	0.88**	-0.72**
Cu		1.00	0.49	0.33	0.06	0.09	0.05	0.12	-0.08	0.53*	0.52*	-0.34
Cd			1.00	0.75**	0.64*	0.58*	0.38	0.74**	0.32	0.37	0.76**	-0.54*
Mn				1.00	0.81**	0.74**	0.38	0.67*	0.49	0.41	0.84**	-0.53*
Fe					1.00	0.78**	0.60*	0.81**	0.69*	0.36	0.77**	-0.56*
Zn						1.00	0.40	0.70**	0.36	-0.05	0.61*	-0.52*
Ni							1.00	0.39	0.13	0.18	0.58*	-0.44
Cr								1.00	0.58*	0.34	0.67*	-0.30
V									1.00	0.52*	0.47	-0.44
As										1.00	0.58*	-0.44
TPH											1.00	-0.64*
pH												1.00
Wet season												
Pb	1.00	0.67*	0.52*	0.49	0.16	0.26	0.33	0.43	0.61*	0.70**	0.76**	-0.77**
Cu		1.00	0.36	0.43	-0.17	0.02	-0.07	0.01	0.14	0.48	0.53*	-0.46
Cd			1.00	0.73**	-0.22	0.59*	0.32	0.57*	0.46	0.28	0.65*	-0.35
Mn				1.00	-0.21	0.57*	0.09	0.61*	0.34	0.40	0.82**	-0.30
Fe					1.00	0.14	0.00	0.20	-0.03	-0.02	-0.07	0.01
Zn						1.00	0.44	0.75**	0.55*	-0.04	0.64*	-0.05
Ni							1.00	0.40	0.40	0.11	0.36	-0.19
Cr								1.00	0.57*	0.42	0.76*	-0.40
V									1.00	0.47	0.65*	-0.59*
As										1.00	0.60*	-0.77**
TPH											1.00	-0.56*
pH												1.00

***Pearson Correlation is significant at the 0.01 level (1-tailed)*Pearson Correlation is significant at the 0.05 level (1-tailed)*

Table 12. Correlation Analysis Second Sampling Year, 2014

	Pb	Cu	Cd	Mn	Fe	Zn	Ni	Cr	V	As	TPH	pH
Dry season												
Pb	1.00	0.49	0.83**	0.85**	0.83**	0.68*	0.37	0.66*	0.53*	0.58*	0.88**	-0.59*
Cu		1.00	0.30	0.51*	0.02	-0.01	-0.20	-0.06	0.08	0.82**	0.42	-0.17
Cd			1.00	0.57*	0.78**	0.68*	0.41	0.65*	0.15	0.38	0.74**	-0.43
Mn				1.00	0.63*	0.70**	0.06	0.44	0.59*	0.53*	0.84**	-0.64*
Fe					1.00	0.78**	0.56*	0.78**	0.46	0.19	0.75**	-0.64*
Zn						1.00	0.25	0.69*	0.28	0.07	0.73**	-0.63*
Ni							1.00	0.39	-0.04	0.14	0.47	-0.37
Cr								1.00	0.36	-0.09	0.64*	-0.27
V									1.00	0.10	0.31	-0.17
As										1.00	0.52*	-0.38
TPH											1.00	-0.64*
pH												1.00
Wet season												
Pb	1.00	0.58*	0.55*	0.70**	0.47	0.58*	0.25	0.29	0.45	0.75**	0.80**	-0.78**
Cu		1.00	0.50*	0.47	-0.13	0.04	-0.25	-0.23	-0.12	0.52*	0.40	-0.53*
Cd			1.00	0.85**	0.44	0.51*	-0.02	0.43	0.27	0.37	0.72**	-0.31
Mn				1.00	0.58*	0.68*	0.05	0.61*	0.49	0.39	0.88**	-0.52*
Fe					1.00	0.49	0.68*	0.82**	0.43	0.28	0.55*	-0.31
Zn						1.00	0.18	0.62*	0.69*	0.13	0.76**	-0.35
Ni							1.00	0.42	0.13	0.20	0.20	-0.10
Cr								1.00	0.54*	0.07	0.55*	-0.19
V									1.00	0.22	0.63*	-0.41
As										1.00	0.52*	-0.82**
TPH											1.00	-0.56*
pH												1.00

***Pearson Correlation is significant at the 0.01 level (1-tailed)*Pearson Correlation is significant at the 0.05 level (1-tailed)*

3.5.6 Principal Component Analysis (PCA)

PCA is a reduction method that correlates attributes and identifies orthogonal linear recombinations of the attributes that summarize the principal sources of variability in the data (Kaplunovsky, 2004). PCA was used to determine the sources of metals in the soil impacted by crude oil. The factors obtained were rotated using a Varimax-normalized algorithm, which facilitates easy interpretation of the principal component loadings and maximization of the variance explained by the extracted components. The PCA results for metals in crude oil-impacted soils are displayed in Figures 2-5.

In the first year (dry season), three components or factors were extracted, accounting for 80.49% of the total variance. Factor 1 accounted for 57.48% of the total variance and was heavily dominated by Cd, Cr, NI, Mn, Zn, Fe, and TPH. The association of metals in the factor with TPH suggests that the concentration of these metals in the soil arises from the crude oil spillage. Additionally, this association indicates that Cd, Cr, Niand Zn are present in the Fe-Mn oxides phase in the crude oil , and Zn are present in the Fe-Mn oxide phase of the crude oil. Furthermore, Zn is present in the Fe-Mn oxide phase of the crude oil-impacted soil. Factor 2 accounts for 13.8% of the total variance and has positive loadings in Pb, Cu and As. The factor indicates that Pb, Cu, and As in the impacted soil are from a common source. As and Cu pollution can result from agricultural activities such as the application of organic manure and pesticides. Factor 3 accounts for 9.21% of the total variance and was dominated by V. This indicates that the source of V in the crude oil-impacted soils was different from that of the other metals. In the wet season of the first sampling year, four components were extracted, accounting for 83.34% of the total variance. Factor 1 accounts for 44.94% of the total variance and has positive loadings for Cd, Cr, Mn, Zn, and TPH. This factor indicates that Cd, Cr, Mn, and Zn in these soils are associated with crude oil spillage. Factor 2 accounted for 17.44% of the total variance with high positive loadings in Pb, Cu, and As.

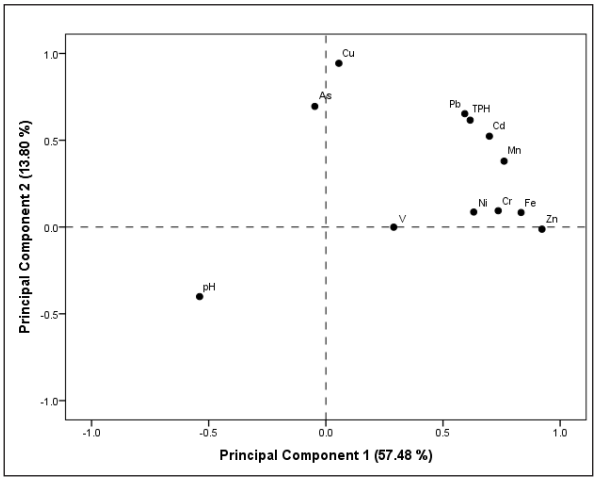

Figure 2. The loading plot of PCA of heavy metals for the first year in the dry season.

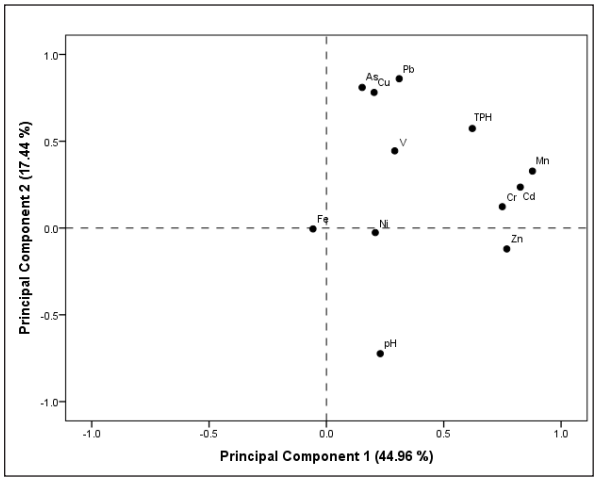

Figure 3. The loading plot of PCA of heavy metals for the first year in the wet season.

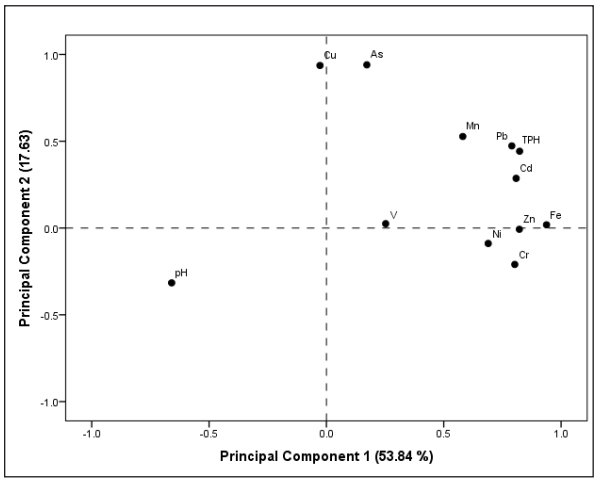

Figure 4. The loading plot of PCA of heavy metals for the second year in the dry season.

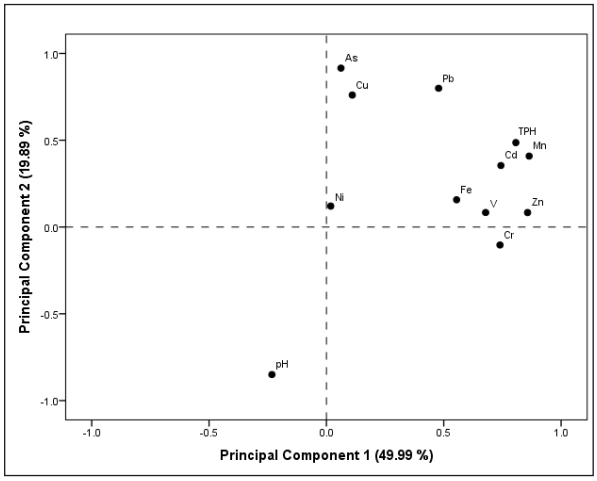

Figure 5. The loading plot of PCA of heavy metals for the second year in the wet season

The sources of Pb, Cu, and As have been previously described above. Factor 3 accounted for 11.39% of the total variance and was dominated by Ni and V. The Ni/V ratio has been used as an indicator for differentiating the origins of crude oil. Factor 4 accounted for 9.55% of the total variance

with positive loading in Fe. Factor 4 indicates that the sources of Fe in the impacted soils were entirely different from those of the other metals. In the second year, three components were extracted, accounting for 81.86% of the total variance. Factor 1 accounted for 53.84% of the total variance and was heavily dominated by Cd, Pb, Cr, Ni, Mn, Fe, Zn, and TPH. Again, as discussed earlier, these concentrations of these metals could possibly be from crude oil spillage and association with Fe-Mn oxides. Factor 2 accounted for 17.63% of the total variance and was dominated by Cu and V with moderate loadings of Mn. Factor 3, accounting for 10.39% of the total variance, was dominated by V and moderate loading in Mn. For the second year's wet season, three factors were extracted, accounting for 81.25% of the total variance. Factor 1 accounted for 49.99% of the total variance and was heavily dominated by Cd, Cr, Zn, Mn, Fe, V, and TPH, while Factor 2, accounting for 19.89% of the total variance, was dominated by Pb, Cu, and As. As mentioned earlier, the metals in factor are associated with crude oil spillage.

4. Conclusion

The spatiotemporal dynamics of selected physicochemical properties, metals, and total petroleum hydrocarbons (TPH) contents in crude oil-impacted soil in part of the Niger Delta Region of Nigeria were investigated in this study. The results showed that impacted sites generally had higher concentrations of metals than the control site. Additionally, the results revealed the presence of spatiotemporal variations in the studied physicochemical properties, as well as the contents of metals and total petroleum hydrocarbons in the impacted soil. The concentrations of metals in this study were higher than their respective FAO/WHO permissible limits. The pollution indices indicated that the soil in the study area is polluted with metals as a result of the anthropogenic impact of crude oil exploration and exploitation. The clean-up of the impacted site is recommended in order to restore the soil's fertility for productive agricultural activities, which are the major source of economic survival of the inhabitants in the study area.

References

Abii, T.A. and Nwosu, P.C. (2009). The effect of oil spillage on the soil of Eleme in Rivers state of the Niger Delta area of Nigeria. Research Journal of Environmental Science, 3: 316-320.

Agbogidi, O.M., Okonta, B.C. and Dotor, D.E. (2009). Social-economic and environmental impact of crude oil exploration and production on agricultural production: a case study of Edjeba and Kokori communities in Delta state of Nigeria. Global Journal of Environmental Science, 4: 171-176.

Akani, N.P., Amadi, E.N. and Braide, S.A. (2009). Long-term effects of spilled crude oil on a loam soil in Ejama-Ebubu in Rivers State, Nigeria. Nigerian Journal of Microbiology, 23: 1939-1947.

Ambo, A.I., Saleh, S.A., Igboanusi, P. and Iyakwari, S. (2013). Chemical composition analysis of soil from selected oil producing communities in the Niger Delta region of Nigeria. International Journal of Basic and Applied Chemical Science, 3: 84-92.

Aniekan, E., Aniedionbong, U. and Therese, N. (2014). The concentrations of potentially toxic elements and total hydrocarbon in soils of Niger Delta Region (Nigeria). Journal of Environmental and Earth Science 4: 2224-3216.

Bada, B.S. and Olarinre, T.A. (2012). Characteristics of soils and heavy metal content of vegetation in oil spill impacted land in Nigeria. Proceedings of the Annual International Conference on Soils, Sediments, Water and Energy, 17: 1-11.

Bakker, M.I., Casado, B., Koerselman, J.W., Tolls, J. and Kolloffel, C. (2000). Polycyclic aromatic hydrocarbons in soils and plant samples from the vicinity of an oil refinery. Science of Total Environment, 263: 91-100.

Bouyouocas, G.H. (1962). Determination of particle sizes in soil. Journal of Agronomy, 43: 434-438.

Chibowski, S. (2000). Studies of radioactive contaminations and heavy metal content in vegetables from Lublin, Poland. Polish Journal of Environmental Studies, 9: 247-249.

Department of Petroleum Resources (DPR) (2018). Environmental guideline and standards for the petroleum industry in Nigeria (Revised Edition). Department of Petroleum Resources, Ministry of Petroleum and Mineral Resources, Abuja, Nigeria.

Edema, N.E., Obadoni, B.O., Erhenhi, H. and Osakwuni, U.E. (2009). Ecophytochemical studies of plants in a crude oil polluted terrestrial habitat in Iwhrekan Ughelli, Delta State. Nature and Science, 7: 49-52.

Erhayimwen, A.M., Jayeola, O.E. and Efenudu I.U. (2024). Assessment of soil phosphorus forms on oil palm plantation in Songhai, Amukpe Delta State, Nigeria. Journal of Agriculture, Food and Ecology 2(2): 15–20

Essiett, U.A., Effiong, G.S., Ogbemudia, F.O. and Bruno, E.J. (2010). Heavy metal concentrations in plants growing in crude oil contaminated soil of Akwa Ibom state, South Eastern Nigeria. African Journal of Pharmacy and Pharmacology, 4: 565-470.

Etchie, T.O., Etchie, A.T. and Adewuyi, G.O. (2011). Source identification of chemical contaminants in environmental media of a rural settlement. Research Journal of Environmental Science, 5: 730-740

Fagbote, O.E. and Olanipekun, E.O. (2010). Evaluation of status of heavy metal pollution of the soil and plants (Chromolena Odorata) of Agbabu Bitumen deposit area, Nigeria" " " "", American and Eurasian Journal of Scientific Research, 5: 241-248.

FAO (2006). Sampling methods for the monitoring of the soil quality parameters https://www.fao.org/fileadmin/user_upload/faowater/docs/WASAG/Soil_sampling_FG.pdf Accessed on 10th February, 2025.

FAO (2021). Standard operating procedure for soil pH determination https://openknowledge.fao.org/server/api/core/bitstreams/6ad6862a-eadc-437c-b359-ef14cb687222/content Accessed on 10th February, 2025.

FAO/WHO (2011). Joint FAO/WHO food standards programme codex committee on contaminants in foods. Working document for information and use in discussions related to contaminants and toxins in the Gsctff. Fifth Session. Hague, The Netherlands. pp. 90.

Fatoba, P.O., Ogunkunle, C.O. and Ihaza, C.O. (2015). Assessment of metal pollution of soil and diagnostic species associated with oil spills in the Niger Delta, Nigeria. Environmental Research, Engineering and Management, 71: 13-22.

Gighi, J.G., Tanee, F.B.G. and Albert, E. (2012). Post-impact soil assessments of crude oil spill site in Kpean community in Khana LGA of Rivers State, Nigeria. Journal of Science, 2: 2325-2336.

He, Z.L., Xiao, E.Y. and Stooffelia, P.T. (2005). Trace elements

in agro-ecosystems and impacts on the environment. Journal of Trace Elements and Medical Biology, 19: 307-317.

Hu, X., Zhang, Y., Luo, J., Wang, T., Lian, H. and Ding, Z. (2011). Bioaccessibility and health risk of arsenic, mercury and other heavy metal in urban street dust form a mega-city, Nanjing China. Environmental Pollution, 159: 1215-1221

Ideriah, T.J.K., Ikpe, F.N. and Nwanjoku, F.N. (2013). Distribution and speciation of heavy metals in crude oil concentrated soils from Niger Delta, Nigeria. World Environment, 3: 18-28.

Idodo-Umeh, G. and Ogbeibu, A.E. (2010). Bioaccumulation of heavy metals in cassava tubers and plantain fruits grown in soils impacted with petroleum and non-petroleum impacted activities" " " " "", Research Journal of Environmental Science, 4: 33-41.

Ikhajiagbe, B., Chijioke-Osuji, C.C. and Osazee, J.O. (2014). Heavy metal contents and microbial diversity of waste engine oil-polluted soil in some public and commercial centres in Benin city metropolis, Nigeria. The Bioscientist, 2: 41-53

Iwegbue, C.M.A. (2014). Impact of land use types on the concentrations of metals in soils of urban environment in Nigeria. Environmental Earth Science, 72: 4567–4585

Iwegbue, C.M.A. Egobueze, F.E. and Opune, K. (2006). Preliminary assessment of heavy metal levels of soil of an oil field in the Niger Delta, Nigeria. International Journal of Environmental Science and Technology, 3: 167-172.

Iwegbue, C.M.A., Bassey, F.I., Nwajei, G.E. and Tsafe, A.I. (2013). Assessments of heavy metal contamination in soils around cassava processing mills in sub-urban areas of Delta State, Southern Nigeria. Nigerian Journal of Basic and Applied Science, 21: 96-104.

Iwegbue, C.M.A., Lari, B., Osakwe, S.A., Tesi, G.O., Nwajei, G.E. and Martincigh, B.S. (2018). Distribution, sources and ecological risks of metals in surficial sediments of the Forcados River and its Estuary, Niger Delta, Nigeria. Environmental Earth Sciences, 77: 227

Iwegbue, C.M.A., Nwajei, G.E. and Arimoro, F.O. (2007). Characteristic levels of total petroleum hydrocarbons in soil, sediment and surface water of an oil impacted area in the Niger Delta. Pakistan Journal of Science and Industrial Research, 50: 247-250

Iwegbue, C.M.A., Osakwe, S.A., Elokozie, C.I. and Nwajei, G.E. (2015). Concentrations, human and ecological risks of metals in soils in the vicinity of asphalt plants in Delta State, Nigeria. Jordan Journal of Earth and Environmental Sciences, 7: 49-63.

Iwegbue, C.M.A., Williams, E.S. and Isirimah, N.O. (2009). Study of heavy metal distribution in soils impacted with crude oil in southern Nigeria. Soil and Sediment Contamination, 18: 136-143.

Jaboro, A.G. and Omonigho, S.E. (2019). Dominant bacterial and archaeal phyla associated with top soils sourced from commercial farm holding in Delta State, Nigeria. J. Appl. Sci. Environ. Manage. 23(1): 13–19.

Kaplunovsky, A.S. (2004). Factor analysis in environmental studies. Journal of Science and Engineering, 2: 54-94

Lacutusu, R. (2002). Appraising levels of contamination and pollution with heavy metals. European Soil Research, 5: 51-59.

Lloyd, A.D. and Solomon, A.B. (2002). The impact of accidental oil spill on cultivated and natural vegetation in a wetland Area of Niger Delta, Nigeria. Journal of the Human Environment, 31: 441- 442

Malik, R.N., Husain, S.Z. and Nazir, I. (2010). Heavy metal contamination and accumulation in soil and wild plant species from industrial areas of Islamabad, Pakistan. Pakistan Journal of Botany, 42: 291-301.

Mihaly-Cozmuta, A.L., Viman, G. and Varga, C. (2005). Spectrometric methods used to determine heavy metals and total cyanides in accidental polluted soils"""""""""", American Journal of Applied Science, 2: 358-362.

NEST (1991). ' 'Nigeria's Threatened Environment: A National Profile. Environmental Study/Action Team, NEST, Ibadan.

Nkwocha, E.E. and Duru, P.O. (2010). Micro-analytical study on the effect of oil pollution on local plant species and food crops. Advances in Bioresearch, 1: 189-198.

Nwachukwu, M.A. Feng, H. and Alinnor, J. (2010). Assessment of heavy metal pollution in soil and their implications within mechanic villages. International Journal of Environmental Science and Technology, 7: 347-358.

Nwadinigwe A.O. and Onyeidu, E. (2012). Bioremediation of crude oil polluted soil using bacteria monitored through soya bean productivity. Polish Journal of Environmental Studies, 21: 171-176.

Nwaichi, E.O., Chuku, L.C. and Ighoavwogan, E. (2016). Polycyclic aromatic hydrocarbons and selected heavy metals in some oil polluted sites in Delta State Nigeria. Journal of Environmental Protection, 7: 1389-1410

Nwajei, G.E. (2009). Trace Elements in soils and vegetations in the vicinity of Shell Petroleum Development Company operating area in Ughelli, Delta State of Nigeria. American-Eurasian Journal of Sustainable Agriculture, 3: 574-578.

Nwajei, G.E. (2011). Assessment of pollution trend of heavy metals in soils in the vicinity of Nigerian Gas Company in Ughelli, Delta State. International Journal of Biological and Chemical Science, 5: 845-850.

Nwandinigwe, C.A., Udo, G.J. and Nwandinigwe, A.O. (2014). Seasonal variations of some heavy metals concentrations in sediment samples around major tributaries in Ibeno coastal area, Niger Delta, Nigeria. International Journal of Scientific and Technological Research, 3: 254-265.

Nwandinigwe, C.A., Udo, G.J., Nwadinigwe, A.O. and Ubuo, E.E. (2014). Dry and wet 'seasons' dynamics in concentrations of Ni, V, Cd, Pb, Mn, Fe, Co, and Zn in soil samples within farm lands in Ibeno Coastal Area, Akwa Ibom State, Niger Delta, Nigeria. International Journal of Scientific and Technological Research, 3: 96-106.

Obi-Iyeke, G.E. (2022). Effect of crude oil spillage on plant species and diversity. Journal of Biodiversity and Environmental Sciences, 20: 29-40.

Odjuvwuederhie, I., Douglaston, G.O. and Adun, N.F. (2006). The effect of oil spillage on yield and farm income in Delta State Nigeria. Journal of Central European Agriculture, 7: 41-48.

Ogboi, E. (2012). Heavy metal movement in crude oil polluted soil in Niger Delta region. Journal of Agricultural and Veterinary Sciences, 4: 71-78.

Ogri, O.R. (2001). A review of the Nigerian petroleum industry and associated environmental problems. Environmentalist, 21: 11-21.

Oluyemi, E.A., Feuyi, G. and Oyekunle, J.A.O. (2008). Seasonal variations in heavy metal concentrations in soil and some selected crops in a landfall in Nigeria. African Journal of Environmental Science and Technology, 2: 89-96.

Osam, M.U., Wegwu, M.O. and Uwakwe, A.A. (2011). The Omoku old pipeline oil spill: total hydrocarbon content of affected soils and the impact on the nutritive value of food crops. Archives of Applied Science Research, 3: 514-521.

Osuji, L.C. and Nwoye, I. (2007). An appraisal of the impact of petroleum hydrocarbons on soil fertility: the Owaza experience.

African journal of Agricultural Research, 2: 318-324.

Osuji, L.C. and Onojake, C.M. (2004). Trace heavy metals associated with crude oil: A case study of Ebocha-8 oil-spill-polluted site in Niger Delta, Nigeria. Chemistry and Biodiversity, 1: 1708-1715

Osuji, L.C. and Udoetok, S.G. (2008). Impact of contaminable hydrocarbons on some soil physicochemical properties. Journal of Oil Field Chemistry, 1: 25-34.

Osuji, L.C., Adesiyan, S.O. and Obute, G.C. (2004). Post impact of oil pollution in Agbada west plain of Niger Delta, Nigeria: field reconnaissance ant total extractable hydrocarbon content. Journal of Chemistry and Ecology, 1: 1569-1577.

Osuji, L.C., Idung, I.D. and Ojinnaka, C.M. (2006). Hydrocarbon speciation by finger printing techniques and diagnostic vanadium nickel ratio of Mgbede-20 oil impacted site in the Niger Delta basin of Nigeria" " " """, Environmental Forensics, 7: 259-265.

Shell Petroleum Development Company (SPDC) (2014). Oil spill in the Niger Delta monthly data for 2014. HSE-ENV, XII: 19-25.

Tesi, G.O., Ojegu, J.O. and Akporido, S.O. (2020). Distribution and risk of metals in soils of refuse dumpsites in some urban towns in Delta State, Nigeria. African Scientist, 21: 211-224

Tesi, G.O., Ojegu, J.O. and Akporido, S.O. (2020). Distribution and risk of metals in soils of refuse dumpsites in some urban towns in Delta State, Nigeria. African Scientist, 21(1): 211-224

Tse, A.C. and Nwankwo, A.C. (2013). An integrated geochemical and geoelectrical investigation of an ancient crude oil spill site in South East Portharcourt, Southern Nigeria. Ife Journal of Science, 15: 125-133.

Walkley, A. and Black, I.A. (1959). Determination of organic carbon in soils. Soil Science, 37: 27-38.

Wegwu, M.O., Uwakwe, A.A. and Enyi, C.N. (2011). Post-impact assessment of oil spilled sites: four years after recorded incidence. Annals of Biological Research, 2: 72-78.

Yakubu, M.B. (2007). Biological approach of oil spills remediation in the soil. African Journal of Biotechnology, 24: 2735-2739.

JJEES

Jordan Journal of Earth and Environmental Sciences

JJEES (2025) 16 (4): 391- 399
ISSN 1995-6681

Hydrogeochemical Characterization of Groundwater Resources in the Northern Part of Amman-Zarqa Basin, North-East El Mafraq/Jordan

Qaher N.Al Qadi, Sara M. Al-Khalidy,* Eid A. Al-Tarazi

Department of Earth Sciences and Environment, Faculty of Prince EL Hasan Bin Talal for Natural Resources and Environment, The Hashemite University, Zarqa, Jordan

Received on March 20, 2025, Accepted on May 11, 2025

Abstract

In one of the world's most water-scarce regions, the Amman-Zarqa Basin, specifically North-East Mafraq, Jordan, is a crucial groundwater resource. In this regard, this study focuses on the hydrogeochemical properties of groundwater within this area and its suitability for drinking and domestic use. Careful collection and analysis of groundwater samples in terms of physicochemical parameters like pH, total dissolved solids (TDS), electrical conductivity (EC) and major ions of nitrate (NO3-), sulphate (SO42), bicarbonate (HCO3-), chloride (Cl-), magnesium (Mg2+), calcium (Ca2+), potassium (K +), and sodium (Na +) were done. Our results show that groundwater quality was highly variable across the study area, which is a function of both natural geologic formations and human activities. However, most of the samples meet the World Health Organization (WHO) and Water Authority of Jordan (WAJ) drinking water standards, while some are found to be high in TDS, chloride, and nitrate, and then require treatment before use. Historical data from 1998 indicate that, while overall water quality has not changed remarkably, there have been increases in some areas of salinity and nitrate, illustrating the ongoing effect of agricultural practices and groundwater extraction. An important implication from this study is the critical need for continuous monitoring and management of groundwater resources in Amman-Zarqa Basin, North-East El Mafraq area to support the sustainability of this resource. The insights provide valuable information to policymakers and stakeholders, enabling the development of a strategy for protecting and managing groundwater and ensuring its long-term availability to cater to the growing population and agricultural needs in the region.

Keywords: *Groundwater; Quality Index; Quality Assessment; Amman-Zarqa Basin; Hydrogeochemistry North-East EL-Mafraq*

1. Introduction

Jordan relies on groundwater to meet the water demands of households, businesses, and farms; the country is the world's second most water-scarce (UNICEF, 2020; Radaideh, 2022). According to Radded (2005), Jordan extracts around 520 million cubic meters (MCM) of groundwater total. The agricultural sector consumes about 54% of this water, followed by municipal use at 40% and industrial use at 6% (Radded, 2005). The majority of Jordan's water comes from underground basins, which vary in volume and quality. These basins cover nearly the entire nation and account for approximately 61% of the country's total accessible water supply. Of these twelve basins, two are being underutilised, four are near their equilibrium abstraction limit, and six are being overextracted (Odeh et al., 2019). The overexploitation of groundwater resources has led to a decline in water quality and a reduction in the amount available for use (Jordan, Geography and Population, 2001). According to the Ministry of Water and Irrigation (2017), groundwater basins are heavily pumped from both public and private wells. Reikat and Al Kharabsheh (2020) note that groundwater levels have dropped significantly over the last several decades due to pumping that surpasses the aquifers' safe yield.

Groundwater levels have been steadily declining since the 1980s, and this trend has accelerated in recent decades due to rising abstraction to meet the demands of an expanding human population, increased migration from neighboring countries, and intensified agricultural development (MWI and BGR, 2017). Jordan relies heavily on groundwater due to the country's scarce surface water resources. Water levels have dropped, total dissolved solids (TDS) have increased, and groundwater flows westward instead of eastward because of these restrictions (BGR 2013). Since then, it has become critically necessary to preserve the region's current water resources (MWI, 2017). The goal of this study was to catalogue the hydrogeochemical characteristics of the groundwater in Jordan's North East El Mafraq, which is part of the Amman-Zarqa Basin.

2. Description of the study area

The study area is situated in the northern part of the Amman Zarqa Basin, including 35.67°W, 36.82°E, 32.40°N, and 31.70°S, with a total area of 3860 km² (95% of the basin area is in Jordan and 5% is in southern Syria). (USAID, 2000). Located between an elevation of 1460 m above sea level at Salkhad city in Jebel Al Arab in Syria and Amman the South direction (Al Shibli et al., 2017). The four governorates of Amman, Zarqa, Mafraq, and Balqa, which are densely populated, consider this basin as a main source of water. A

* Corresponding author e-mail: saramahommado205@gmail.com

particularly north-eastern part of the EL Mafraq basin was selected, covering an area of approximately 965 km². The water divisions with the neighboring basins' boundary can be roughly determined by (Yarmouk, Azraq-Dulail). The elevation of this basin ranges from 700 to 1200 meters, characterized by undulating topography in the west and flat areas in the east and south. The area covered by this study was approximately 50 km² out of a total of 985 km², and the elevation of the wells in the study area falls within the specified. The elevation of wells in the study area is within the elevation rangepproximately 50 km² out of a total of 985 km². The elevation of the wells in the study area ranges from 500 to 1,000 m above sea level. (Fig. 1).A semi-arid climate is present in this place, which is characterized by hot, dry summers and mild, wet winters. It has varied topography, featuring both flat plains and hilly terrains. The Amman-Zarqa basin is a key element in the larger Jordan Rift Valley system, which is of great importance in terms of regional hydrogeology. Agricultural activities represent our study area of the basin, for which traditional irrigation practices have a significant impact on the groundwater resources.

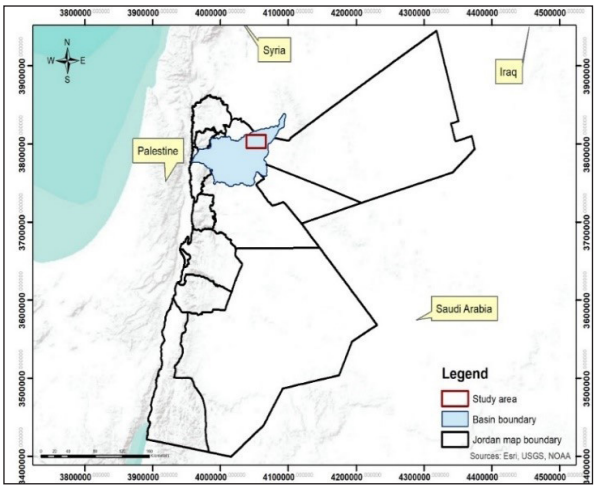

Figure 1. Location map of the study area

3. Hydrogeology of Northern Amman-Zarqa Basin

The Amman–Zarqa basin is one of the primary sources of fresh groundwater in Jordan. The basin is divided into three main aquifers (BGR 2013): basalt aquifer, limestone aquifer (the generally most important aquifer of the basin), comprised as Amman Wadi Es Sir Aquifer, and sandstone (Kurnub) aquifer (Figure 2). The later is a regional aquifer recharges from limited outcrop areas of Baqa and Jerash and leakage from the upper carbonate aquifers. It is estimated that the total recharge for this aquifer in the basin is about 8 MCM/year (MWI, 2000). The aquifer is isolated from the upper Zarqa aquifer by the bluish green shale and marls of the upper Zarqa formation and capped by the Nau'r marls.

The Amman–Wadi Es Sir Aquifer (B2/A7) is a semi-confined aquifer with parts of it unconfined (Al-Momani et al. 2007). It has high permeability and storage capacity, and is rechargeable annually over a wide geographic area, particularly in densely populated areas. The aquifer comprises three formations, Amman Formation (B1), Ghudran Formation (B2), and Wadi Sir Formation (A7). The three formations are hydraulically connected and so are considered one aquifer. The B2/A7 unit has a varying thickness, ranging from approximately 100 m in the north of Amman to about 500 m in the south (Al-Momani et al. 2007). The depth of the water table cannot be determined, and it varies depending on the location as well as the hydrogeological conditions. The water table in some areas near the Zarqa River ranges from less than 50 m to greater than 150 m (AlMomani et al., 2007). The unconfined part of the aquifer with an effective porosity of 10−30 % and the confined part is characterized by a storage coefficient (Al-Mamani et al. 2007) of about $5x10^{-5}$. BS is the top formation of the B2/A7 sequence of formations in the Amman-Zarqa Basin. Basaltic lava flows have been extruded onto an eroded surface of older rocks, forming it. This unit varies in thickness from less than 10 meters to more than 100 meters. However, six lava flows were determined to extend from North to South to Al Hashmyiha area (MWI, .2000). The estimated recharge to the whole Basalt aquifer in Jordan is about 45 MCM/y of fresh water suitable for all types of usages. From that amount, 28 MCM/y is available within the Amman-Zarqa Basin in Jordan; the rest is discharged from this basin into the Azraq Basin. Transmissivity: 2-113,000 m^2/d, Storage Coefficient: 0.0001-0.003 (MWI,.2000).

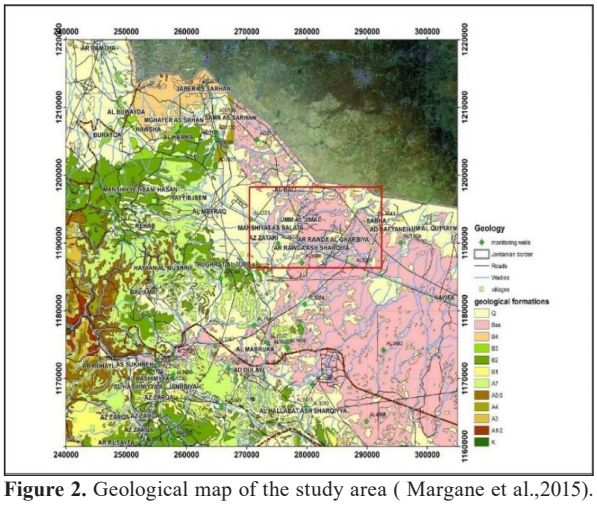

Figure 2. Geological map of the study area (Margane et al.,2015). The basin is divided into three main aquifers: basalts aquifer (at the top); limestone aquifer (in the middle, comprised of as Amman Wadi Es Sir Aquifer), and sandstone aquifer (Kurnub Aquifer (K), at the bottom).

4. Materials and Methods

During March and April 2023, eight water samples were collected from different wells in the study area and underwent laboratory analysis at the Jordanian Ministry of Water and Irrigation for physicochemical parameters, including major and minor elements pH, TDS, and EC, at a temperature of 25 °C (Tables 1 and 2). Concentrations of cations (Ca^{+2}, Mg^{+2}, Na^{+}, K^{+}), anions (HCO_3^{-}, $SO_4^{-2,}$ Cl^{-}), and nitrate (NO_3^{-}), in addition to pH, TDS, and EC are also determined. Figure 3 shows the locations of the wells where these samples were collected in addition to four samples investigated by the ministry of water and irrigation (MWI) during the same period.

Table 1. The coordination of wells in the study area (WGS84 coordinate system)

NO	ID	Latitude (N)	Longitude (E)	Elevation m (A.S.L)	Aquifer type
1	AL1453	32.306073	36.410086	727	B2/A7
2	AL1558	32.287751	36.391879	693	BS
3	AL1482	32.271608	36.365288	674	B2/A7
4	AL1480	32.277561	36.400323	706	BS
5	AL1481	32.238237	36.362903	615	B2/A7
6	AL3027	32.330888	36.390543	672	B2/A7
7	AL3018	32.304439	36.442042	747	B2/A7
8	AL2447	32.255617	36.369586	648	B2/A7
Data from MWI					
9	AL3467	32.345616	36.236409	681	B2/A7
10	AL2457	32.299714	36.481346	757	BS
11	AL3007	32.329178	36.508418	849	B2/A7
12	AL3087	32.287376	36.510215	825	B2/A7

Table 2. Physicochemical characteristics of groundwater samples in the study area in the years 1998-2023.

					2023						
ID	No_3^-	SO_4^{-2}	HCO_3^-	CL^-	Mg^{+2}	Ca^{+2}	K^+	Na^+	TDS	PH	EC
AL2447	48.83	31.26	157.37	120.72	18.32	23.71	5.39	93.78	546.49	7.91	858
AL2457	60.17	136.75	133.47	128	27.35	18.6	8.75	133.47	654.21	8.34	1032.74
AL3007	11.26	181.26	105.11	95.46	22.52	53.63	9.65	90.09	622.08	8.16	971.74
AL3018	26.84	98.5	114.74	134.22	22.73	19.48	7.58	130.98	568.29	8.42	900.6
AL3027	35.34	152.75	139.07	304.37	70.68	54.72	17.1	153.89	1016.84	8.25	1607.34
AL3087	34.6	167.58	66.38	127.32	22.85	20.68	5.44	121.88	617.01	8.13	950
AL1482	165.99	228.87	306.83	1026.12	148.39	192.4	18.86	428.81	2540.16	8	3968.68
AL1480	68.69	111.9	189.46	237.1	31.02	33.24	13.3	189.46	839.83	7.53	1311.82
AL1481	31.39	193.95	163.68	338.57	48.21	39.24	13.45	225.34	1127.81	7.63	1597.54
AL3467	30.49	115.41	239.53	139.36	47.91	60.97	7.62	103.43	745.8	7.64	1197.63
AL1558	32.73	115.63	119.99	217.08	57.81	43.63	8.73	103.63	752.68	8.11	1172.65
AL1453	56.83	236.7	183.97	508.56	132.41	70.31	9.37	205.06	1412.01	8.38	2167.81
					1998						
ID	No_3^-	SO_4^{-2}	HCO_3^-	CL^-	Mg^{+2}	Ca^{+2}	K^+	Na^+	TDS	PH	EC
AL2447	45.3	29	146	112	17	22	5	87	507	7.68	796
AL2457	55	125	122	117	25	17	8	122	598	8.1	944
AL3007	10.5	169	98	89	21	50	9	84	580	7.92	906
AL3018	24.8	91	106	124	21	18	7	121	525	8.17	832
AL3027	31	134	122	267	62	48	15	135	892	8.01	1410
AL3087	31.8	154	61	117	21	19	5	112	567	7.89	873
AL1482	132	182	244	816	118	153	15	341	2020	7.77	3156
AL1480	62	101	171	214	28	30	12	171	758	7.31	1184
AL1481	28	173	146	302	43	35	12	201	1006	7.41	1425
AL3467	28	106	220	128	44	56	7	95	685	7.42	1100
AL1558	30	106	110	199	53	40	8	95	690	7.87	1075
AL1453	48.5	202	157	434	113	60	8	175	1205	8.14	1850

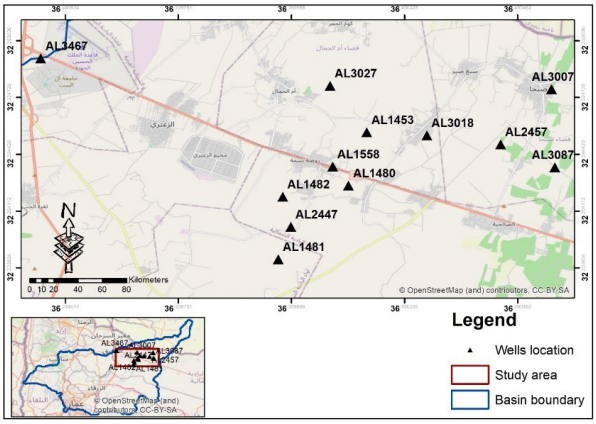

Figure 3. Wells locations map used in this

The pH value of the somewhat alkaline groundwater ranged from 7.53 to 8.42, with an average of 8.04. According to Detay, the groundwater type in the Za'atri area is highly mineralised water, as shown by the EC value. Based on the total dissolved solids (TDS) readings, which ranged from 546.49 to 2540.16 mg/L on average (Table 3), the groundwater samples were classified as either fresh or brackish. Based on this classification, 33.3 percent of the groundwater samples in the research region were brackish water from the Za'atri and Umm Al-Jamal areas, which is within the permitted range for TDS according to the Jordanian norm, which is 300 to 1000 mg/L, and according to the WHO guideline, which is less than 1000 mg/L. Because there are approximately 1,600 water wells in our study area, which leads to higher salt levels, groundwater is moving from east to west, especially in the Al Ba'ej area.

Table 3. Classification of samples based on TDS and EC Concentrations

ID	TDS (mg/L)	EC (µS/cm)	WHO Classification	Jordan Classification
AL2447	546.49	858	Freshwater	Freshwater
AL2457	654.21	1032.74	Freshwater	Freshwater
AL3007	622.08	971.74	Freshwater	Freshwater
AL3018	568.29	900.6	Freshwater	Freshwater
AL3027	1016.84	1607.34	Brackish	Brackish
AL3087	617.01	950	Freshwater	Freshwater
AL1482	2540.16	3968.68	Brackish	Brackish
AL1480	839.83	1311.82	Freshwater	Freshwater
AL1481	1127.81	1597.54	Brackish	Brackish
AL3467	745.8	1197.63	Freshwater	Freshwater
AL1558	752.68	1172.65	Freshwater	Freshwater
AL1453	1412.01	2167.8	Brackish	Brackish

5. Spatial Distribution of Major Ions

The concentrations of nitrate, sulfate, bicarbonate, chloride, magnesium, calcium, potassium, and sodium in the water samples indicate the sources and types of dissolved salts in the groundwater. Nitrate in groundwater originates from both natural sources, such as soil organic matter and plant residues, and anthropogenic sources, including fertilizers, animal manure, sewage, and industrial effluents. The nitrate concentration in the groundwater samples in the study area ranged from 11 to 166 mg/L, with an average of 50.3 mg/L. The acceptable limit for nitrate, according to the Jordanian standard, is 50 mg/L as NO_3^-, and according to the WHO standards, it is also 50 mg/L as NO_3^- (Figure 4-a).

Sulfate is a naturally occurring anion in groundwater that can originate from the weathering of rocks and minerals containing sulfur compounds, or from anthropogenic sources such as industrial waste, mining activities, and combustion of fossil fuels. The sulfate concentration in the groundwater samples in the study area ranged from 31.26 to 236.7 mg/L, with an average of 147.55 mg/L. The acceptable limit for sulfate according to both the Jordanian standard and the WHO standard is 250 mg/L as SO_4^{-2} (Figure 4-b).

Bicarbonate is a naturally occurring anion in groundwater that can originate from the dissolution of carbonate rocks such as limestone and dolomite, or from biological processes, such as photosynthesis and respiration. Bicarbonate is the main component of alkalinity, which is the capacity of water to neutralize acids.

Bicarbonate can affect the pH, hardness, and corrosion potential of water. The bicarbonate concentration in the groundwater samples in the study area ranged from 66.4 to 236.7 mg/L, with an average of 159.97 mg/L (Figure 4-c). There is no specific limit for bicarbonate in drinking water according to the Jordanian standard or the WHO standard, but it is generally recommended to keep it below 500 mg/L to avoid scaling and corrosion problems.

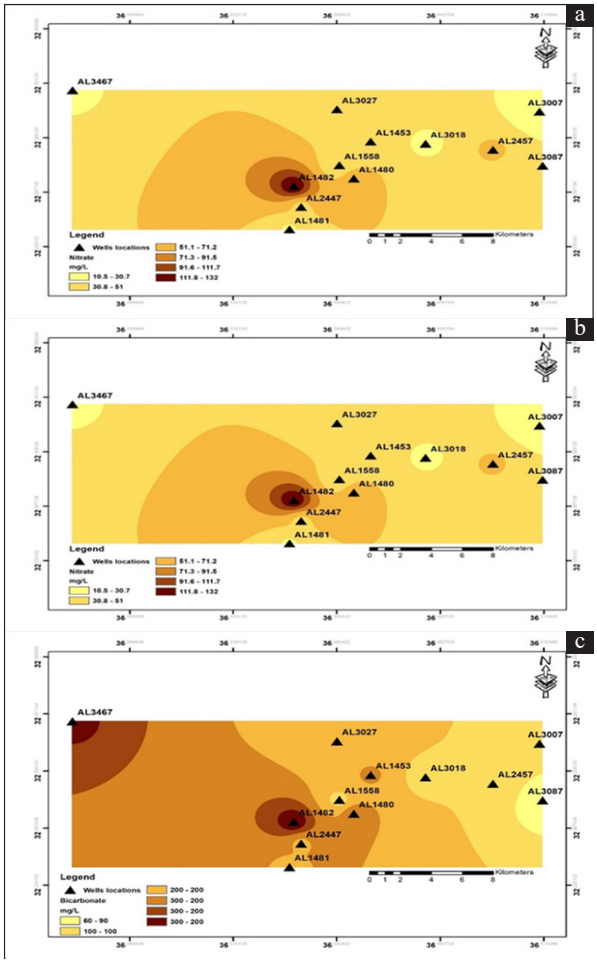

Figure 4. Spatial distribution maps of (a) Nitrate (NO_3^-), (b) Sulphate (SO_4^{-2}), and (c) Bicarbonate (HCO_3^-) generated using the Inverse Distance Weighted (IDW) method in ArcGIS 10.6.1.

Chloride is a naturally occurring anion in groundwater that can originate from the dissolution of halite and other salt minerals, as well as from anthropogenic sources such as seawater intrusion, irrigation return flows, sewage, and industrial effluents. The chloride concentration in the groundwater samples in the study area ranged from 95.46 to 1026.12 mg/L, with an average of 281.41 mg/L. The acceptable limit for chloride, according to the Jordanian standard, is 250 mg/L as Cl^-, and according to the WHO standard, is 250 mg/L as Cl^- or 600 mg/L as NaCl (Figure 5-a).

Magnesium is a naturally occurring cation in groundwater that can originate from the dissolution of dolomite and other magnesium-bearing minerals, or from anthropogenic sources such as fertilizers, detergents, and industrial wastes. The magnesium concentration in the groundwater samples in the study area ranged from 18.32 to 148.4 mg/L, with an average of 54.2mg/L. There is no specific limit for magnesium in drinking water according to the Jordanian standard or the WHO guideline, but it is generally recommended to keep it below 150 mg/L to avoid adverse effects (Figure 5-b).

Calcium is a naturally occurring cation in groundwater that can originate from the dissolution of calcite and other calcium-bearing minerals, as well as from anthropogenic sources such as fertilizers, lime, and cement. The calcium concentration in the groundwater samples in the study area ranged from 18.60 to 192.4 mg/L, with an average of 54.2 mg/L. There is no specific limit for calcium in drinking water according to the Jordanian standard or the WHO guideline. Still, it is generally recommended to keep it below 200 mg/L to avoid adverse effects. Potassium is a naturally occurring cation in groundwater that can originate from weathering of feldspar and other potassium-bearing minerals, or from anthropogenic sources such as fertilizers, detergents, and industrial wastes (Figure 5-c).

The potassium concentration in the groundwater samples in the study area ranged from 5.39 to 18.9 mg/L, with an average of 10.44 mg/L. There is no specific limit for potassium in drinking water according to the Jordanian standard or the WHO guideline, but it is generally recommended to keep it below 50 mg/L (Figure 5-d). Sodium is a naturally occurring cation in groundwater that can originate from the dissolution of halite and other

sodium-bearing minerals, or anthropogenic sources such as seawater intrusion, irrigation return flows, sewage, and industrial effluents. The sodium concentration in the groundwater samples in the study area ranged from 84 to 341 mg/L, with an average of 144.92 mg/L. The acceptable limit for sodium according to the Jordanian standard is 200 mg/L as Na^+, and according to the WHO guideline is 200 mg/L as Na^+ or 500 mg/L as NaCl (Figure 5-e).

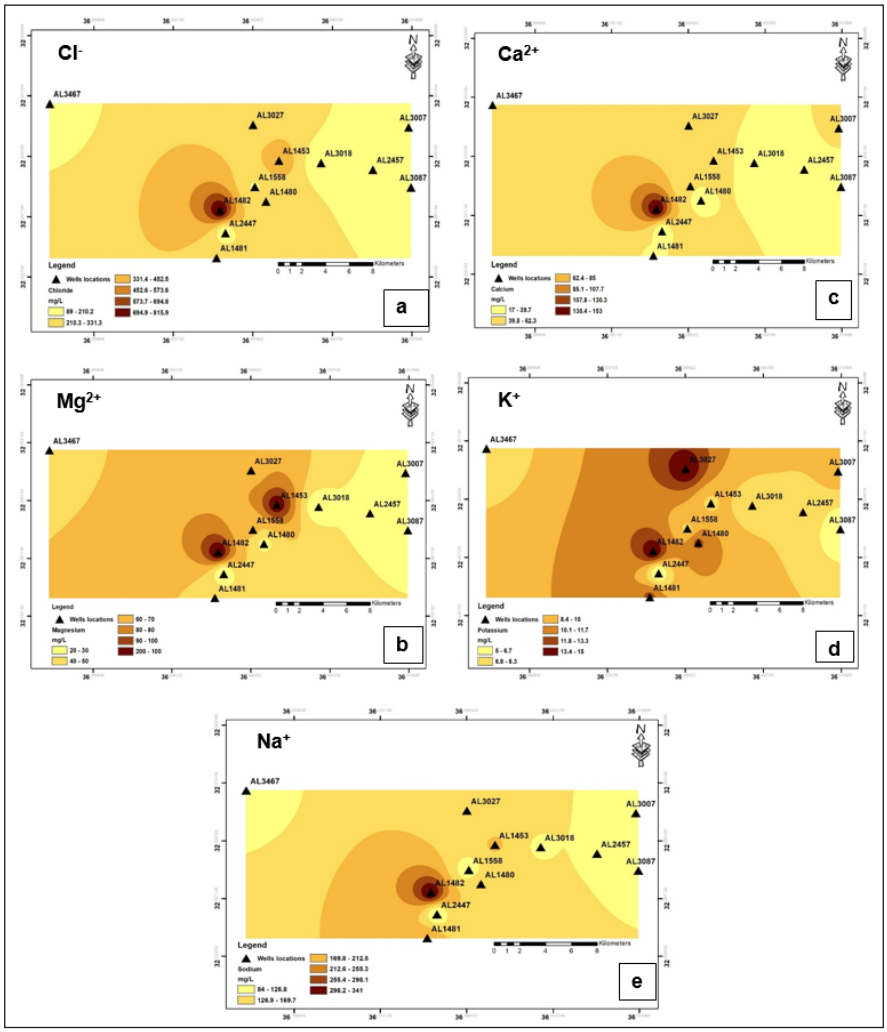

Figure 5. Spatial distribution maps of (a) Chloride), (b) Magnesium, (c) Calcium , (d) Potassium, and (e) Sodium generated using the Inverse Distance Weighted (IDW) method in ArcGIS 10.6.1.

Groundwater samples exhibit a wide range of values, indicating high variability in their hydrogeochemical characteristics. These samples can be categorized into three primary groups based on their dominant anions and cations: the Chloride Group (Cl^- dominant), the Bicarbonate Group (HCO_3^- Dominant), and Sodium Group (Na^+ Dominant). The Chloride group is the most prevalent, with six samples having Classicism, the dominant anion, and the sodium group is the most common among the cations, with nine samples showing Na^+ as the dominant cation. The Chloride group has the highest salinity, with an average TDS of 810 mg/L. The Bicarbonate group has the highest alkalinity, with an average HCO_3^- concentration of 153 mg/L. The Magnesium group is noted for its hardness, with an average Mg^{+2} concentration of 44 mg/L. The groundwater can be classified into three types based on the combination of dominant anions and cations: Saline Water (Cl^- and Na^+), Carbonate Water (HCO_3^- and Ca^{+2}), and Sulfate Water (SO_4^{-2} and Mg^{+2}).

6. Statistical analysis

Through statistical analysis, we can sift through vast amounts of data and draw conclusions about broader patterns. This analysis aims to determine the relationship between the water quality measures. All eleven of the observed parameters have their calculated correlation matrices presented in Table 4. We measured eleven parameters: NO, SO, HCO, Cl, Mg, Ca, K, Na, TDS, pH, and EC. Almost all of the parameters exhibit unidirectional variation, except for pH, which exhibits bidirectional variation, as shown in Table 4. Overall, there are strong positive correlations ($r > 0.9$) between all the parameters, except for pH, which exhibits a slight negative correlation ($r < -0.3$) with the other parameters. The strongest relationships are observed when there is a relationship between total dissolved solids (TDS) and electrical conductivity (EC), between chloride (Cl^-) and TDS, between Cl^- and EC, between calcium (Ca^{+2}) and Cl^-, between Ca^{+2} and TDS, between Ca^{+2} and EC, between magnesium (Mg^{+2}) and Cl^-, between Mg^{+2} and TDS, between Mg^{+2} and EC, between sodium (Na^+) and Cl^-, between Na^+ and TDS, and between Na^+ and EC. The evaporite minerals halite (NaCl) and gypsum ($CaSO_4$) have the and most significant impact on these parameters because their concentration in groundwater increases, as seen in these correlations. The weakest correlations were observed between pH and nitrate (NO_3^-), sulphate (SO_4^{-2}), and magnesium (Mg^{+2}), among others. These metrics appear to be loosely associated according to the correlations, and their content in water samples may originate from several sources or be the result of distinct processes. To illustrate, pH is primarily controlled by the carbonate equilibrium and the partial pressure of carbon dioxide; NO_3^- is primarily produced by organic matter decomposition and agricultural fertilisers; SO_4^{-2} is obtained mainly from the dissolution of gypsum and the oxidation of sulphide minerals; and Mg^{+2} is primarily derived from the dissolution of dolomite. Parameters such as K^+ and Cl^-, K^+ and Ca^{+2}, NO^- and SO_4^{-2}, SO_4^{-2} and bicarbonate (HCO_3^-), and so on exhibit moderate correlations with each other ($0.7 < r < 0.9$). A closer examination of the correlations between these factors and their concentrations in water samples reveals that they are relatively interconnected and share a common source of influence. So, K^+ and Cl are produced by silicate weathering and halite dissolution; dolomite dissolution and ion exchange by fertilisers and organic matter oxidation; NO_3^- and SO_4^{-2} by gypsum dissolution and sulphide oxidation; and so on.

Table 4. Correlation coefficient matrix of water quality parameters

parameters	No_3^-	SO_4^{-2}	HCO_3^-	CL^-	Mg^{+2}	Ca^{+2}	K^+	Na^+	TDS	PH	EC
No_3^-											
SO_4^{-2}	1										
HCO_3^-											
CL^-	0.20056	1									
Mg^{+2}	0.67233	0.07215	1								
Ca^{+2}	0.83488	0.54906	0.6469	1							
K^+	0.61947	0.61045	0.5774	0.8927	1						
Na^+	0.75784	0.49082	0.7166	0.8989	0.80784	1					
TDS	0.47752	0.41648	0.4337	0.6516	0.50863	0.59075	1				
PH	0.85207	0.52422	0.6288	0.9424	0.72589	0.7979	0.69522	1			
EC	0.81689	0.59469	0.6761	0.9936	0.88853	0.91859	0.67591	0.9431	1		
	-0.1021	0.20099	-0.4894	-0.017	0.15615	-0.0681	-0.1905	-0.153	-0.058	1	
	0.83349	0.57229	0.6879	0.9925	0.89231	0.93353	0.67067	0.9333	0.998	-0.0381	1

7. Groundwater quality assessment

The data obtained by hydrogeochemical analyses of 12 groundwater samples of the study area were evaluated in terms of their suitability for drinking and domestic uses.

7.1 Portability of groundwater for drinking and domestic uses

The physical and chemical parameters of the analytical results of groundwater were compared with the standard guideline values recommended by the World Health Organisation (WHO 2011) and the Water Authority of Jordan (WAJ 2002). for drinking and domestic purposes (Table 5).

Table 5. Guidelines of the WHO and WAJ standards of water for drinking and domestic purposes

		WHO (2011)		WAJ (2002)	
Parameters	**Unit**	**Guideline value (the maximum desirable limit for drinking purposes**	**Highest permissible limit (highest permissible limit for domestic purposes**	**Maximum desirable limit (Maximum desirable limit for drinking purposes**	**Maximum permissible limit (the highest permissible limit for domestic purpose**
SO_4^{-2}	mg/L	250	400	250	400
HCO_3^-	mg/L	N/A	N/A	N/A	N/A
Cl^-	mg/L	250	600	250	600
NO_3^-	mg/L	50	50	50	50
Mg^{+2}	mg/L	N/A	N/A	N/A	150
Ca^{+2}	mg/L	N/A	N/A	N/A	200
Na^+	m g/L	200	200	200	200
K^+	m g/L	N/A	N/A	N/A	N/A
TDS	m g/L	1000	N/A	1000	1500
EC	µS/cm	N/A	N/A	N/A	N/A
PH	Unitless	6.5-9.5	7.0-8.5	6.5-9.5	7.0-8.5

The groundwater quality in the study area varies according to different parameters and standards. While the pH is within the safe range of 6.5–8.5 for both WHO and WAJ standards, some samples have high concentrations of TDS, SO_4^{-2}, Cl^-, NO_3^-, Na^+, Ca^{+2}, and Mg^{+2} that exceed the desirable or permissible limits for drinking water quality. The most common parameters that exceed both standards are TDS, Cl^- and Na^+, affecting more than a third of the samples. NO_3^- is another parameter that exceeds both standards, affecting about a quarter of the samples, and poses serious health risks such as methemoglobinemia, gastric cancer, goiter, birth malformations, and hypertension.

Evaluation of water quality index WQI is a critical way to assess the quality of water because it helps to understand water quality issues by integrating complex data. For computing WQI, each of the 11 parameters (pH, TDS, Cl^-, NO_3^-, SO_4^{2-}, HCO_3^-, Ca^{+2}, Mg^{+2}, Na^+, K^+, and EC) is assigned a weight (wi) according to its relative importance in the overall quality of water for drinking purposes.

The relative weight (Wi) for each parameter is computed according to Tiwari & Mishra (1985). The calculated relative weight value of each parameter is presented (Table 6).

$$Wi = \frac{wi}{\sum_{i=1}^{n} wi} \quad (1)$$

Table 6. Relative weights of chemical parameters

Parameter	Weight (wi)	Standards (WHO, JS286)	Relative weight (Wi)
K^+	1	6.5-8.5	0.022
Na^+	2	1000	0.044
Ca^{2+}	3	250	0.067
Mg^{2+}	3	50	0.067
SO_4^{-2}	4	250	0.089
Ph	4	200	0.089
TDS	5	150	0.111
Cl^-	5	200	0.111
NO_3^-	5	200	0.111
HCO_3^-	5	50	0.111

The maximum weight of 4 is assigned to pH due to its major importance in quality assessment. The minimum weight of 1 is given to K^+ as it plays an insignificant role in the water quality assessment. Other parameters are assigned weights between 2 and 5 depending on their importance in water quality determination.

The quality rating scale (qi) for each parameter was obtained by using the following equation

$$qi = \frac{ci}{si} * 100 \quad (2)$$

where qi is the quality rating, Ci is the concentration of each chemical parameter in each water sample in mg/L, and JISM standard for each chemical parameter is in mg/L. Finally, the calculated water quality index determined the SI for each chemical parameter

$$SI = wi * qi \quad (3)$$

$$WQI = \sum SIi \quad (4)$$

Where SIi is the sub-index of the i^{th} parameter; qi is the rating based on the concentration of the i^{th} parameter. The WQI for each sample is shown in Table 7.

Table 7. Water Quality Index (WQI) value of groundwater in the study area

ID	WQI
AL1453	**66.67**
AL1480	**39.72**
AL1481	**53.33**
AL1482	**119.64**
AL1558	**35.63**
AL2447	**25.81**
AL2457	**30.94**
AL3007	**36.42**
AL3018	**26.89**
AL3027	**48.12**
AL3087	**38.1**
AL3467	**35.28**

WQI classifies the waters into five categories (Excellent, Good, Poor, etc.) as shown in Table 8.

Table 8. Classification of WQI range and category of water

WQI Range	Category of water
0-50	Excellent
51-100	Good
101-175	Fair
176-300	Poor
<300	Very poor

The average WQI of 46.38 for all samples indicates that the groundwater quality in the research area is excellent. But the fact that water quality varies geographically means that this average can be misleading. Water quality index (WQI) values ranging from 119.64 for the sample taken at Al 1482 indicate that the water quality is fair and might require substantial treatment prior to use. The high quantity of TDS in this sample is primarily responsible for the high WQI result (Table 9). According to the statistics, 75% of the samples scored an Excellent on the Water Quality Index (WQI), meaning they don't need any treatment to be suitable for consumption or other uses. Water quality that is satisfactory but may benefit from treatment is indicated by 16.67% of the samples classified as Good. The water may require substantial treatment before consumption, as just 8.33% of the samples are classified as fair, suggesting slight contamination. The samples are not usable because they are not in the poor or very poor categories, which means they are not highly or seriously polluted.

Table 9. Water Quality Index (WQI) Classification of the study area

ID	Category
AL1453	Good
AL1480	Excellent
AL1481	Good
AL1482	Fair
AL1558	Excellent
AL2447	Excellent
AL2457	Excellent
AL3007	Excellent
AL3018	Excellent
AL3027	Excellent
AL3087	Excellent
AL3467	Excellent

8. Conclusion

The Amman-Zarqa Basin can be a great source of fascination, considering that it is characterized by many diverse geological formations, which primarily affect groundwater quality. Groundwater in this region is highly varied in its chemical composition, reflecting the diverse rock types and human activities present. The water quality in general complies with the standards for drinking and domestic use as defined by the World Health Organization (WHO) and the Water Authority of Jordan (WAJ). Yet, in certain areas, some elevated concentrations of total dissolved solids (TDS), chloride (Cl^-), and nitrate (NO_3^-) can be observed, which may potentially occur as a result of agricultural activity and groundwater overabstraction. Salinity variation between different points is notable. With high agricultural activities in Za'atri and Umm Al-Jamal, the salinity is high.

' 'It's probably related to growers using fertilizers and overpumping the water table, concentrating salt in the water. The hydrochemical facies of the groundwater samples are observed to be different, with bicarbonate–calcium and chloride–sodium varieties. Such an outcome indicates that both natural geological formations and human activities influence water chemistry. Overall, the current groundwater quality remains relatively stable compared to data from 1998. Nevertheless, a few increases in TDS and nitrate levels in certain parts of the basin show continuing effects from agricultural practices and groundwater pumping. The sustainability of groundwater resources in the Amman-Zarqa Basin must be ensured through continuous monitoring and good management.

This study provides policymakers and stakeholders with valuable insights for planning effective groundwater management and protection strategies. In essence, the groundwater in the Amman Zarqa Basin is suitable for use, but management is required to address areas with a higher level of contamination, as well as to ensure the future sustainability of this valuable natural resource.

References

Al-Momani, Mohammed, El-Naqa, Ali, Kilani, Suzan , & Hammouri, Nezar. (2007). Groundwater Deterioration of Shallow Groundwater Aquifers Due to Overexploitation in Northeast Jordan. CLEAN- WILEY-VCH Verlag GmbH & Co. KGaA, Weinheim, 35 (2), 156 – 166

Alshibli, F., Maher, W., & Thompson, R. M. (2017). The need for a quantitative analysis of risk and reliability for formulation of water budget in Jordan. Journal of Water Security, 3(1), 1–12. https://doi.org/10.15544/jws.2017.001

BGR (2013): Inventory of Shared Water Resources in Western Asia. - 606 p., ISBN-13. 978-92-1-128361-7 (PDF, 28 MB)

JGP (Jordan Geography and Population) (2001) Irrigation in the Near East Region in Figures. Amman, Jordan

Jordanian Standards for Drinking Water (2002) Ministry of Water and Irrigation, Amman, Jordan

Ministry of Water and Irrigation. (2000). Outline hydrogeology of the Amman-Zarqa basin

MWI and BGR. (2017). TC Jordan: Groundwater Resources Management. Bundesanstalt für Geowissenschaften und Rohstoffe. https://www.bgr.bund.de/EN/Themen/Wasser/Projekte/abgeschlossen/TZ/Jordan ien/gwrm_fb_en.html

MWI, Ministry of Water and Irrigation (2017). Groundwater Resource Assessment of Jordan 2017

Odeh T, Mohammad AH, Hussein H (2019) Over-pumping of groundwater in Irbid governorate, northern Jordan: a conceptual model to analyze the effects of urbanization and agricultural activities on groundwater levels and salinity"""""""""""""". Environ Earth Sci 78:40

Radaideh, J. A. (2022). Status of Groundwater Resources in Jordan. American Journal of Water Resources, 10(2), 59-67. Retrieved from http://article.journalofwaterresources.com/pdf/ajwr-10-2-4.pdf

Raddad, K. (2005). Water supply and water use statistics in Jordan. In Proceedings of the International Work Session on Water Statistics, Vienna, June 20-22, 2005 (pp. 1-6). Vienna:

Department of Statistics, Jordan. Water supply and water use statistics in Jordan (un.org)

Tiwari TK, Mishra MA (1985) A preliminary assignment of water quality index of major Indian rivers. Indian J Environ Prot 5:276–279

UNICEF. (2020). Water, sanitation and hygiene. UNICEF Jordan. Retrieved from https://www.unicef.org/jordan/water-sanitation-and-hygiene

United States Agency for International Development. (2000). Outline Hydrogeology of the Amman-Zarqa Basin.

WHO World Health Organization (2011) Guidelines for drinking water quality(4thed).Geneva.http://www.who.int/water_sanitation_health/publications/2011/dwqguidelines/en/

Wreikat, A. L., & Kharabsheh, A. (2019). Impact of over-pumping on groundwater resources sustainability at Amman Zarqa basin, Jordan: a case study of arid areas affected by Syrian refugees crisis. Environmental Earth Sciences, 78(16), 1-12. https://doi.org/10.1007/s12665-019-8768-0

JJEES

JJEES (2025) 16 (4): 400-406
ISSN 1995-6681

Jordan Journal of Earth and Environmental Sciences

Problems of cartographic representation of contour lines in the district of a country and techniques to resolve them

مشكلات التمثيل الخرائطي لخطوط الكنتور في قضاء بلد وطرائق معالجتها

Saad Thamer Ibrahim*

سعد ثامر ابراهيم

Tikrit University / College of Arts / Department of Applied Geography, Tikrit, Iraq

جامعة تكريت / كلية الآداب / قسم الجغرافية التطبيقية

Received on August 13, 2024, Accepted on March 3, 2025

Abstract

The research aims to investigate the most significant cartographic problems related to contour lines, which many map designers encounter. A sample of contour maps with scientific and technical issues in their representation was taken from research published in the Iraqi Academy Journal. These issues were identified, and the best scientific solutions were proposed based on cartographic principles for designing this type of map. The study concluded that the main problems faced by researchers in contour map design are variation in the resolution of the digital elevation model, excessive curvature of contour lines, shading of contour lines, inappropriate colors used for contour lines, and the scale of the contour map. The study recommended solutions for these problems, such as improving contour line accuracy by considering pixel size and using automatic generalization, and selecting an appropriate vertical interval that matches the characteristics of the area, such as 2 meters for flat terrain.

الملخص :

يهدف البحث الى تسليط الضوء إلى اهم المشكلات الخرائطية لخطوط الكنتور"Contour lines" والتي يقع بها أغلب مصممو الخرائط، حيث تم أخذ عينة للخرائط الكنتورية التي ينتابها مشكلات علمية وفنية في عملية التمثيل، من البحوث المنشورة في المجلة الأكاديمية العراقية، وتم تحديد هذه المشكلات مع إيجاد أفضل الحلول العلمية، من خلال الإستناد على القواعد الكارتوكرافية في تصميم هذا النوع من الخرائط، وتوصلت الدراسة إلى أهم المشكلات التي يعاني منها الباحثين في تصميم الخرائط الكنتورية وهي: مشكلة التباين في الدقة التمييزية لنموذج الارتفاع الرقمي، ومشكلة شدة تعرجات خطوط الكنتور، ومشكلة تظليل خطوط الكنتور، ومشكلة الألوان المستخدمة في خطوط الكنتور، ومشكلة مقياس رسم خريطة خطوط الكنتور، وتوصلت الدراسة إلى معالجة هذه المشكلات من خلال تحسين دقة خطوط الكنتور عبر مراعاة حجم البكسل واستخدام التعميم الآلي، واختيار فاصل رأسي مناسب يتماشى مع طبيعة المنطقة مثل (2) متر للأراضي السهلية.

Keywords: *Discriminative accuracy; Contour map; Terrain shapes; Cartography*

الكلمات المفتاحية : الدقة التمييزية، الخريطة الكنتورية، الأشكال التضاريسية، الكارتوكرافية.

1. المقدمة:

تعد الخريطة الوسيلة الفعالة لترجمة البيانات المكانية بتمثيلها على سطح مستو، و أن تصميمها يحظى بإهتمام كبير في الدراسات الجغرافية، لأنها تعد وسيلة من وسائل المعرفة ولغة اتصال قناة لنقل المعلومات المكانية والوصفية إلى قارئها ومستخدمها، ولم يقتصر دور الخرائطي على تصميم وإعداد وتمثيل الخرائط فحسب، بل يشمل طرائق الاستفادة من التقنيات الجغرافية الحديثة المتمثلة بنظم المعلومات الجغرافية GIS، وبيانات الاستشعار عن بعد RS في استخلاص هذه المعلومات (Awawdehetal,2023)، وخاصة منهجيتها التي تمثل مجالا تطبيقيا جديدا يسمى بالخرائط الرقمية أو الآلية.

ينتمي خط الكنتور إلى مجموعة الرموز الكارتوغرافية التي تعرف بإسم "خطوط التساوي"، وخط التساوي هو الخط الذي تتساوى على طوله نفس القيمة لظاهرة معينة على الخريطة، وقد أمكن، باستخدام طريقة الكنتور، التغلب على معظم أوجه النقص في طرق تمثيل السطح القديمة، فمن حيث إمكانية الدقة، لا نجد هناك طريقة لتمثيل السطح يمكن أن تناظر خط الكنتور، وطريقة الكنتور لا تمكن الإنسان من أن يتصور شكل سطح الأرض بأبعاده الثلاثة فحسب، وإنما تمكنه أيضا من استنتاج العديد من البيانات والمعلومات المفيدة من شكل خطوط الكنتور وأنماطها، مثل الارتفاع ودرجة الانحدار والحافات الفقرية والأخاديد والسهول المستوية وغيرها من مظاهر سطح الأرض، وكان الكارتوغرافيون قد توصلوا إلى أسلوب خط الكنتور في أواسط القرن الثامن عشر، وظهر استخدامه أولاً في تمثيل خطوط الأعماق في الأنهار والبحار، ثم في تمثيل سطح الأرض اليابس بعد ذلك في حوالي سنه 1749، ولما كان سطح الأرض وثيق الصلة بحياة الإنسان، وكانت طريقة الكنتور هي أبرز وأعظم طرق التمثيل هذا السطح (سطيحة,1977)، ففوائد خطوط الارتفاعات المتساوية كالتالي (جاد,1987):

1. التخطيط لمشروعات تسوية الأراضي واستصلاحها ومشاريع الري والصرف والخزانات والسدود.
2. تخطيط المدن والمرافق العامة كالمدارس والمستشفيات وأماكن الترويح وأحياء السكن وخدمات الصرف الصحي.
3. مد الطرق المختلفة وبناء المطارات والقناطر والجسور.
4. إقامة مشاريع التنمية مثل محطات توليد الكهرباء والمنشآت الصناعية واستثمار الثروات المعدنية.

* Corresponding author e-mail: saad.t.ibrahim@tu.edu.iq

1.1 مشكلة الدراسة:

تمثلت مشكلة الدراسة بأن عملية إعداد الخرائط الكنتورية ذات النمط الخطي تواجه العديد من المشكلات، مما يؤثر على سرعة إدراكها وفهمها، والتي تسبب الارباك في تفسير العلاقة بين منشئ وقارئ الخريطة وبالتالي تؤثر على دقة التمثيل والفهم والإدراك، مما يتطلب ايجاد الحلول المناسبة لها، ومن خلال هذه المشكلة يمكن طرح التساؤلات الآتية:

1. كيف يمكن تحديد المشكلات التي تواجه إعداد الخرائط الكنتورية الخطية الكمية؟
2. كيف يمكن إيجاد الحلول المناسبة لهذه المشكلات من خلال بناء نماذج تتوفر فيها استجابة بصرية وإدراكية للقارئ والمستخدم بعد تشخيص النماذج المختارة؟

1.2 فرضية الدراسة:

أما فرضية الدراسة فقد تمثلت في الآتي: من الممكن تحديد المشكلات التي تواجه اعداد الخرائط الكنتورية الكمية، ويتم ذلك بالرجوع الى القواعد الأساسية المستخدمة في عملية تصميم هذا النوع من الخرائط، ويمكن إيجاد الحلول المناسبة لهذه المشكلات من خلال بناء نماذج تتوفر فيها استجابة بصرية وإدراكية عالية للقارئ والمستخدم بعد اختبارها، ويمكن تحديد أهداف الدراسة من خلال تحديد أبرز المشكلات الخاصة بالخرائط الكنتورية عند تمثيل البيانات الجغرافية غير الدقيقة وإيجاد الحلول المناسبة لهذه المشكلات من خلال اعداد نماذج ادراكية خاصة بالخريطة الكنتورية ذات البعد الواحد و الثنائي، والوصول إلى إعداد خريطة كنتورية دقيقة ذات النمط الخطي، والتي تستجيب للقارئ والمستخدم معا. وتبرز أهمية هذه الدراسة في أنها تقدم طرقاً مبتكرة لتحسين تصميم الخرائط الكنتورية بإستخدام التقنيات الجغرافية الحديثة مثل نظم المعلومات الجغرافية (GIS) وبيانات الاستشعار عن بعد (RS)، مما يعزز من قدرة الخرائط على نقل المعلومات بشكل أكثر دقة ووضوح، كما تسهم في تطوير نماذج خرائطية قابلة للنمذجة والتطبيق، مما يسهم في بناء قاعدة بيانات جغرافية دقيقة تتماشى مع متطلبات الفهم والإدراك لدى القارئ.

1.3 موقع منطقة الدراسة:

تتمثل منطقة الدراسة بقضاء بلد التابع الى محافظة صلاح الدين / العراق، والواقع بالجزء الشمالي الشرقي من السهل الرسوبي (شمال بغداد 90 كم)، وتقع منطقة الدراسة بين دائرتي عرض (37 ″ 43 ′ 37 ° - 27 ″ 96 ′ 37 °) شمالاً، وبين خطي طول (33 ″ 57 ′ 45 ° - 49 ″ 80 ′ 39 °) شرقاً وتشكل مساحة قدرها (1480.36 كم²) (الجهاز المركزي للإحصاء وتكنلوجيا المعلومات,2024)، أما حدوده الإدارية فيحدها من الشمال قضاء الدور ومن الشرق محافظة ديالى ومن الجنوب قضاء الدجيل ومن الغرب قضاء سامراء، والشكل (1) يوضح منطقة الدراسة.

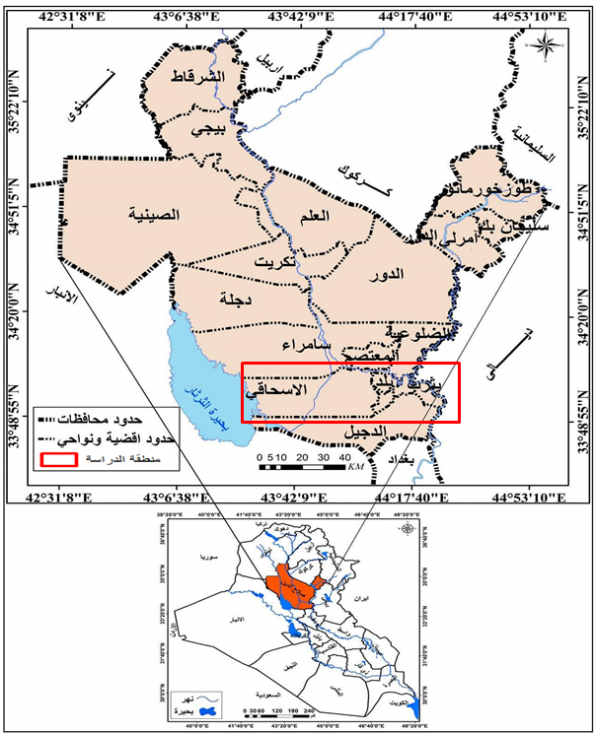

الشكل 1. موقع منطقة الدراسة

المصدر: بالاعتماد على جمهورية العراق, الهيأة العامة للمساحة خريطة العراق وصلاح الدين الإدارية لعام 2023, مقياس رسم 1/100,000 باستخدام برنامج (Arc Map 10.3).

2. مشكلات تمثيل الخرائط الكنتورية:

تحتوي طريقة التوزيع بخطوط التساوي بعض المشكلات التي تواجه الكارتوكرافي عندما يقوم برسم خريطته، ولكن من الممكن التغلب على هذه المشكلات (حسن,2011)، ويرجع الفضل في ذلك إلى الجهود والتجارب التي قام بها علماء الكارتوكرافية بكثير من الدراسات من اجل الوصول إلى الحلول المناسبة لهذه المشاكل، ويمكن التطرق إلى المشاكل العلمية في خرائط خطوط التساوي وهي كالآتي:

2.1 مشكلة مقياس رسم خريطة خطوط الكنتور:

كما هو معروف، فإن مقياس الرسم هو النسبة الثابتة بين الأبعاد الخطية على الخرائط وما يقابلها من أبعاد أصلية في الطبيعة (البدوي، الشريعي، 2011). فكلما كان مقياس الرسم صغيرًا، فإن الفترة الكنتورية الصغيرة تزحم الخريطة، فلا يمكن تتبع الخطوط بسهولة. وعموماً، فإن الفترة الكنتورية تتناسب تناسباً عكسياً مع مقياس الرسم؛ فتصغر مع مقياس الرسم الكبير وتكبر مع مقياس الرسم الصغير (مصطفى، 2000). والجدول (1) يبين ذلك.

فالخرائط ذات المقياس الكبير أي الخرائط الطبوغرافية والكدسترالية[1] ويكون الفاصل الكنتوري بها صغيراً، ويمكن الرجوع إلى الخرائط الطبوغرافية المصرية مقياس(1:100,000 و 1:25,000)، وسيتضح أن قيمة الفاصل الكنتوري المستخدم في خرائط الدلتا المصرية مثل لوحات (القاهرة، طنطا، طريق السويس، والزقازيق، والمنصورة متر واحد فقط)، أما في حالة الخرائط الصغيرة المقياس وتسمى أحيانا الخرائط المليونية أو العالمية فهي ذات فاصل كنتوري كبير.

الجدول 1. يوضح مواصفات الفترة الكنتورية وارتباطها بمقياس رسم الخريطة

مقياس الرسم	طبيعة التضاريس	الفترة الكنتورية / متر
مقاييس كبيرة يكون 1:10,000 أو أكبر.	منبسطة	1.0 – 5.0
	متوسطة التضرس	3.0 – 1.0
	شديدة التضرس	5.0 – 0.2
مقاييس متوسطة يتراوح بين 1:10,000 إلى 1:50,000	منبسطة	1 – 3
	متوسطة التضرس	5.1 – 3
	شديدة التضرس	3 – 6
مقاييس صغيرة أقل من 1:50,000، مثل 1:100,000أو أكثر.	منبسطة	3 – 10
	متوسطة التضرس	10 – 20
	شديدة التضرس	20 – 100

المصدر: جمعة محمد داود, تطبيقات إحصائية ومكانية متقدمة,القاهرة,مصر, 2018،ص94.

يتبين من الجدول (1) أن مقياس الرسم الكبير يعكس تفاصيل دقيقة، وبالتالي تُستخدم فترات كنتورية صغيرة، أما المقياس المتوسط يتناسب مع التضاريس المعتدلة حيث لا حاجة لتفاصيل دقيقة جدًا، ويستخدم المقياس الصغير في مناطق ذات تغطية واسعة أو عندما تكون دقة التفاصيل أقل أهمية، لذلك تكون الفترات الكنتورية أكبر، والقاعدة تقول: كلما زاد المقياس (أي اقترب من الواقع)، زادت دقة الخريطة وبالتالي قلت الفترة الكنتورية.

2.2 مشكلة شدة تعرجات خطوط الكنتور:

يقصد بتعرج سطح الأرض هو العلاقة بين الأشكال التضاريسية ومدى امتدادها وأبعادها بالنسبة للمساحة الكلية للمنطقة، ويمكن معرفة درجة التضرس من خلال حساب مدى تقارب أو تباعد السلاسل الجبلية والخوانق النهرية عن بعضها البعض من خطوط الكنتور بالخريطة الطبوغرافية (الزيدي، الحمداني، 2020).

يمكن تقسيم سطح الأرض من حيث درجة الوعورة و التضرس إلى نوعين هما: منطقة شديدة تتقارب فيها خطوط الكنتور وتكون دلالاتها إما السلاسل الجبلية أو الخوانق النهرية، ومنطقة بسيطة تتباعد فيها خطوط الكنتور وتكون دلالاته أسطح البيد مونت أو سهول تحاتية أو منخفضات، وبناءً على ما سبق تستخدم طريقة تعرجات خطوط الكنتور لتتبع الروافد غير المحددة بالخط الأزرق، وتعتمد على تتبع خطوط الروافد النهرية من خلال انحنائات خطوط الكنتور حتى تصبح خفيفة التقوس، يستخدم جهاز استيريوسكوب لتتبع الروافد الغير واضحة بالأسلوبين السابقين (سطيحة، 1977).

1. الخرائط الكدسترائية : هي خرائط توضح توزيع الأراضي واستخداماتها بشكل دقيق، وتستخدم هذه الخرائط لتحديد الحدود العقارية والملكية، وتساعد في تنظيم الأراضي وإدارة الموارد، وتتضمن معلومات مثل المساحات، الأبعاد، المواقع، وأرقام القطع، وتعتبر من الأدوات الأساسية في إدارة الأراضي والأنظمة القانونية، وتعتمد على مسح ميداني دقيق وتُحدَّث بشكل مستمر لضمان دقة المعلومات.

ويمكن معالجة هذه المشكلة بطريقة كارتوغرافية التي يستخدمها برنامج ARC GIs عن طريق انتخاب نسبة التنعيم عن تصغير المقياس، وفي حالة تصغير مقياس خريطة المصغرة أصلاً نضاعف قيمة التنعيم السابقة، على سبيل المثال عند الانتقال من مقياس 250.000 إلى 500.000 تكون نسبة التنعيم 200% (Maximumallowable offset) وعند الانتقال الى 1:1.000.000 تكون نسبة التنعيم 400% (جاد، 1987).

2.3 مشكلة التباين في الدقة التمييزية لنموذج الارتفاع الرقمي:

هناك عدة أشكال معروفة لهذه البيانات، منها ما هو شعاعي (Format Vector) ومنها ما هو مصفوفي Raster Format، ولكل منها حسناته وسلبياته، أي معظم الأحيان يكون الشكل المصفوفة للنماذج الارتفاعية هو الشكل الأولي الناتج من معالجة التحريات والصور الرقمية المجمعة بواسطة تقنيات الاستشعار عن بعد، سواء بالتصوير الجوي أو بالأقمار الصناعية، وتأتي الأشكال الشعاعية نتيجة للمعالجة اللاحقة لهذه الملفات بواسطة برامج مخصصة لهذه الأغراض مثل برامج نظم المعلومات الجغرافية (GIS) على اختلاف أسمائها التجارية، أو بمعالجتها ببرامج تحليل الصور وتفسيرها للتوابع الصنعية (العزاوي، علي، 2011)، في الملفات المصفوفة يتم تمثيل سطح الأرض بشبكة من الخلايا المربعة، وكل خلية تغطي مساحة من الأرض تختلف من نموذج لآخر ومن تقنية لأخرى، وهو ما يعرف بدقة التمييز لهذا النموذج (Resolution)، تعرف الخلية بقيمة الارتفاع لها الذي يكون ممثلا لقيم الارتفاعات لجميع نقاط سطح الأرض الواقعة ضمنها، إضافة إلى ترتيبها في السطر والعمود اللذين تقع فيهما هذه الخلية (عبدالرحمن، 2013)، وبالتالي فإن أفضل تمثيل على الإطلاق لسطح الأرض يمكن أن نحصل عليه عندما تتناهى أبعاد الخلية المربعة إلى الصفر وتنتهي في النقطة ذاتها مما يؤدي إلى الحصول على ملف رقمي بعدد منتهي من النقاط الارتفاعية، وهذا بالطبع مستحيل، إذ لا تقنيات الاستشعار عن بعد تسمح بذلك ولا إمكانيات الحواسب المتوفرة لدى الأشخاص أو لدى المؤسسات البحثية تسمح بمعالجة ملفات ذات حجوم كبيرة إلى هذه الدرجة، إذ لا بد من القبول ببعض التقريب المبرر لدى التصدي لنمذجة سطح الأرض، بما يتوافق مع إمكانيات الاستشعار عن بعد المعروفة حتى تاريخه من جهة، وبما يتوافق مع إمكانيات الحاسب الذي نستخدمه في عملية النمذجة، وأيضا بما يسمح لنا بالحصول على نموذج صحيح ودقيق وممثل فعليا وبشكل مرض للمسألة المطروحة بحسب المقياس الذي تغطيه.

3. مشكلات وحلول النموذج المختار والدقيق لخرائط خطوط الكنتور في قضاء بلد (حمادة،2010):

استخدمت هنا خريطة خطوط الكنتور لتوضيح الارتفاعات المتساوية لقضاء بلد، هذه الخريطة تحتوي على عدة مشكلات في عملية رسم الخريطة وفي إخراجها، وهنا يجب توضيح هذه المشكلات التي تحتويها الخريطة ومعالجتها، وهذا المشكلات هي:

3.1 مشكلة عدم دقة خطوط الكنتور:

يقوم أغلب المصممين باستخراج خطوط الكنتور دون مراعاه حجم البكسل لنموذج ثلاثي الابعاد، إذ يجب أن يتناسب خطوط الكنتور مع الحجم الحقيقي للبكسل، على سبيل المثال حجم النموذج (30) متر يجب مراعاة ذلك عن استخراج الخطوط الكنتور وذلك من خلال الإيعاز (environment) وبالتالي يكون الشذوذ بالخطوط قليل، أما الطريقة الثانية فهي اللجوء الى عملية التعميم الآلي من خلال تحويل النموذج الى raster ثم اجراء عمليات التعميم عليه (Generalization) وبالتالي يمكن القضاء على عملية الشذوذ في خطوط الكنتور.

3.2 مشكلة عدم وضوح الفاصل الرأسي:

الفاصل الرأسي أو الفترة الكنتورية هي الفرق العمودي في الارتفاع بين خطين متتاليين في الخريطة، وكلما كانت الفترة الكنتورية أصغر كانت الخريطة أكثر دقة في تمثيل التباينات الطفيفة في التضاريس والعكس صحيح، وتعتمد دقة وأهمية الخريطة الكنتورية على قيمة الفترة الكنتورية، وكلما كانت قيمة الفترة قليلة، كانت دقة الخريطة اعلى وتوجد بعض الاعتبارات التي تحدد الفترة الكنتورية وهي (مصطفى، بدون سنة نشر):

أ. الغرض الذي سوف تستعمل فيه الخريطة الكنتورية، فعندما يراد من الخريطة اظهار تفاصيل كثيرة فعندها يجب استعمال فترة كنتورية صغيرة.

ب. كلما ازداد عدم انتظام سطح الارض، فيجب أن تقل الفترة الكنتورية.

ت. كلما تطلب ان تكون الخريطة واضحة، فعند إذن، يجب استعمال فترة كنتورية صغيرة.

في النموذج المختار، تم استخدام فاصل رأسي قدره 20 متر علماً أنه أراضي سهلية، مما أدى إلى ظهور دوائر صغيرة وخطوط متقطعة، علماً أن خطوط الكنتور هي خطوط وهمية مستمرة في الامتداد غير منقطعة، يشكل أي خط من خطوط الكنتور حلقة مقفلة، ولا يتلاشى، ولا يتقاطع مع أي خط كنتور آخر إلا في بعض الحالات النادرة، مثل الجرف الرأسي أو النتوءات الأفقية في المناطق الجبلية، وهذا لا ينطبق على منطقة الدراسة باعتبارها مناطق مستوية تقريباً.

ولمعالجة هذا النموذج، لابد من اختيار فاصل رأسي يتناسب مع طبيعة المنطقة كما أشرنا سابقا هي أراضي سهلية منبسطة لابد من اختيار فاصل رأسي قليل كأن يكون (2 متر)، ومن ثم معالجة الخطوط أي يمكن حذف الشواذ الصغير في الخطوط الكنتور والتي تمثل الوديان الصغيرة جداً والتي لا تتكرر في الخطوط الكنتور في الجانب الأعلى والاوطأ، ويوضح الشكل (2) خطوط الكنتور في النموذج المختار، والشكل (3) يوضح النموذج الصحيح للنموذج المختار، إذ إن النموذج المختار استخدم فاصل كنتوري 20متر، والنموذج الصحيح الدقيق الذي تم انشائه استخدم فاصل كنتوري 2 متر.

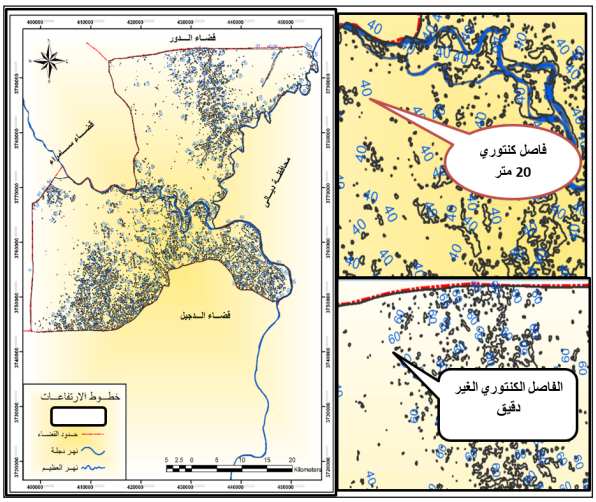

الشكل 2. يوضح خطوط الكنتور في النموذج المختار لقضاء بلد

المصدر: ياسين عبد النبي حمادة, مشكلة الملوحة وأثرها في التباين المكاني للإنتاج الزراعي في قضاء بلد، رسالة ماجستير (غير منشورة)، كلية التربية، جامعة تكريت، 2010،ص 35.

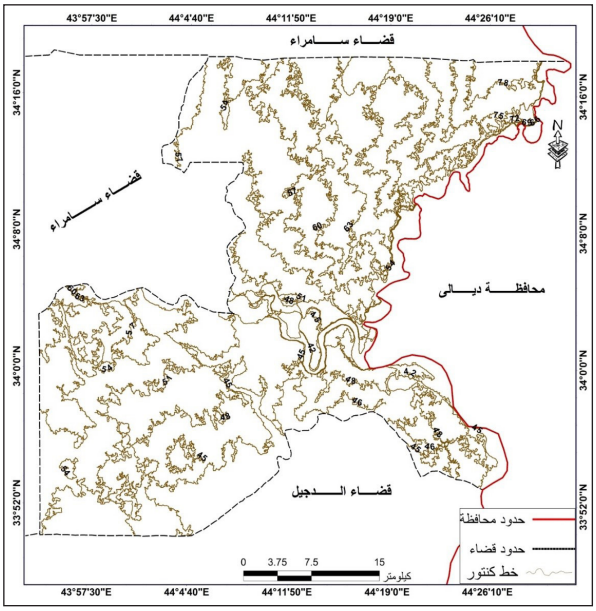

الشكل 3. النموذج الدقيق للنموذج المختار لرسم خطوط الكنتور في قضاء بلد

المصدر : بالاعتماد على DEM ومخرجات برنامج ARCGIS.V.10.3

3.3 مشكلة عدم تلوين خطوط الكنتور بالاعتماد على القياسات العالمية:

أستخدم اللون الأسود للدلالة على خطوط الكنتور، وهذا أدى إلى تشوه الخريطة وعدم قدرتها على توصيل المعلومة الى قارئها، إضافة إلى تداخلها مع حدود منطقة الدراسة باللون الأسود وعدم تطبيق القياسات العالمية في عملية التلوين، إذ أن هناك طريقتان لتلوين خرائط خطوط الكنتور: الطريقة الأولى تكون باستخدام لون واحد متدرج الكثافة، وتسمى طريقة الظلال، حيث يستخدم اللون البني بدرجاته المختلفة، بدءً من البني الخفيف (الفاتح) للمناطق الأقل ارتفاعا، حيث البني الداكن للمناطق الأعلى ارتفاعاً، ولكن اللون البني يطمس المعالم والكتابة، الطريقة الثانية هي استخدام عدة ألوان، بهدف تجنب طمس المعالم، وهذا ينبغي اختيار الألوان التي تعطي إحساسا بالتدرج، مثل اللون الأصفر الفاتح للمناطق الأقل ارتفاعاً، ثم الأصفر الداكن والأخضر الداكن للسهول الساحلية، إذ أن الشكل السابق (2) يوضح التلوين في النموذج المختار بالاعتماد على المقاييس العلمية في تلوين خرائط خطوط الكنتور.

3.4 مشكلة اعتماد نموذج الارتفاع الرقمي بدقة منخفضة:

تعد البيانات الرادارية من أهم مصادر الحصول على البيانات للارتفاعات الرقمية التي توضح طبيعة التضاريس التي تعلو فوق منسوب سطح البحر، إذ أن هذه البيانات تمكننا من رسم خرائط الارتفاعات المتساوية (الخرائط الكنتورية) بالدقة العالية والكفاءة العالية، إذ اعتمد في رسم الخريطة الكنتورية على نموذج ارتفاع رقمي منخفض الدقة، والذي أكد ذلك هو خطوط الكنتور التي كانت على شكل دوائر وحلقات مغلقة لا معنى لها ولا تمثل خطوط الكنتور بشيء، إضافة إلى عدم القدرة على إخراج الخريطة بفاصل رأسي واضح، وكان من الأجدر الاعتماد على نموذج ارتفاع رقمي عالي الدقة، وأفضل نموذج يتم الاعتماد عليه هو 30 متر وأقل من ذلك ، أو الاعتماد على الخريطة الطبوغرافية ورسم خطوط الكنتور من خلالها، والشكل (4) يوضح مدى دقة الاعتماد على نماذج الارتفاع الرقمي لقضاء بلد ذات دقة تميزية مختلفة مثل (30متر، 90متر)

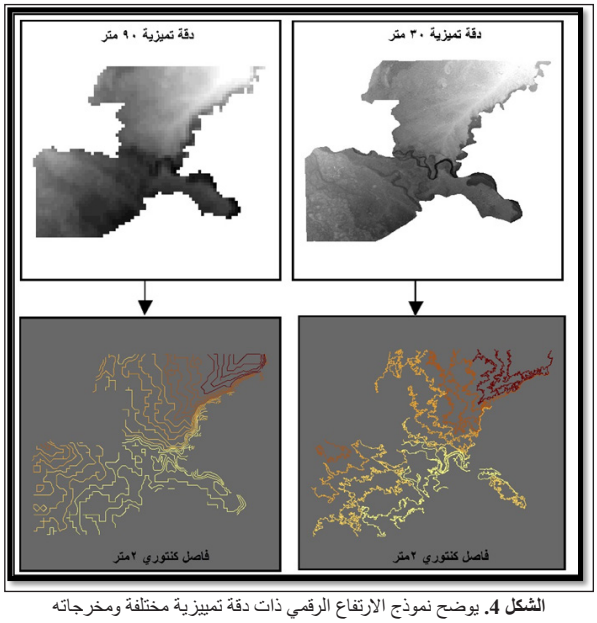

الشكل 4. يوضح نموذج الارتفاع الرقمي ذات دقة تميزية مختلفة ومخرجاته
المصدر: من عمل الباحث بالاعتماد على DEM ذات دقة تميزية (30 متر - 90 متر) ومخرجات برنامج ARCGIS10.3

يتضح من الشكل (4) أن نموذج الارتفاع الرقمي (DEM) هو تمثيل رقمي للسطح الأرضي، يعتمد على شبكة من القيم الارتفاعية، وكلما زادت دقة التمييز المكاني (Spatial Resolution)، زادت كمية التفاصيل التي يمكن تمثيلها، مما ينعكس على دقة التحليل الطبوغرافي، وعند استخدام DEMمنخفض الدقة (90 متر)، يتم فقدان الكثير من التفاصيل الطبوغرافية، مما يجعل خطوط الكنتور غير دقيقة ومتباعدة، وتظهر بشكل متعرج وزاوي، وفي حالة استخدام DEMعالي الدقة (30 متر)، يتم تمثيل التضاريس بشكل أكثر دقة، مما يسمح بإنشاء خطوط كنتور أكثر تفصيلا، توضح الفروقات في الارتفاعات والانحدارات الصغيرة، ومن خلال ذلك نستنتج تؤثر دقة التمييز المكاني بشكل مباشر على دقة تمثيل التضاريس وخطوط الكنتور، مما يحدد مدى موثوقية التحليلات الطبوغرافية والخرائط المصممة.

3.5 مشكلة وجود شذوذ كبير في خرائط الكنتور:

إذ إن المعروف بخطوط الكنتور هو عبارة عن حلقة مقفلة، ولا يتلاشى، ولا يتقاطع مع أي خط كنتور آخر إلا في بعض الحالات النادرة مثل الجرف الرأسي أو النتوءات الأفقية في المناطق الجبلية (الزيدي، الحمداني، 2020)، وفي النموذج المختار نجد نقاط مغلقة ودوائر مقطعة وخطوط منفصلة مرتبطة مع حدود منطقة الدراسة مما يؤثر على عدم اجراء تحسينات للنموذج وهذا ما ينعكس على الإخراج وعدم استطاعة المتلقي في أي تخصص بتمييز ماهو محتوى هذه الخريطة فقط الاعتماد على عنوان الخريطة.

3.6 مشكلة عدم وضوح منطقة الدراسة :

وهذه المشكلة تتعلق بالجانب الفني في إخراج الخريطة إذ أدى اندماج خطوط الكنتور مع خطوط منطقة الدراسة إلى تشوه الخريطةإ وعدم ايصال المعلومة بصورة صحيحة الى المتلقي، وهذا ناتج عن عدم الخبرة في إخراج الخرائط في نظم المعلومات الجغرافية، إضافة إلى ضعف الجانب العملي وطرق تطبيقها على أساسيات الخريطة، ويوضح الشكل (5) المشكلات الفنية المتعلقة بإخراج الخرائط في نظم المعلومات الجغرافية، إذ نلاحظ أن منطقة الدراسة لها خطان من الحدود: أحدهما بالون الأحمر، والآخر باللون الأسود فوقه، وهذا ما أدى إلى تشوه الخريطة وصعوبة فهم الرسالة التي تحتويها.

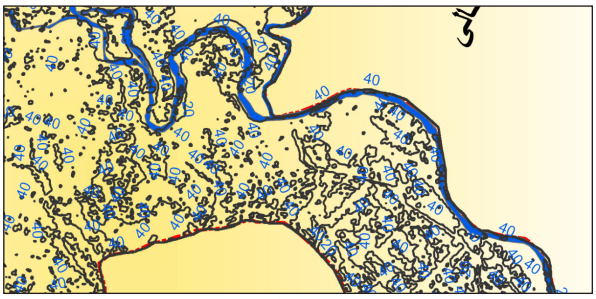

الشكل 5. يوضح المشكلات الفنية في اخراج الخريطة
المصدر: ياسين عبد النبي حمادة، مشكلة الملوحة وأثرها في التباين المكاني للإنتاج الزراعي في قضاء بلد، رسالة ماجستير (غير منشورة)، كلية التربة، جامعة تكريت، 2010، ص 35.

يُظهر الشكل (5) أبرز الإشكالات الفنية في إخراج الخرائط باستخدام نظم المعلومات الجغرافية، حيث يلاحظ بشكل واضح تداخل خطوط الكنتور مع حدود منطقة الدراسة، ما أدى إلى تشوه بصري في الخريطة وصعوبة في إيصال المعلومة الجغرافية بشكل دقيق وواضح إلى القارئ أو المستخدم، ونلاحظ أن منطقة الدراسة محاطة بخطين متداخلين؛ أحدهما مرسوم باللون الأحمر والآخر باللون الأسود، وهو ما يشير إلى خلل في تحديد وإبراز الحدود الفعلية لمنطقة الدراسة، وهذا التكرار في عرض حدود المنطقة يُفقد الخريطة وضوحها ويُربك المتلقي، خاصة في حالة عدم تمييز الألوان، ما قد يؤدي إلى تفسير خاطئ للبيانات المكانية المعروضة، وتُعد هذه المشكلات ناتجة بشكل أساسي عن ضعف في الجانب الفني لإخراج الخرائط، والذي يرتبط غالبا بقلة الخبرة في استخدام أدوات نظم المعلومات الجغرافية، وخاصة في مرحلة التصميمcartographic design، حيث لم تُراعى مبادئ التباين، والبساطة، وتسلسل الطبقات layer hierarchy بالشكل الصحيح.

3.7 النموذج ثلاثي الأبعاد 3D في منطقة الدراسة:

إن النموذج ثلاثي الأبعاد في الشكل (6) يعكس التضاريس السطحية في قضاء بلد، حيث يظهر تفاوتا واضحًا في الارتفاعات عبر خطوط شبكية متصلة، ويعكس هذا التمثيل تفاصيل دقيقة للسطح، مع وجود انقطاعات حادة تشبه الصدع، مما يشير إلى تحولات فجائية في الارتفاع، يمكن أن تكون ناتجة عن فوالق جيولوجية أو تغييرات طبيعية مفاجئة.

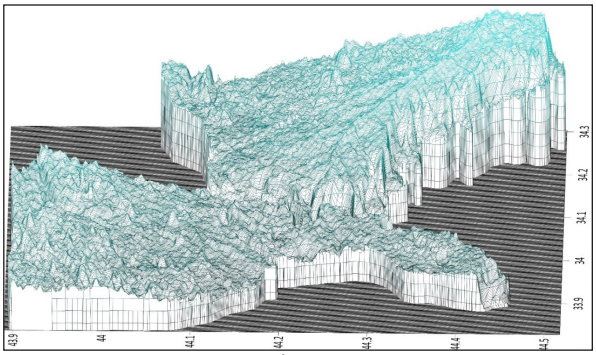

الشكل 6. النموذج ثلاثي الأبعاد 3D في قضاء بلد
المصدر : بالاعتماد على DEM ومخرجات برنامج ARCGIS.V.10.3

يتبين من الشكل (6) أن استخدام الخطوط الشبكية الدقيقة يوضح التدرجات والانحدارات، حيث تمثل المناطق ذات الكثافة العالية للخطوط التضاريس الوعرة أو ذات الانحدار الشديد، بينما تشير المناطق الأقل كثافة إلى مساحات أكثر استواءً، ومن الناحية البصرية، يعتمد هذا النموذج على متغيرات مثل الشكل والخط واللون، حيث تساهم الخطوط الشبكية في إبراز التغيرات في التضاريس من خلال تكوينات مختلفة تعكس التدرج في الارتفاع، كما أن استخدام اللون الأزرق الفاتح للخطوط الشبكية يمنح إحساسا بالعمق والمسافة، أما التأثير على خطوط الكنتور فإن هذا النموذج يسهم في دقة رسمها من خلال تحديد المناطق ذات الانحدارات الحادة والانقطاعات المفاجئة، حيث تقترب الخطوط الكنتورية من بعضها في المناطق الوعرة وتبتعد في المناطق المستوية، مما يسمح بفهم أكثر تفصيلاً لطبيعة السطح، ويساعد هذا التمثيل الثلاثي الأبعاد في تحسين دقة الخرائط الجغرافية خاصة في الدراسات الجيومورفولوجية والتخطيط الهندسي، حيث يتيح رؤية شاملة للارتفاعات والتغيرات الطبوغرافية، مما يسهل عملية تحليل الظواهر الطبيعية واتخاذ القرارات في مجالات مثل التخطيط العمراني وإدارة الموارد الطبيعية.

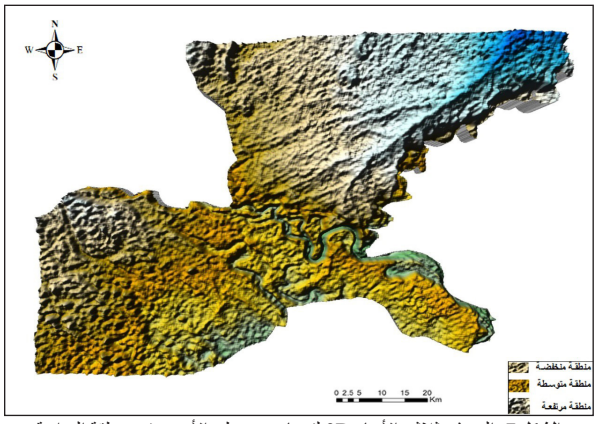

الشكل 7. النموذج ثلاثي الأبعاد 3D لتضاريس سطح الأرض في منطقة الدراسة
المصدر : بالاعتماد على DEM ومخرجات برنامج ARCGIS.V.10.3

يتبين من الشكل (7) الذي يمثل سطح الأرض بشكل ثلاثي الأبعاد الخاص بمنطقة الدراسة، إذ تظهر التضاريس الطبيعية بتفاصيل دقيقة، ويعتمد التصميم على استخدام التظليل والتدرج اللوني لإبراز التغيرات في الارتفاعات، مما يسهل فهم شكل السطح الطبوغرافي، ويظهر النموذج تضاريس وعرة مع وجود وديان ومنخفضات نهرية تميّزها الانحناءات الحادة، إضافةً إلى مناطق مرتفعة ذات سطح خشن توحي بوجود تكوينات صخرية صلبة أو هضاب متآكلة بفعل العمليات الجيولوجية، ويمثل اللون الأصفر الارتفاعات المتوسطة، بينما يشير اللون الغامق في الجزء الشمالي الشرقي إلى المناطق الأكثر ارتفاعًا أو ذات الانحدار الشديد، مما يساعد على تمييز الأجزاء المختلفة من التضاريس بسهولة.

ويتميز الشكل (7) بكونه مفيد في دراسات علوم الأرض والجيولوجيا، لأنه يساعد في تحليل العمليات الجيومورفولوجية، مثل التعرية والتجوية وتأثير المياه الجارية على تشكيل التضاريس، كما يمكن استخدامه لتحديد الفوالق والانقطاعات الجيولوجية، مما يسهم في فهم البنية التحتية للصخور ودراسة المخاطر الجيولوجية مثل الانهيارات الأرضية أو الفيضانات، ويساهم هذا النوع من النماذج أيضًا في التخطيط العمراني، حيث يساعد في تحديد أفضل المواقع للبنية التحتية وتقييم المخاطر الجغرافية المحتملة، بالإضافة إلى كونه أداة أساسية في رسم الخرائط الطبوغرافية الدقيقة.

الجدول 2. يبين اصناف الارتفاعات في منطقة الدراسة مع استخدام متغير اللون

فئات الارتفاع	اللون الخرائطي	المساحة كم2	%
44.8 - 32		172	10.3
50.3 - 44.9		474	28.3
56 - 50.4		412	24.6
62.5 - 56.1		325	19.4
70.6 - 62.6		182	10.9
82.2 - 70.7		112	6.7
المجموع		1677	100.0

المصدر: بالاعتماد على DEM ومخرجات برنامج ARCGIS.V.10.3

عند تحليل فئات الارتفاع في منطقة الدراسة، يتبين من الجدول (2) أن النطاق الأكثر انتشاراً هو فئة 44.9 - 50.3 متر، والتي تمثل نسبة 28.3% من إجمالي مساحة القضاء، تليها فئة 50.4 - 56 متر بنسبة 24.6%، ثم فئة 56.1 - 62.5 متر بنسبة 19.4%، إذ أن هذا التوزيع يعكس طابعاً طبوغرافياً متجانساً نسبياً، تتراكم فيه معظم المساحات في نطاقات ارتفاع متوسطة، بالمقابل فإن الفئات الأقل شيوعاً كفئة 70.7 - 82.2 متر (6.7%) و32 - 44.8 متر (10.3%) تشير إلى وجود مناطق محدودة الانخفاض أو الارتفاع، غالبًا ما تكون ذات أهمية خاصة في التحليل الجغرافي (مثل المرتفعات المعزولة أو الأراضي الزراعية المنخفضة)

إن هذا التوزيع المكثف ضمن نطاقات ضيقة من الارتفاع يتطلب عناية خاصة في تمثيل خطوط الكنتور، إذ أن استخدام فاصل رأسي غير مناسب يؤدي إلى تكرار خطوط الكنتور بشكل مزدحم أو متباعد بدرجة تقلل من دقة القراءة البصرية للخريطة، كما أن كثافة الفئات الوسطى تفرض أهمية اعتماد تدرج لوني واضح ومتدرج، يدعم التمييز البصري بين مستويات الارتفاع المختلفة، وهو ما تم أخذه بعين الاعتبار من خلال استخدام متغير اللون في التمثيل الكارتوغرافي، ومن هنا تبرز إحدى المشكلات الأساسية في الخرائط الكنتورية، وهي سوء اختيار الفاصل الرأسي وتدرج اللون، ما يستدعي تطوير معايير دقيقة تتماشى مع الخصائص الفعلية للتضاريس عند تصميم هذا النوع من الخرائط.

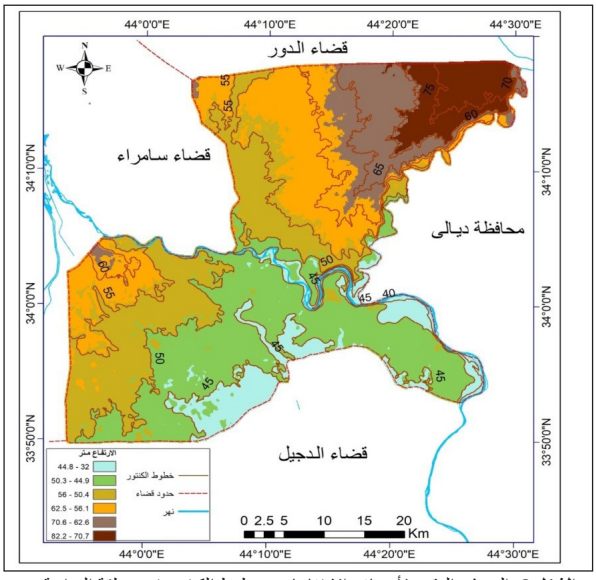

الشكل 8. النموذج الدقيق لأصناف الارتفاعات وخطوط الكنتور في منطقة الدراسة مع استخدام متغير اللون
المصدر : بالاعتماد على DEM ومخرجات برنامج ARCGIS.V.10.3

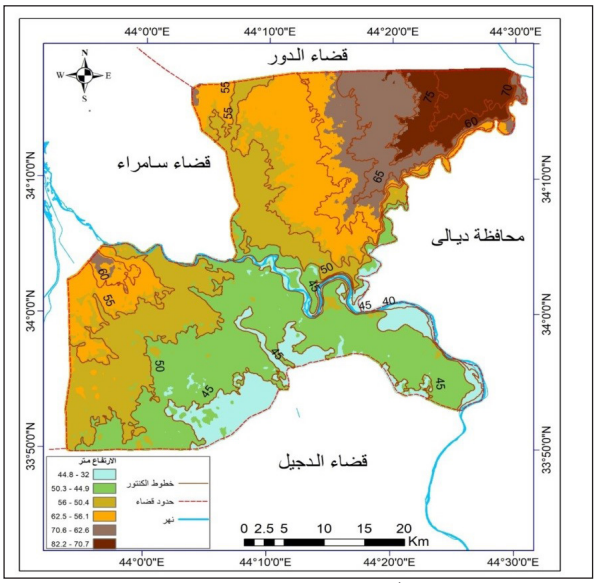

الشكل 9. النموذج الدقيق لأصناف الارتفاعات وخطوط الكنتور في منطقة الدراسة مع استخدام متغير اللون
المصدر: بالاعتماد على DEM ومخرجات برنامج ARCGIS.V.10.3

يعكس الشكل (8) و(9) تطوراً ملحوظاً في دقة إخراج الخرائط الكنتورية باستخدام نظم المعلومات الجغرافية، ويُعدان نموذجان مثاليان لتجسيد الارتفاعات وخطوط الكنتور بطريقة علمية مدروسة تعكس الواقع الجغرافي بأعلى درجات الاحترافية، ويتّضح في هذين النموذجين دمج دقيق واحترافي لخطوط الكنتور مع التدرج اللوني الذي يمثّل أصناف الارتفاعات، مما يجعل الخريطة سهلة الفهم، غنية بالمعلومات، وتقدم رؤية مكانية واضحة للمتغيرات الطوبوغرافية ضمن منطقة الدراسة، فقد تم استخدام برامج GIS التي تمثل البيانات المكانية بكفاءة، من خلال تقسيم منطقة الدراسة إلى ست فئات ارتفاع مختلفة، كل منها ملونة بلون مميز ومتدرج بدقة.

ومن خلال ذلك نستنتج إن الشكل (8) و(9) يمثلان نقلة نوعية في أسلوب إخراج الخرائط الكنتورية، حيث تم توظيف أدوات نظم المعلومات الجغرافية الحديثة بشكل فعّال لإنتاج خريطة دقيقة، ذات دلالة مكانية واضحة، ومنسجمة من حيث الشكل والمحتوى، ويعد الشكل (8)و(9) مرجعاً بصرياً متقدماً يمكن الاعتماد عليه في التحليلات المكانية المختلفة.

3.8 مميزات النماذج المصممة:

- وضوح خطوط الكنتور دون أن تتداخل أو تندمج مع حدود منطقة الدراسة، كما كانت المشكلة في الاشكال السابقة.
- دمج التدرج اللوني وخطوط الكنتور، مما يتيح للقارئ تحليل المعطيات الطوبوغرافية بشكل بصري مباشر.
- تصميم خريطة منظم ومتوازن من حيث استخدام الرموز والألوان، حيث تم استخدام الألوان بطريقة علمية تعكس تدريج الارتفاعات بدقة وبدون تشويش بصري.
- وجود مقياس رسم وشبكة إحداثية دقيقة ومفتاح خريطة شامل يوضّح الفئات بدقة، وهو ما يضيف مصداقية ودقة أكاديمية للنموذج.

4. الاستنتاجات :

تحدد الدراسة مجموعة من مشكلات التمثيل الخرائطي لخطوط الكنتور في قضاء بلد، من خلال اختيار بعض الرسائل والأطروحات والبحوث المنشورة في بعض الجامعات العراقية ومحاولة إيجاد الحلول المناسبة، بعد تشخيص هذه المشكلات بصورة دقيقة.

أثبتت الدراسة أن أغلب مصممو الخرائط يفتقدون إلى أبسط قواعد بناء الصورة البصرية الصحيحة، والتي تسمح باستنباط ما تحويه من معلومات بصيغة شمولية، ولا يمكن اعتبارها كخريطة مستقلة لمعرفة العلاقات المكانية ولتخزين المعلومات الجغرافية وعرضها بما يتفق مع طبيعتها الجغرافية، أي أن تلك الخرائط لا تعد وسيلة اتصال بين منشئ الخريطة و قارئها.

أظهرت الدراسة أن مصمم الخريطة الموضوعية بشكل عام والخريطة الكنتورية بشكل خاص يجب أن تراعى الشروط الخاصة بملائمة الخريطة لطبيعة الإدراك وللمستويات الدراسية وكثافة المتغيرات البصرية، لأن كثافة المعطيات ينشأ عنها التداخل والتشويش، وهذا يؤدي إلى تشتت الذهن وبالتالي تفقد عملية الإتصال دورها، لأن الخريطة هي نشاط إدراكي أكبر.

بينت الدراسة أن النموذج المختار للخريطة الكنتورية والتي وقع الإختيار عليه ينتابه بعض الغموض وقلة الدقة من الناحية العلمية والفنية والإثارة البصرية والتعميمات والتصنيفات غير الدقيقة ربما تطبق لكي ترسل كصورة واضحة للظاهرة والتي ستنتج اشكالا عديدة من المعلومات التي لا تتطابق مع الواقع الحقيقي لتلك المعلومات بسبب ترجمة المصممين المعلومات الأصلية لشكل غير صحيح أو تعرضوا فيها إلى مشاكل في العمليات الخرائطية أثناء تمثيل المعلومات.

التوصيات :

1. من الواجب أن تكون خطوط الكنتور عند التمثيل بالنمط الخطي واضحة وبعيدة عن التحاشي والتداخل أو التقاطع، لكي يتم قراءتها وادراكها من قبل القارئ بصورة سلسة وسهلة.
2. على مصمم الخريطة أن يهتم في عملية استخدام الالوان المتدرجة في القيمة من الفاتح الى القاتم وان يختار لون واحد عند التمثيل بهذا النوع من الخرائط.
3. الاهتمام في اختيار مقياس رسم مناسب لحجم الخريطة الكنتورية عند تصميمها، لتلافي مشكلة تداخل الخطوط فيما بينها.
4. من الضروري اضافة اساسيات الخريطة مثل العنوان والمقياس والموقع وسهم الشمال والإطار والإحداثيات وغيرها، لكي يتمكن مصمم الخريطة من ايصال المعلومة للقارئ بسهولة ووضوح.
5. يجب إنشاء مقياس بصري لفعالية إدراك الخرائط الجغرافية من خلال تبني المتخصصين في هذا المجال مع المتخصصين في مجالات تربوية اخرى تضمن تحقيق الشروط الواجب توفرها في الخريطة الجغرافية لإدراك القارئ السريع مهما كانت درجة ثقافته وعمره.

التمويل:

لم يتلقَّ هذا البحث أي منحة محددة من أي جهة تمويلية في القطاع العام أو التجاري أو غير الربحي.

تضارب المصالح:

يُقرّ المؤلف بأنه لا توجد لديه أي مصالح مالية متضاربة أو علاقات شخصية معروفة من شأنها أن تؤثر على العمل المذكور في هذه الورقة.

المصادر :

جاد، طه محمد. (1987). تحليل الخريطة الكنتورية «باهتمام جيمورفولوجي». ط2، مكتبة الانجلو المصرية.

حسين، سيد حسن. (2011). أساليب التمثيل الكارتوغرافي «المستخدمة في خرائط التوزيعات الطبيعية والبشرية». ط1، مكتبة الانجلو المصرية.

حمادة، ياسين عبد النبي. (2010). مشكلة الملوحة وأثرها في التباين المكاني للإنتاج الزراعي في قضاء بلد. رسالة ماجستير (غير منشورة)، كلية التربة، جامعة تكريت.

الزيدي، نجيب عبدالرحمن، والحمداني، سعد ثامر إبراهيم. (2020). الخرائط التحليلية. دار الإبداع، صلاح الدين/تكريت/العراق.

سطحية، محمد محمد. (1977). الجغرافيا العملية وقراءة الخرائط. ط1، دار النهضة، القاهرة.

الشريعي، أحمد البدوي محمد. (2011). الخرائط العملية «نماذج وتطبيقات». ط1، دار الفكر العربي، القاهرة.

عبد الرحمن، عباس. (2013). تقييم دقة تمييز النموذج الارتفاع الرقمي في دراسات تحديد الأحواض الساكبة للأنهار المتشاطئة، مجلة جامعة تشرين للبحوث والدراسات العلمية – سلسلة العلوم الهندسية، المجلد 35(9).

العزاوي، علي عبد عباس، وصباح حسين علي. (2006). استخدام نظم المعلومات الجغرافية في إنشاء وتمثيل بيانات نموذج الارتفاع الرقمي لنماذج مختارة في شمال العراق. مجلة التربية والعلم، المجلد 12.

مصطفى، أحمد أحمد. (2000). الجغرافيا العملية والخرائط. ط1، دار المعرفة الجامعية.

مصطفى، أحمد أحمد. (n.d). الخرائط الكنتورية تفسيرها وقطاعاتها. دار المعرفة الجامعية.

وزارة التخطيط والتعاون الإنمائي، الجهاز المركزي للإحصاء وتكنلوجيا المعلومات، المجموعة السنوية الاحصائية لسنة 2017، بغداد، 2024 .

References

Abdel Rahman, A. (2013). Evaluating the Accuracy of Digital Elevation Model Recognition in Studies of Determining the Drainage Basins of Riparian Rivers. Tishreen University Journal for Research and Scientific Studies, Engineering Sciences Series, 35(9), Syria.

Al-Azzawi, A. A., & Ali, S. H. (2006). Using Geographic Information Systems to Create and Represent Digital Elevation Model Data for Selected Models in Northern Iraq. Journal of Education and Science, 12, Tikrit University.

Al-Shari'i, A. A. M. (2011). Practical Maps: Models and Applications. 1st Ed., Dar Al-Fikr Al-Arabi, Cairo.

Al-Zaidi, N. A. R., & Al-Hamdani, S. T. I. (2020). Analytical Maps. Dar Al-Ebdaa, Saladin/Tikrit, Iraq.

Awawdeh, M., Alkhateeb, E., & Al-Radaideh, N. (2023). The Use of Remote Sensing and GIS for Mapping Silica Sand Deposits in Jordan. Jordan Journal of Earth and Environmental Sciences.

Gad, T. M. (1987). Analysis of the Contour Map: With Geomorphological Interest. 2nd Ed., Anglo-Egyptian Library, Cairo.

Hamada, Y. A. N. (2010). The Problem of Salinity and Its Impact on the Spatial Variation of Agricultural Production in Balad

District. M.Sc. Thesis (Unpublished), College of Soil, Tikrit University, Iraq.

Hassan, H. S. (2011). Cartographic Representation Methods: Used in Maps of Natural and Human Distributions. 1st Ed., Anglo-Egyptian Library, Cairo.

Ministry of Planning and Development Cooperation, Central Bureau of Statistics and Information Technology. (2024). Annual Statistical Collection for the Year 2017, Baghdad, Iraq.

Mustafa, A. A. (2000). Practical Geography and Maps. 1st Ed., Dar Al-Ma'rifa Al-Jami'a, Cairo.

Mustafa, A. A. (n.d.). Contour Maps, Their Interpretation and Sections. University Knowledge House, Cairo.

Satiha, M. M. (1977). Practical Geography and Map Reading. 1st Ed., Dar Al-Nahda, Cairo.

JJEES

JJEES (2025) 16 (4): 407-417
ISSN 1995-6681

Jordan Journal of Earth and Environmental Sciences

Petro graphic and geochemical characterization of volcanic rock in Debre Tabor area, Northwestern Ethiopia: Implication for petrogenesis of felsic volcanic rock

Yaregal Bayih* and Amare Getaneh

Department of Geology, Debre Markos University, P.O. Box. 269, Debre Markos, Ethiopia

Received on April 10, 2025, Accepted on June 5, 2025

Abstract

Debre Tabor area, located on the Northwestern Ethiopian plateau and composed of Cenozoic volcanic rocks with minor intertrappean sediments. To understand the petrogenesis of these rocks, we conducted field investigations, petrographic studies, and geochemical analyses. The main volcanic products include basalt, trachyte, Ignimbrite, rhyolite, phonolite, and pyroclastic fall and flow deposit. Basalt rocks in the study area occur as a flat-lying topography, and under petrographic microscope view, they exhibit porphyritic and trachytic textures with phenocrysts of olivine, pyroxene, Fe-Ti Oxides, and P gioclase. Rhyolite rocks found by forming huge domes and show porphyritic and glomeroporphyritic texture with phenocrysts of sanidine, biotite and plagioclase minerals. The phonolite rock unit exhibit phenocryst of alkali feldspar, feldesphathoids (nepheline) and neason. The trachyte rock unit is formed by a volcanic plug. Debre Tabor volcanic rocks were formed from evolved magma as compared to a primary magma (with Ni: 400–500 ppm, Cr: > 1000 ppm and MgO: 10–15 wt.%, Hess, 1992). In chondrite and primitive mantle normalized REE patterns, both basaltic and felsic rocks exhibit enrichment of LREE (with a (La/Yb)N ratio ranging from 12.37 to 16.11), likely due to crustal contamination and an enriched mantle source of magma. In this pattern basaltic rocks show depleted trend of HREE, due to garnet or deep mantle source of magma. But felsic rocks show flat trend of HREE due to mafic crustal rock contamination effect. From the ratio of Ce/Pb versus MgO and Ce/Pb versus Nb/U, data points for Debre Tabor volcanic rocks fall outside of the mantle value (Ce/Pb; 25 ± 5; Nb/U = 47 ± 10) and plotted in the field of crustal/ lithospheric values, which give a strong indication for the crustal contamination effect of mantle-derived magma. All mafic rock samples in the study area have low Rb/Nb (0.5-0.97) and La/Nb (0.72-0.97) ratios and chondrite, primitive mantle normalized incompatible trace element patterns for basaltic rock that overlap with OIB, which confirms that the source of magma in the study area is from deep mantle with lower degree of partial melting. The geochemical analysis (positive correlation of Hf vs. La) shows that the basaltic rocks in the study area are co-genetic with felsic rocks and evolved through fractional crystallization and crustal contamination effects.

Keywords: *Crustal contamination; Crystal fractionation; Geochemistry and Petrogenesis, Magma evolution*

1. Introduction

The Ethiopian volcanic series can be divided into two main categories, based on their general lithological grouping: (I) Continental Flood Basalt (CFB), which is often covered by shield basalts and spans large swaths of the Balad's highland northwest and southeast plateaus in the Ter-tiary period, and (II) Rift volcanism, which is still actively occurring. One of the world's largest continental flood basalts (CFBs) is the Ethiopian CFB, which is among the youngest, least de-formed, and best-preserved uppermost volcanic rocks (Kieffer et al., 2004). One of the best instances of plume-related magmatism in an area of active extension is the volcanic province (Stewart et al., 1996, and references therein). It is a typical model to investigate how continen-tal crustal materials, sub-continental lithospheric mantle, and mantle plume contributed to the formation of plateau basalts (e.g. Courtillot et al., 1999). The Continental Flood Basalts (CFB) and the ensuing shield basalts have been the subject of studies on the Ethiopian plateau (e.g., Hofmann et al., 1997; Yirgu, 1997; Pik et al., 1998, 1999; Kieffer et al., 2004; Beccaluva et al., 2009; Corti, 2009; Natalie et al., 2017). According to Hofmann et al. (1997), the majority of the Ethiopian flood basalts formed a vast volcanic plateau 30 million years ago. Volcan-ism was mostly restricted along rifting regions following this formation, and several sizable shield volcanoes formed on the volcanic plateau's surface (Mohr & Zanettin, 1988).

Along the Ethiopian and Afar rifts, volcanic activity is still occurring today (Chazot & Bertrand, 2003). An area of over 600 000 km2 is covered by the Ethiopian flood basalts, also known as the trapseries, which are composed of a layer of basaltic and felsic volcanic rocks. In certain places, the layer is as thick as 2 km (Pik et al., 1999).

Transitional to tholeiitic, basaltic lava flows make up the majority of the Northern Ethiopian plateau, which is situated along the western flanks of the Afar Depression and the main Ethiopian Rift (MER) (Fig. 1a) (Mohr and Zanettin, 1988). Basalt makes up the majority of the volcanic rocks that cover the vast Ethiopian and Somalian plateau, which are part of the trap series (Abbate and Sagri, 1980). According to

* Corresponding author e-mail: yaregalbayih081@gmail.com

Hofmann et al. (1997), the continental flood basalts (CFB) found on the Ethiopian Plateaus in the south and north are among the youngest, least deformed volcanic rocks developed during the Oligocene time. Paleosoils are found at the base of the plateau's dominant basaltic lava flows (Pik et al., 1998). Plagioclase, clinopyroxene, and occasionally olivine phenocrysts characterize the mineralogical composition of the flood basalts, which often exhibit aphyric to sparsely phyric textures (Kieffer et al., 2004).

In Northern Ethiopia, the flood basalts are composed of high-Ti theoliites (HT1, HT2) in the southeast and generally low-Ti (LT) in the northwest (Pik et al., 1998). The Eastern section features the first high-Ti lava (HT1), while the Lalibela area, which is nearer the Afar depression, exposes the second high-Ti (HT2) series. Higher amounts of incompatible elements and extensive fractionation of REE are present in both the HT2 and HT1. In comparison to the HT1 basalts, the HT2 basalts are more magnesian and contain olivine and clinopyroxene phenocrysts. Although the flood basalt episode is dominated by basalts, it also includes substantial amounts of felsic lava flows and pyroclastic materials in the upper portions of the series, either interbedded in or covering the flood basalt (Ayalew and Yirgu, 2003). The Lima Limo rhyolites are interbedded with the low-Ti flood basalts in the Northwestern section of the plateau. In contrast, the Wegel Tena rhyolites are outcropped over the high-Ti basalts close to the Eastern Afar border. The plateau ignimbrites have a similar phenocryst assemblage of orthoclase, quartz, sanidine, and clinopyroxene, and their textures range from porphyritic to glassy (Ayalew & Yirgu, 2003).

The geochemistry of trace elements indicate that the majority of melts beneath the rift originate from the mantle, possibly from depths of 40–80 km, which correlates with the change from spinel to garnet peridotite (Latin et al., 1993). According to Peccerillo et al. (2003), the MER's mafic rocks have a porphyritic texture with phenocrysts of olivine, clinopyroxene, and Plagioclase. These rocks include hydrovolcanic lapilli, strombolian scoria, and lavas. On the other hand, felsic volcanic products dominate the Northern MER. According to Peccerillo et al. (2007), zoned magma chambers are responsible for the predominance of acidic volcanic products over mafic ones. Rhyolitic melt builds up at the top of these chambers, while mafic melts erupt when fractures reach the chamber's deeper layers. Silicic centers and a younger phase of basaltic volcanism are characteristics of Quaternary magmatism in the MER. While the silicic rocks are peralkaline, the basaltic lavas are slightly alkaline (Trua et al., 1999; Peccerillo et al., 2003). The plume, asthenosphere, and lithosphere are hypothesized to contribute to the partial melting of the mantle that produces mafic magmas (Gibson et al., 2006).

The majority of earlier research conducted on the volcanic plateau in Northern Ethiopia was limited to regional scale (e.g., Ayalew and Yirgu, 2003, Desta et al., 2014; Natali et al., 2016; Pik et al., 1998, 1999) and lacked a comprehensive study on the felsic volcanic rocks. In this study, petrographic and geochemical ' 'data's investigated to get information about the origin of felsic rocks and magma evolution processes.

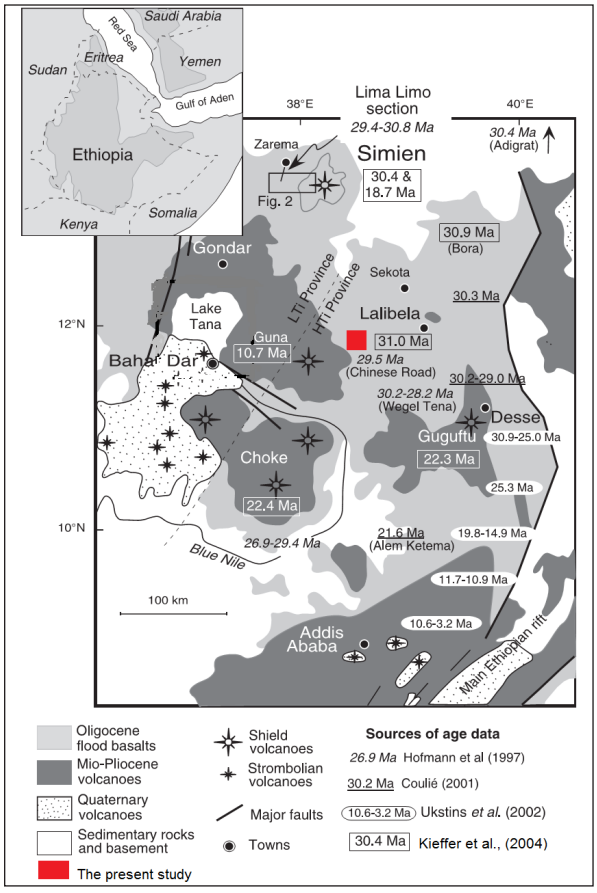

Figure 1. Map of the Northern part of the Ethiopian plateau showing the extent of the flood volcanism and the location and ages of the major shield volcanoes after Hofmann et al. (1997), Kieffer et al. (2004), and Ukstins et al. (2002). The dashed line shows the boundary between the LT and HT provinces as defined by Pik et al. (1999).

2. Sampling and Analytical Techniques

Sampling

In order to cover the complete volcanic succession, geological surveys and sampling were carried out using road and river cuttings that clearly display the volcanic rocks. Several lithological units were systematically mapped and described for various analytical investigations. The representative rock samples were taken from phonolite, rhyolite, trachyte, and basalt rocks, taking into account differences in texture, color, and weathering severity. Forty-five rock samples, each weighing between 0.75 and 1 kg, were gathered, labeled, and put in a plastic bag for various laboratory examinations.

Sample analysis

Nineteen representative rock samples - eight basalts, four rhyolites, four phonolites, and three trachytes were chosen, and each sample was split in half: one half was used for major and trace element chemistry, while the other half was used for thin section preparation. Thin sections were made in the Geological Survey of Ethiopia's (GSE) laboratory. The preparation process involves removing worn portions of the rock surface and using a diamond blade to cut each sample to the appropriate size.

Using a transmitted light microscope at Bahir Dar University's School of Earth Sciences, a thorough thin section description was completed, including rock name, mineral

identification, modal proportion, and textural descriptions. Geochemical investigations of bulk rocks were conducted at the Australia Laboratory Service (ALS) in Ireland. In a steel jaw crusher, materials were first cleaned, dried, and crushed into coarse chips that passed through a 70% 6 mm or fine rock chips that passed through 85% of a 2 mm. The samples were broken down using lithium metaborate, and the major and trace element contents were ascertained using a combination of Inductively Coupled Plasma-Mass Spectrometry (ICP-MS) and Inductively Coupled Plasma Atomic Emission Spectrometry (ICP-AES). Furthermore, a thermal decomposition furnace was used to calculate the loss on ignition (LOI) for each sample (1.0g) heated to 800°C for one hour. At last, all of the evaluated data were arranged and interpreted using several computer programs, including Microsoft Excel, ArcGIS, and GCDkit 4.1.

3. Results and Discussion

3.1 Results

3.1.1 Geology

Various volcanic rocks and their weathering derivatives comprise the majority of the research region (Figure 3b). These include unwelded tuff, phonolite, ignimbrite, trachyte, rhyolite, and basalt. In the area around Debre Tabor Town, basaltic rock was abundantly exposed and covered a flat terrain. It is black to dark grey, fine-grained, and aphyric to porphyritic. The phenocryst contains plagioclase, olivine, and pyroxenes. In the northwest of Debre Tabor town, a plug volcanic feature has exposed trachyte (figure B). On the outside of the plug, it is light gray and has an aphanitic texture; nevertheless, in the middle of the plug, phenocrysts of plagioclase and alkali feldspars were seen to have a coarse-grained structure. The loosely to more compacted form of tuff is its defining feature. Ignimbrite is found on top of tuffaceous rock, which has a range of clast sizes. Greenish to grey in color, the phonolite unit has a greasy sheen. Alkali feldspar and feldspatoids (nepheline) phenocrysts are present in this poorly to strongly porphyritic material. Several rhyolitic domes (figure A) were created when viscous magma rose effusively onto the surface and subsequently accumulated around the vent.

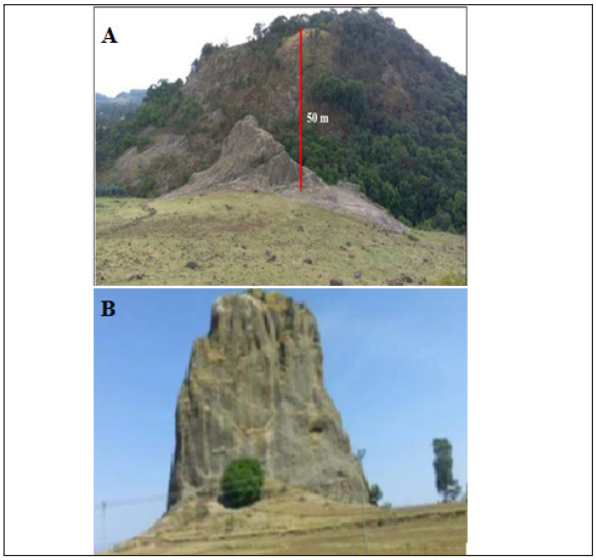

Figure 2. A and **B**: Rhyolitic dome and trachyte plug at Magere Mariam church and Amora Gedel, respectively.

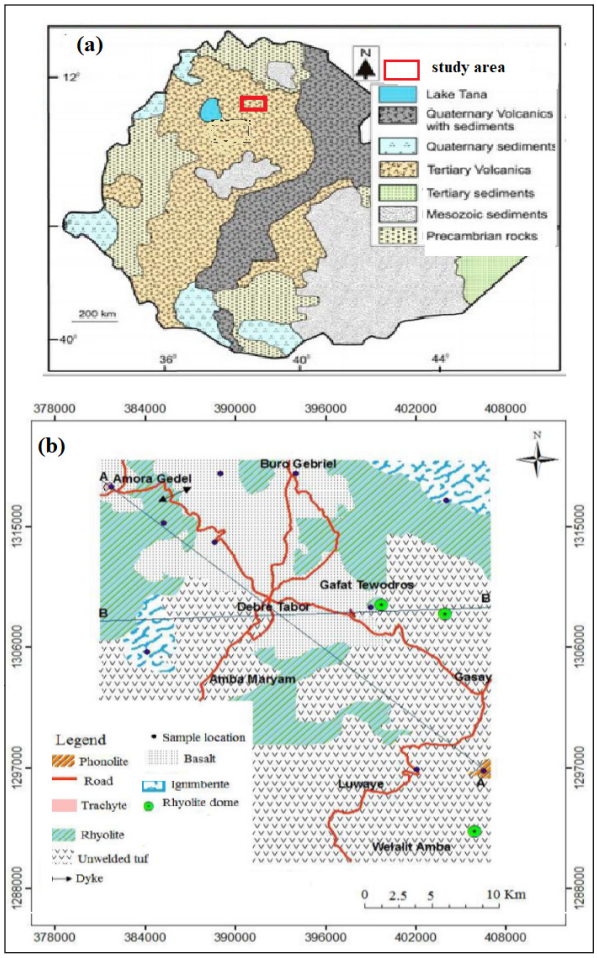

Figure 3. (**a**) Geological map of Ethiopia (modified after Merla et al. 1973), (**b**) simplified geological map of the study area

3.1.2 Petrography

The porphyritic texture of basaltic rock can be seen under a petrographic microscope to display euhedral to subhedral phenocrysts of pyroxene, olivine, and plagioclase (Figure 4A & B). The phenocryst assemblage is composed of 2-4 Vol.% pyroxene (augite), 5-7 Vol.% euhedral plagioclase lath, and approximately 3–4% olivine. Furthermore, the ground mass is composed of opaque, lath-shaped plagioclase, pyroxene (augite), and volcanic glass material. Rhyolite has 84 vol.% ground mass with a porphyritic structure and 16 vol.% phenocyst. The crystals are plagioclase, quartz, and subhedral alkali-feldspar. 6 Vol.% sanidine, 4-6 Vol.% plagioclase, 1-2 Vol.% opaque, and 1 Vol.% biotite are the phenocrysts. Quartz, plagioclase, and sanidine make up the groundmass. Trachyte is composed of 86 vol.% groundmass and 14 vol.% phenocrysts (figure 5 C & D). The phenocryst phases consist of <1 Vol.% Na-rich pyroxene, 2-3 Vol.% plagioclase, and 10-12 Vol.% massive euhedral to subhedral crystals of alkali feldspar (sanidine). Alkali feldspar (sanidine), Na-rich pyroxene, opaque, hornblende, biotite, and small amounts of volcanic glass are also found in the groundmass. Phonolite makes up 85 vol.% of ground mass and 13–20% of the phenocryst. 5-8 Vol.% lath-shaped alkali feldspar (sanidine), 7-9 Vol.% nepheline, 1-2 Vol.% sodic (Na-rich) pyroxene, and 2-3 Vol.% nosean make up the euhedral to subhedral phenocrysts. The groundmass consisted of nepheline, sanidine, opaque minerals, and pyroxene, high in sodium.

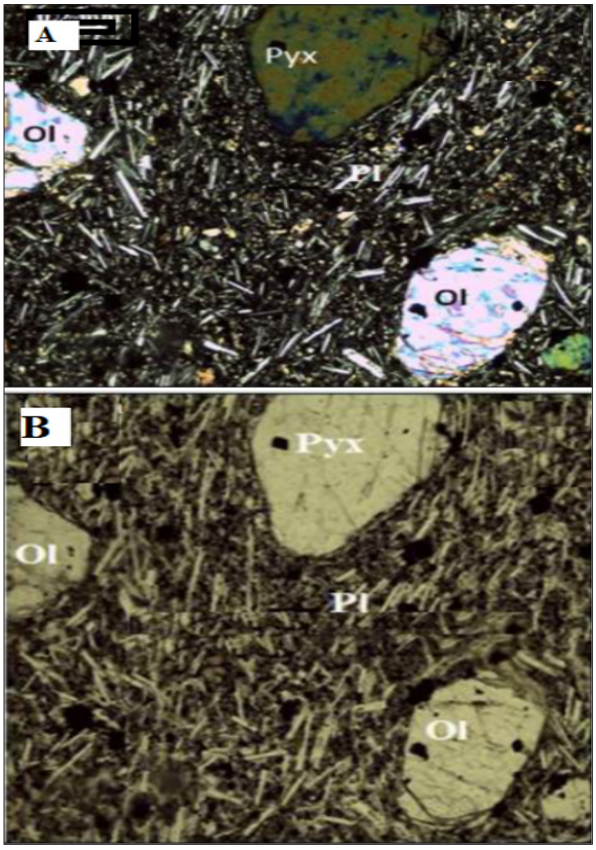

Figure 4. A & B. PPL and XPL view of Oligocene basalt with phenocrysts and microphenocrysts of olivine, pyroxene and plagioclase with inclusion of Fe-Ti Oxide in olivine minerals.

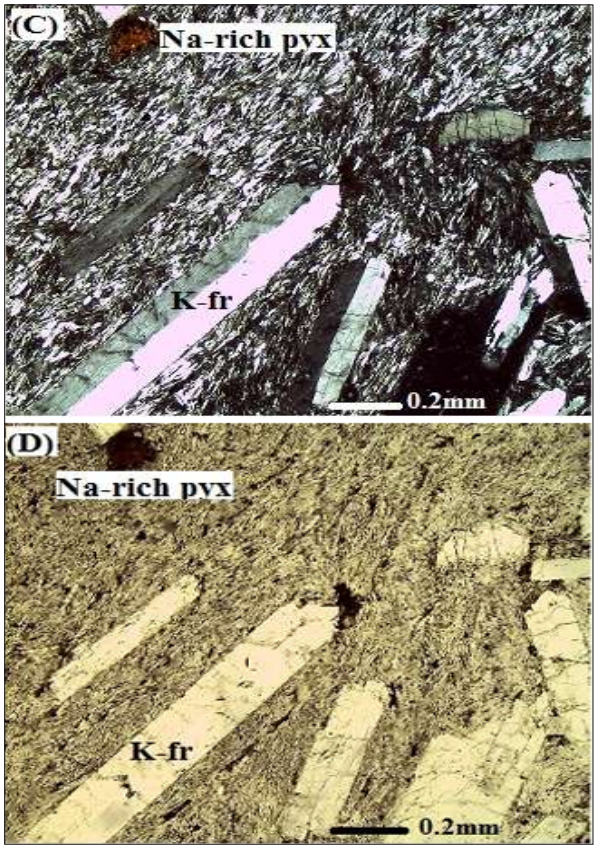

Figure 5. C & D. PPL and XPL view of trachyte unit having phenocrysts of biotite, k-feldspar, and Na-rich pyroxene with trachytic texture.

3.1.3 Geochemical results

The geochemical results in Table 1 show that all volcanic rock samples in the study area are characterized by low Ni (0.35-178 ppm) and Cr (7.54-350 ppm) contents, as well as low MgO contents (0.03–9.5 wt.%). These values are very low compared to those of a primary magma (with Ni: 400–500 ppm, Cr: > 1000 ppm, and MgO: 10–15 wt. %, Hess, 1992). This confirms that all volcanic rocks in the study area are not primary magma, instead all are fractionated.

Table 1. Major (wt. %) element ' 'data's of volcanic rock in the Debre Tabor area

Samples	SiO_2	Al_2O_3	Fe_2O_3	FeOt	CaO	MgO	Na_2O	K_2O	TiO_2	MnO	P_2O_5	SrO
DT1	43.3	16.4	12.85	11.565	9.86	5.47	3.37	1.72	3.43	0.21	1.25	0.14
DT2	42.2	14.95	13.2	11.88	10.43	8.06	3.11	1.12	3.66	0.18	1.3	0.19
DT3	46.25	15.54	12.77	9.57	9.07	6.31	3.27	1.62	3.41	0.21	1.26	0.14
DT4	43.8	15.01	12.25	10.05	9.16	9.5	3.85	1.61	2.65	0.17	0.93	0.12
DT5	47.1	16.5	12.63	7.55	8.54	5.36	4.01	1.74	3.32	0.201	1.23	0.13
DT6	43.2	15.1	13.4	11.56	8.54	7.76	4.55	1.54	2.42	0.21	1.09	0.1
DT7	44.1	15.02	12.01	10.02	9.07	6.41	3.77	1.72	3.4	0.41	1.46	0.24
DT8	45	14.22	11.03	9.85	9.76	5.47	3.47	1.42	3.53	0.31	1.35	0.24
DT9	58.1	23.4	3.41	2.93	0.87	0.29	8.62	6.01	0.39	0.31	0.03	0.02
DT10	59.5	21.73	4.32	2.03	0.45	0.17	9.06	6.45	0.32	0.31	0.13	0.02
DT11	62.1	19.2	2.21	1.97	0.22	0.03	6.72	5.8	0.42	0.01	0.67	0.01
DT12	57	19.76	3.21	1.98	1.02	0.25	7.03	6.58	0.57	0.09	0.27	0.03
DT13	55.3	20.34	3.78	3.57	1.54	0.5	8.53	5.03	0.54	0.06	0.34	0.02
DT14	68.3	15.05	2.43	2.187	0.33	0.15	6.56	5.17	0.42	0.11	0.06	0.01
DT15	56.4	22.2	3.52	3.168	0.91	0.4	8.17	5.84	0.43	0.3	0.02	0.01
DT16	61.8	19.55	2.32	2.088	0.29	0.06	6.12	5.72	0.51	0.01	0.66	0.01
DT17	71.1	14.91	1.64	1.476	0.6	0.3	5.59	5.19	0.6	0.02	0.11	0.02
DT18	67.5	16	2.45	2.23	0.43	0.25	6.45	5.05	0.45	0.11	0.05	0.01
DT19	66.1	16.97	2.46	2.35	0.41	0.15	5.43	4.12	0.39	0.12	0.03	0.01

Table 2. Trace element ‘ ‘data’s of Debre Tabor volcanic rock

Sample	Sc	V	Cr	Co	Ni	Cu	Zn	Cs	Rb	Ba	Sr	Th
DT1	19	295	30	33	11	26	116	0.29	43.4	695	1225	2.95
DT2	21	273	210	44	115	39	101	0.27	23.9	695	1615	2.65
DT3	19.2	298	33	33.6	11.02	25.2	115	0.29	43.21	687	1226	2.94
DT4	22	228	310	47	178	50	96	0.39	32.3	551	1060	4.92
DT5	18.37	271	29.7	32.82	11.3	26	118	0.28	44.1	691	1223	2.95
DT6	18.77	289	54.7	35.82	12.3	37	117	0.47	45.01	581	1013	3.45
DT7	17.02	268	53	36.6	10.02	35.2	99	0.28	39.21	677	1226	2.91
DT8	17	275	34	35.3	11.5	86	115	0.39	45.4	690	1235	2.85
DT9	1.3	14.23	9.4	1.5	1.2	1	192	1.33	199.5	17	21.3	33.4
DT10	1.2	12.23	7.54	0.45	0.35	1	189	1.04	199.8	19	21	34.4
DT11	1	25	9.7	0.9	2	2	75	0.23	128	116	87	17.3
DT12	1.13	26.3	9.82	1.03	2.01	2	72	0.21	124	113	89	16.5
DT13	1.04	16	11.02	1.09	1.2	1	193	1.34	193	14.9	23	31.3
DT14	4	9	10	1	1	1	81	0.43	109.5	366	51.2	15.8
DT15	1	15	10	1	1	1	194	1.35	199	15.6	22.3	32.3
DT16	1	26	10	1	2	2	80	0.26	126.5	115	89	16.15
DT17	2	8	30	1	1	1	36	0.61	94.4	367	173.5	11.4
DT18	3	9.83	10	1.3	1	1.2	78	0.4	98.7	364	51	13
DT19	3.2	9.87	10	1.4	1	1.2	77	0.3	83.45	302	43.3	12

Table 3. Trace element ‘ ‘data’s of Debre Tabor volcanic rock

Sample	La	Ce	Pr	Nd	Sm	Eu	Gd	Tb	Dy	Ho	Er	Yb	Lu
DT1	46.2	95.5	11.5	50.7	9.97	3.56	9.33	1.19	6.57	1.19	3.39	2.49	0.39
DT2	36.1	75.4	9.52	44.3	9.54	3.22	7.89	1.1	5.5	1.02	2.61	1.92	0.26
DT3	45.7	95.2	11.03	49.9	9.97	3.2	9.22	1.17	5.54	1.05	3.43	2.53	0.43
DT4	45.9	86.7	9.71	40.3	7.66	2.73	6.65	0.93	5.33	0.94	2.38	1.9	0.32
DT5	47.1	95.7	11.3	50.3	9.96	3.21	9.34	1.19	6.58	1.01	2.73	1.93	0.25
DT6	47.1	95.7	11.3	50.3	9.96	3.21	9.34	1.19	6.58	1.01	2.73	1.93	0.25
DT7	45.7	95.2	11.03	49.9	9.97	3.2	9.22	1.17	5.54	1.05	3.43	2.53	0.43
DT8	46.2	95.5	11.5	50.7	9.97	3.56	9.33	1.19	6.57	1.19	3.39	2.49	0.39
DT9	98.7	174	23.1	60.01	6.58	1.05	5.85	1.02	7.21	1.43	4.78	5.67	0.83
DT10	102	194	23.1	59	6.57	1.03	5.87	1.03	8.54	1.32	4.01	5.07	0.76
DT11	98.3	164	16.4	54.1	7.85	1.32	5.6	0.98	5.77	1.32	3.44	3.97	0.65
DT12	94.1	163	15.4	52.4	6.85	1.54	5.06	0.91	4.99	1.34	3.47	4.2	0.68
DT13	96.45	178	22.7	60.06	7.04	1.14	5.48	0.8	6.97	1.53	5.01	5.76	0.87
DT14	92.4	173	18.7	65.4	10.05	2.06	7.61	1.19	7.68	1.5	4.72	5.38	0.87
DT15	96.73	197	23.3	61.6	7.58	1.06	5.84	1	7.03	1.48	4.93	5.77	0.86
DT16	97.8	163	16.6	53.6	7.84	1.38	5.5	0.91	5.67	1.1	3.51	4.05	0.68
DT17	81.4	139	17.2	63.3	11.45	2.58	8.58	1.36	8.77	1.58	4.67	4.87	0.72
DT18	87	166	17.3	64	10.3	2.7	6.71	1.19	7.58	1.6	4.87	5.39	0.88
DT19	83.3	153	13.2	60.02	8.3	2.34	6.72	1.18	6.98	1.7	4.93	5.41	0.88

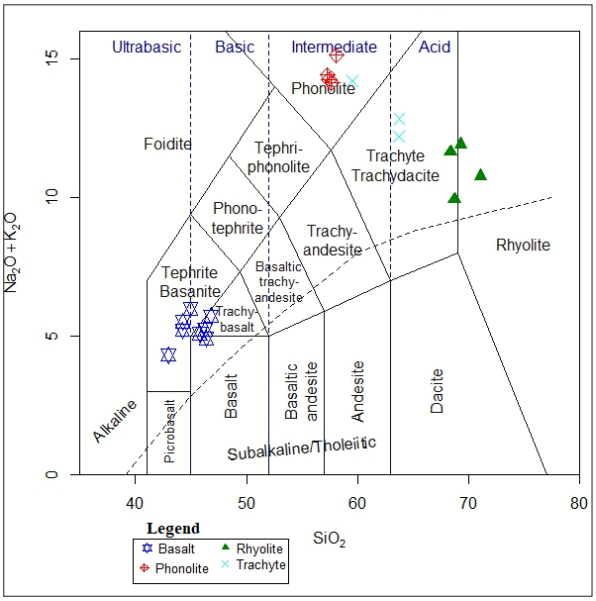

Figure 6. Total alkalis-silica (TAS) classification after Le Bas et al. 1986 for Debre Tabor volcanic rock.

All volcanic rock samples in the research area were plotted in the alkaline field using the total alkalis-silica (TAS) categorization following Le Bas et al. (1986) Figure 6.

In Debre Tabor volcanic rocks, the concentration of FeOt, CaO, TiO_2, and P_2O_5 declines as the weight percentage of SiO_2 increases from basalt to rhyolite (Figures 7 B, C, E, and F). Figure 7A and D show that while the SiO_2 concentration in weight percentage rises from basalt to phonolite, the concentration of Al_2O_3 and K_2O falls from phonolite to trachyte and from trachyte to trhyolite.

The mafic and felsic rocks of the study area (Figure 8 A and B) exhibit highly enriched lighter rare earth elements (LREE) and depletion of heavy rare earth elements (HREE) in basaltic rock samples, according to the chondrite and primitive mantle normalized incompatible trace element patterns (Boynton, 1984;McDonough and Sun, 1995).

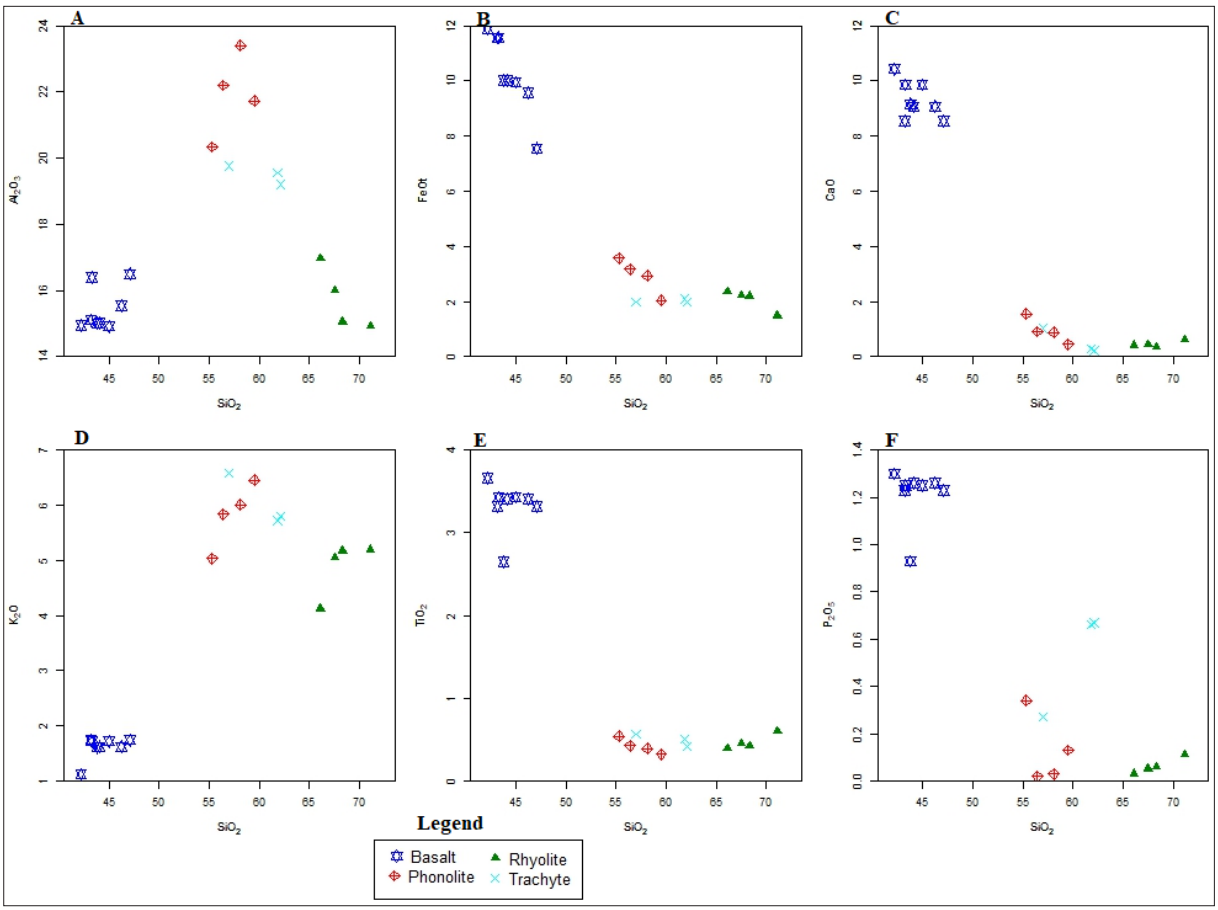

Figure 7. A – **F**. Variation diagrams of major elements versus SiO2 in wt% for Debre Tabor volcanic rocks

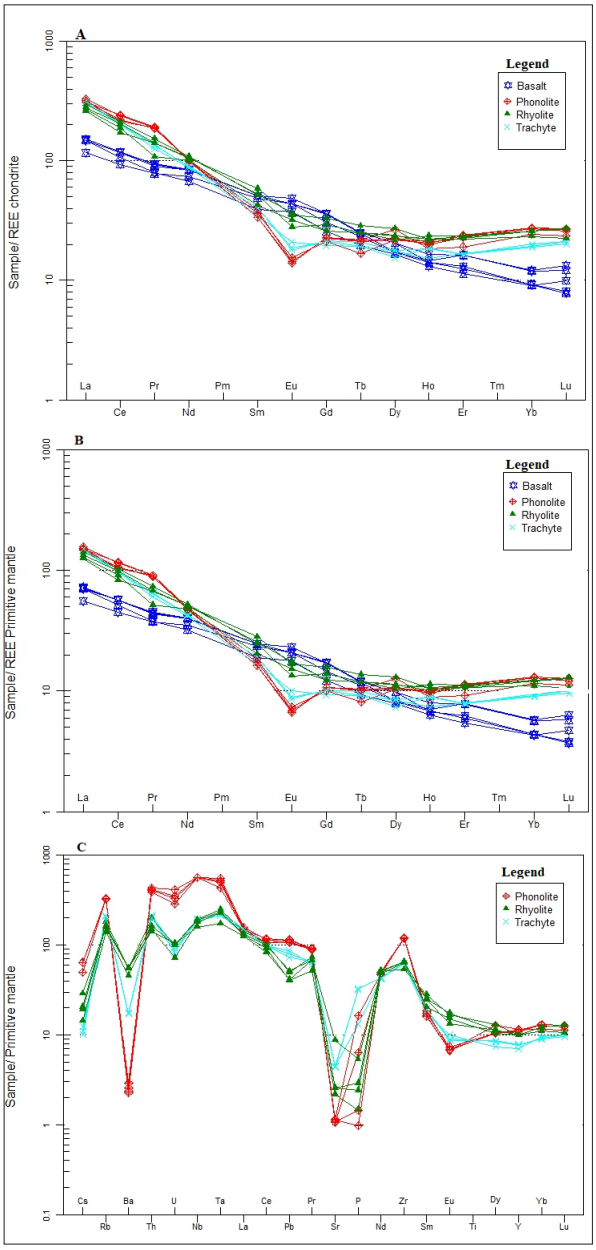

Figure 8. A, **B**, and **C**: Chondrite, primitive mantle REE, and primitive mantle normalized abundance pattern (Boynton, 1984, and Mc Donough and Sun 1995) for Debre Tabor volcanic rocks

4. Discussion

4.1. Fractional crystallization and crustal contamination

According to petrographic analysis, the main phenocryst phases for volcanic rocks in the study area are olivine, clinopyroxene, nepheline, opaque minerals, biotite, feldspars (including sanidine), and nosean. Figure 4 shows that olivine, clinopyroxene, plagioclase, and opaques are found as phenocryst phases in thin sections of basaltic rocks, but they are absent from felsic rocks, indicating that magma fractionation took place in the study area.

The geochemical results (Tables 1 & 2) indicate that the volcanic rocks in the study area have low concentrations of Ni (1 - 178 ppm), Cr (10 - 310 ppm), and MgO (0.03 - 9.5 wt.%), which is very low when compared to a primary magma (with Ni: 400–500 ppm, Cr: > 1000 ppm, and MgO: 10-15 wt. %, Hess, 1992). This result indicates that all the volcanic rocks in the study area are fractionated, and that the concentrations of MgO (wt.%), Ni, and Cr (ppm) decrease from basaltic rocks to felsic rocks as a result of olivine and clinopyroxene fractionation.

The concentration of FeOt, CaO, TiO_2, and P_2O_5 in weight percentage decreases with increasing SiO_2 concentration from basalt to rhyolite, according to variation diagrams of major elements versus SiO_2 in weight percentage (Figures 7 B, C, E, and F). This pattern indicates the fractionation (removal) of olivine or clinopyroxene, Ca-rich plagioclase, Fe-Ti Oxide, and apatite, respectively, in mafic rocks. The concentration of Al_2O_3 and K_2O in weight percentage increases from basalt to phonolite and then decreases from phonolite to trachyte and from trachyte to rhyolite (Figures 7 A & D) with increasing SiO_2 concentration. The data points for felsic, intermediate, and mafic rocks exhibit a positive correlation (the same orientation) (Figures 7 B, C, E, and F), confirming the co-genetic nature of these rocks. The fractional crystallization process was responsible for the evolution of magma from mafic to felsic.

The lighter rare earth elements (LREE) exhibit enrichment as a result of crustal contamination and magma derivation from enriched mantle sources in chondrite and primitive mantle normalized incompatible trace element patterns (Boynton, 1984 and Mc Donough and Sun, 1995) (Figures 8 A & B). In these patterns, the heavy rare earth elements (HREE) exhibit a depleted trend in basaltic rock samples due to garnet mineral fractionation, but a flat trend in felsic rock samples due to the mafic crustal rock contamination effect of magma. A negative anomaly in Eu suggests the fractionation of feldspar from the magma.

In felsic rock samples, the primitive mantle normalized incompatible trace element pattern (figure 8C) reveals a significant negative anomaly in the concentrations of P, Eu, Ba, and Sr. Fractional removal of apatite and garnet causes depletion in P and Eu, while fractionation of feldspar (sanidine and/or plagioclase) in mafic rocks causes depletion in Ba and Sr.

The Ce/Pb versus MgO weight percentage (Figure 9) and Ce/Pb versus Nb/U ratios (Figure 10) are beneficial because the OIB mantle value range is well established (Ce/Pb = 25 ± 5; Nb/U = 47 ± 10; Hofmann et al., 1986). The data points for the Debre Tabor basaltic rocks in figures 9 and 10 below are shown in the field of crustal/lithospheric values and fall outside of the mantle value (Ce/Pb; 25 ± 5; Nb/U = 47 ± 10). This provides clear evidence of the crustal contamination effect of mantle-derived magma.

Pearce (2008) states that volcanic rocks impacted by the crustal contamination effect will have data points above the MORB–OIB array in Nb/Yb versus Th/Yb plots, or that crustal input through contamination produces oblique trends to MORB–OIB that extend into the volcanic arc array. The existence of crustal contamination during the development of volcanic rocks in the research area is shown by data points of basaltic rocks that fall above the MORB–OIB array (Figure 11) below.

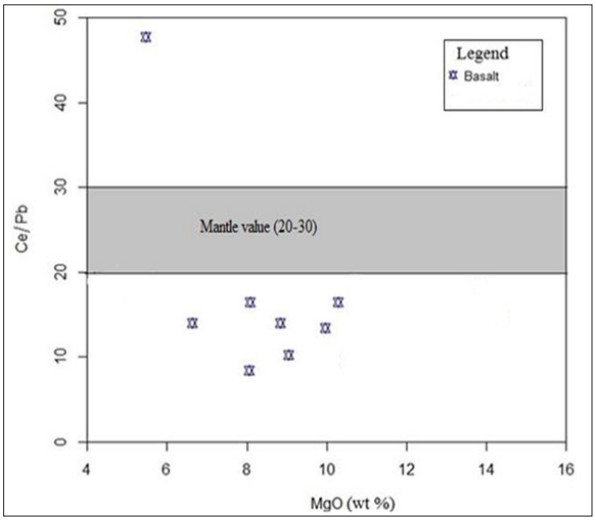

Figure 9. The ratio of Ce/Pb against MgO (wt.%) for Debre Tabor basaltic rocks. The shaded region indicates Ce/Pb ratio of the mantle value (25±5) after Hofmann et al. (1986)

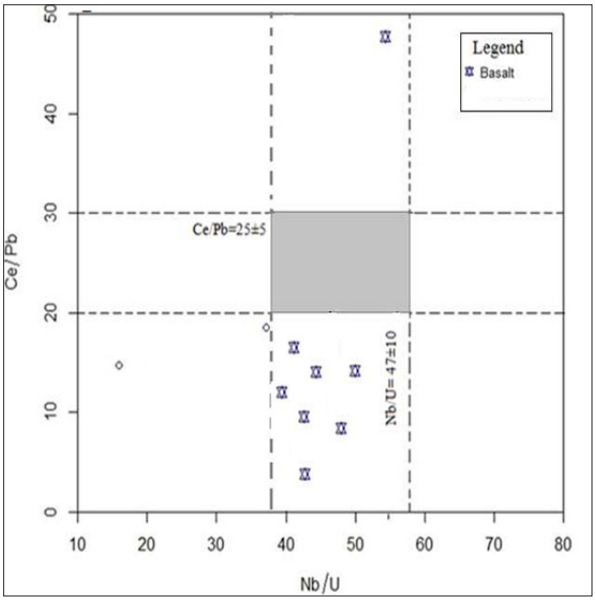

Figure 10. The ratio of Ce/Pb versus Nb/U for Debre Tabor basaltic rocks. The shaded region indicates the ratios of Ce/Pb (25±5) and Nb/U (47±10) for the mantle value after Hofmann et al. (1986)

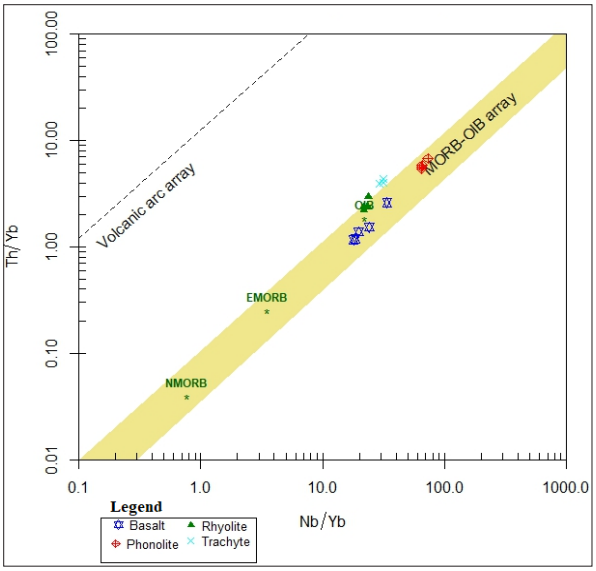

Figure 11. Nb/Yb versus Th/Yb diagram for the identification of crustal contamination (modified from Pearce 2008).

According to Dostal et al. (2017), the positive trends of incompatible trace elements (La vs. Hf) in both felsic and mafic rocks support the idea that both come from similar sources and effectively rule out melting of unrelated crustal rocks. Fessic volcanic rocks were formed from basaltic magma by a fractional crystallization process, according to the observed linear arrays of (Hf vs. La) (Figure 12) in the mafic and felsic rocks of the Debre Tabor volcanic rocks.

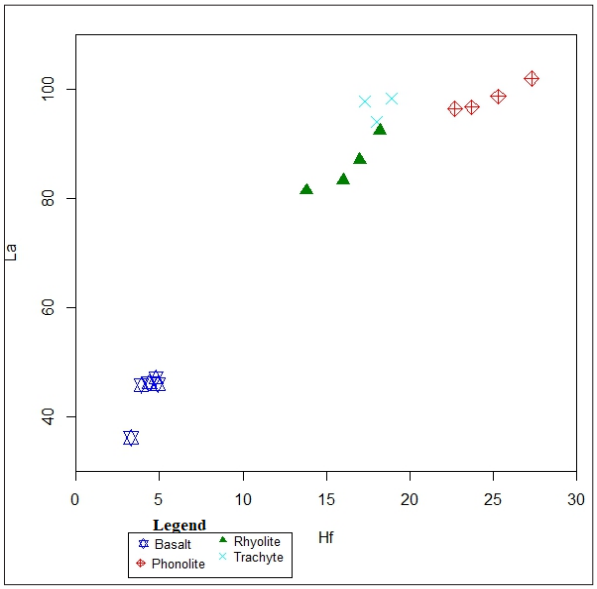

Figure 12. Variations of La vs. Hf (ppm) after (Dostal et al., 2017) for Debre Tabor volcanic rocks, showing the genetic relationship between the mafic and felsic rocks

4.2 Magma types

Hagos et al. (2010) state that the HT basalts have significantly greater TiO_2 levels (2.6–4.4 weight percent) than the LT basalts, which have the lowest TiO_2 values (1.99–2.56%). In the research area, the TiO_2 concentration of the basaltic rock sample ranges from 2.42 to 3.66, confirming that the volcanic rocks are classified as HT basalts. Ti/Y and Nb/Y ratios in high-Ti basalts range from over 450 to 0.4, respectively (Pik et al., 1998). Data points for the study area's basaltic rock fall within the high-Ti basalt (HT) field, as shown in Figure 13 below.

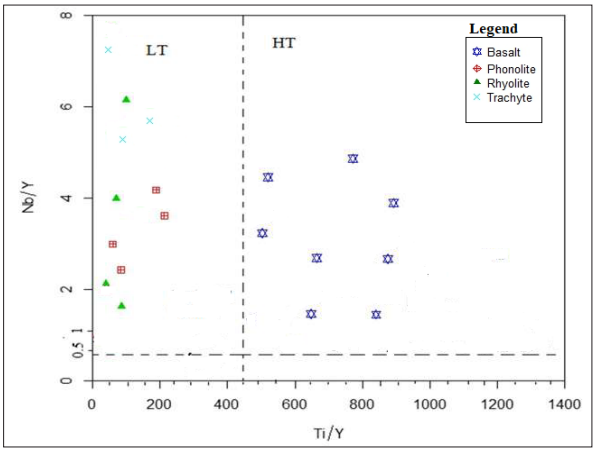

Figure 13. Nb/Y versus Ti/Y diagram of Debre Tabor volcanic rocks for the identification of low-Ti (LT) and high-Ti (HT) basalts (the figure is modified after Pik et al., 1998).

4.3 Degree of partial melting

Following the classification of total alkalis-silica (TAS) by Le Bas et al. (1986), all volcanic rock samples in the study area were plotted in the alkaline field (Figure 6). Figures 8A and B, which depict the pattern of chondrite and primitive mantle normalized rare earth elements (REEs) for basaltic rocks in the research area, demonstrate a reduction in heavy rare earth elements (HREEs). The alkaline field in the TAS diagram and the heavy rare earth element depletion patterns so indicate that the magma in the studied area originated from the deep mantle with a reduced degree of partial melting.

Pearce (2008) asserts that the Nb/Yb against TiO2/Yb plot can be used to determine the magma's origins. The point data for basaltic rocks in the research area (Figure 14A) fall within the OIB array's field, indicating that the deep mantle, which had a low degree of partial melting, was the source of the magma in the study area. To differentiate between garnet peridotite and spinel melting, the ratios of La/Sm and Sm/Yb are beneficial (Lassiter and DePaolo, 1997).

Consequently, the Debre Tabor volcanic rocks are plotted in the primitive mantle value (Figure 14B) and have high La/Sm (2.65–5.99) and Sm/Yb (2.52–4.97) ratios. In general, a smaller degree of partial melting of garnet peridotite produced the magma in the research location.

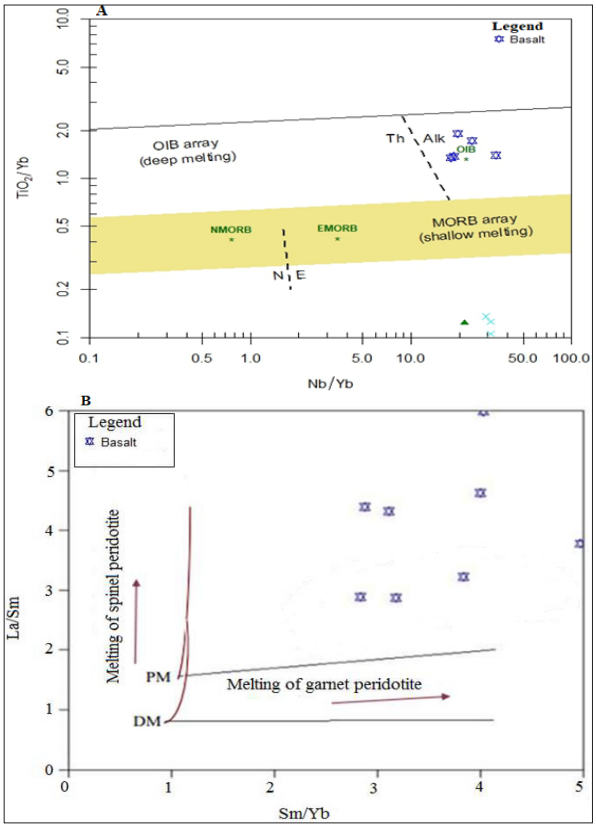

Figure 14. A & B. Nb/Yb versus TiO2/Yb diagram (Pearce, 2008) and Ratios of La/Sm versus Sm/Yb for Debre Tabor volcanic rocks with primitive mantle (PM) and depleted mantle (DM) compositions (Ayalew et al. 2006).

4.4 Comparison with N - MORB and OIB

4.4.1 Mantle source composition

Pyroxene and olivine were found as phenocrysts in basaltic rocks, as shown by petrographic views of thin sections (Figure 4). This phenocryst provided support for the mantle source of magma in the research area. The composition of volcanic rocks that are created by the fractional crystallization of magma from the mantle should continuously shift from mafic to intermediate to felsic rocks (Kessel et al., 1998). The research area's volcanic rocks exhibit a consistent compositional shift from mafic to intermediate to felsic, confirming the mantle as the source of the magma.

Very high LILE/HFSE ratios (such as Rb/Nb and La/Nb) are characteristic of magmacreated by the partial melting of crustal rock (Pearce et al., 1984). However, the ratio of this element in Debre Tabor volcanic rock is extremely low (0.72 – 0.97), confirming that the volcanic rocks in the research area originated from the mantle.

Figures 15A and B, which represent the chondrite and primitive mantle normalized incompatible trace element patterns for basaltic rocks in the study, demonstrate a depletion of heavier rare earth elements (HREE) in comparison to N-MORB and a high enrichment of lighter rare earth elements (e.g., the (La/Yb)N ratio ranges from 12.37 to 16.11) (after Sun and McDonough, 2016). The deep mantle is the source of magma in the research area, as confirmed by the normalized patterns (Figures 15A and B) for the basaltic rocks in the area overlaid on OIB (following Sun and McDonough, 2016). Because of the enriched mantle source, fractional crystallization, and crustal contamination effects on the magma, there is a high enrichment in lighter rare earth elements.

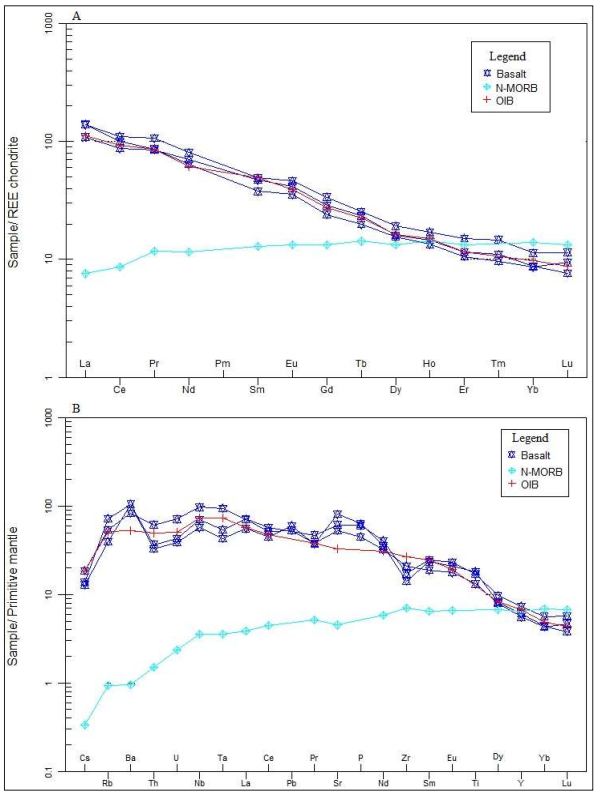

Figure 15. A & B. Chondrite and Primitive mantle normalized incompatible trace elements abundance pattern for Debre Tabor basaltic rocks after Nakamura (1974) and McDonough and Sun (1995), respectively. OIB and N-MORB data are used for comparison after Sun and McDonough (2016)

5. Conclusion and Recommendation

5.1. Conclusion

Based on field observations, petrography, and whole-rock geochemical studies (major and trace elements), the geology of the study area is mainly composed of basalt, ignimbrite, rhyolite, phonolite, trachyte flows, pyroclastic flow and fall deposits.

Debre Tabor volcanic rocks were not formed by solidification of primary magma; instead, it was formed from evolved magma, which was affected by crustal contamination and crystal fractionation evolutionary process. The LREE and highly incompatible trace element enrichment in felsic rocks is due to crystal fractionation, an enriched mantle source, and the effect of magma contamination on the crust.

The geochemical analysis (major and trace element analysis) shows that the mafic and felsic rock units in the Debre Tabor area have a co-genetic origin and formed by partial melting of deep mantle rock which is garnet peridotite with lower degree of partial melting. The Rb/Nb and La/Nb depleted character of the mafic lavas reflects the dominant contribution from the mantle plume during the genesis of volcanic rocks in the study area.

Basaltic rocks in the study area are grouped under high-Ti basalt, but the point data for felsic rocks fall under the low-Ti field.

5.2. Recommendations

For a better understanding of the properties of the magma source, age determinations, and geochemical processes involved in producing the rock suites of the Debre Tabor area, isotope geochemistry, mineral chemistry, and whole-rock studies should be conducted. Near Magere Mariam Church, there are also iron resources, and qualified businesses should be announced for exploration.

References

Ayalew, D., Yirgu, G., 2003. Crustal contribution to the genesis of Ethiopian plateau rhyolitic ignimbrites: basalt and rhyolite geochemical provinciality. J. Geol. Soc. 160 (1), 47–56.

Beccaluva et al. (2009). Continental flood basalts and mantle plumes: a case study of the northern Ethiopian Plateau. J. Petrology.37, 743–854.

Berhe, S.M., Desta, B., Nicoletti, M., Teferra, M., (1997). Geology, geochronology and geodynamic implications of the Cenozoic magmatic province in W and SE Ethiopia. J. Geol. Soc.London 144, 213–226.

Chazot G, Bertrand H (2003). Mantle sources and magma-continental crust interactions during early Red Sea-Aden rifting in Southern Yemen:. Journal of Geophysical Research 98:1819–1835.

Desta, M.T., Ayalew, D., Ishiwatari, A., Arai, S., Tamura, A., (2014). Ferropicrite from the Lalibela area in the Ethiopian large igneous province. J. Mineral. Petrol. Sci. 109 (4), 191–207.

Dostal, J., Hamilton, T.S., Shellnutt, J.G., (2017). Generation of felsic rocks of bimodal volcanic suites from thinned and rifted continental margins: geochemical and Nd, Sr, Pb-isotopic evidence from Haida Gwaii, British Columbia, Canada. Lithos 292, 146–160.

G. Corti. (2009). Continental rift evolution: from rift initiation to incipient break-up in the Main Ethiopian Rift, East Africa. Earth Sci. Rev.

Hagos M, Koeberl C, Kabeto K, Koller F (2010), Geochemical characteristics of the alkaline basalts and the phonolite-trachyte plugs of the Axum area, northern Ethiopia. Austrian J Earth Sci 103:153–170.

Hofmann, C., Courtillot, V., Feraud, G., Rochette, P., Yirgu, G., Ketefo, E. and Pik, R. (1997). Timing of the Ethiopian flood basalt event and implications for plume birth and global change . Nature .389, 338-341.

K. Stewart et al.(1996). Mantle plume and lithosphere contributions to basalts from southern Ethiopia. Earth Planet Sci. Lett.

Kessel, R., Stein, M. and Navon, O.,(1998). Petrogenesis of late Neoproterozoic dikes in the northern Arabian-Nubian Shield: implications for the Origin of A-type granites. Precambrian Research 92, 195–213.

Kieffer, B., Arndt, N., Lapierre, H., Bastien, F., Bosch, D., Pecher, A., Yirgu, G., Ayalew, D.,Weis, D., Jerram, D.A., Keller, F., Meugniot, C., (2004). Flood and shield basalts from Ethiopia: magmas from the African superswell. Journal of Petrology 45, 793–834.

Lassiter, J. C. and DePaolo, D. J. (1997). Plume/lithosphere interaction in the generation of continental and oceanic flood basalts: chemical and isotopic constraints. Large Igneous Provinces, Geophys. Monogr. 100, 335–355, American Geophysical Union, Washington, D.C.

Le Bas, M. J., Le Maitre, R. W., Streckeisen, A. and Zanettin, B. (1986). A chemical classification of volcanic rocks based on the total alkali-silica diagram. Journa of Petrology. 27, 745–750.

Natali, C., Beccaluva, L., Bianchini, G., Ellam, R.M., Savo, A., Siena, F., Stuart, F.M., 2017. High-MgO lavas associated to CFB as indicators of plume-related.

S.A. Gibson et al. (2006). The late Cretaceous impact of the Trinidade mantle plume: evidence from large volume mafic potassic magmatism in SE Beazil. J. Petro.

Sun and McDonough (2016). Chemical and isotopic systematics of oceanic basalt: implications for mantle composition and processes. Pennsylvania State University, 313-341.

Trua et al. (1999). Origin by fractional crystallization of transitional basalt for the Asela-Ziway pantellerites. Crustal control in the genesis of Plio-Quaternary bimodal magmatism of the Main Ethiopian Rift (MER) : Geochemical and isotopic (Sr, Nd, Pb) evidence. Chemical Geology 168(1):1-3

Merla G, Abbate E, Canuti P, Sagri M, Tacconi P. (1973). Geological map of Ethiopia and Somalia, scale 1:2,000,000. Consiglio Nazionale delle Ricerche, Roma.

Merla, G., Abbate, E., Azzaroli, A., Bruni, P., Fazzuoli, M., Sargi, M. and Tacconi, P. (1979). A geological map of Ethiopian and Somalia: Comment. Petgamon, 95p.

Mohr, P. and Zanettin, B. (1988). The Ethiopian flood basalt province. In: Macdougall, J. D. Continental Flood Basalts. Dordrecht:Kluwer Academic, pp. 63-110.

P.C. Hess. (1992). Phase equilibria constraints on the origin of ocean floor basalts

Pearce, J.A. and Cann, J.R. (2008). Tectonic setting of basic volcanic rocks determined using trace elements analyses. Earth and Planetary Science Letters, 19, 290-300.

Peccerillo, A., Barberi, M.R., Yirgu, G., Ayalew, D., Barbieri, M.W.U.T.W., Wu, T.W. (2003). Relationships between mafic and peralkaline silicic magmatism in continental rift settings: a petrological, geochemical and isotopic study of the Gedemsa volcano, central Ethiopian rift. J. Petrol. 44 (11), 2003–2032.

Pik, R., Deniel, C., Coulon, C., Yirgu, G., Hofmann, C., Ayalew, D., 1998. The northwestern Ethiopian Plateau flood basalts: classification and spatial distribution of magma types. J. Volcanol. Geoth. Res. 81 (1), 91–111.

Pik, R., Deniel, C., Coulon, C., Yirgu, G. and Marty, B. (1999).

Isotopic and trace element signatures of Ethiopian basalts: evidence for plume-lithospheric interactions. Geochimical Cosmochimica Acta 63,2263-2279.

Ukstins, I.A., Renne, P.R., Wolfenden, E., Baker, J., Ayalew, D., Menzies, M., 2002. Matching conjugate volcanic rifted margins: 40Ar/39Ar chrono-stratigraphy of preand syn-rift bimodal flood volcanism in Ethiopia and Yemen. Earth Planet Sci. Lett. 198 (3–4), 289- 30.

V. Courtillot et al. (1999). On causal links between flood basalts and continental breakup. Earth Planet Sci. Lett.

JJEES

JJEES (2025) 16 (4): 418-432
ISSN 1995-6681

Jordan Journal of Earth and Environmental Sciences

Spatiotemporal Analysis of Wetland Environmental Changes Using Machine Learning and Remote Sensing Data

Yulia Fitriani, Nurlina Abdullah* , Ichsan Ridwan

Geophysics, Faculty of Mathematics and Natural Sciences, Universitas Lambung Mangkurat, Banjarbaru, Kalimantan Selatan, Indonesia

Received on March 23, 2025, Accepted on June 5, 2025

Abstract

Wetlands are essential ecosystems that provide vital services but are vulnerable to degradation. Hulu Sungai Utara (HSU)) Regency, South Kalimantan, hosts extensive tropical peatland wetlands spanning over 64,821 hectares. These wetlands are significant but face considerable shrinkage due to reduced water flow and land conversion. This study examined spatiotemporal changes in wetland cover in HSU from 2000 to 2024 using Landsat 7 ETM+ and Landsat 8 OLI data on Google Earth Engine (GEE). We used NDWI, NDVI, and MNDWI indices along with Machine Learning algorithms—Random Forest (RF) and Support Vector Machine (SVM)—for classification into water, vegetation, built-up, and barren land. RF achieved higher accuracy (97.33% overall accuracy, 96% average kappa), effectively mapping transitions. Results reveal a long-term decline in wetlands (loss of 71.4 km²), driven by development, climate change, and human activity. Notably, a significant regeneration trend appeared over the past 15 years, with gains exceeding losses in this recent period. This highlights the potential of GEE-based geospatial technology for data-driven tropical wetland conservation, suggesting positive effects from recent initiatives.

Keywords: *Wetland Water Index; Machine Learning; Google Earth Engine; Land Cover*

1. Introduction

A wetland is an environment where land meets water, often partially adjacent to a body of water. These systems can contribute significantly to the surrounding environment, including being important to unique species of plants and animals that live there (Mahdavi et al., 2018). A wetland is a rich source of food, raw materials, and water resources for people. The area also strengthens water sources, replenishes groundwater, and controls soil erosion. For this reason, wetland is called "Kidney of the Earth" (Zhang et al., 2023). A wetland is an area that contains water, has hydric soils, and supports certain vegetation that is adapted to wet environments. Additionally, the land is also waterlogged during certain seasons of the year (Mirmazloumi et al., 2021). Over the last few decades, wetlands in tropical countries such as Indonesia have experienced severe degradation. This decline is attributed to several factors, including population growth, infrastructure development, pollution, resource overexploitation, climate change, and poor governance. The facts show the importance of wetland risk assessment and monitoring using modern geospatial technologies and analytical methods (Aslam et al., 2024).

Remote sensing (RS), combined with wetland science, is being used more effectively than ever to accurately measure wetland quality and changes over time. Wetland mapping using Earth observation data captures information about the Earth's surface at low to very high resolution (Awawdeh et al., 2023). Additionally, the application of earth observation data is essential for managing natural resources at the regional, national, and international levels. Wetland monitoring is challenging, specifically at large scales, due to the diverse and fragmented wetland ecosystems and the spectral similarities among different wetland types (Abdelmajeed et al., 2023). To collect wetland cover information from Landsat, the image will be categorized, tagged, and entered into a GIS to undergo the the image interpretation process. Moreover, the spatiotemporal dynamics of the Hulu Sungai Utara Regency wetland in South Kalimantan are monitored using remote sensing images at a the spatiotemporal scale (Wu et al., 2020; Nurlina et al., 2024). Actual annual wetland areas can be mapped at the regional level using multitemporal Landsat 8-OLI and 7-ETM+ water change data collected from 2000 to 2024. This process is performed using several satellite-derived applications for land cover, including the Normalized Difference Water Index (NDWI), Normalized Difference Vegetation Index (NDVI), and Modified Normalized Difference Water Index (MNDWI) (Ashok et al., 2021).

NDVI in wetland mapping is utilized for drought monitoring, assessing plant cover, monitoring vegetation, and evaluating agricultural drought. However, remote sensing tools operating in near-infrared (NIR), shortwave infrared (SWIR), and thermal infrared (TIR) bands can identify water stress (Shashikant et al., 2021). Non-dimensional index known as NDVI uses the difference between visible and NIR reflectance to determine vegetation cover. A frequently used index to track vegetation dynamics at regional and global levels is NDVI. Following this discussion, vegetation density is estimated using NDVI measurements (Ashok et al., 2021). Using NDWI allows monitoring of vegetation

* Corresponding author e-mail: nurlina_abdullah@ulm.ac.id

moisture content by focusing on a specific area of the spectrum. This index is often applied to check the evaluation of drought conditions through the analysis of vegetation (Shashikant et al., 2021). Landsat TM Bands 2 and 4 are used to extract water features for NDWI. The index uses two improved Random Forest (RF) classifiers with Landsat 8 OLI to classify possible water bodies (Ichsan Ali et al., 2019). MNDWI is used to define landscape patterns, water bodies, and ecological study. Therefore, to assess how drainage systems and flooded areas have changed over the past decades. Drainage system studies and MNDWI analysis are used to find the upward trend in flooded areas over a predetermined period (Rashid, 2023).

Machine learning is a practical method for simulating complex ecological events using multivariate geographic data. Algorithms such as Support Vector Machine (SVM), RF, and artificial neural networks have been highly effective in mapping wetlands and detecting change across various areas globally. This model enables the forecasting of wetland hazards in the context of potential future environmental changes, utilizing RF categorization on Google Earth Engine (GEE) and Landsat image collections. GEE is a cloud platform for viewing, computing, and analyzing planetary-scale satellite imagery. This platform has been utilized in numerous studies, including land cover analysis, urban expansion, vegetation change, and disaster monitoring, as well as wetland change (Yan et al., 2022). The main focus of GEE is to develop highly interactive online algorithms, applying big data analysis expertise to remote sensing with a significant impact that enables data-driven science based on global challenges, including large geospatial datasets. Moreover, the platform deliverables are designed to analyze and store vast datasets at the petabyte level (Ashok et al., 2021).

Prior studies have demonstrated the efficacy of remote sensing and machine learning techniques for wetland monitoring and change detection in various regions globally and within Indonesia (Long et al., 2021; Waleed et al., 2023). Previous research utilized time series remote sensing data and the extreme gradient boosting (XGBoost) method to generate land use maps of the Yellow River Delta (YRD) in China from 2000 to 2020 (Zhu et al., 2024). This method proved to be effective, with land use classification achieving an accuracy of 90.45% based on Landsat time series data and the XGB method. Other research explored the use of ten machine learning algorithms available on Google Earth Engine (GEE) for multi-temporal land use mapping in the Segara Anakan coastal wetland area, using Landsat imagery from 1978, 1991, 2001, and 2014. The results show that the CART (Classification and Regression Tree) algorithm achieved the highest accuracy of 96.98% (Overall Accuracy) using K-Fold Cross Validation (K=10), demonstrating the effectiveness of GEE and machine learning for multi-temporal land use mapping (Farda, 2017).

However, a comprehensive spatiotemporal analysis focusing specifically on the extensive and vulnerable tropical peatland wetlands of Hulu Sungai Utara Regency, South Kalimantan, using a combined approach of multiple spectral indices (NDVI, NDWI, MNDWI) and advanced machine learning classifiers (Random Forest and Support Vector Machine) over a long-term period (2000-2024) implemented on the Google Earth Engine platform has not been previously conducted. This research fills a critical gap by providing a detailed, multi-decadal assessment of wetland dynamics in this ecologically significant area, leveraging the computational power of GEE to process large volumes of Landsat data and offering novel insights into the patterns and drivers of change, including the identification of recent regeneration trends. The main objective is to develop and analyze various Landsat 7 and 8 time series methods to map wet areas using GEE. Based on NDVI, NDWI, and MNDWI, the proposed algorithm can accurately record changes in wetland cover. This study examines the spatial and temporal changes of a selected wetland from 2000 to 2024, both quantitatively and qualitatively. The results can serve as the basis for a deeper understanding of how thewetland regime has changed over the years. The objectives include (i) Evaluating wetland areas based on Landsat images based on NDVI, NDWI, and MNDWI, (ii) Identifying the presence of permanent water bodies during the 5-year interval from 2000 to 2024, (iii) Performing image classification using guided classification RF and SVM.

2. Methodology

2.1 Study Area

The study area was located in the Peat Hydrology Unit (PHU), Hulu Sungai Utara Regency, South Kalimantan Province, Indonesia. Wetland cover in this area had an area of 648 km^2 with coordinates 2^o 26'26.81 "S 115^o 11'12.44" E (Figure 1), which was a wetland in South Kalimantan where most of the soil was peat and swamp land. Following the description, the area was located about 79 km from Banjarbaru City.

The primary issue with this wetland was the gradual reduction in size resulting from changes in sedimentation and infrastructure development. Therefore, this study aimed to understand the intensity of wetland cover change, focusing on the temporal and spatial changes of Hulu Sungai Utara Regency wetlands between 2000 and 2024 using histograms of surface water events. Understanding the relevance of water levels at the study site during this time was aided by an examination of worldwide surface water events and seasonal water changes, facilitated by an analysis of global surface water events and seasonal water fluctuations.

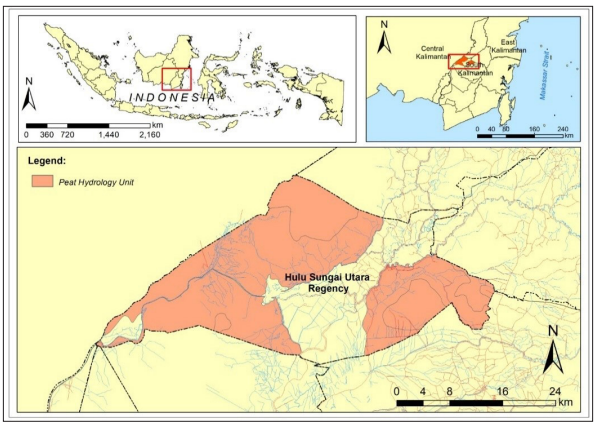

Figure 1. Map of the Study Area at Hulu Sungai Utara Regency, Indonesia

2.2 Data Collection

Multi-temporal satellite imagery was acquired to record changes in Hulu Sungai Utara Regency over the past 24 years, from 2000 to 2024. Landsat 7 ETM+ and 8 (OLI) missions provided this imagery, which had a temporal frequency of 16 days and a spatial resolution of 30 m. Specifically, Landsat 7 Enhanced Thematic Mapper Plus (ETM+) data for the years 2000 to 2010, and Landsat 8 Operational Land Imager (OLI) data for 2015-2024 were used (Aslam et al., 2024). NDVI, NDWI, and MNDWI time series from 2000 to 2024 were calibrated using 5-year gaps, utilizing Landsat 7 and 8 Collection 2 Tier 1 Raw Scenes. Table 1 shows the details of Bands 1 to 7 with their original spatial resolution using GEE. This platform included Landsat-specific processing methods to calculate sensor radiance, TOA reflectance, surface reflectance (SR), cloud score, and cloud-free composite. GEE also provided an algorithm to create a simple composite of the Landsat image, namely ee.Algorithms.Landsat. simple Composite(). The algorithm combined composites of multiple Landsat images to produce a clean image by minimizing the effects of disturbances such as clouds and cloud shadows. Moreover, cloud computing technology was used in this platform to process Landsat data (https://earthengine.google.org/). This process enabled parallel computing and processing of large data in the study area.

Table 1. Landsat data description

ID	Description
LANDSAT/LE07/C02/T1	Landsat 7, Collection 2, Tier 1 Raw Scenes
LANDSAT/LC08/C02/T1	Landsat 8, Collection 2, Tier 1 Raw Scenes

2.3 Spectral Water Index Calculation

NDVI has been widely used to analyze changes in vegetation cover over time and space (Andini et al., 2024). By applying the Red and NIR bands, the vegetation index determines the balance between energy absorbed and released by Earth objects (Hashim et al., 2019). In addition, NDVI was calculated based on the surface reflectance bands of 7 and 8 in the following Equation.

$$NDVI = \frac{(NIR-RED)}{(NIR+RED)} \quad (1)$$

Where NIR and RED represented the reflectance of bands 4 & 3 on Landsat 7 and bands 5 & 4 on Landsat 8, respectively. Following this discussion, vegetation changed over time with the application of atmospheric correction.

NDWI is used in Landsat image analysis to identify open water features using NIR and visible green (GREEN) spectral bands (Laonamsai et al., 2023). The model value was a useful indicator of plant water stress because it was closely related to the moisture content of plants sensitive to built-up land. This study primarily focused on the reflectance characteristics of dry and green vegetation. During the analysis, water bodies were extracted from a satellite image using the reflectance index, which varied from -1 to +1. The surface reflectance of NIR and SWIR bands of Landsats 7 and 8 was used to calculate NDWI (Ashok et al., 2021). Additionally, the index calculated based on the surface reflectance bands of Landsat 7 and 8 was shown in the following Equation.

$$NDWI = \frac{(GREEN-NIR)}{(GREEN+NIR)} \quad (2)$$

Where GREEN and NIR represented the reflectance of band 2 & 4 on Landsat 7 and band 3 & 5 on Landsat 8, respectively.

During this study, MNDWI distinguished between non-watery and watery areas. This method used shortwave infrared 1 (SWIR1) and GREEN spectral bands (Laonamsai et al., 2023). Xu (2006) formed an algorithm that efficiently suppressed and even eliminated the effects of noise from the ground and vegetation, as well as from the water surface. Therefore, improving the final MNDWI results led to more precise data extraction from an image containing vegetation, soil, and built-up land (Sherstobitov et al., 2021). The index was calculated based on land surface reflectance bands 7 and 8 was conducted using the following Equation.

$$MNDWI = \frac{(GREEN-SWIR1)}{(GREEN+SWIR1)} \quad (3)$$

Where GREEN and SWIR1 showed the reflectance of band 2 & 5 on Landsat 7 and band 3 & 6 on Landsat 8, respectively.

A total of 648 km^2 formed a truncated geometry (the area under study) in and around Hulu Sungai Utara Regency wetland, as shown in Figure 1. Based on the difference between NDVI, NDWI, and MNDWI values, the wetland hidden in Landsats 7 and 8 images was cloud-free in late July and early August. Moreover, Landsat data had gone through an automatic cloud masking process. The selected wetland plant image depicted the plants during the budding phase, encompassing vegetative growth, reproduction, and maturation. The image was distinguished by having higher NDVI values than NDWI and MNDWI. This outcome signified that permanent water bodies had - -1 < NDVI-NDWI-MNDWI < 0, while pixels covered by vegetation had a relationship of 0 < NDVI-NDWI-MNDWI < 1. The result was used to calculate the area related to vegetation, soil, built-up areas, and water bodies in summer, specifically from late July to early August from 2000 to 2024, as indicated by the algorithm. During the analysis, a process for mapping wetland areas using GEE was proposed.

2.4 Image Classification

Class information from a multi-band raster image was extracted using image classification. Supervised classification methods, such as CART, RF, Naïve Bayes, and SVM, were applied to handle guided classification using conventional machine learning methods within the GEE framwwork. In this case, Random Forest and SVM classifiers were used from 2000 to 2024. The defined classes were divided into four classification categories, namely water, vegetation, built-up, and barren land. This process determined how RF and SVM classifiers performed.

RF was an ensemble learning method that built a large number of decision trees during training for tasks such as regression and classification. The class selected by the majority of the trees was the output of RF for classification problems. By reducing overfitting and improving prediction accuracy through feature randomness during tree splitting

and packing (bootstrap aggregating), RF outperformed single decision trees. RF was well known for its resistance to overfitting and its capacity to manage very large datasets with high dimensionality (Aslam et al., 2024).

The concepts of classification and regression were the main focus of SVM, which was an implementation of the supervised learning paradigm. SVM only classified data linearly at an early stage by creating a hyperplane. Later in 1992, Vapnik, Boser, and Guyon presented a method for forming nonlinear classifiersusing Kernel functions (Vapnik and Cortes first introduced kernels in a 1995 study paper). Following the occurrence, SVM has become a popular classification algorithm for supervised learning, i.e., datasets categorized by class labels and attributes. Unsupervised learning, or datasets without output features and class labels, was implemented using SVM clustering (Ghosh et al., 2019).

A land cover map of Hulu Sungai Utara Regency was created and assessed using Landsat 8 surface reflectance data by applying eight different combination procedures. During this process, training was conducted using MODIS land cover data from the IGBP classification. To train the sample data, both the RF classifier and SVM were used, and multiple random seeds were employed to obtain validation data. After the process, any zero pixels were removed from the results by filtration, and the data was verified based on the smiling RF. By specifying land cover category characteristics as attributes of four classes, RF classifieree. Classifier.smileRandom Forest(100).train() was applied to the training data. The output results showed that all eight datasets produced land cover maps with moderate to highly accurate accuracy with a total accuracy of more than 90%.

The Confusion Matrix and its derived accuracy index were used to evaluate the classification accuracy of each scenario data set. Each pixel in each polygon was categorized as a training point when the training dataset consisted of polygons representing homogeneous regions. Additionally, a machine learning algorithm was trained using these polygons (Stehman, 1997). The confusion matrix was a way to review how well a classification algorithm performed and provided a better understanding of the classification model and its errors. The method, sometimes referred to as an error matrix, was a quantitative method used to describe the accuracy of image classification. The matrix showed the relationship between the reference image and the classification result. The matrix requires ground-truth information, such as geographic data and the results of manual image digitization. During this study, the classification of Hulu Sungai Utara Regency wetland images was performed using GEE and Landsat 7 and 8 images. Training samples of polygon feature classes or shapefiles were provided to perform classification. In addition, the attribute table of the training samples and the format of the feature class were the same. The "Training Samples Manager" was used to build a reference dataset to ensure this process by reading and writing the dataset. A total evaluation of the classification accuracy was provided by the Kappa agreement statistic. Table 2 shows the accuracy statistic ranging from 0 to 1, with 1 signifying 100% accuracy. The overall research method is described in Figure 2.

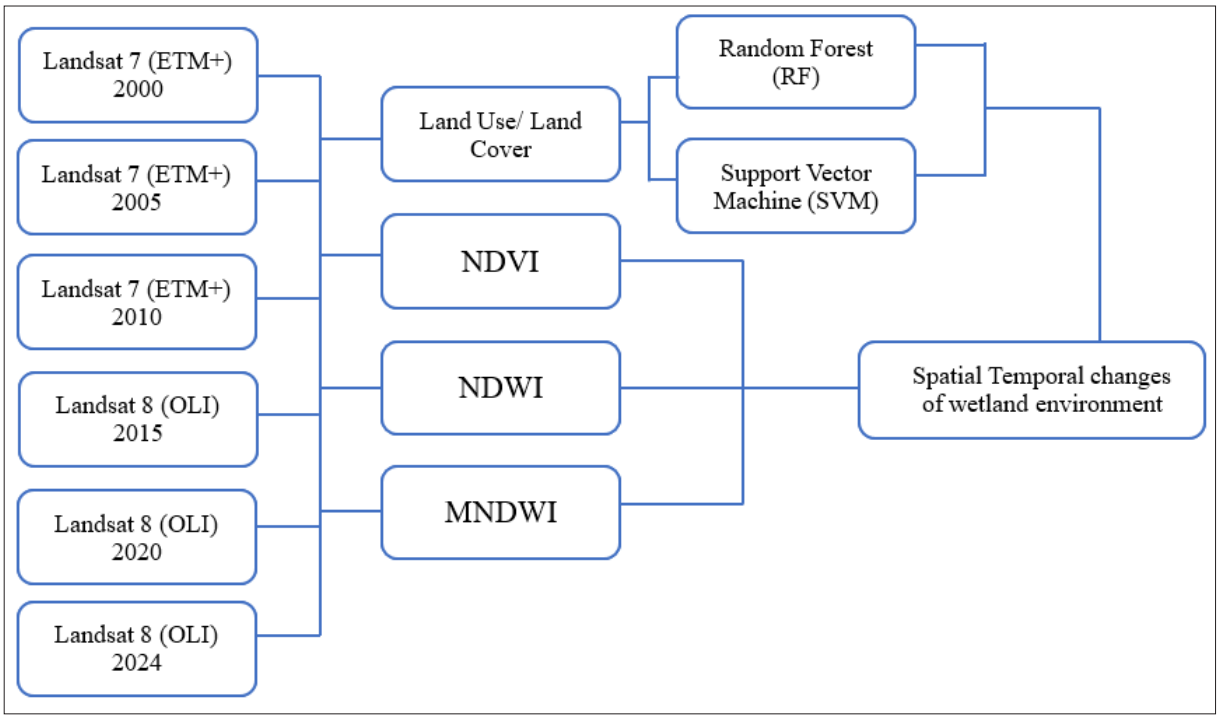

Figure 2. Study Flow Chart

3. Results and Discussion

3.1 Accuracy Assessment

Landsat image data that was classified using a Region of Interest (ROI) as a reference was applied to determine land use/cover factors. There were two types of ROI samples used, namely, testing and training samples. A testing sample was used as a representative sample for land cover classification in Google Earth, which was applied to evaluate the classification accuracy. Meanwhile, the training sample was used as a representative sample for land cover classification

(Nurlina et al., 2023). These samples were subsequently used for validation and a total accuracy test. The hue of pixels corresponding to vegetation or water bodies in the wetland was determined based on the samples. Regarding the process, JavaScript programming on the GEE platform was used to determine the areas covered by vegetation and water.

Based on Table 2, the RF model had a high average kappa accuracy of 96% and a total accuracy of 97.33% for the six years studied (2000, 2005, 2010, 2015, 2020, and 2024). An average user validation accuracy of 87.8% over 6 years showed the condition of land cover class assignment. RF showed higher classification accuracy than Support Vector Machine (SVM) in mapping wetland change. On the GEE platform, RF is efficient for large datasets as it can be parallelised, while SVM with complex kernels may be more computationally intensive. RF tends to be more robust to noise and outliers than SVM. The advantages of RF are its ability to handle complex data and its robustness, while SVM is versatile with kernels but sensitive to noise and requires careful parameter tuning (Aljanabi & Dedeoğlu, 2025; Thanh Noi & Kappas, 2017). The superior performance of RF in this study is likely due to its robustness in handling the complexity of multi-temporal data in dynamic tropical wetland environments. This outcome characterized the multitemporal variability of the wetland as well as map, and track changes over time using extended time series imagery. Landsat 7 and 8 images were used to extract the land cover shape of Hulu Sungai Utara Regency. Landsat 7 and 8 imagery spanned from 2015 to 2024, and 2000 to 2010.

Table 2. Comparison accuracy between Landsat 7 and 8 image collections over Wetland of Hulu Sungai Utara Regency (2000–2024).

Random Forest (RF)						
	Landsat 7			Landsat 8		
	Year 2000	Year 2005	Year 2010	Year 2015	Year 2020	Year 2024
Total Accuracy	0.98	0.96	0.96	0.99	0.97	0.99
Validation Accuracy	0.96	0.74	0.92	0.89	0.9	0.84
Kappa Coefficient	0.97	0.94	0.94	0.98	0.9	0.98

The main parameters in the accuracy assessment included total accuracy, i.e., the proportion of training samples that were correctly classified (70%). Other parameters included the Kappa coefficient, a measure that considered the chance of agreement. In addition, validation accuracy consisted of the proportion of training samples that were correctly classified (30 %).

3.2 Land Use and Land Cover (LULC)

Using two machine learning algorithms on GEE, RF, and SVM, land use and land cover (LULC) analysis conducted in this study revealed important changes in the distribution. The analysis also found an interesting proportion of major land cover classes surrounding the wetland in the ecologically important Hulu Sungai Utara Regency between 2000 and 2024. Following the discussion, two important physical components that measure the surface of the Earth were LULC. To distinguish between these components, a categorization system was necessary. The system provided a fundamental structuring function by offering tools to name, classify, and recognize objects on Earth (Nedd et al., 2021).

The results shown in Figure 3 were obtained from RF classification, which consisted of 4 land cover classes. Land cover classes consisted of water, vegetation, built-up, and barren land. Images from Landsat 7 and 8 were captured in the year 2000-2024, as the RF model showed higher accuracy than SVM. The results showed a decrease in the exposed and unvegetated land surface around the wetland, which was attributed to artificial reforestation initiatives in the area as well as climate change-related variables. The climate variables included increased rainfall that promoted the growth of vegetation cover (Khalaf, 2024; Aslam et al., 2024).

Machine learning based on the supervised learning model is called SVM. Statistical learning theory served as the foundation for SVM, which classified data by identifying a set of support vectors from a sample (Mohammadi et al., 2021). Moreover, the results shown in Figure 4 were divided into the same four classes as RF. The high rainfall pattern in the multitemporal analysis from 2000 to 2005 led to a slight increase in water area. The significant decrease in water area between 2005 and 2010 was offset by an increase in vegetation area. Additionally, rapid growth led to substantial changes in vegetation from 2010 and 2015. The amount of green land decreased as the number of buildings increased between 2015 and 2020. Due to urbanization around wetland, there was a reduction in water bodies in 2020-2024. Relating to this discussion, combining studies of land use and population change led to a more comprehensive knowledge of interconnected environmental as well as human factors that impacted the vulnerability of wetland in the area (Mohammadi et al., 2021).

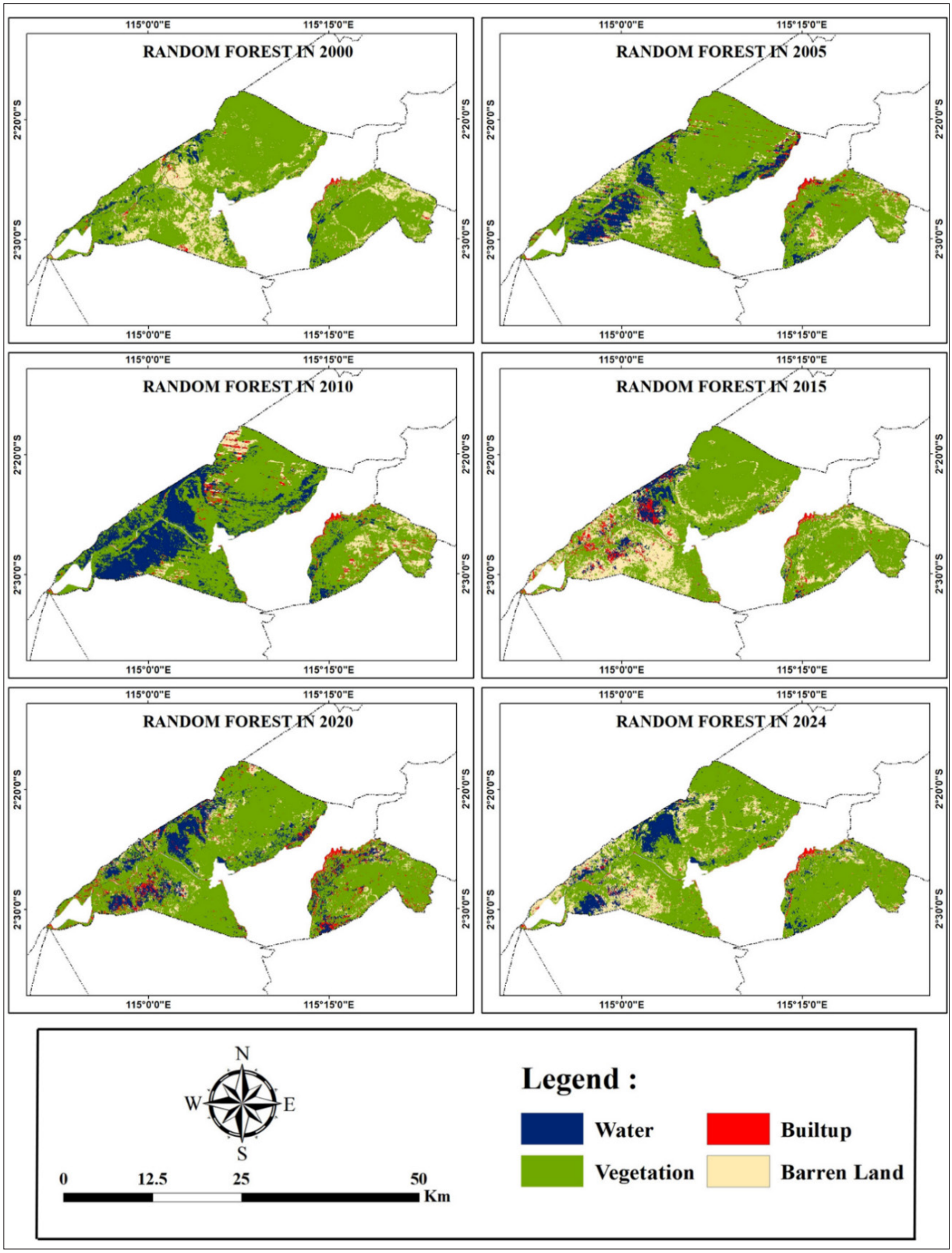

Figure 3. Land cover classification RF map from 2000 to 2024

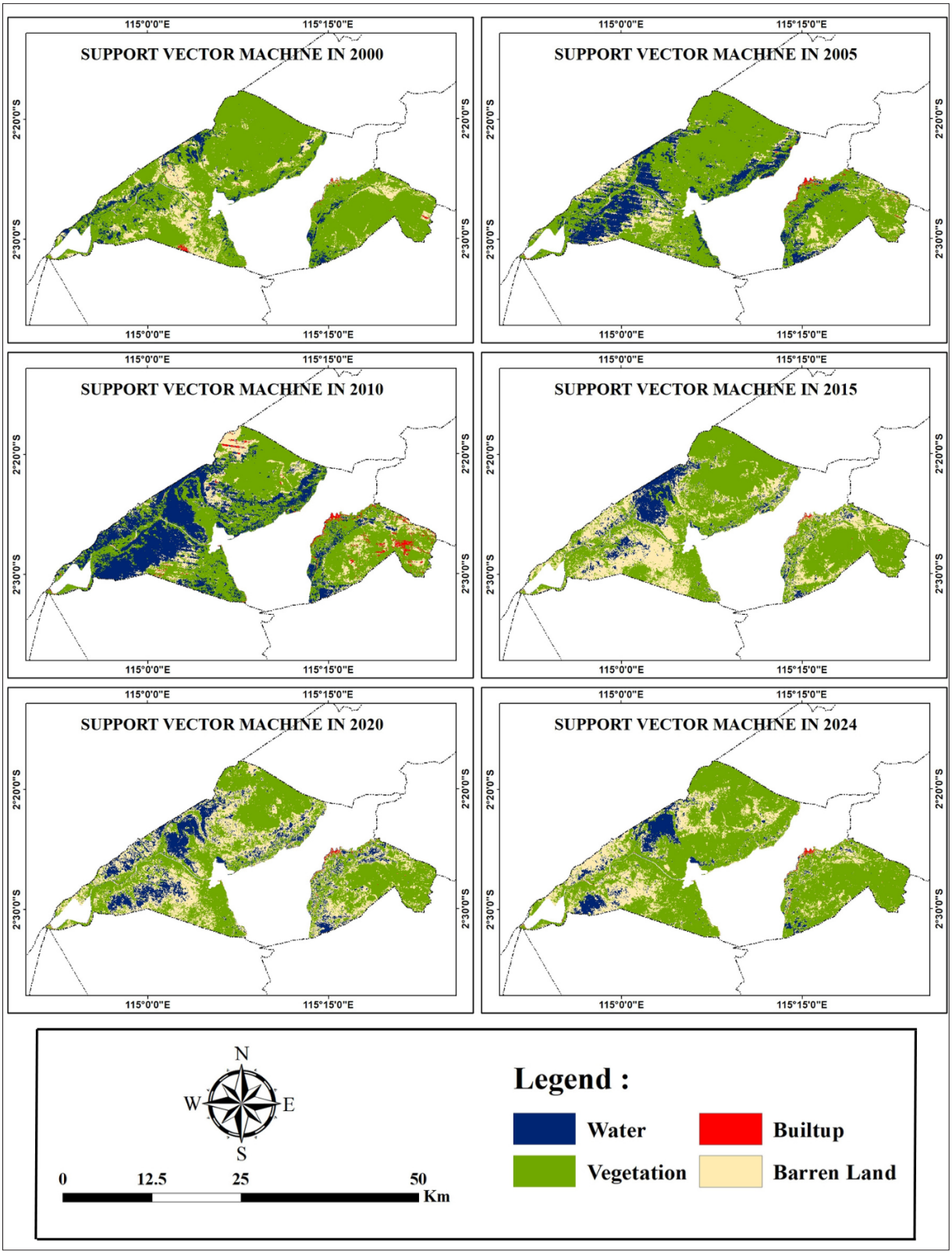

Figure 4. Land cover classification with SVM from 2000 to 2024

3.3 Transition of Wetland

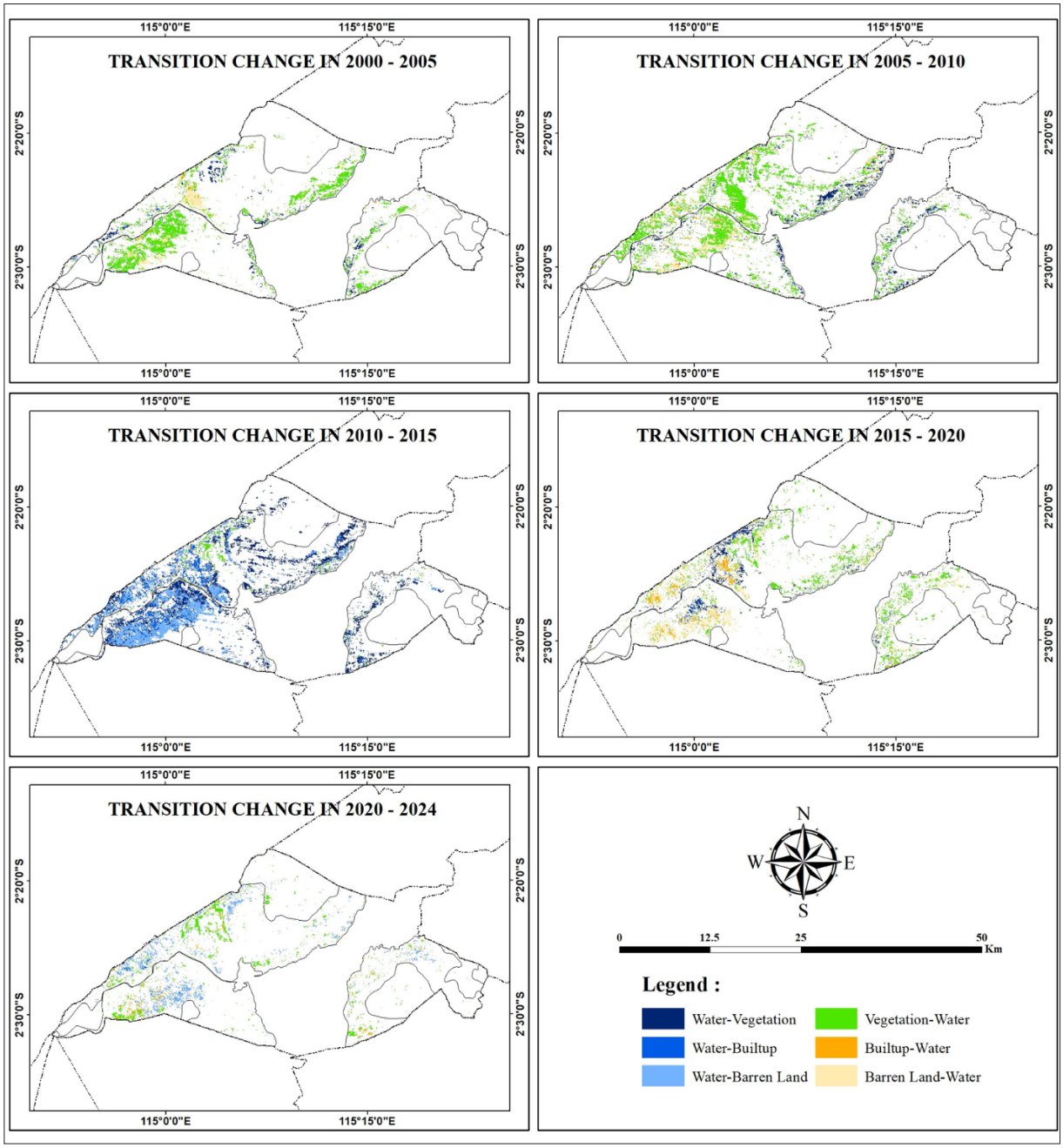

Figure 5. Transition change in wetland classes

Figure 5 presents a comprehensive wetland change detection study, which found significant transitions between wetland and other major land cover classes, such as vegetation, built-up land, and barren land, around the Hulu Sungai Utara Regency wetlands between 2000 and 2024. Specifically, during this period, 83.4 km^2 of vegetation cover and 34.7 km^2 of bare land changed to wetland. The outcome signified that wetland shrank significantly into previously unvegetated bare areas and also former forests or shrublands. This occurrence might be due to the lowered water table and low rainfall, which allowed the swamp habitat to not thrive. Consequently, 111.9 km^2 of wetland changed to vegetation cover, and 78.8 km^2 changed to bare land. Table 3 showed the conversion of a small area of 17.1 km^2 from built-up land to wetland signifying the regeneration of wetland into pavement zones that were previously built-up land. However, only 18.5 square kilometers of marsh changed to built-up land between 2000 and 2024. Table 3 showed the main transitions from bare surfaces to vegetated surfaces to wetland, signifying that wetland expansion mostly occurred on bare, non-vegetated land. Table 4 showed how the area of wetland change decreased and increased. Relating to the discussion, the area decreased as the result became negative, and it increased when the value was positive. Table 3 also measured the minimal interaction that occurred around Hulu Sungai Utara Regency between wetland and constructed impervious surfaces (DeLancey et al., 2022).

Table 3. LULC Area from 2000 to 2024

Classifier	Name	2000		2005		2010		2015		2020		2024	
	Class	km²	%	km²	%	km²	%	km²	%	km²	%	km²	%
RF	Water	21.9	3	78.3	12	161.3	25	35.7	6	90.4	14	60.7	9
	Vegetation	505.8	78	486.3	75	422.2	65	444.9	69	484.8	75	471.8	73
	Builtup	6.8	1	16.7	3	18.3	3	26.5	4	33.6	5	12.3	2
	Barren Land	113.5	18	66.7	10	46.2	7	140.9	22	39.2	6	103.3	16
	Total	648	100	648	100	648	100	648	100	648	100	648	100
SVM	Water	44.8	7	120.5	19	204.8	32	64.3	10	99.6	15	50	8
	Vegetation	509.6	79	445.3	69	347.2	54	391.8	60	332.9	51	450.2	69
	Builtup	2.6	0	3.8	1	12.6	2	1.1	0	1.9	0	1.8	0
	Barren Land	91	14	78.4	12	83.3	13	190.8	29	213.7	33	146	23
	Total	648	100	648	100	648	100	648	100	648	100	648	100

Table 4. LULC Area change from 2000 to 2024

Classifier	Name	Area Km² Change					Area % Change				
	Class	2000-2005	2005-2010	2010-2015	2015-2020	2020-2024	2000-2005	2005-2010	2010-2015	2015-2020	2020-2024
RF	Water	-56.4	-83	125.6	-54.7	29.7	-8.7	-12.8	19.4	-8.4	4.6
	Vegetation	19.5	64.1	-22.7	-39.9	13	3.0	9.9	-3.5	-6.2	2.0
	Builtup	-9.9	-1.6	-8.2	-7.1	21.3	-1.5	-0.2	-1.3	-1.1	3.3
	Barren Land	46.8	20.5	-94.7	101.7	-64.1	7.2	3.2	-14.6	15.7	-9.9
SVM	Water	-75.7	-84.3	140.5	-35.3	49.6	-11.7	-13.0	21.7	-5.4	7.7
	Vegetation	64.3	98.1	-44.6	58.9	-117.3	9.9	15.1	-6.9	9.1	-18.1
	Builtup	-1.2	-8.8	11.5	-0.8	0.1	-0.2	-1.4	1.8	-0.1	0.0
	Barren Land	12.6	-4.9	-107.5	-22.9	67.7	1.9	-0.8	-16.6	-3.5	10.4

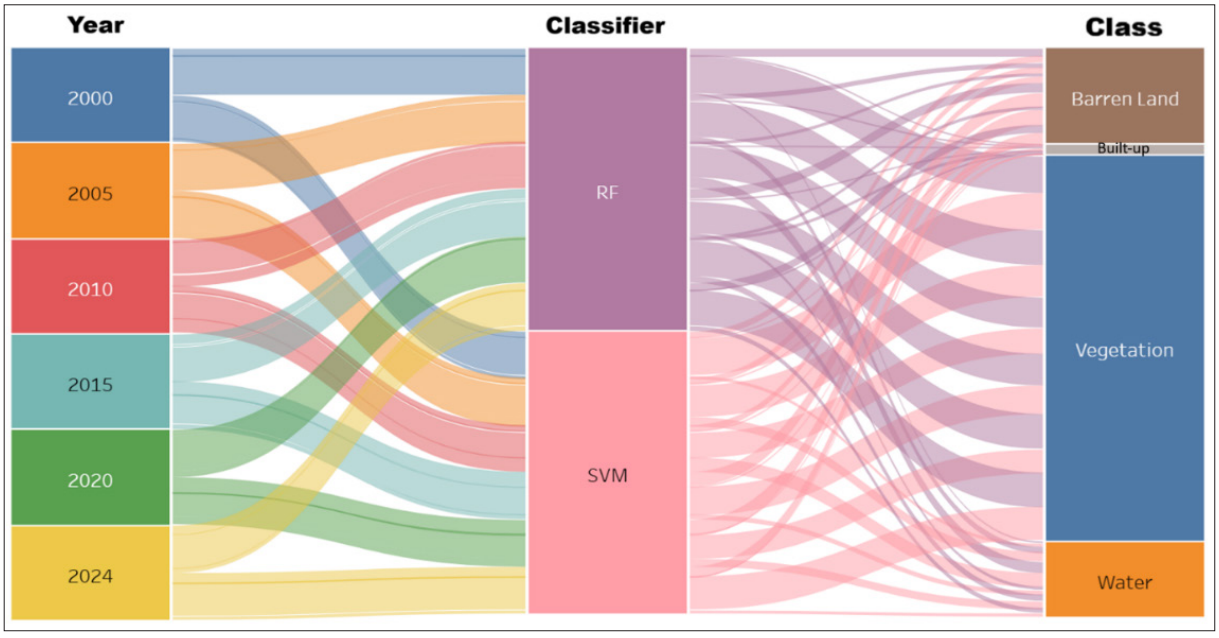

Figure 6. Trend of Land cover change from 2000 to 2024

Figure 6 shows the long-term trend from 2000 to 2024, which reveals a net decrease in wetland cover. This visually demonstrates the movement of area between the barren land, vegetation, and water classes at each time interval. While there are areas of wetlands converting to vegetation or bare land, there is also the reverse process of areas of vegetation and bare land converting to wetlands. There is a significant trend of wetland regeneration over the last 15 years (approximately 2015-2024), where the gains in wetland area outweigh the losses in this more recent period. The Sankey diagram visually supports a transition towards the ‘‘‘Water’ class in the later years (2015, 2020, 2024),

3.4 Wetland Change

According to wetland change analysis compiled in Tables 3 and 4, there was a net decrease in wetland cover over the first 15 years, as the loss of 7.7 sq. km exceeded the increase of 34.3

sq. km between 2015 and 2024. However, there was a reversal of the trend, with wetlands increasing by a total of 86.7 km², greater than the loss of 63.7 km². This reversal demonstrated that, over the last 15 years, wetland regeneration had outpaced loss, largely due to increased conservation efforts in the area. The total wetland loss of 71.4 km² for the 24 years from 2000 to 2024 was greater than the total wetland increase of 237.6 km², signifying a long-term decline. This outcome showed ecological resilience as prominent wetland ecosystems persisted despite certain losses. Although there was a late decline in wetland between 2015 and 2024, regenerative processes outpaced losses in the following 15 years. Figure 7 showed that the long-term trend was an accumulative loss with some resilience (Amani et al., 2022).

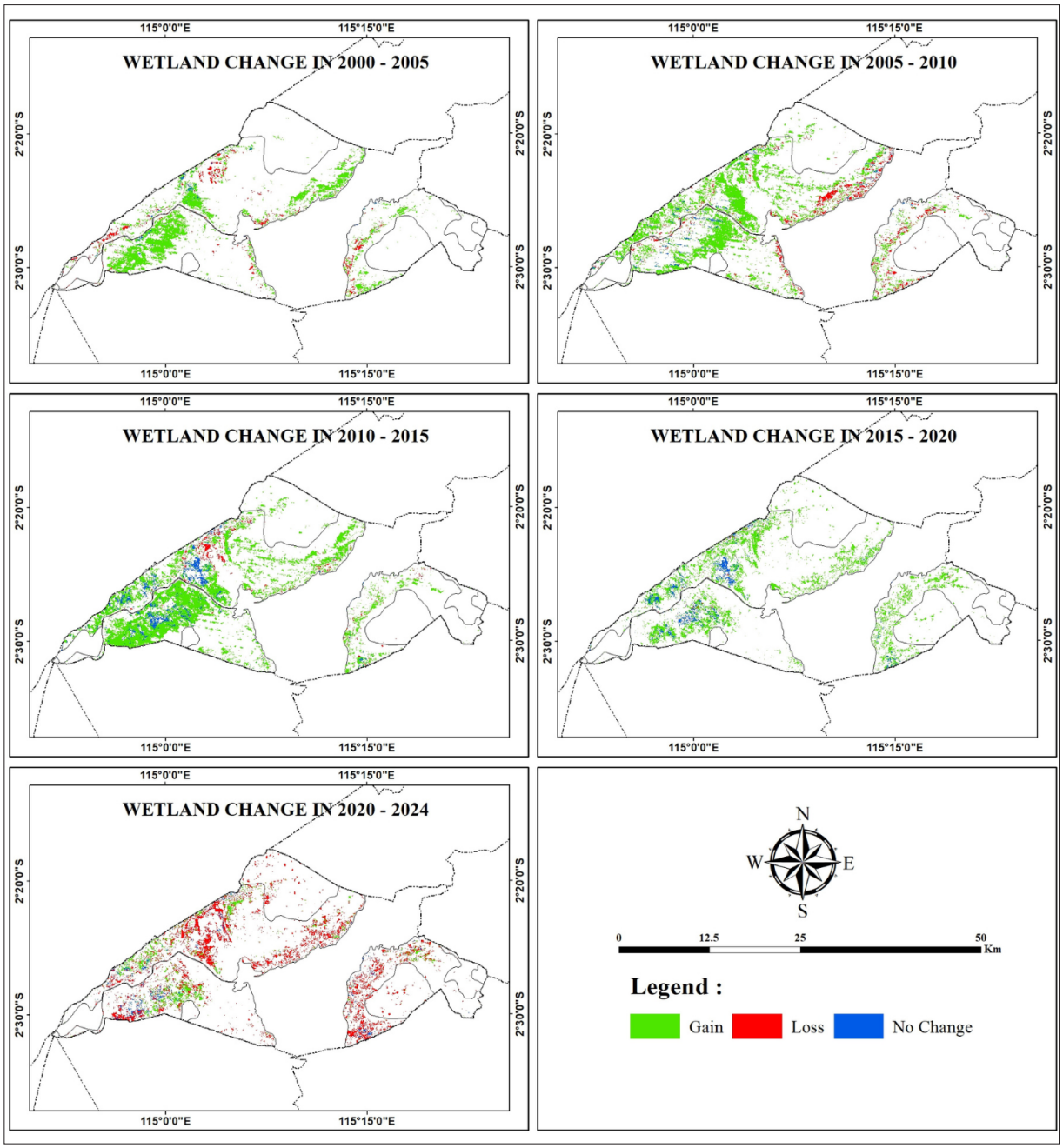

Figure 7. Wetland change and no change

3.5 Index Results

The dynamics of surface moisture and vegetative vigor surrounding the Hulu Sungai Utara wetland were illustrated by spectral water and vegetation indices derived from multitemporal satellite imagery between 2000 and 2024. Figure 8 shows the observed NDVI values from 2000 and 2024, with the lowest score being -0.69 and the highest being +0.87. Since the value of the NDVI parameter was less than zero, the red color signified no vegetation. Wetland was added between 2005 and 2010, specifically the larger water bodies. Due to the long dry season during that time, the wetland area was reduced between 2015 and 2020.

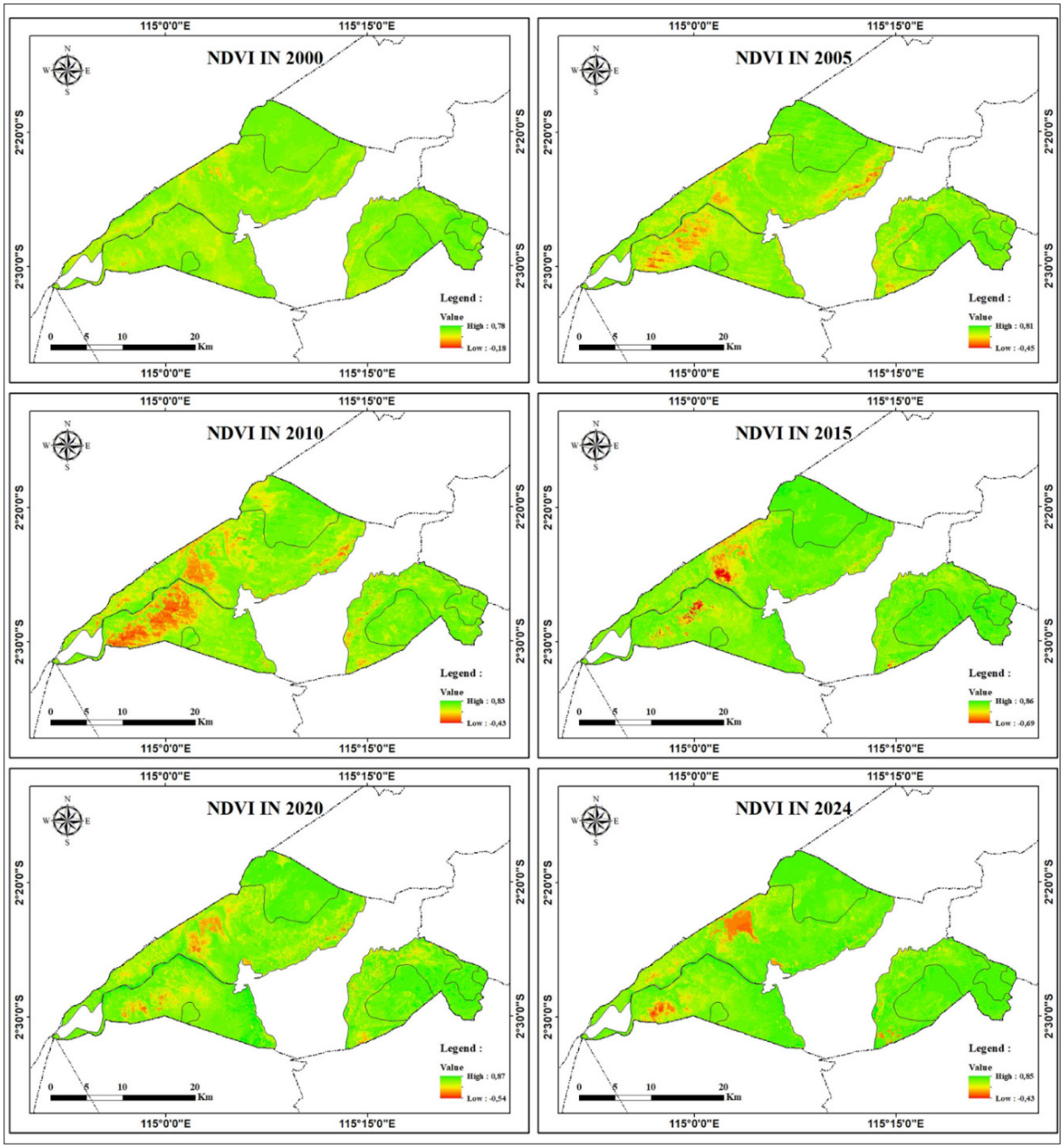

Figure 8. Result from NDVI

NDWI high-resolution satellite image data for the period from 2000 to 2024 was used to identify surface water bodies in the study area, as shown in Figure 9. During the analysis, the values ranged on average from -0.77 to +0.67. High plant water content and low vegetation content were represented by positive and negative NDWI values. Additionally, levels drop during the water stress phase, where low vegetation water content and vegetation fraction cover correlated with low NDWI results. NDVI values were greater than NDWI during the post-harvest wetland planting phase.

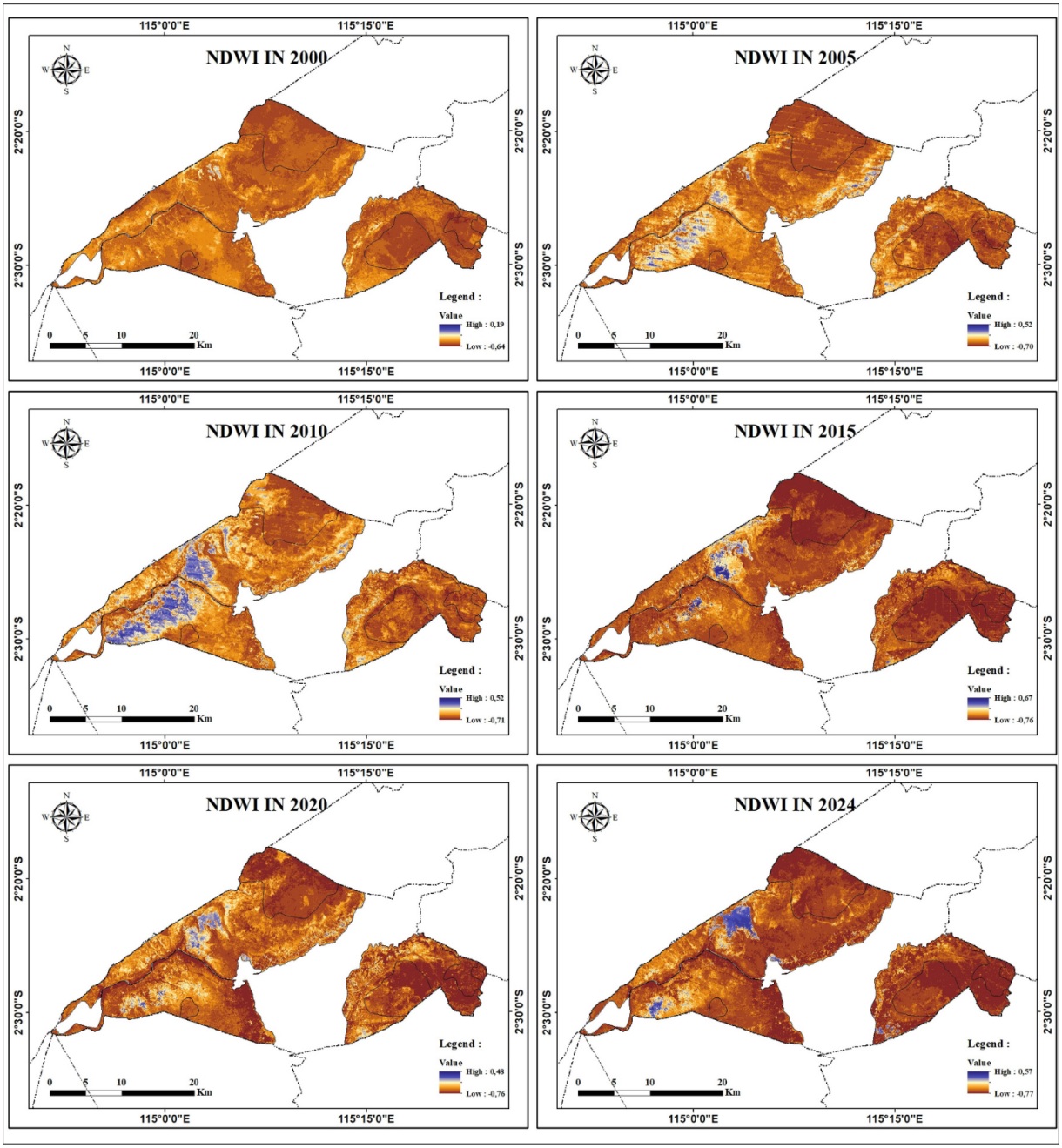

Figure 9. Result from NDWI

The surface water level decreased during the analysis period as observed from the decrease in the upper range of MNDWI values, which ranged from 0.62 in 2015 to 0.99 in 2005 and 2010 as shown in Figure 10. This result was consistent with the shrinkage observed in change studies of peatland regions. The lower limit of MNDWI decreased over time, signifying that even a slight loss of surface moisture occurred in some wetland areas (Ridwan et al.. 2022).

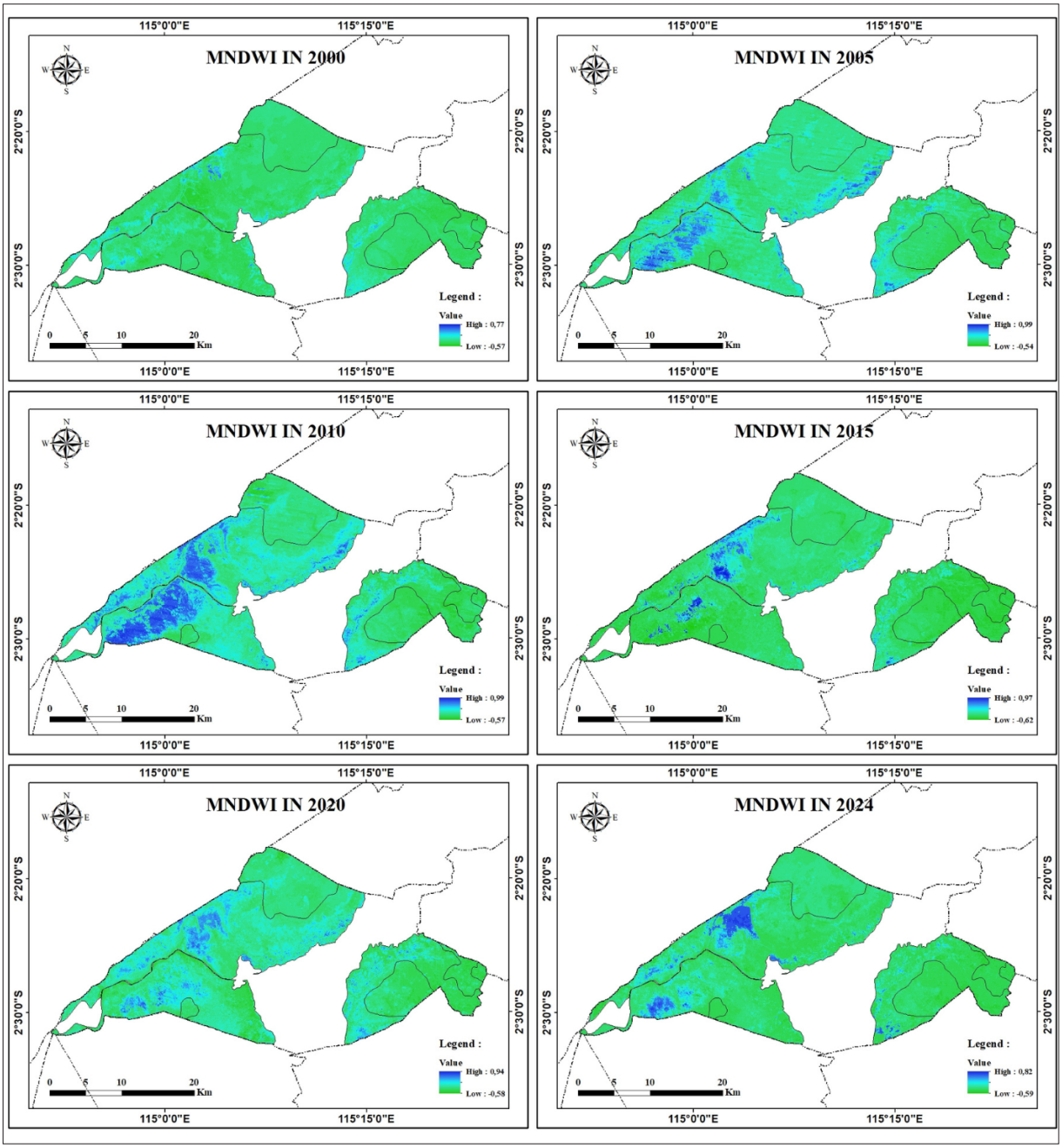

Figure 10. Result from MNDWI

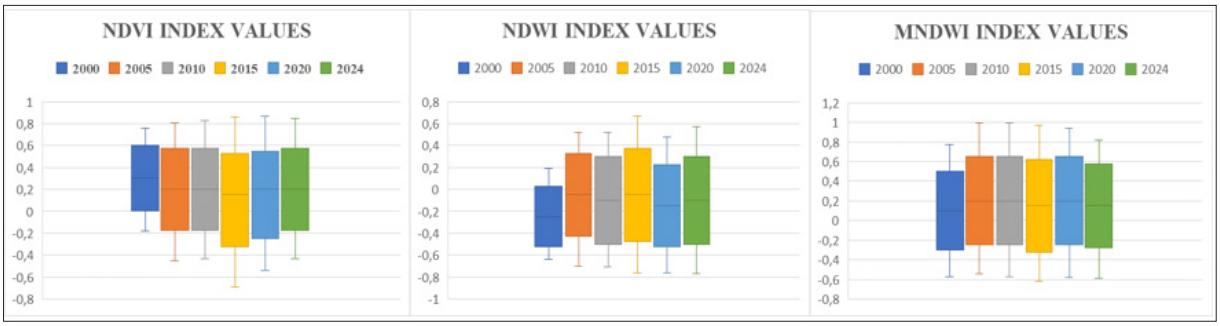

Figure 11. Distribution of NDVI, NDWI, and MNDWI index values for different years (2000, 2005, 2010, 2015, 2020, and 2024)

Figure 11 shows the distribution of NDVI, NDWI, and MNDWI index values for different years (2000, 2005, 2010, 2015, 2020, and 2024) in the study area. It is clear that the distribution and median values for each index (NDVI, NDWI, MNDWI) vary from year to year. This variation indicates changes in land cover conditions (vegetation, water) in the study area from 2000 to 2024. An increase in the median NDVI value or a higher scatter on the positive side tends to indicate an increase in vegetation cover or health in the study area. Conversely, a decrease in NDVI indicates

degradation of vegetation or land conversion (Jia et al., 2019). Higher values of these indices are generally associated with the presence of water or higher humidity. Changes in the median values and distribution of the MNDWI and NDWI from year to year may indicate fluctuations in the extent of waterlogging, soil moisture levels, or other hydrological changes in the wetland. A shift of the box towards more negative values could indicate a decrease in surface water availability or moisture. The NDVI is high, but the NDWI/MNDWI is low, indicating vegetated dry conditions, or vice versa, indicating waterlogging with vegetation less prominent in the image at the time of acquisition.

4. Conclusion

In conclusion, wetlands serve as essential ecosystems, providing natural resources, biological habitats, and ecological buffers. However, the land was also vulnerable to degradation as a result of overexploitation, infrastructure expansion, and climate change. The dynamic changes in wetland cover in Hulu Sungai Utara Regency from 2000 to 2024 were examined both temporally and spatially by applying NDVI, NDWI, and MNDWI indices along with machine learning methods, such as RF and SVM, using data from Landsat 7 and 8. During this analysis, RF performed better than other methods, achieving a total accuracy of 97.33% and an average kappa of 96%. Although the long-term trend still signified a total decline, the results showed a significant shift in wetlands, including greater regeneration than loss over the previous 15 years. The need for GEE-based geospatial technologies to aid data-driven decision-making in managing and protecting tropical wetland ecosystems is evident, as recent conservation initiatives are starting to have a positive impact.

Beyond summarizing changes, this study offers a key scientific contribution by providing a detailed, quantitative understanding of long-term wetland dynamics in Hulu Sungai Utara using a robust GEE-based approach that combines spectral indices and machine learning. It uniquely highlights a significant recent regeneration trend amidst overall decline, offering novel insights into ecosystem resilience and the effectiveness of conservation efforts The findings provide essential data and a framework for data-driven land-use planning, environmental management, and targeted conservation strategies, which are crucial for the sustainable future of these vital tropical wetlands.

Acknowledgments

The authors are grateful to the Ministry of Education, Culture, Study, and Technology for funding this study through the National Competitive Applied Study Grant [Number 056/E5/PG.02.00.PL/2024]. This support was instrumental in conducting and completing this study.

Authors Contribution

Conceptualization, N.N and I.R.; Methodology, N.N.; Software, I.R.; Validation, Y.F., N.N. and I.R.; Formal Analysis, Y.F.; Writing – Original Draft Preparation, Y.F.; Writing – Review & Editing, N.N.; Visualization, I.R.; Supervision, N.N.; Funding Acquisition, I.R.

Declaration Of Competing Interest

"The authors declare no conflict of interest."

References

Abdelmajeed. A. Y. A. Albert-Saiz M. Rastogi. A. & Juszczak. R. (2023). Cloud-Based Remote Sensing for Wetland Monitoring-A Review. In Remote Sensing (Vol. 15. Issue 6). MDPI. https://doi.org/10.3390/rs15061660

Amani. M. Kakooei. M. Ghorbanian. A. Warren. R. Mahdavi. S. Brisco. B. Moghimi. A. Bourgeau-Chavez. L. Toure. S. Paudel. A. Sulaiman. A. & Post. R. (2022). Forty Years of Wetland Status and Trends Analyses in the Great Lakes Using Landsat Archive Imagery and Google Earth Engine. Remote Sensing. 14(15). https://doi.org/10.3390/rs14153778

3. Aljanabi, F. K., & Dedeoğlu, M. (2025). Machine learning algorithms and geographic information system techniques to predict land suitability maps for wheat cultivation in the Central Anatolia Region. Journal of Ecological Engineering, 26(1), 373–387. https://doi.org/10.12911/22998993/196044

Andini, W. T., Nurlina, & Ridwan, I. (2024). Monitoring Vegetation Change Using Forest Cover Density Model. Ecological Engineering and Environmental Technology, 25(9), 369–378. https://doi.org/10.12912/27197050/190928

Awawdeh, M., Alkhateeb, E., & Al-Radaideh, N. (2023). The Use of Remote Sensing and GIS for Mapping Silica Sand Deposits in Jordan. Jordan Journal of Earth and Environmental Sciences, 14(3), 232–240.

Ashok. A. Rani. H. P. & Jayakumar. K. V. (2021). Monitoring of dynamic wetland changes using NDVI and NDWI based landsat imagery. Remote Sensing Applications: Society and Environment. 23. https://doi.org/10.1016/j.rsase.2021.100547

Aslam. R. W. Shu. H. Naz. I. Quddoos. A. Yaseen. A. Gulshad. K. & Alarifi. S. S. (2024). Machine Learning-Based Wetland Vulnerability Assessment in the Sindh Province Ramsar Site Using Remote Sensing Data. Remote Sensing. 16(5). https://doi.org/10.3390/rs16050928

DeLancey. E. R. Czekajlo. A. Boychuk. L. Gregory. F. Amani. M. Brisco. B. Kariyeva. J. & Hird. J. N. (2022). Creating a Detailed Wetland Inventory with Sentinel-2 Time-Series Data and Google Earth Engine in the Prairie Pothole Region of Canada. Remote Sensing. 14(14). https://doi.org/10.3390/rs14143401

Farda, N.M. (2017) 'Multi-temporal Land Use Mapping of Coastal Wetlands Area using Machine Learning in Google Earth 'Engine', IOP Conference Series: Earth and Environmental Science, 98(1). Available at: https://doi.org/10.1088/1755-1315/98/1/012042

Ghosh. S. Dasgupta. A. & Swetapadma. A. (2019). A Study on Support Vector Machine based Linear and Nonlinear Pattern Classification. In 2019 International Conference on Intelligent Sustainable Systems (ICISS).

Hashim. H. Abd Latif. Z. & Adnan. N. A. (2019). Urban Vegetation Classification With Ndvi Threshold Value Method With Very High Resolution (Vhr) Pleiades Imagery. International Archives of the Photogrammetry. Remote Sensing and Spatial Information Sciences - ISPRS Archives. 42(4/W16). 237–240. https://doi.org/10.5194/isprs-archives-XLII-4-W16-237-2019

Ichsan Ali. M. Darma Dirawan. G. Hafid Hasim. A. & Rais Abidin. M. (2019). Detection of Changes in Surface Water Bodies Urban Area with NDWI and MNDWI Methods. 9(3).

Jia, M., Wang, Z., Wang, C., Mao, D., & Zhang, Y. (2019). A new vegetation index to detect periodically submerged mangrove forest using single-tide Sentinel-2 imagery. Remote Sensing, 11(17), 1–17. https://doi.org/10.3390/rs11172043

Khalaf. A. B. (2024). Using Geospatial Techniques to Analysis the Impact of Climate Change on Water and Agriculture Resources: Case study Khanaqin District in Diyala. Iraq.

Basrah Journal of Agricultural Sciences. 37(1). 55–70.

https://doi.org/10.37077/25200860.2024.37.1.05

Laonamsai. J. Julphunthong. P. Saprathet. T. Kimmany. B. Ganchanasuragit. T. Chomcheawchan. P. & Tomun. N. (2023). Utilizing NDWI. MNDWI. SAVI. WRI. and AWEI for Estimating Erosion and Deposition in Ping River in Thailand. Hydrology. 10(3). https://doi.org/10.3390/hydrology10030070

Long, X. et al. (2021) 'Mapping the vegetation distribution and dynamics of a wetland using adaptive-stacking and Google Earth Engine based on multi-source remote sensing 'data', International Journal of Applied Earth Observation and Geoinformation, 102, p. 102453. Available at: https://doi.org/10.1016/j.jag.2021.102453

Ludwig. C. Walli. A. Schleicher. C. Weichselbaum. J. & Riffler. M. (2019). A highly automated algorithm for wetland detection using multi-temporal optical satellite data. Remote Sensing of Environment. 224. 333–351. https://doi.org/10.1016/j.rse.2019.01.017

Mahdavi. S. Salehi. B. Granger. J. Amani. M. Brisco. B. & Huang. W. (2018). Remote sensing for wetland classification: a comprehensive review. In GIScience and Remote Sensing (Vol. 55. Issue 5. pp. 623–658). Taylor and Francis Inc. https://doi.org/10.1080/15481603.2017.1419602

Mirmazloumi. S. M. Moghimi. A. Ranjgar. B. Mohseni. F. Ghorbanian. A. Ahmadi. S. A. Amani. M. & Brisco. B. (2021). Status and trends of wetland studies in Canada using remote sensing technology with a focus on wetland classification: A bibliographic analysis. Remote Sensing. 13(20). https://doi.org/10.3390/rs13204025

Mohammadi. M. Rashid. T. A. Karim. S. H. T. Aldalwie. A. H. M. Tho. Q. T. Bidaki. M. Rahmani. A. M. & Hosseinzadeh. M. (2021). A comprehensive survey and taxonomy of the SVM-based intrusion detection systems. In Journal of Network and Computer Applications (Vol. 178). Academic Press. https://doi.org/10.1016/j.jnca.2021.102983

Nedd. R. Light. K. Owens. M. James. N. Johnson. E. & Anandhi. A. (2021). A synthesis of land use/land cover studies: Definitions. classification systems. meta-studies. challenges and knowledge gaps on a global landscape. In Land (Vol. 10. Issue 9). MDPI. https://doi.org/10.3390/land10090994

Nurlina. Ridwan. I. Muslimin. S. & Roup. A. (2024). Peatlands changes analysis in Banjar District using three decades of Landsat imagery. Journal of Physics: Conference Series. 2866(1). https://doi.org/10.1088/1742-6596/2866/1/012073

Nurlina. Kadir. S. Kurnain. A. Ilham. W. & Ridwan. I. (2023). Impact of Land Cover Changing on Wetland Surface Temperature Based on Multitemporal Remote Sensing Data. Polish Journal of Environmental Studies. 32(3). 2281–2291. https://doi.org/10.15244/pjoes/157495

Rashid. M. B. (2023). Monitoring of drainage system and waterlogging area in the human-induced Ganges-Brahmaputra tidal delta plain of Bangladesh using MNDWI index. Heliyon. 9(6). https://doi.org/10.1016/j.heliyon.2023.e17412

Ridwan. I. Nurlina. & Putri. W. E. (2022). Estimation of Peatland Fire Carbon Emissions Using Remote Sensing and GIS Physics Study Program. Faculty of Mathematics and Natural Sciences Lambung Mangkurat. International Journal of Biosciences. 20(6). 246–253. http://dx.doi.org/10.12692/ijb/20.6.246-253

Shashikant. V. Shariff. A. R. M. Wayayok. A. Kamal. R. Lee. Y. P. & Takeuchi. W. (2021). Utilizing TVDI and NDWI to classify severity of agricultural drought in Chuping. Malaysia. Agronomy. 11(6). https://doi.org/10.3390/agronomy11061243

Sherstobitov. D. N. Ermakov. V. V. Bochkina. A. A. Tupitsyna. O. V. Bykov. D. E. & Chertes. K. L. (2021). Monitoring of the hydrological regime of the Saratov reservoir using the MNDWI index. IOP Conference Series: Earth and Environmental Science. 818(1). https://doi.org/10.1088/1755-1315/818/1/012048

Stehman. S. V. (1997). & Forestry. 320 Bray Hall. Syrxusr. NY 13210. In Remote Sens. Envihon (Vol. 62). OElsevier Science Inc.

Thanh Noi, P., & Kappas, M. (2017). Comparison of Random Forest, k-Nearest Neighbor, and Support Vector Machine Classifiers for Land Cover Classification Using Sentinel-2 Imagery. Sensors (Basel, Switzerland), 18(1). https://doi.org/10.3390/s18010018

Waleed, M. et al. (2023) 'Machine learning-based spatial-temporal assessment and change transition analysis of wetlands: An application of Google Earth Engine in Sylhet, Bangladesh (1985–2022)', Ecological Informatics, 75(March), p. 102075. Available at: https://doi.org/10.1016/j.ecoinf.2023.102075

Wu. L. Li. Z. Liu. X. Zhu. L. Tang. Y. Zhang. B. Xu. B. Liu. M. Meng. Y. & Liu. B. (2020). Multi-type forest change detection using BFAST and monthly landsat time series for monitoring spatiotemporal dynamics of forests in subtropical wetland. Remote Sensing. 12(2). https://doi.org/10.3390/rs12020341

Yan. X. Li. J. Yang. D. Li. J. Ma. T. Su. Y. Shao. J. & Zhang. R. (2022). A Random Forest Algorithm for Landsat Image Chromatic Aberration Restoration Based on GEE Cloud Platform—A Case Study of Yucatán Peninsula. Mexico. Remote Sensing. 14(20). https://doi.org/10.3390/rs14205154

Zhang. X. Liu. L. Zhao. T. Chen. X. Lin. S. Wang. J. Mi. J. & Liu. W. (2023). GWL-FCS30: a global 30m wetland map with a fine classification system using multi-sourced and time-series remote sensing imagery in 2020. Earth System Science Data. 15(1). 265–293. https://doi.org/10.5194/essd-15-265-2023

Zhu, Y. et al. (2024) 'Monitoring Land Use Changes in the Yellow River Delta Using Multi-Temporal Remote Sensing Data and Machine Learning from 2000 to '2020', pp. 1–18.

المملكة الأردنية الهاشمية

صندوق دعم البحث العلمي

الجامعة الهاشمية

المجلة الأردنية
لعلوم الأرض والبيئة

JJEES

مجلة علمية عالمية محكمة

المجلد (١٦) العدد (٤)

http:// jjees.hu.edu.jo/

ISSN 1995-6681

المجلة الأردنية لعلوم الأرض والبيئة

مجلة علمية عالمية محكمة

المجلة الأردنية لعلوم الأرض والبيئة: مجلة علمية عالمية محكمة ومفهرسة ومصنفة، تصدر عن عمادة البحث العلمي في الجامعة الهاشمية وبدعم من صندوق البحث العلمي - وزارة التعليم العالي والبحث العلمي، الأردن.

ترسل البحوث إلكترونيا إلى البريد الإلكتروني التالي:

رئيس تحرير المجلة الأردنية لعلوم الأرض والبيئة

jjees@hu.edu.jo

لمزيد من المعلومات والأعداد السابقة يرجى زيارة موقع المجلة على شبكة الانترنت على الرابط التالي:

www.jjees.hu.edu.jo

المملكة الأردنية الهاشمية
صندوق دعم البحث العلمي
Scientific Research Support Fund
الجامعة الهاشمية
THE HASHEMITE UNIVERSITY
JORDAN

JJEES

المجلة الأردنية لعلوم الأرض والبيئة

Indexed by Scopus
ELSEVIER

المجلد (16) العدد (4)

مجلة علمية عالمية محكمة تصدر بدعم من صندوق دعم البحث العلمي

ISSN 1995-6681
jjees.hu.edu.jo
كانون الأول 2025